DURBAN UNIVERSITY OF TECHNOLOGY
INYUVESI YASETHEKWINI YEZOBUCHWEPHESHE

Development of an adaptive protection scheme for compensated transmission network with high level penetration of renewable energy sources.

By

Ntombenhle Mazibuko

20818546

Submitted in fulfilment of the requirements of the degree of Doctor of Engineering in Electrical Engineering in the Department of Electrical Power Engineering, Faculty of Engineering and the Built Environment

Durban University of Technology

August 2025

Supervisor: Professor K.T. Akindeji

Co-Supervisor: Professor K. Moloi

DECLARATION

This dissertation is the student's own work, all cited work or text has been appropriately referenced. It has not partially or fully submitted at any other University. Prof. K.T Akindeji and Prof K. Moloi at the Durban University of Technology duly supervised this research.

Submitted by

……03 August 2025…….

Ntombenhle Mazibuko Date

Durban University of Technology

Department of Electrical Power Engineering

Student Number: 20818546

18 August 2025

……

Supervisor: Prof. Kayode T Akindeji Date

Durban University of Technology

Power Engineering

…18/08/2025…..

Co-Supervisor: Prof. Katleho Moloi Date

Durban University of Technology

Department of Electrical Power Engineering

DEDICATION

This work is dedicated to my Late mother Philile Margaret Sibisi and my kids Amahle, Abongwe and Mnotho.

ACKNOWLEGMENTS

I would like to begin by expressing my gratitude to God for providing me with the strength necessary to complete this work. I extend my appreciation to the Department of Electrical Power Engineering at the Durban University of Technology for their role in enhancing my skills from my undergraduate studies to this advanced level. I am also grateful to my supervisors, Professor K. Moloi and Professor K.T. Akindeji, for their unwavering support throughout this endeavour. Additionally, I wish to recognize Mrs. N. Chilli and Miss L. Bopape for their encouragement and belief in my abilities. I acknowledge my children and family for their understanding and cooperation during this journey. Finally, I commend myself for persevering and striving to the very end. I extend my sincere gratitude to the Faculty of Engineering and the Department of Electronics Engineering for providing me with the support that has expedited my academic progress. I participated in the THENSA PhD proposal writing program, and I would like to express my appreciation for their role in shaping the research from its inception, which significantly facilitated a seamless journey throughout.

ABSTRACT

The 2030 Agenda for Sustainable Development, adopted by all United Nations Member States in 2015, presents a unified framework designed to promote peace and prosperity for individuals and the planet, both in the present and for future generations. At the heart of this agenda are the 17 Sustainable Development Goals (SDGs), which call for immediate action from all countries regardless of their development status through a global partnership. Specifically, SDG 7 seeks to guarantee access to affordable, reliable, sustainable, and modern energy for everyone by 2030. South Africa, recognized as one of the most developed nations in Africa, is also the continent's largest energy consumer. The combination of a growing population and an ongoing power crisis has resulted in heightened electricity demand and a need for alternative energy solutions. In recent years, the country has launched various projects focused on renewable energy sources (RESs). However, despite these investments, the contribution of renewables—particularly wind, solar photovoltaic (PV), and concentrated solar power (CSP)—remains limited, accounting for only 13.7% of the total energy mix, which decreases to 7.3% when hydroelectric sources are excluded. Nuclear and diesel energy make up 4.6% and 1.6%, respectively. The ongoing gap between energy supply and demand remains a critical issue. Additionally, transmission line compensation techniques have emerged as a promising method to enhance transmission capacity, minimize losses, and improve stability within power systems.

Although these technique increases the energy availability factor, they frequently present technical challenges in the routine functioning of power systems, especially regarding network protection systems. Protection is crucial not only for ensuring system stability but also for the safety of equipment and personnel. Fundamental principles of any protection strategy encompass accuracy, selectivity, and reliability. This research introduces a machine learning-based protection scheme tailored for a compensated transmission line within a renewable energy network. Initially, a simple two-bus network is created, and a series capacitor compensation method is integrated to assess the impact of transmission line compensation on protection systems. Data is gathered and utilized across three different machine learning detection and classification techniques: K-Nearest Neighbours (K-NN),

Medium Neural Network (MNN), and Quadratic Support Vector Machine (QSVM). Additionally, the network is expanded to incorporate both solar and wind energy sources to evaluate performance with the inclusion of renewables. The classifiers are then tested and fine-tuned for enhanced performance. Performance metrics, including confusion matrix analysis, precision-recall curves, and ROC curves, are employed to assess the effectiveness of each machine learning approach. The results indicate that the accuracy and reliability of protection are influenced by the application of these techniques, as evidenced by the rate of fault misclassification. Moreover, machine learning methods show promise in enhancing the protection scheme's performance for a network architecture that includes a compensated transmission line and renewable energy sources. Among the classifiers, the SVM has emerged as the most effective machine learning classifier, achieving an average accuracy of 99.2%.

PUBLICATIONS ARISING FROM THIS WORK

The following publications emanated from this research investigation and form part and/or include research presented in this dissertation.

Published:

1. Mazibuko Ntombenhle, Kayode T. Akindeji, and Katleho Moloi. "A Review on the Impact of Transmission Line Compensation and RES Integration on Protection Schemes." Energies 17.14 (2024): 3433.
2. N. Mazibuko, K. T. Akindeji and K. Moloi, "Performance comparison of Machine Learning (ML) based fault detection scheme for a compensated transmission line," *2024 IEEE PES/IAS Power Africa*, Johannesburg, South Africa, 2024, pp. 1-5, doi: 10.1109/PowerAfrica61624.2024.10759459.
3. N. Mazibuko, K. T. Akindeji and K. Moloi, "The Application of Machine Learning Techniques to Evaluate the Impact of Transmission Line compensation on Fault Classification," *2024 International Conference on Emerging Trends in Networks and Computer Communications (ETNCC)*, Windhoek, Namibia, 2024, pp. 1-5, doi: 10.1109/ETNCC63262.2024.10767536.
4. N. Mazibuko, K. T. Akindeji, K. Moloi and G. Sharma, "Improved Model Predictive controller (MPC) for an Automatic Voltage Regulator (AVR)," 2024 32nd Southern African Universities Power Engineering Conference (SAUPEC), Stellenbosch, South Africa, 2024, pp. 1-6, doi: 10.1109/SAUPEC60914.2024.10445066.

Accepted for presentation

1. N. Mazibuko and T. K. Akindeji, K Moloi "The impact of RES integration on fault detection and classification for a compensated network," *2025 International Conference on Electrical, Computer and Energy Technologies (ICECET)*, Cape Town, France, 2025

CONTENTS

LIST OF FIGURES

LIST OF TABLES

LIST OF ACRONYMS

AC	Alternating current
ADFS	Adaptive droop frequency support
ANN	Artificial Neural Network
AUC	Area under the curve
CCM	Continuous conduction mode
CNN	Convolutional neural networks
CPS	Concentrated solar power
CSRI	Scientific and Industrial Research
DC	Direct Current
DCM	Discontinuous conduction mode
DC-OPF	DC optimal power flow
DFIG	Doubly Fed Induction Generators
DL	Deep learning
DPS	Distance protection scheme
DSOGI	Dual Second Order Generalized Integrator
ELM	Extreme Learning Machine
EMDAN	Empirical Mode Decomposition with Adaptive Noise
ESR	Energy Strategic Roadmap
ESS	Energy storage systems
FACTs	Flexible AC transmission system
FCCSC	Forced Commutation -controlled series capacitor
FCL	Fault current limiter
FFT	Fast Fourier Transform
FL	Fuzzy logic
FLL	Frequency Locked Loop
FPR	False positive rate
FRT	Fault ride-through
FRTC	Fault Ride Through Capability
FS	Fourier transform

GPU	Graphics processing units
GT	Gabor transform
GTOs	Gate Turn-Off
GTOs	Gate-turn-off thyristors
HAWT	Horizontal Axis Wind Turbines
HBO	Heap-based optimization
HHT	Hilbert-Huang transform
HT	Hilbert transform
HVDC	High voltage direct current
IBG	Inverter based generators
IGBT	Insulated-gate bipolar transistor
IGBTs	Gate-insulated bipolar transistors
IoT	Internet of things
IPPs	Independent Power Producers
IRP	Integrated Resource Plan
JET	Just Energy shift
KNN	K-Nearest Neighbors
KVL	Kirchhoff's Voltage Law
L-G	Line to ground
L-L	Line to Line
L-L-L	Line to Line to Line
L-L-L-G	Line to Line to Line to ground
MCTs	MOS-controlled thyristors
MIPPP	Municipal Independent Power Producer Programme
ML	Machine learning
MLI	Multi-Level Inverter
MNN	Medium Neural Network
MOSFET	Metal-oxide-semiconductor field-effect transistor
MOV	Metal Oxide Varistor
MPP	Maximum power point
MPPT	Maximum power point tracking
MTCs	Metal-Oxide-Semiconductor Controlled Thyristor

OSB	Out-of-step blocking
OVR	One-Versus-Rest
P&O	Perturb & Observe
PCA	Principal component analysis
PFR	Primary frequency response
PLL	Phase-lock-loop
PMUs	Phasor measurement units
PST	Phase shifting transformer
PV	Photovoltaic
PWM	Pulse Width Modulation
QSVM	Quadratic Support Vector Machine
RBFNN	Radial Basis Function Neural Network
REDZ	Renewable energy development zones.
RES	Renewable Energy Sources
RMS	Root-mean-square
RNN	Recurrent neural networks
ROC	Receiver operating characteristic
SC	Series capacitor
SCIs	Current source inverters
SCL	Short circuit levels
SLFNL	Single layer feedforward neural networks
SMIB	Single machine infinite bus
SPFS	Smart Power Flow controlled
SSR	Sub-synchronous resonance
SSSC	Synchronous Series Compensator
SSTIs	Sub synchronous torsional interactions
STATCOM	Static Synchronous Compensator
STC	Standard Test Conditions
STFT	Short-Time Fourier Transform
SVM	Support Vector Machine
SVO	Stator Voltage Orientation
SVR	Static VAR Compensator

TCR	Thyristor-controlled reactor
TCR	Thyristor-switched capacitors
TCSC	Thyristor Controlled Series Capacitor
THD	Harmonic distortion
TNEP	Transmission Network Expansion Project
TPR	True positive rate
UPF	Unified Power Flow Controller
VAWT	Vertical Axis Wind Turbines
VIC	Virtual inertia control
VSC	Voltage source converters
VSS	Virtual synchronous generators
WECS	Wind energy conversion system
WF	Wing Farm
WPPs	Wind Power Plants
WT	Wavelet Transform
ZCS	Zero current switching

Chapter one: Introduction

1.1 Research Background

South Africa is currently experiencing energy crises because of a mismatch between energy supply and demand. Increasing energy demand necessitates adequate operation of generation and transmission facilities to maintain the reliability of the power system. Transmission line compensation is used to increase the ability to transfer power, thereby enhancing system stability, voltage regulation, and reactive power balance. Also, in recent years, the introduction of renewable energy sources (RES) has proven to be effective in supporting the grid by providing additional energy. As a result, the dynamics of power systems have changed, and many developing nations are adopting the integration of renewable energy to the grid to increase the aspect ratio of energy availability factor. While both techniques contribute to the grid's ability to meet energy demand, they frequently introduce technical challenges that affect the stability and protection of the systems.

According to the Council for Scientific and Industrial Research (CSRI) report from February 2023, renewable energy technologies such as wind, solar PV, and CSP saw an increase in installed capacity in 2022, reaching a total of 6.2 GW and contributing 7.3% to the overall energy mix. Furthermore, the eThekwini Renewable Energy Roadmap technical report, building upon the Energy Strategic Roadmap (ESR), outlines the municipality's climate action objectives for 2030 and 2050. Through its Municipal Independent Power Producer Programme (MIPPP), eThekwini seeks to secure 400 MW of capacity from IPPs to ensure a reliable and diverse energy supply. These advancements highlight a clear change in the dynamics of power systems, as numerous developing countries are progressively embracing the integration of renewable energy to improve their energy accessibility. However, technical challenges arise due to this widespread adoption of renewable energy.Compensated transmission lines are utilized within power system networks to boost energy transmission capacity, enhance system stability, reduce transmission losses, and offer greater flexibility in managing power flow[1]. The non-linear properties of a series capacitor used for line compensation cause the impedance characteristics of the system to change rapidly, resulting in the generation of high-frequency signals. These signals interfere with the proper operation of relays by affecting voltage (V) and current (I). Consequently, the relay faces challenges in accurately identifying, categorizing, and locating faults[2]. When designing a protection

system for a compensated transmission line, two main occurrences must be considered which are current inversion and voltage inversion resulting from compensation. The majority of the extant literature has conducted the investigation without considering the incorporation of RES and the associated complexities. Although certain researchers have assessed the impact of RESs on conventional protection schemes, most researchers have investigated for a condition where the lines at point of penetration are not compensated, only the methodologies involving time-frequency analysis and real-time evaluation have been examined and windfarms are used as RES, most schemes are not tested or subjected to various system dynamics like power swing, higher levels of compensation. While adaptive distance protection strategies have addressed the issue of these schemes not being subjected to testing under dynamic system conditions. The investigation of the impact of various compensation levels and high penetration of different types of renewable energy sources is lacking in the literature. This research aims to investigate the impact of renewable energy integration into compensated transmission network, furthermore to develop an adaptive protection scheme for such networks.

1.2 Problem statement

Distance protection schemes generally consist of three sub-components, namely, fault detection, classification and location. Reliable performance of the schemes depends on good estimation of voltage, current and subsequently, impedance of transmission lines in frequency domain. Introduction of series compensation in transmission network as well as integration of generation based on renewable energy sources affect the apparent impedance seen by protection relays during normal and abnormal situation. In addition, issues like low frequency oscillation, voltage and current inversion, voltage regulation, low fault ride through are of great concern in modern transmission network with series compensation and a high level of renewable energy penetration. In this work we develop an adaptive scheme that can dynamically detect, classify faults in such afore mentioned network-based machine learning.

1.3 Aim and objectives

AIM: The aim of this research is to develop an adaptive protection scheme for a heavily compensated transmission line with high penetration of RESs can dynamically detect, classify and locate faults based on machine learning.

The Objectives are:

- Developing a simulation model and investigate the impact of transmission line compensation in protection scheme and assess its performance.
- Developing a machine learning based protection scheme to improve the performance of the model above.
- Developing wind and solar based RES simulation model, integrate this model into the existing compensated network to test the impact of RES in protection scheme.
- Proposing the Best Machine learning detection and classification technique of this network architecture.

1.4 Hypothesis

The combination of high levels of compensation on transmission lines and a high penetration RES will have a significant impact on the performance of conventional protective relaying systems. This effect will make detection, classification and location of faults in the protection of heavily compensated lines more difficult. In order to support this hypothesis, this study will investigate the following important points:

- The effect of heavily compensated lines on system performance: This study will examine how the presence of compensation in transmission lines impacts voltage regulation, power flow, fault currents, and system stability.
- The effect of RES integration on heavily compensated lines: This study will investigate the effect of renewable energy sources, such as solar and wind, on the performance of heavily compensated lines. This will entail studying the variations in power generation, reactive power compensation, and fault characteristics caused by the intermittent nature of renewable energy sources.
- Evaluation of existing protective relaying systems: This research will evaluate the performance of traditional protection schemes, including distance relays, in the context of significantly compensated lines with high penetration of renewable

energy sources. The efficacy of fault detection, classification accuracy, and coordination between protective devices will be evaluated.

- Development of a simulation model: Using simulation software such as Dig-Silent Power Factory, a detailed model of a power system network with an extensively compensated transmission line and high RES penetration will be developed. This model will precisely represent the system's electrical properties and dynamics.

By addressing these objectives and conducting a thorough analysis, the research seeks to shed light on the effect of compensation and integration of RES on transmission line protection schemes. It also aims to propose an optimized protection scheme that addresses the challenges posed by these factors, ultimately contributing to the development of the security and dependability of power systems with a significant contribution from renewable energy sources.

1.5 Research methodology

This research uses quantitative approach. Mathematical and simulation models, software tools are used to develop the machine learning based protection scheme. The research approach/strategy will can be summarised as followed

1. Developing a mathematical and simulation model of a power systems network that consists of heavily compensated transmission lines. Use the model to test the impact of degree of compensation energy on existing traditional protection scheme in this type of a network.
2. Use the model developed, integrating a model of the renewable energy source into this network to further investigate the impact of RES and compensation combination into traditional protection schemes.
3. Develop a machine learning fault detection and classification scheme for a compensated transmission line, a RES integrated network into a compensated line.
4. Develop a fault location algorithm based on machine learning, to be implemented on the above developed network.

1.6 Significance of the research

Transitioning to a low-carbon energy system, meeting renewable energy targets, and improving grid efficiency and reliability are all factors driving the market for integrating renewable energy sources in heavily compensated transmission lines. More and more nations and regions are embracing renewable energy legislation, which means there will be a greater need for renewable energy integration solutions. This market is primarily driven by utilities, renewable energy developers, researchers and technology providers specializing in grid integration solutions. Advanced power electronics, energy storage devices, and grid management software are just a few of the tools they offer to facilitate the incorporation of renewable energy sources. The current existing literature explores the integration of renewable energy, however at the point of coupling most of the lines are not compensated. Since transmission line also offers a wide range of advantages into supporting the grid in matching the supply with demands, and also improving the system stability it is an exciting opportunity to investigate the impact of these technologies combination of traditional protection schemes. Furthermore, Literature has also suggested certain proposals that utilize signal processing methods, involving a series of mathematical operations, to analyse signals of varying characteristics and recently the trend is focused on implementation of machine learning techniques to perform the fault detection and classification task which are major section for a protection scheme. Based on the literature it is observed that ML techniques are being explores as a solution is addressing challenges in transmission line challenges, however, this has been limited to un-compensated line are studied . Hence this research investigates the application of machine learning faults identification and classification for a compensated line using an IEEE 9 bus.

1.7 Limitations and delimitations

- Only transmission lines will be studied.
- Only PV and Wind Energy systems are covered in this research.
- ONE compensation technique will be used at one position along the protected line.
- The protection scheme only detects and classifies faults.

1.8 Contribution of this research

- In this work we develop an adaptive scheme that can dynamically detect and classify faults based on time-frequency measurements and machine learning.
- The scheme is developed for network with RESs integrated into a compensated line. It is tested for various faults and will be fast and accurate.

1.9 Thesis structure

Chapter 1: Introduction. This chapter elaborates on the research background of the study introducing the problem statement, the aim and objectives to solve the existing problem **Chapter 2:** Literature Review. This chapter provides the existing literature in the context of transmission network, compensated transmission line, RES integration, different concept on adaptive protection schemes and later identify the gaps missing in the literature.

Chapter 3: Compensated transmission network. This chapter discuses in details models of compensation techniques, their principle of operation, the impact of compensation onto current and voltage signals as well as the impact of compensation into voltage profile of a transmission line.

Chapter 4: Renewable Energy integration. This chapter discusses into details the concept of developing models for renewable energy integration including wind and solar energy sources. it also discussed the concept of power conversion circuits for renewable energy integration.

Chapter 5: Machine learning fault detection and classification scheme. This chapter discusses into details the mathematical representation sampling techniques, signals preprocessing, future extraction and classification techniques.

Chapter6: Methodology. This chapter elaborates on modelling and simulation of the models from Compensated transmission line, 9bus system and load flow analysis. Furthermore, the integration of 12MW RES and development of the Machine learning fault detection and classification scheme.

Chapter 7: Results, analysis and discussion. The findings of the study are discussed in this section for all the models developed in chapter 6.

Chapter 8: Conclusion and recommendations Conclusions on the preceding chapters and recommendations for future studies are presented in this chapter.

Chapter two: Literature Review

2.1 Introduction

Global energy cost increases, combined with the desire to minimize harmful fossil-based emissions, are driving the demand for global clean and efficient energy sources and systems [3]. As per the Department of Energy's report in South Africa, by the end of June 2017, 3,162 MW of electricity generation capacity had been added to the national grid through 57 independent power producer (IPP) projects. According to the CSRI report from February 2023, renewable energy technologies such as wind, solar PV, and CSP saw an increase in installed capacity in 2022, reaching a total of 6.2 GW and contributing 7.3% to the overall energy mix. The Department of Mineral Resources and Energy (DMRE) is inviting interested parties to register potential bids for the Seventh Bid Submission Phase (Bid Window 7) of the Renewable Energy Independent Power Producers Procurement Programme (REIPPPP). This call for proposals aims to solicit bids from Independent Power Producers (IPPs) to develop 5000 MW of new generation capacity, including 1800 MW of Solar PV and 3200 MW of Wind Power. Furthermore, the eThekwini Renewable Energy Roadmap technical report, building upon the Energy Strategic Roadmap (ESR), outlines the municipality's climate action objectives for 2030 and 2050.

Through its Municipal Independent Power Producer Programme (MIPPP), eThekwini seeks to secure 400 MW of capacity from IPPs to ensure a reliable and diverse energy supply. The MIPPP will be implemented in phases, with the aim of having this new generation capacity operational by July 2025 or sooner. These advancements highlight a clear change in the dynamics of power systems, as numerous developing countries are progressively embracing the integration of renewable energy to improve their energy accessibility. However, technical challenges arise due to this widespread adoption of renewable energy. These challenges include issues such as reduced inertia due to the replacement of traditional synchronous generators with virtual synchronous generators, fault ride-through capabilities to ensure the continuous operation of renewable energy sources (RES) during faults, uncertainties, voltage and frequency fluctuations, high fault currents, low generation reserves, and diminished power quality [4]. Compensated transmission lines are utilized within power system networks to boost energy transmission capacity, enhance system stability, reduce transmission losses, and offer greater flexibility in managing power flow[1]. The non-linear properties of a series

capacitor used for line compensation cause the impedance characteristics of the system to change rapidly, resulting in the generation of high-frequency signals. These signals interfere with the proper operation of relays by affecting voltage (V) and current (I). Consequently, the relay faces challenges in accurately identifying, categorizing, and locating faults[2].When designing a protection system for a compensated transmission line, two main occurrences must be considered: current inversion and voltage inversion resulting from compensation. If a fault arises where the total reactance is capacitive, it triggers current inversion, also known as current reversal. During this inversion, the current leads the voltage instead of lagging behind it. The probability of current inversion increases with greater levels of compensation. While current inversion is not a major issue at lower compensation levels, it becomes a concern as compensation increases. At higher levels, current inversion can affect faults along an extended section of the line, potentially reaching beyond the receiving end of the compensated line[5]. If a fault happens on a series-compensated transmission line and the impedance from the fault location to the relay point is capacitive while the overall impedance from the power system source to the fault stays inductive, it results in what's known as a voltage inversion in the power system.[6].

According to *Pilotto* in [7] it has been noted that compensating transmission lines can unintentionally increase the likelihood of encountering sub-synchronous resonance (SSR). This challenge arises from the interplay between an electrical mode of the series-compensated network and a mechanical shaft mode of a turbine-generator group. The repercussions of these interactions could potentially lead to the generation of harmful torsional forces. Transmission line are formally compensated using Flexible AC transmission system (FACTS) devices brings forth novel power system dynamics that necessitate thorough examination by system protection engineers[8]. Normally transmission lines are subjected to various fault conditions, such as L-L (line to line), L-G (line to ground), and even three-phase fault [9]. When these faults happen the protection, system is expected to isolate faulty system, reliability, accuracy and speed is one of the major priorities for any protection scheme. Distance protection relay is used to protect transmission line, these schemes used the system impedance seen by the relay to issue a trip signal. The effectiveness of the distance protection scheme (DPS) is significantly impacted by the integration of FACTS devices, as their inclusion may interfere with the coordination of protective relays, leading to both under-reaching and over-reaching of the relays [10]. Distance relays are commonly employed for the

protection of transmission lines. Distance relays face several challenges when protecting compensated lines, such as fault detection, classification, and location, due to voltage inversion, current inversion, and low-frequency oscillation and the presence of harmonics in the context of compensated transmission line protection, hence the relay perceives a defect as an impedance mismatch with the compensation surface. From [11] in stated that many instances, protective relays for transmission lines have unfortunately triggered due to harmonics present in the power system.

The other concept that affects the distance relay when protecting compensated line is compensation level. This is described as the percentage of the reactive impedance to cancel the inductive reactance of the line. The added reactive impedance to the system to the compensation level is dependent upon the quantity of capacitors connected to the line, and a proficient understanding of the compensation level on the relay-side is imperative for the accurate functioning of distance relays. The presence of fluctuation in the reactance of capacitors requires the implementation of adaptive distance protection mechanisms [12] to improve the performance of the relays protecting such systems. It is hypothesized that the complexity of a transmission line protection system may be further increased when the integration of RES into a compensated transmission line. Consequently, the conventional transmission line protection schemes may not be sufficient, this necessitates further investigation into the impact of integrating RES on existing protection schemes for heavily compensated lines [13]. The majority of the extant literature has conducted the investigation without considering the incorporation RESs and the associated complexities. Although certain literature have assessed the impact RESs on conventional protection schemes, most researchers have investigated for a condition where the lines at point of penetration are not compensated, and only the methodologies involving time-frequency analysis and real-time evaluation have been examined particularly for windfarms, it is also noted that most schemes are not tested or subjected to various system dynamics like power swing, higher levels of compensation.

While adaptive distance protection strategies have addressed the issue of these schemes not being subjected to testing under dynamic system conditions. The investigation of the impact of various compensation levels and high penetration of different types of renewable energy sources is lacking in the literature. This research work provides a thorough examination of the challenges posed by the integration of Renewable Energy Sources (RES) and the significant

compensation levels on transmission line protection schemes. It also explores various techniques employed to address these challenges. This paper reviews the techniques available in literature to address the challenges presented by lines compensation and RES integration into power systems network operation including the protection systems, it then makes recommendation for further research that maybe conducted to improve the protection system of compensated transmission line with penetration of RES.

2.2 The landscape of renewable energy in south Africa

Recent investments in renewable energy technologies have not significantly altered the energy landscape, as wind, solar photovoltaic (PV), and concentrated solar power (CSP) collectively represent a mere 13.7% of the overall energy mix, which drops to 7.3% when excluding hydroelectric power. In contrast, coal remains the dominant energy source in South Africa, contributing to 80% of the country's electricity generation. Additionally, diesel and nuclear energy account for 2.6% and 4.6% of the energy supply [14]. In 2003, South Africa introduced a white paper outlining a strategy aimed at generating 10 TWh of electricity from renewable energy sources such as biomass, wind, solar, and small-scale hydroelectric power. Following this initiative, an integrated resource plan was adopted in May 2011, which set a new target to enhance the contribution of renewable energy to the energy mix, aiming for a capacity of 17,800 MW by the year 2030 [15]. RSA's annual power demand is predicted to increase from 345 TWh to 416 TWh by 2030, compared to the Department of Energy's 454 TWh projection in the Integrated Resource Plan (IRP) for power document [16]. Furthermore, Eskom's Just Energy Transition (JET) Office was founded in early 2020 and has advanced the shift towards a greener and cleaner energy future with notable advancements.[17]. "Just" clarifies that there won't be any detrimental effects on society, employment, or livelihoods from this transition, which is defined as the progressive shift towards lower carbon technology. The future growth and sustainability of the nation depend on the Just Energy Transition

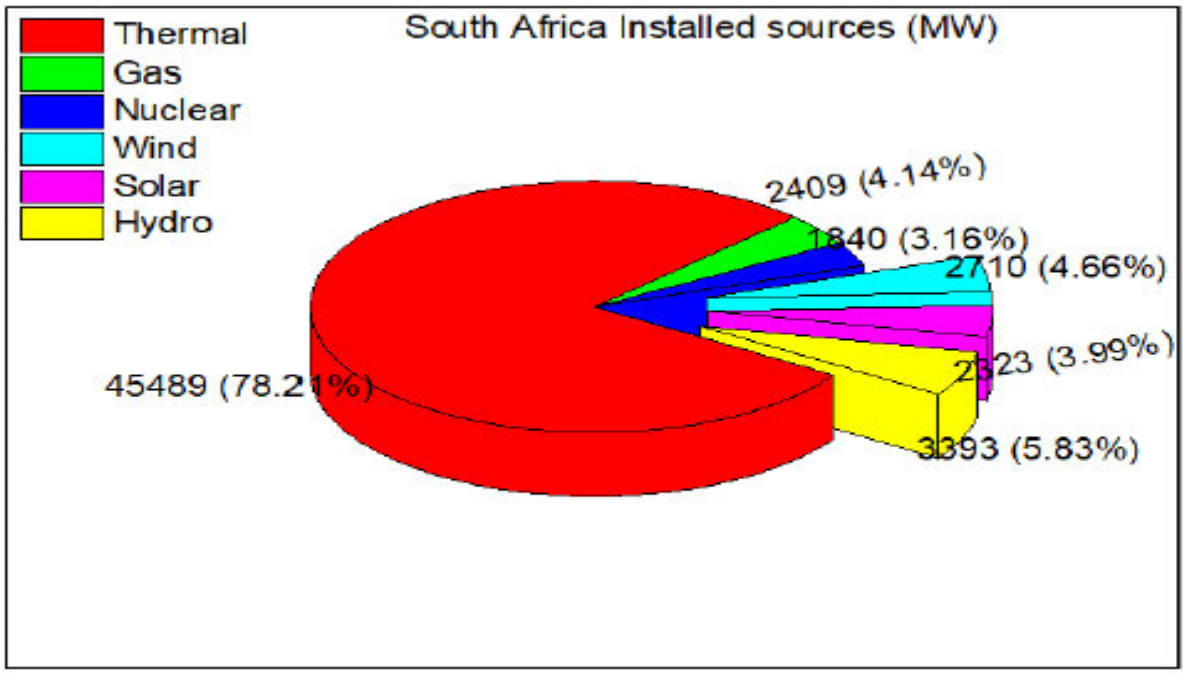

Figure 2. 1 The status of installed RESs in South Africa [18].

The installed capacity of renewable energy sources in South Africa is illustrated in Figure 2.1, which emphasizes the dominance of hydroelectric, solar, and photovoltaic energy systems. This observation is corroborated by the real-time data presented in Table 2.1 on the Eskom website. Access to this report is available through the Eskom website[19]. Furthermore, Table 2.1 outlines the total annual contributions of renewable energy, based on information supplied by various operators. The contributions from both Eskom and Independent Power Producers (IPPs) are included in the wind energy statistics. Table 2.2 details the annual quantity of renewable energy integrated into Eskom's grid for the years 2023–2024

Table 2. 1Renewable energy statistics as at 23/06/2024

Indicator	Current installed capacity (MWh)
CPS	500.00
PV	2287.1
Wind	3442.6
Total	6280.2

Table 2. 2 Annual contribution of Renewable energy contribution based on operator's data.

Year	Indicator	CPS	PV	Wind	Total
All	Annual energy	1670540	5095753	11576709	18186108
2023-24	Total energy	1307048	5095753	11576709	18186108
2024-25	Total Energy	229474	941593	2382877	3615973

Figure 2.2 illustrates the hourly contributions to the energy grid. The data presented clearly indicates that wind energy serves as the dominant contributor to grid enhancement, with an output exceeding 2500 MWh, whereas photovoltaic systems contribute more than 1750 MWh. This evidence underscores the growing incorporation of renewable energy sources within the South African grid network. The integrated resource plan represents a comprehensive long-term energy strategy that outlines the necessary infrastructure and electricity generation mix for South Africa, aiming to ensure affordable and sustainable energy security while minimizing water consumption and reducing carbon dioxide emissions [6].

Eleven geographic areas identified as conducive to the extensive development of solar photovoltaic and wind energy are designated as renewable energy development zones. The REDZs facilitate geographical dispersion in the placement of renewable energy (RE) facilities by optimizing the allocation mix of RE capacity and determining future plant locations within the framework of national grid support [20], these zones are shown in figure 2.3 and highlights a great potential for renewable energy integration in South Africa.

The coal industry in South Africa is facing significant job losses, compounded by the absence of local manufacturing for renewable energy components. Additionally, high entry barriers hinder competitiveness within the renewable energy sector, while a critical skills shortage and insufficient grid capacity for integrating renewables in resource-rich areas further complicate the situation. To tackle the performance challenges associated with renewable technologies, it is recommended to conduct research and perform a cost-benefit analysis on alternative complementary technologies that can provide essential grid services. Furthermore, in the context of networks that incorporate renewable energy, our research advocates for the development of enhanced protective systems, support for grid stability, and improved

technologies to facilitate the integration of renewables, thereby ensuring the stability of the grid is preserved.

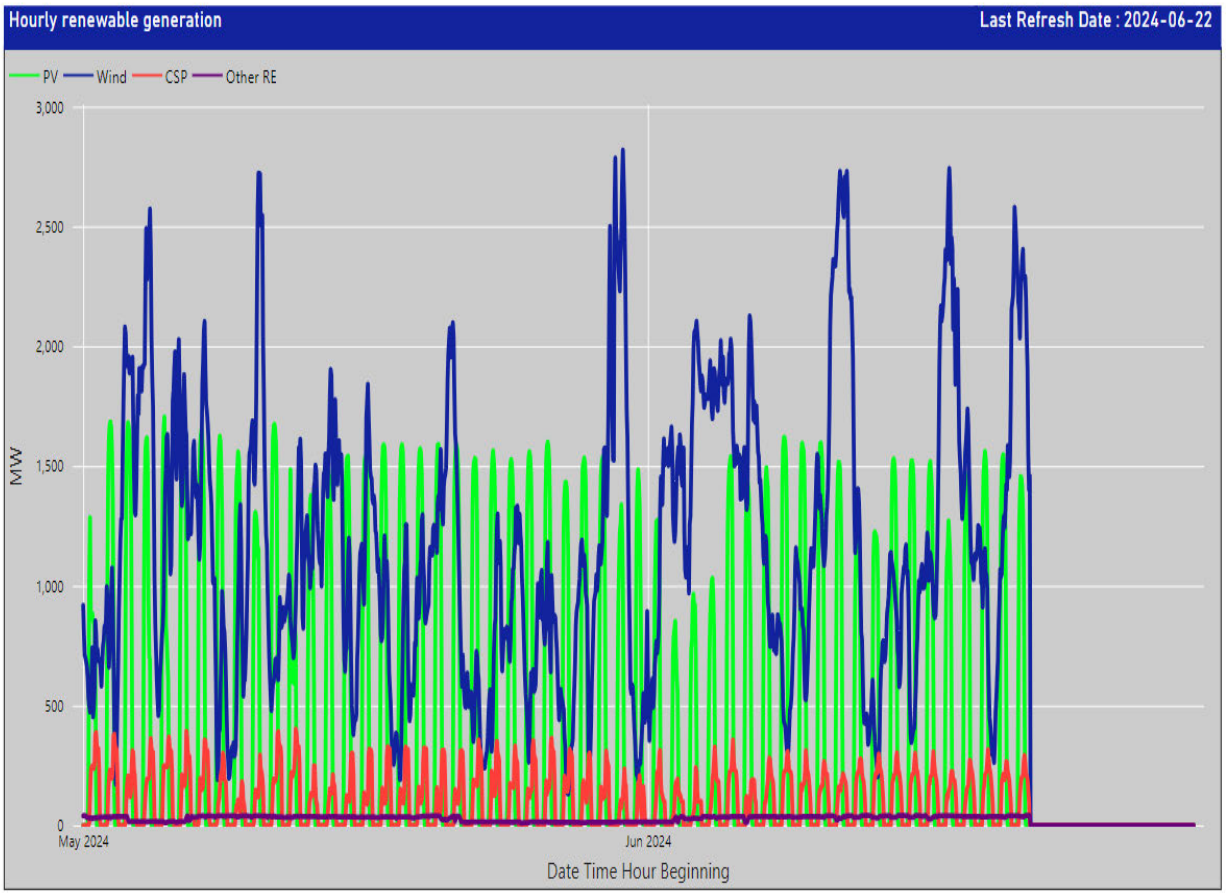

Figure 2. 2 Eskom's hourly renewable energy generation[21]

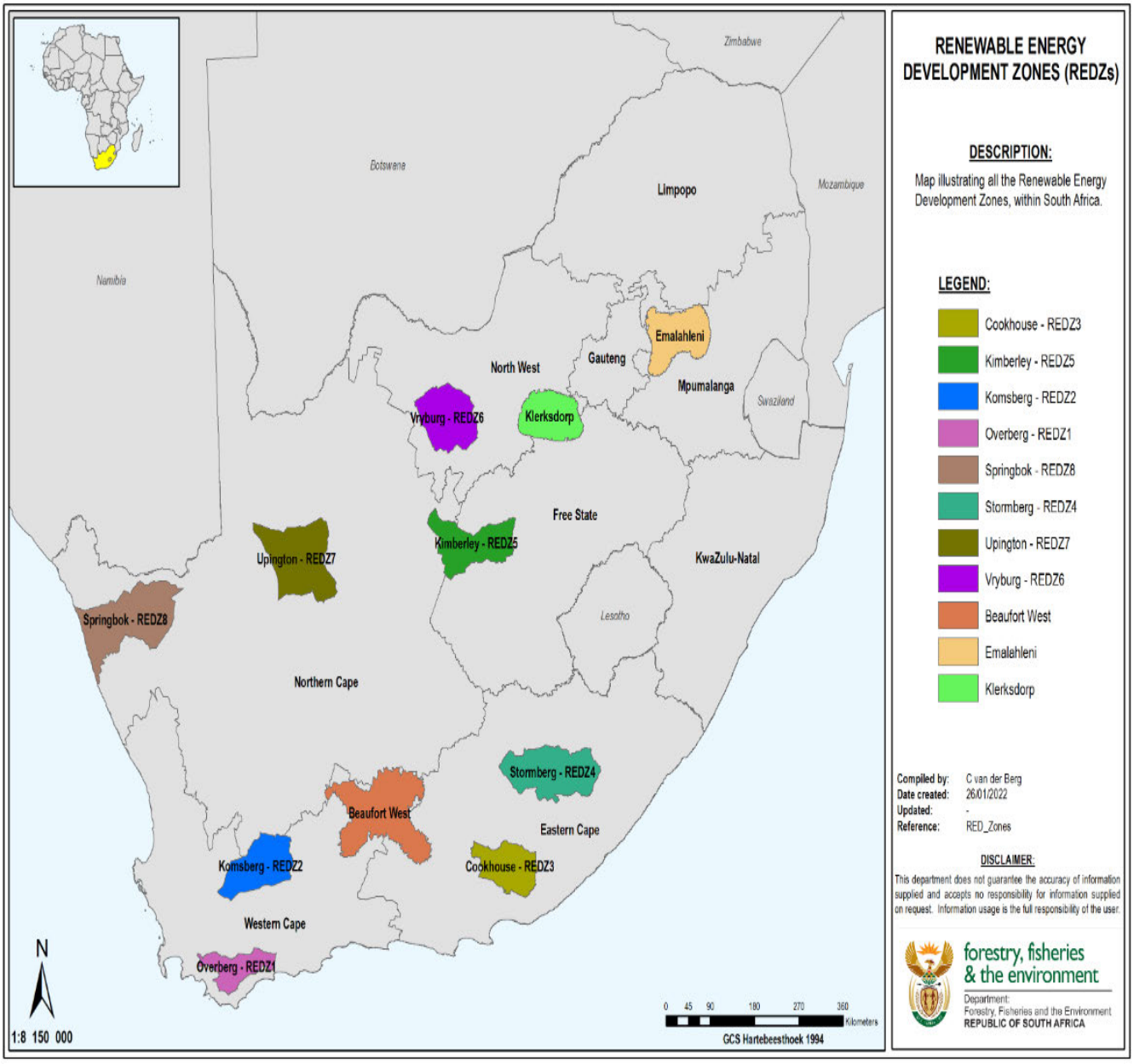

Figure 2. 3 South African Renewable Energy Development Zones. [22]

2.3 The Concept of Transmission Line Compensation

Energy transfer plays a crucial role in the functioning of power systems. The management of Power Transmission Lines is essential for maintaining voltage stability, minimizing losses, and regulating the flow of reactive power to mitigate harmonics. To achieve these objectives, Flexible Alternating Current Transmission Systems (FACTS) devices are employed [23]. The evolution of contemporary power systems has resulted in heightened complexity in the analysis of these systems, simultaneously introducing new challenges related to their stability.

This is particularly evident in the domains of transient stability, protection mechanisms, and small-signal stability [24]. FACTS devices play a crucial role in the compensation of transmission networks. Among these, the Static VAR Compensator (SVC) is one of the pioneering types of FACTS devices, specifically engineered to manage voltage levels at particular buses. This regulation significantly improves the voltage profile of the electrical network. The primary purpose of an SVC is to maintain the voltage at a specified bus by providing reactive power compensation, which is accomplished through the modulation of the thyristors' firing angle [9]. SVCs have been employed for enhanced performance in both steady-state and transient voltage regulation, surpassing traditional shunt compensation methods. Additionally, SVCs play a crucial role in mitigating power oscillations, enhancing transient stability, and minimizing system losses through the optimization of reactive power management [25].

The Thyristor Controlled Series Capacitor (TCSC) represents a significant component within the FACTS family, gaining prominence in contemporary power systems, particularly in the context of long transmission lines utilized by utility companies. Its functionality encompasses a range of critical roles in the management and regulation of power systems, including the optimization of power flow scheduling, the reduction of asymmetrical components, the minimization of net losses, the provision of voltage support, the limitation of short-circuit currents, the mitigation of sub-synchronous resonance (SSR), the damping of power oscillations, and the enhancement of transient stability [24]. The Unified Power Flow Controller (UPFC) possesses the capability to independently regulate various parameters due to its integration of the Static Synchronous Compensator (STATCOM) and the Static Synchronous Series Compensator (SSSC). Numerous studies have indicated that the UPFC enhances the stability of both single machine infinite bus (SMIB) systems and multimachine systems [26].

The UPFC possesses the capability to independently regulate various parameters due to its integration of the STATCOM and the SSSC. Numerous studies have indicated that the UPFC enhances the stability of both SMIB systems and multimachine systems[27, 28]. Transmission line compensation can be classified into two main types: shunt compensation and series compensation. This study focuses on the effects of series compensation through the use of a TCSC safeguarded by a Metal Oxide Varistor (MOV). The analysis is conducted by examining the fault characteristics on the R/X plane within a two-bus system. Additionally, a machine

learning-based approach for fault detection and classification is employed to enhance the precision of the compensated network in identifying and categorizing faults

2.3.1 The principle of shunt compensation

The primary aim of implementing shunt compensation within a transmission system is to provide reactive power, thereby enhancing the capacity for power transmission and aligning it more effectively with the existing load requirements. Consequently, the shunt compensator must effectively reduce line overvoltage during light load scenarios while ensuring stable voltage levels during periods of heavy load. An optimal shunt compensator is ideally situated at the midpoint of the transmission line[29], the equivalent circuit is shown in Figure 2.4 .

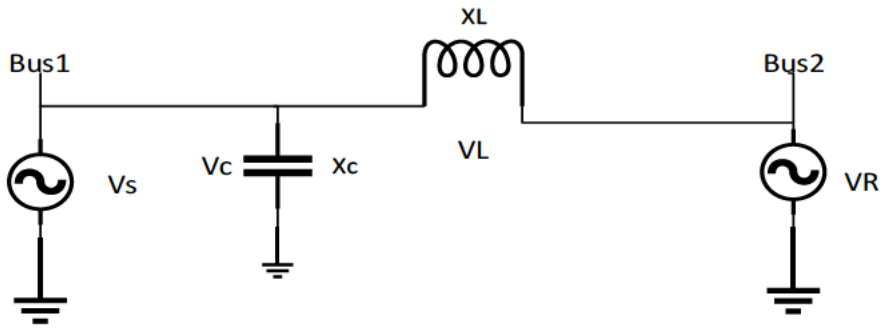

Figure 2. 4 Figure 1 Transmission line model with Shunt capacitor [30]

In shunt compensation, a current is introduced into the system at the connection point. This can be achieved by adjusting a shunt impedance, a voltage source, or a current source. Provided that the injected current is in phase quadrature with the line voltage, the shunt compensator exclusively provides or absorbs variable reactive power [31]. Power converters that utilize thyristors, gate-turn-off thyristors (GTOs), MOS-controlled thyristors (MCTs), or gate-insulated bipolar transistors (IGBTs) are capable of regulating the injected current or the compensating voltage[32]. Shunt compensators can be further classified into three distinct types: Static VAR compensators, Thyristor-controlled reactors, and Thyristor-switched capacitors.

2.3.2 The principle of Series compensation

A voltage can be applied in series with the transmission line to regulate the current flow, consequently influencing the power transfer from the sending end to the receiving end. An optimal series compensator, depicted as the voltage source V_c, is positioned at the midpoint of the transmission line, as illustrated in Figure 2.5.

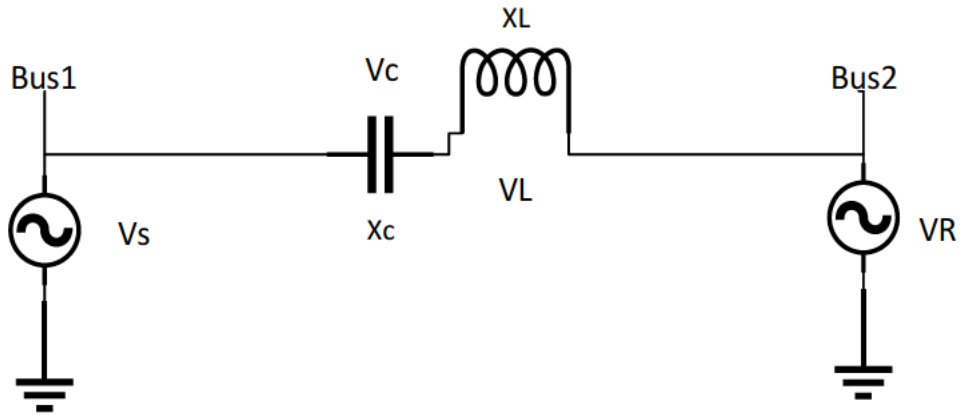

Figure 2. 5: Transmission line with series compensation [33]

A series compensator fundamentally introduces additional voltage in series with the transmission line. This voltage is governed by a variable impedance that is directly proportional to the current flowing through it, thereby generating a series voltage along the line. When this voltage is in phase quadrature with the line current, the series compensator can either supply or absorb variable reactive power exclusively. As a result, the series compensator may take the form of a variable impedance, such as a capacitor or an inductor, or it may utilize power electronics to create a variable source of fundamental frequency, sub-synchronous, and harmonic frequencies, or a combination of these, to achieve the desired control strategy.

2.3.3 Challenges introduced by series compensation

The implementation of series compensation in transmission lines presents numerous challenges for distance protection, especially at the elevated compensation levels that have become increasingly prevalent. Conventional distance protection systems face significant difficulties when confronted with high series compensation. As the level of compensation rises, a greater length of the line undergoes voltage and current inversion during fault conditions. The fault trajectories depicted in the R-X plane indicate that such inversions can lead to directional ambiguities and delays in the operation of the distance relay [34]. A

significant current inversion can adversely affect line current differential schemes, which are predominantly compensated at one terminal and necessitate further analysis to accurately establish the operational and restraint parameters of the line current differential. Lowering the compensation level to mitigate the severity of the current inversion is not a viable solution; instead, an increase in the compensation level is essential to attain the intended enhancements in transmission capacity [6]. The inclusion of series compensation within the fault circuit can lead to notable phase shifts in various electrical parameters, such as fault current, phase currents, sequence currents, and both phase and sequence voltages, relative to their inherent positions. For example, figure 2.6 illustrates a loss of directional integrity that arises when there is a change of 90 degrees or more in the voltage phase angle due to end line compensation, a phenomenon referred to as "voltage inversion." This situation typically arises in faults occurring downstream of the series compensator, where the total source impedance (ZS) significantly exceeds the impedance of the fault line.

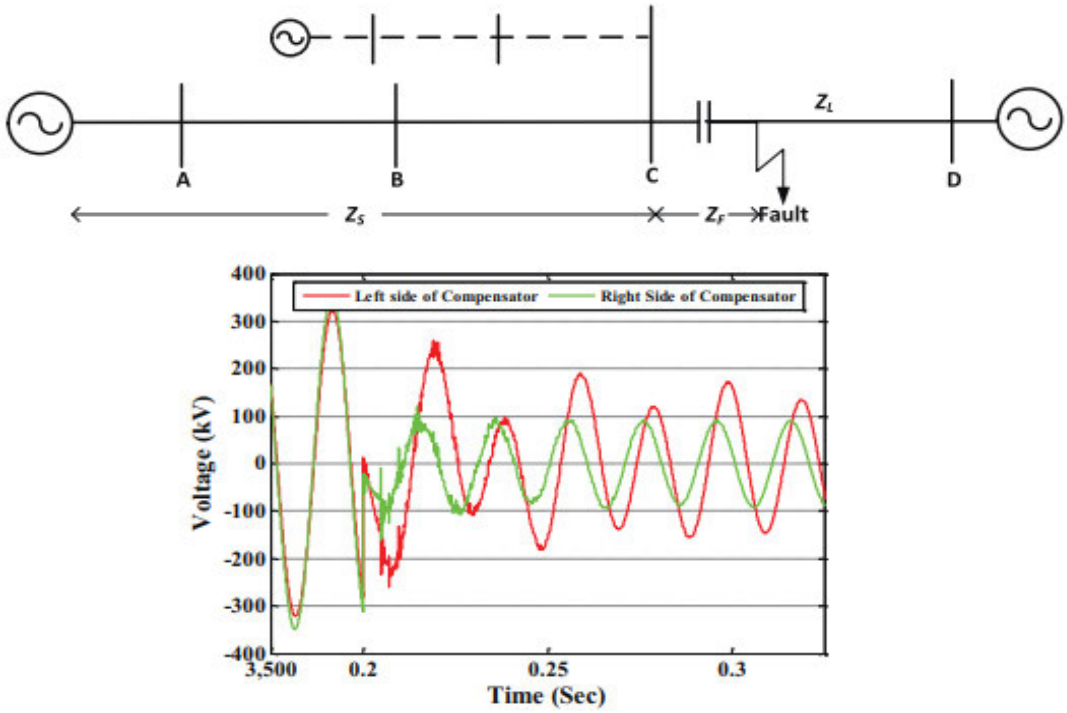

Figure 2. 6 current inversion in compensated lines[6]

2.4 The impact of FACTS devices on protection

FACTS devices introduce an innovative concept that utilizes power electronics and controllers to enhance the controllability and capacity expansion of transmission networks, while also offering opportunities to improve control operations and stability in transmission systems. The underlying technology of FACTS involves advanced high-power electronics that incorporate various thyristor devices for future advancements. These are supported by advancements in digital protective relays, controls, and integrated communication systems. These devices enable the regulation of critical parameters and characteristics of transmission lines, such as impedance, admittance, and voltage (both angle and phase), which are fundamental constraints on power transmission. Detecting, categorizing, and locating faults in transmission lines compensated by FACTS devices and series capacitor (SC) is considerably more complex than traditional lines due to the presence of time-variant voltage and current sources in the line's structure. Included among these devices are Thyristor-Controlled Series Capacitors (TCSC), Static VAr Compensators, Static Synchronous Compensators (STATCOM), Static Synchronous Series Compensators, and Unified Power Flow Controllers (UPFC). The presence of FACTS devices and SCs in transmission lines results in continuous changes in line impedance, presenting significant challenges for line protection[35]. TCSC and UPFC emerge as the two most crucial devices, widely deployed on high-voltage transmission lines [36].

The UPFC is comprised of a STATCOM and a SSSC , as illustrated as figure 6 of [37]. The parameters of voltage (V), current (I), and phase angle can be adjusted independently. This, consequently, aids in the autonomous regulation of both active and reactive power flows within a transmission line [38]. The voltage and current signals experience significant alterations as a result of the UPFC controllers, both during transient conditions and in a steady state. Hence the performance of the standard distance relay is significantly affected due to the nonlinearity in output power resulting from diverse operational modes of the UPFC [39]. The impedance measurement will exhibit an increase as a consequence of the incorporation of the UPCF due to the aforementioned phenomenon, it is possible for the impedance relay to exhibit overreaching or underreaching. In [40] UPFC was designed to regulate the voltage of transmission lines and bus voltages apart from the reactive and active electrical power they carry. It is suggested that factors such as installation point, operating modes, fault location,

fault resistances, fault inception angles, fault types, and external faults must all be considered while designing the protective system of transmission line compensated using the technique. The STATCOM acts as a controller for reactive power compensation, operating in parallel with the system. Advances in power electronics, particularly with the GTO thyristor, have made it feasible to implement this technology practically, offering a viable alternative to traditional SVCs. The torsional properties of remote generators can be modified by implementing an SVC within an advanced transmission system that utilizes series capacitors for compensation. The torsional interaction is significantly influenced by various parameters such as system loading, the level of series compensation, the operating point and control setting of the SVC, and other relevant factors[41].The management of reactive power flow is governed by the relationship between the AC voltage of the system and the voltage at the STATCOM's AC terminals. If the voltage at the STATCOM terminals exceeds the system voltage, the STATCOM functions as a capacitor, injecting reactive power from the STATCOM into the system. Conversely, if the STATCOM voltage falls below the AC voltage, it behaves as an inductor, causing the reversal of reactive power flow. Under normal operating conditions, both voltages are equal, resulting in no power exchange between the STATCOM and the system[42].

The SSSC, as a series-connected FACTS device, has the capability to provide either inductive or capacitive voltage regardless of the current in the transmission line, within its rated current limits. Additionally, the SSSC has the capacity to exchange both active and reactive power with the AC system, primarily by regulating the angular position of the injected voltage.[43]. In [44] The SSSC, functioning as a series-connected FACTS apparatus, is capable of supplying either inductive or capacitive voltage independently of the current in the transmission line, within its specified current limits. Moreover, the SSSC can exchange both active and reactive power with the AC system, primarily by controlling the angular position of the injected voltage [45]. According to [46] Enhancing the dynamic performance of power systems, regulating power factor, voltage management, and stabilizing power flow can be enhanced through the integration of a STATCOM. Additionally, it can effectively mitigate Sub synchronous Resonance (SSR). However, to adequately suppress SSR, an auxiliary controller needs to be incorporated alongside the STATCOM.

The TCSC consists of a capacitor that is connected in series with a Thyristor Controlled Reactor (TCR) and an antiparallel thyristor [47]. To protect the capacitor against over-voltage, a metal oxide varistor (MOV) is employed. On the contrary, the TCR alters the impedance of the TCSC

by manipulating the firing angle of a thyristor, thereby boosting the fundamental voltage across the fixed capacitor. When the voltage is altered, the series capacitive reactance adapts correspondingly[9]. Hence the impedance seen by the relay is influenced by the presence of a TCSC in the fault loop. These influences affect both the inductive and capacitive modes of operation[48]. When thyristors are triggered in close proximity to the zero crossing of the capacitor voltage, the capacitive reactance has the potential to increase up to 2-3 times the fixed capacitor reactance. Miscoordination, overreaching, and other operational challenges arise when the TCSC switches between different modes of operation. To mitigate these challenges, it is recommended to employ adaptive and pilot protection schemes. Since the positive-sequence impedance as determined by the conventional stand-alone distance relays becomes ineffective in determining the fault distance due to rapid changes brought about by the associated TCSC control actions in the primary-system parameters, including line impedances and load currents, throughout the fault duration[49].

Power swings are also a consequential matter arising from line compensation, as the impedance seen by the distance relay during a power swing may encroach upon the relay's operational region, which is deemed undesirable[50],this occurrence will result in an erroneous trip and instigate instability within a system. The occurrence of an out-of-step issue may arise when the swing exhibits instability, leading to a loss of synchronization within the system [51]. The implementation of an out-of-step blocking (OSB) strategy prevents the inhibition of protection relays' activation in the presence of a stable power swing[50, 52]. The presence of harmonics introduced by implementing transmission line compensation on the power system networks ,affects the accuracy of the distance protection, the first-zone protection would not detect the faults at the reach setting[11].

In [53] Smart Power Flow controlled (SPFC) is introduced, utilizing a 48-pulse converter, compensates for the reactive power of the power grid. The maximum power is achieved in SSSC at an injected voltage angle of 90 degrees when using a 48-pulse STATCOM, and harmonic distortion is minimized. In[54, 55] a VSC-Base STATCOM is investigated using ANN-based closed-loop control techniques, this article shows how to regulate the reactive power produced by a long transmission line across a broad area, keeping the voltage profile at the receiving end constant. Harmonics are reduced to a tolerable level using ANN method and H-bridge multilevel VSC architecture. Authors in [56] uses of fuzzy logic (FL) based controller for UPFC, in their work line currents total harmonic distortion (THD) is reduced below 5%,

reactive power adjustment, and voltage sag mitigation. Furthermore, a comparison is made between the performance of the proposed FL based UPFC and proportional integral (PI) based controller under varying transmission network operating conditions, with the results showing that the FL based UPFC provides superior results.

Depending on the design, these compensation devices may be situated in various locations such as the midpoint of the line, at the busbar near the generating station, or at the distant busbar toward the load. Determining the optimal placement of these devices is crucial for maximizing their benefits. Achieving desired operating characteristics involves continuously adjusting the location of the FACTS device along the transmission line [29, 57]. According to [58] FACTS devices achieve optimal voltage support when strategically positioned at the midpoint of the transmission line. Moreover, an in-depth examination of FACTS device applications is presented in article[57] which reviews research from the past decade on different methodologies for placing FACTS devices. This research utilizes a meta-heuristic approach to address the placement of FACTS devices, aiming to maintain appropriate bus voltages, control line flow, and enhance overall system efficiency. Literature provides an extensive analysis of the prospective methodologies aimed at mitigating the emerging challenges associated with introduction of FACTS devices for transmission line compensation this is summarized in table 2.3 highlighting different techniques, their contribution including the challenges each work is trying to address

Table 2. 3 summary of problems associated with adding FACTs devices

Reference	The problem solved	contributions
[59]	The standard fault characteristics associated with Doubly Fed Induction Generators (DFIG) and (TCSC have a significant impact on the efficacy of traditional distance relays	This article presents a novel relaying algorithm that employs the sign of the half-cycle superimposed positive-sequence current for the purpose of fault detection. Additionally, it incorporates an empirical mode decomposition-assisted random forest classifier for the classification of faults, along with a modified impedance method for estimating the location of faults
[31]	To investigation the impact of sub-synchronous torsional	An advanced linear state model of the power system is developed that allows detailed evaluation of the impact of FACTS controllers for sub

	interactions, an analytical tool is developed	synchronous torsional interactions (SSTIs) between turbine-generator rotors and (SVCs in longitudinal power systems
[60]	Optimal Positioning of TCSC to Enhance Voltage Stability Limits While Considering Effects on the Settings of Distance Protection Relays	Optimal Positioning of TCSC to Enhance Voltage Stability Limits While Considering Effects on the Settings of Distance Protection Relays.
[61]	The research examined how various firing control strategies influence the SSR.	This paper presents a qualitative investigation into the impact of thyristor-controlled series capacitors (TCSC) on distance protection strategies for power systems. Additionally, it proposes enhancements to the traditional distance protection logic

Transmission line compensation can be classified into three distinct categories: shunt compensation, series compensation, and a combination of series and parallel compensation, as illustrated in Figure 2.7. Additionally, the specific technologies employed within each category are detailed for every classification.

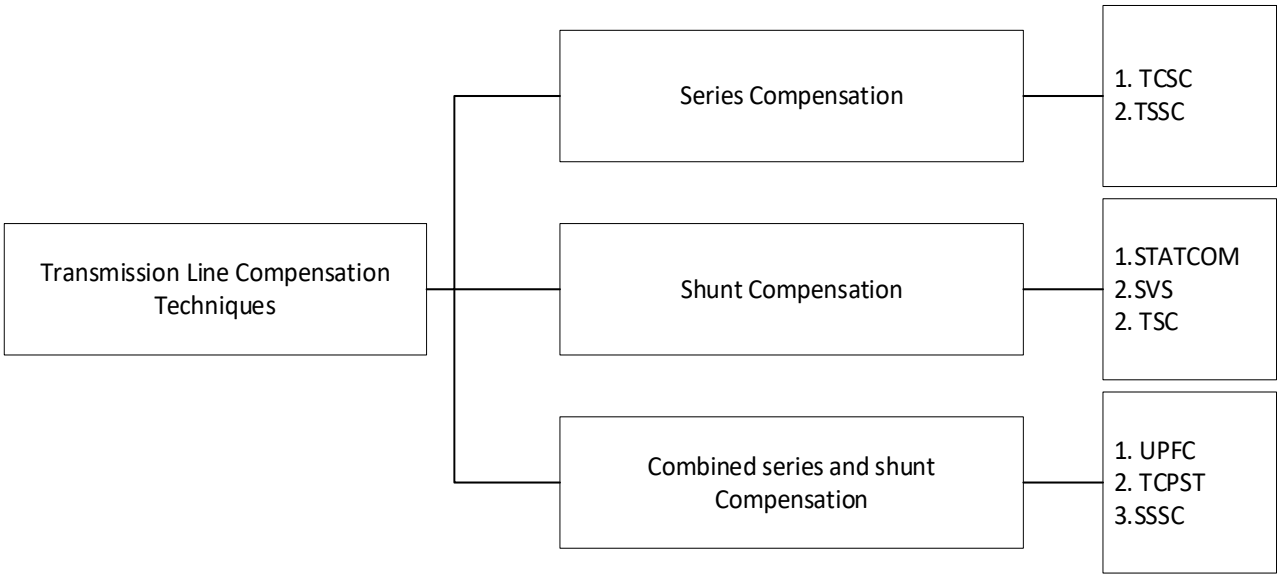

Figure 2. 7 Transmission line compensation

Also, the fault is applied at a time of 0.5 seconds. Following the occurrence of a fault, from figure 2.8 it is observed that the fault current in the uncompensated line reaches its maximum value, whereas the fault current in the series capacitor experiences a delayed peak. The aforementioned phenomenon results in a temporal lag in the operational functionality of the

protection system, as indicated by [62]. Moreover, in the aforementioned series compensated illustration, an oscillation characterized by a low frequency range spanning from 0.1 to 0.25 is observable. The figure depicted in Figure 2.9 illustrates the manifestation of delays in the estimation of impedance caused by series compensation. Both of these pathways depict the identical fault scenario, one for a compensated line and the other for an uncompensated line. The trip signal from the distance relay can be generated within a time frame of 1-2 power-frequency cycles, assuming the absence of a series capacitor that would otherwise impede the trajectory's transition from the pre-fault state to the final operating region. However, by implementing compensation techniques, the relay is able to cover the same distance in approximately 80 milliseconds, thereby enabling the delivery of a trip signal within a span of 4-5 cycles. In the realm of safeguarding high-voltage transmission lines, any form of delay is deemed unacceptable [63].

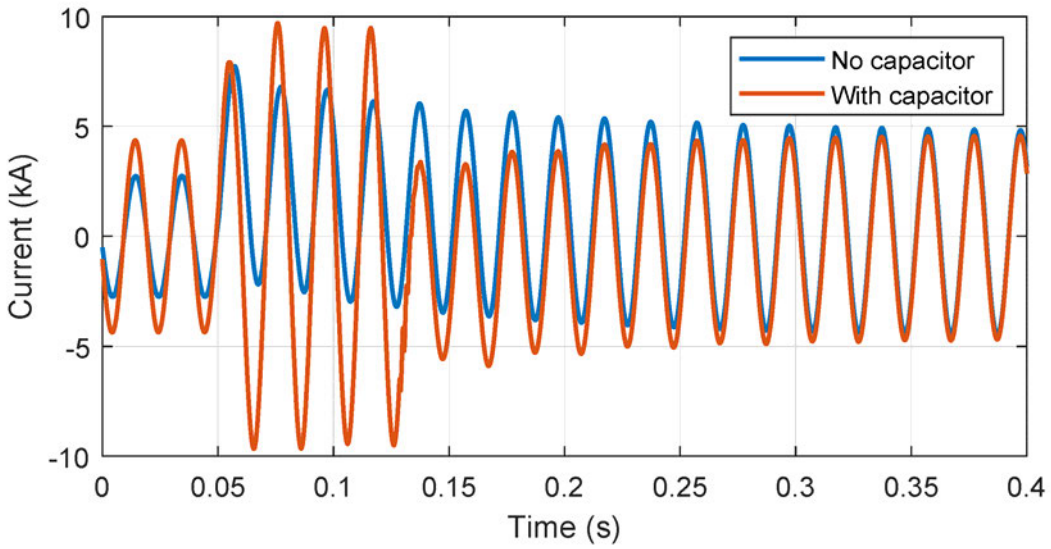

Figure 2. 8 Fault levels comparison for compensated and uncompensated lines [64].

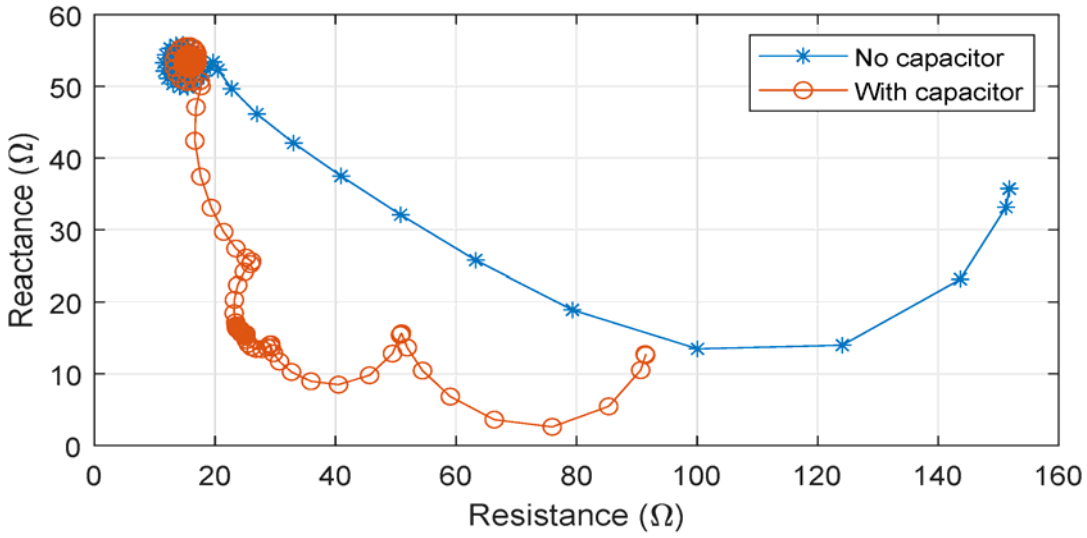

Figure 2. 9 Delays caused in impedance estimation in series compensated lines [64].

Power swings are a consequential matter arising from line compensation, as the impedance encountered by the distance relay during a power swing may encroach upon the relay's operational domain, which is deemed undesirable[50], this occurrence will result in an erroneous trip and instigate instability within an impacted system. The ability of the transmission lines to transfer power and the rotor angle are the key factors that determine their stability or instability. At a certain juncture, the power oscillation will reach a state of equilibrium. The occurrence of an out-of-step issue may arise when the swing exhibits instability, leading to a loss of synchronization within the system [51]. The implementation of an out-of-step blocking (OSB) strategy entails the inhibition of protection relays' activation in the presence of a stable power swing. In the event of synchronization loss, it becomes imperative to effectively isolate the sections that are experiencing faults. This is commonly denoted as an out-of-step tripping (OST) scheme[50, 52]

2.5 Renewable energy integration

While the integration of high-level RESs mitigates adverse environmental effects in contrast to traditional fossil fuel-based energy generation, it also presents technical challenges. These challenges include decreased total inertia, limited fault ride-through capability, increased uncertainties, fluctuations in voltage and frequency, elevated fault currents, diminished generation reserves, and reduced power quality. [4]. Another challenge with integration of RES into the grid is the significant issues is the increased in short circuit levels (SCLs), which can result in poor power quality and the failure of some protection schemes (such as distance

and over-current protection) [65]. Solar PV plants have zero inertia to contribute to the power grid and variable speed wind turbines have a negligible amount, it is crucial to develop suitable controlling mechanism for RESs that mimic the characteristics of a synchronous generator to enhance the grid's frequency response. The frequency of RESs integrated systems is supported by the notion of virtual inertia technologies, which make use of, energy storage systems (ESSs), PE converters and control algorithms. Grid-connected solar PV always works at its maximum power point (MPP) with no reserve margin, it cannot contribute to frequency management during negative frequency excursion. To address these challenges these methods are discussed in the literature which are energy storage devices[66], [67] de-loading [68-71] and inertial response [72] . Security considerations arise regarding the practicality of integrating large-scale wind RES into the current electrical grid, particularly concerning transmission infrastructure [46] . Frequency responsiveness of wind integrated systems can be enhanced by the application of virtual inertia technologies such de-loading, inertia emulation, droop controller, and energy storage.

Also, the prompt response to disturbances by disconnecting photovoltaic (PV) and wind plants can have adverse effects on the stability of the system. Hence, it is imperative for photovoltaic (PV) and wind power plants to maintain grid connectivity in the event of faults for a specified duration, ensuring their fault ride-through (FRT) capabilities. The stipulation is primarily attributed to the contemporary grid code, which may vary across countries based on various criteria. The requirements specified by the south African grid code include voltage limits of +/-1 per unit (pu), frequency limits of +/-5%, and limits on current/voltage harmonic distortions, specifically a total harmonic distortion voltage (THDv) of 0.1% and a total harmonic distortion current (THDi) of 5% [73].For the purpose of enhancing fault ride-through (FRT), a concise summary of various methodologies as presented on the literature is categorized in accordance with figure 2.8. They are classified as per their configuration that requires auxiliary devices and those that does not require these devices [73].

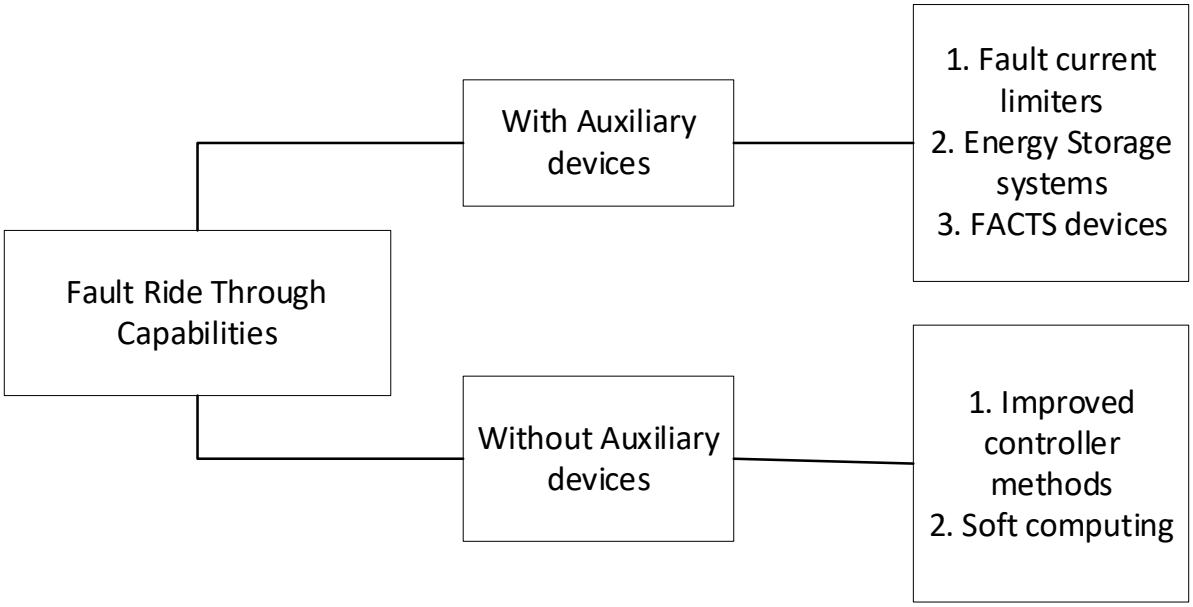

Figure 2. 10 Summary of different techniques to improve fault ride through capabilities in RES.

Power electronic converters play a crucial role as the central processing units of a renewable energy system and grid integrated systems. The presence of these components induces harmonic injection, leading to system destabilization in the entire system. The enhancement of power quality in RES is achieved through the implementation of diverse techniques, such as the integration of advanced control systems and the utilization of various ancillary equipment [74]. These can be classified based into four categories which are use of Facts devices, using energy storage technologies, the use of filtering technologies and different design for converter control as shown in figure 2.9. Furthermore, each category uses specific technologies to achieved an improved power quality for example under battery storage system there is use of batteries, supercharged capacitors etc.

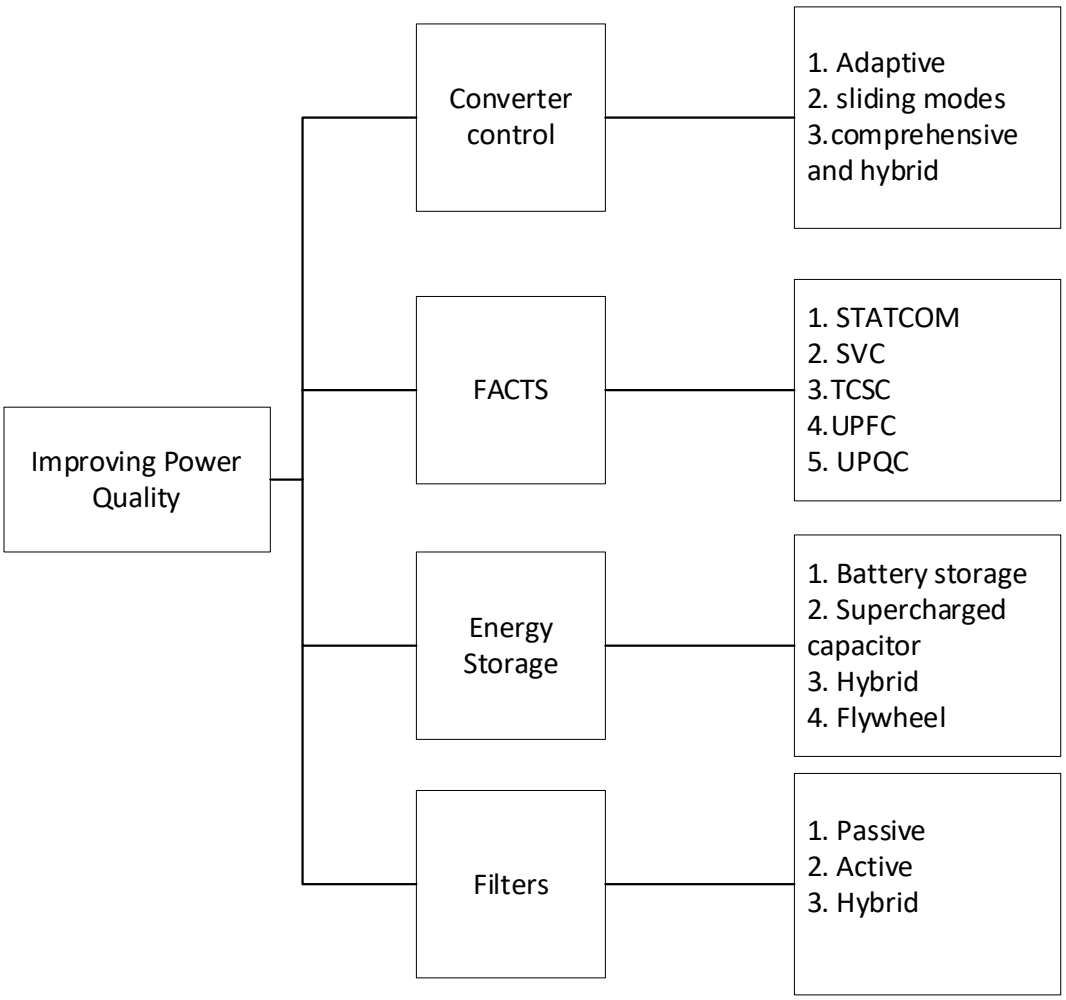

Figure 2. 11 Control strategies used to improve power quality in RES.

It's evident that integrating RESs affects the operation and stability of the power systems network. Frequency fluctuations is one of the challenges these integrated systems encounter. The incorporation of frequency support is increasingly crucial in evolving standards for grid-connected renewable energy sources to maintain the safety and reliability of these power systems with low inertia. Given this prevailing situation, it becomes essential to integrate inverter-based renewable energy generators to improve the frequency stability of modern electrical grid [75]. The primary frequency response (PFR) and inertia work together synergistically to actively mitigate power frequency fluctuations, thus preventing potential negative outcomes like the activation of under-frequency load-shedding (UFLS) relays, false tripping of protection relays, damage to machinery, or the occurrence of unstable frequencies that could result in a blackout [76]. Renewable Energy Storage Systems (RESS) maintain a greater power reserve to offset the reduced levels of power system inertia. To bolster the grid's resilience against frequency disturbances, an accelerated frequency-Watt

response can be integrated [77] . Improvements in frequency response for PV inverters can be deemed impractical [78], hence the power reserve is an essential requirement for providing complete support to the frequency [79].

The task of ensuring frequency stability in advanced grids is progressively growing in complexity, necessitating the development of grid codes and standards in numerous countries as a means to address this challenge. As the adoption of RES increases, the number of primary and secondary control reserve power generating units will decrease. This results in a rise in frequency deviation, as indicated in [16]. The integration of the ESS into the power grid is aimed at facilitating frequency support. Nevertheless, the implementation of this particular approach for delivering frequency support is deemed expensive [80]. The construction of the ESS can be accomplished through the utilization of diverse energy storage devices, such as batteries [81-83] , electric double-layer capacitor[68] , and storage buffer units[84]. However the incorporation of virtual synchronous generators (VSG} technology into commercial PV power plants is impacted by the prevalence of ESSs, one of the disadvantage on using batteries for energy reserve is reduced life span due to when a battery is required to sustain a primary frequency, it is subjected to frequent and substantial power fluctuations [85].

Marzebali et.al [86] developed a hybrid energy storage system that incorporates a fuel cell as the primary power source, supplemented by a battery for additional power supply. In [87], in order to mitigate voltage and frequency fluctuations within the isolated micro grids, it is suggested that Battery Energy Storage Systems (BESs) incorporate a synchronized and integrated energy management system, known as coordinated energy management system . The power outputs of renewable sources exhibit significant variability, whereas battery power densities are comparatively low. Following significant voltage fluctuations, batteries encounter difficulties in initiating start-up subsequent to rapid oscillation. A higher magnitude of reserve power is maintained for PV systems when operating at reduced levels of power system inertia.

Overloading, voltage fluctuations, and insufficient frequency support capacity are among the potential issues that may arise from continuous maximum power point tracking (MPPT) operation [88], It is advisable to consider the possibility of implementing a faster frequency-Watt response to enhance grid support during frequency disturbances. In [79] a power reserve control technique based on MPPT has been established. This technique enables real-

time measurement of the MAP at regular intervals, eliminating the requirement for supplementary hardware or intricate computations. The coupling of the MAP measuring loop with the power reserve loop poses a hindrance to the implementation of the virtual inertia control. In order to optimize the frequency response in power networks that have a substantial integration of renewable energy resources, it is advisable to implement frequency droop-based control [89] . The summary of the techniques implemented for frequency support for grid integrated networks is shown in table2.4.

Table 2. 4The summary of the techniques implemented for frequency support

reference	Technique/problem	Contribution
[90]		Pitch angle controller and a rotor speed controller developed to. Assist in restoring grid frequency by adjusting its power output as required
[91, 92]	Examine random loading, nonlinearities, time delays, reduced inertia, and stochastic load fluctuations.	This has been accomplished through the development of Multivector Model Predictive Power Control Consistently, the proposed algorithm has shown positive responses to these scenarios, effectively controlling the voltage and frequency
[93]	Control parameters on frequency stability is determined using a root locus analysis	This scheme can be used as a theoretical framework from which to choose control parameters
[94]	Examine the impact of VSG settings on transient energy demand (TED) and maximum grid frequency deviation (MGFD) considering nonlinearities such as droop dead band.	frequency management using the swing equation, which is based on droop control is developed
[95]	Developed a coordination strategy for the virtual inertia control and the frequency damping control.	The developed strategy is done using droop-control based swing equation.
[96]	An adaptive droop frequency support (ADFS) scheme is developed in	Proposed approach employs an ADFS scheme at each receiving end converter to discern and distinguish the grid experiencing disturbance from the other unaffected grids within the multi-terminal HVDC system

The methods employed in the literature to address the issue of FRT capabilities have been succinctly summarized in Table 2.5.

Table 2. 5 Improvement of fault ride through capabilities techniques.

Reference	Method/technique used	Contribution
[97]	Current limiting	A new control approach that uses both positive and negative sequences to regulate currents independently is proposed. Positive, negative, and zero sequence control is employed simultaneously, and Improved. inverter-grid synchronization is achieved via the employment of a Dual Second Order Generalized Integrator - Frequency Locked Loop (DSOGI-FLL) in the presence of asymmetric faults. To lessen the effects of THD and power losses, an interleaved DC-DC converter and a Neutral Point Clamped Inverter are employed.
[98]	Bridge-type fault current limiter (FCL) with discharging resistor	To improve FRT at a low-cost series dynamic braking resistor (SDBR) has been adopted. There is no lag time in the operation of a dc reactor, which limits the fault current as it increases. Suppressing the immediate voltage drop is a useful property of the bridge-type FCL that can enhance the transient behaviour of a wind energy conversion system (WECS).
[99]	Hybrid genetic algorithm optimized Elman neural network controller	It has been suggested that FRT capabilities could be enhanced by using a tailored dynamic voltage restorer controlled by a hybrid intelligent control method for proton exchange membrane fuel cell supported customized Dynamic Voltage Restorer.
[100]	Novel DVR based Odd-nary Cascaded Asymmetric Multi-Level Inverter (MLI)	Compared to earlier types of MLIs, this new type introduces a staircase sinusoidal voltage with high level numbers against less switch numbers.
[101]	Nonlinear back stepping control scheme	Lyapunov functions are formulated as the negative definiteness or semi-definiteness of the derivatives of these at various stages of the controller design process.
[102]	Fuzzy Logic Controlled Crowbar Protection	The crowbar switch's timing and the WECS's FRT capability have both been enhanced by the addition of a fuzzy logic controller (FLC) block

[103]	Non-superconducting bridge-type FCL	Other research exploring and implementing low-cost BFCLs needs to fill the gap left by the lack of attention paid to proper impedance design as a potential option for fault impact mitigation in DFIG wind integrated HVDC systems. With BFCL-based fault current control, DFIG wind coupled VSC-HVDC systems can improve both their fault ride through capabilities and transient stability.

Furthermore figure 2.12 shows a summarized model of strategies that can be used to improve frequency response of RES integrated networks. They are categorized into three which are mathematically based, Equipment based and control based as shown in figure 7. Also, under each category the list of specific technique falling under each category for example under mathematically based there is root cause analysis and frequency-based calculations.

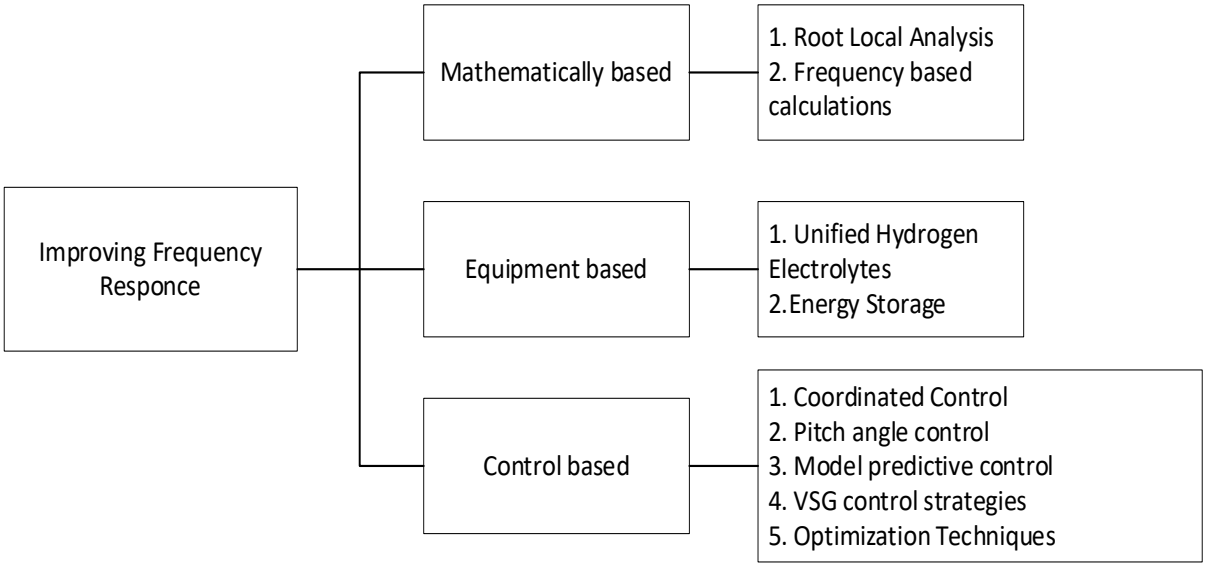

Figure 2. 12 Technique used to improve frequency response of grid connected RES

In the event of a power system fault resulting in a voltage drop, it is imperative that the integrated RESs exhibit the capability to sustain uninterrupted operation while remaining connected to the grid for an extended duration. Furthermore, these RESs should promptly contribute to the power grid's swift restoration following a fault-induced disconnection. The primary objective behind these measures is to guarantee the ongoing safe and stable functioning of the grid. Consequently, it is imperative that wind generators possess specific low voltage ride-through capability. To ensure a secure and efficient integration into the power system, it is necessary that grid-feeding inverters possess significantly improved monitoring capabilities for operation and enhanced performance. These specific inverters are

required to enhance grid stability during fault conditions while maintaining continuous connection to the system. When the primary grid is experiencing an imbalance, addressing this situation becomes challenging .According to [98] has been identified that there are two primary challenges encountered during a fault condition in RES integrated networks which are systems frequency response and fault ride through capabilities

The investigation of wind energy utilization has been the subject of numerous investigations by researchers [66], and recently, there has been a significant increase of wind farms having a capacity of one megawatt or higher, to attain Fault Ride Through Capability (FRTC) even under zero system voltage conditions, various techniques and their corresponding control systems are thoroughly examined during both symmetrical and asymmetrical breakdown scenarios.

The incorporation and integration of renewable energy sources into the current power infrastructure have significantly increased the complexity of the network. Managing this intricate system presents a considerable challenge for regulatory bodies. It is crucial for wind farm developers, manufacturers, and network operators to accurately understand these regulations, as they define the operational constraints of renewable energy sources connected to the grid. These regulations include essential parameters such as frequency range, voltage tolerance, power factor, and fault ride-through capability. The emergence of new power-electronic technology assumes a crucial role in facilitating the integration of renewable energy sources into the grid. This technology should enable the development of power-electronic interfaces tailored to accommodate the highest projected turbine ratings. This entails optimizing energy conversion and transmission, managing reactive power, minimizing harmonic distortion, achieving high efficiency across a broad power spectrum, ensuring reliability, and withstanding subsystem component failures. Additionally, it's imperative to comprehend the impact of these device characteristics on protection systems.

2.6 The impact of Renewable energy on protection schemes

Designing relay tripping characteristics presents a significant challenge for distance relays on transmission lines, particularly given the increased pressure on power system operation. The increasing presence of non-synchronous and inverter-connected generating plants, driven by the rise of RES in electricity generation, poses unique challenges. Unlike conventional plants,

RES plants utilize active control systems or sophisticated software to manage disturbances. Protecting grid-integrated RES presents several issues, including reduced fault current leading to protection blindness, false or sympathetic tripping due to bidirectional fault current flow, and coordination problems where relays may trip prematurely. The Distance relay may face challenges of both underreach and overreach, due to the factors mentioned. Additionally, islanding problems may arise, causing unstable operation, while loss of coordination can disrupt relay operation in a cascade manner. Auto-recloser challenges may result in the conversion of temporary faults into permanent ones, and selectivity issues can make it difficult for relays to distinguish between healthy and unhealthy system conditions. Distance relay challenges further complicate the task of accurately detecting faults within the network. These complexities highlight the importance of implementing effective protection systems for grid-integrated RES.

Changes in wind conditions notably affect the reach of distance relays designed for transmission line protection. Wind speed fluctuations cause voltage level changes at local network buses, causing variations in apparent impedance detected by protective relays. These fluctuations in impedance also result in adjustments to the distance relay's reach setting [104].

The implementation of new grid regulations regarding FRTC, requiring DFIG to remain connected to the grid during fault conditions, may result in converter damage due to current fluctuations. In order to safeguard the converter, crowbar protection is employed to divert current away from it. As a result of the crowbar resistance, DFIG exhibits varying fault current values compared to normal operating conditions for specific durations [105].

This leads to issues with the reach of transmission line protection connecting these RESs to the grid. The short-circuit behaviour of various Distributed Generators (DGs), including induction generators and conventional synchronous generators, differs and influences the settings for distance protection. Moreover, the increased presence of RES may disrupt the operation of transmission line relays. The effectiveness of transmission-line distance protection can be influenced by factors such as the capacity, size, and density of RES plants. Other factors impacting the performance of distance protection include the proximity of the fault to the bus, fault location, the type of fault (transient or steady-state), fault inception angle, power swing, voltage level, fault level, frequency matching, mutual coupling,

compensation techniques, and the use of FACTS devices in transmission lines to optimize power transfer[106].

These difficulties underscore the importance of exploring novel technologies for safeguarding transmission lines. Researchers in the literature have explored various parameters influenced by the characteristics of integrated networks. Furthermore, the inclusion of FACTS devices in the transmission system significantly influences the performance of distance relays by changing apparent impedance. Additionally, the reach setting of the relay is significantly affected by ongoing fluctuations in relay end voltage when offshore wind farms are connected to the power transmission system. Consequently, developing tripping characteristics for suitable operating conditions remains a challenging issue[107].

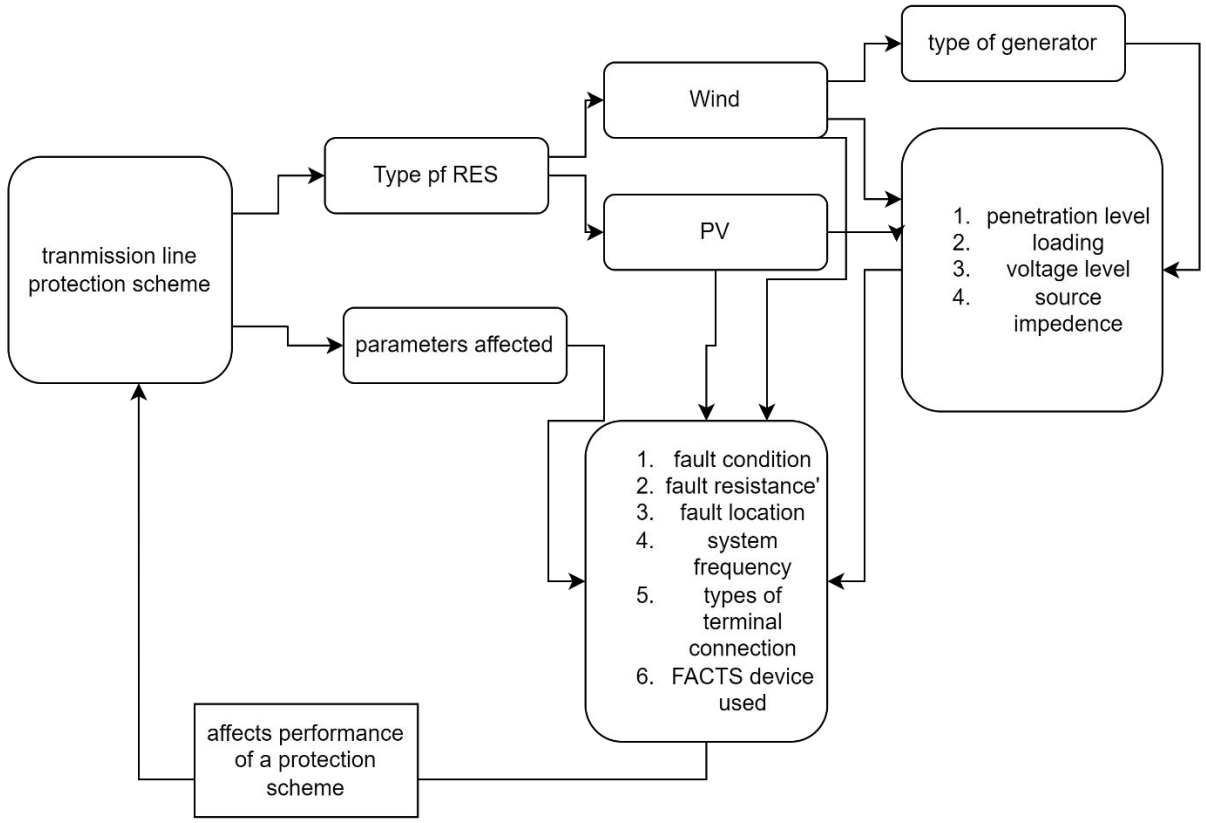

Figure 2. 13 The impact of RES penetration of protection schemes

In figure 2.13 the number of factors affecting the performance of the distance relay when protecting RESs. From this figure is shown that there are two major contributing factors which are the type of RES, penetration level, voltage level which affects parameters such as impedance. Furthermore, it can be noted that these parameters affect fault condition, systems frequency response etc. which directly affects the effectiveness of the protection relay. The influence of source impedance is an essential factor to take into account as it is

closely linked to the number of wind farms integrated into the transmission network [107]. This is because the equivalent source impedance of the generators will change depending on the number of units connected to the bus simultaneously[108].

The traditional distance protection philosophy, tailored for lines connected to synchronous generators (SG), functions effectively due to the homogeneity of SG-connected systems. This is not the case for RESs integrated systems, where fault current and its angle are governed by control strategies, grid codes, and FRT requirements. Additionally, the distinctive fault current behaviour of inverter based generators (IBG) significantly affects the reliability and security of distance relays zones of protection [109] for the faults falling within the 3 zones. According to [110] due to the current source representation of RESs integration [2], The phase difference between line-end currents during Zone 1 faults can be considerable and depends on grid code (GC) specifications. This can lead to inaccurate reactance calculations by the distance relay of such systems, potentially compromising relay reliability.

In the case of Zone 2 faults, discrepancies in both phase and magnitude between local and infeed currents could jeopardize relay security and render FRT schemes ineffective within the integrated RESs. Alternatively, it might bypass backup protection, depending on the system's characteristics. Fast determination of the transient frequency leads to significantly decreased delay time in protection compared to using a fixed-delay method. Theoretical analysis suggests that both the power frequency component distance relay and the phase-comparison distance relay are influenced by the prominent harmonic content and frequency deviation of RES systems. Moreover, the fluctuation in power frequency impacts the distance relay because of the impedance properties of the line connected to renewable RESs [111] is directly affected by frequency variation . the research that has been currently conducted is summarized in table 2.6, highlighting the problem address and the proposed solution.

Table 2. 6 Improved protection schemes for RESs integrated networks

Reference	Problem	solution
[112]	Diminished effectiveness seen in traditional distance	A novel R-L differential equation-based distance protection technique is proposed. This innovative method integrates faulted

	protection systems on the tie line of DFIG-based wind farms	phase selection and considers the influence of high-frequency components, power system disturbances, and measurement errors.
[113]		Implemented a time-domain distance relay using the R-L differential equation algorithm specifically designed for integration with wind power system.
[114]	Enhance real power generation in changing environmental circumstances	Algorithm is employed to. Both solar PV and wind energy systems are controlled using the Perturb & Observe (P&O) MPPT algorithm

Additionally, reactive power compensation objectives are achieved by integrating a Distributed STATCOM at the coupling point. This indicates that there is a need for protection engineers and researchers to focus specifically on enhancing the performance of distance protection relays in the presence of RESs.

2.7 Adaptive Distance protection scheme

Integration of renewable energy affects the performance of conventional protection schemes. According to [115] the conventional relay protection employed for the collector line of a wind farm encounters issues pertaining to inadequate selectivity and diminished sensitivity. This arises due to the utilization of a solitary protection component on the bus-side of the collector line. The fluctuations in wind speed directly impact the variations in voltage, frequency, and power generation of wind farms. Hence, it is of utmost importance to implement an adaptive system for distance protection of the transmission lines that interconnect said farm with the power grid is essential [116]. The effectiveness of a distance relay may be notably influenced by several uncontrolled variables, including fault resistance, fault type, fault location, and noise. Furthermore, the integration of photovoltaic power plants into electrical grids results in unique fault current characteristics compared to conventional power systems with synchronous generators[117].

Firstly, the short-circuit level could either decrease or increase. Secondly, FRTC may decline. All of these factors could lead to inferior power quality and the malfunction of certain protection schemes, such as distance and over-current protection [12]. As the primary aim of a protection system is swift fault elimination, while power quality ensures the consistent

delivery of reliable power within defined parameters, it's crucial to explore how protection systems are impacted by the integration of RES. The challenge stemming from RES integration lies in the fluctuating operating conditions of wind farms (WF), which can result in power, frequency, and voltage fluctuations, potentially introducing new hurdles for existing protection algorithms[118]. The incorporation of renewable energy sources into power networks alters the network topologies. Their fault levels are intermittent, and existing protection schemes may fail to operate due to their predefined conditions. Therefore, it is crucial to design and select an appropriate protection scheme for reliable control and operation of renewable integrated power systems, as conventional line protection schemes rely on preset settings and are not well-suited for dynamic operating conditions. Implementing an adaptive protection scheme may be a viable solution for protecting RES-integrated systems. According to literature, challenges in protecting RES-integrated networks include protection blindness, false or sympathetic tripping, islanding issues, and loss of coordination [104].

According to [119] It has been noted that traditional distance relay features are highly susceptible to malfunctions triggered by both under-reaching and over-reaching the fault point when a transmission line is compensated. As a result, employing these relay features in such situations is considered unsuitable. The influence of positioning the SVC in the middle on the ideal impedance characteristic of a distance relay is simulated in [120], Simulation outcomes of the adaptive distance protection for the single-source power system are examined when a phase A-to-ground fault arises through various transition resistances located 70 km away from the relay. The fault resistance is simulated at 0, 10, 50, and 100 ohms. It is concluded that the proposed scheme remains unaffected by the transition resistance and transmission line compensation. According to [121] with the SVC introduced in the fault loop, the traditional distance relay features are significantly prone to operational errors, including both under-reaching and over-reaching the fault point. Hence, the conventional characteristics cannot be effectively utilized when the static SVC is present. The impact of the SVC on the ideal impedance profile of the distance relay is analyzed in cases where the SVC is positioned at the midpoint and the far end is studied in [122] . The findings indicate that when the SVC is not within the fault loop and the fault resistance is zero, there is minimal impact on the ideal tripping characteristics of the distance relay. However, when the SVC is within the fault loop and the fault resistance is zero, there is a notable alteration in

the tripping characteristics. This is particularly evident when the impedance of the SVC shifts from inductive to capacitive. In [123] Kalman and adaptive Kalman filters and the average classification time of the adaptive model is 1.3 msec. In [124] decision tree-based classifier created in real time, providing out-of-phase safety during power swing. ANFIS and SVM are also used to clear a three-phase to ground fault with a fault resistance of 1ohm in 0.25 seconds. The impacts of phase shifting transformer (PST) is investigated [125], using analytical and computational methods, for the first time the impacts of PST on the distance relays are investigated. Results reveal that the PST causes the distance relays to under-reach. Author in [126] used machine learning model to develop overcurrent and distance protection scheme for transmission line , a hybrid artificial neural network and support vector machine (ANN-SVM) model is proposed for state recognition in microgrids, which utilizes the growing massive data streams in smart grids. The protection scheme based on impedance complex plane is developed in [127] , the proposed scheme is fault-resistance-immune and very flexible, making it suitable for use in a wide variety of system configurations. In [128] An innovative adaptive scheme has been developed for distance protection in transmission lines linked to renewable energy plants, utilizing local data to ascertain the phase angle related to the current. This method computes the phase angle of the faulted loop current by continuously determining the pure-fault impedance of the renewable plant immediately after fault detection, independent of the plant's control scheme. By leveraging this information, the method accurately calculates the line impedance up to the point of fault. An Artificial Neural Network (ANN) based adaptive protection scheme is developed in [129] ,the proposed strategy uses data from locally linked field instruments to calculate fault resistance, which is then used to automatically alter the relay settings. An adaptive protection scheme employing a Radial Basis Function Neural Network (RBFNN) is discussed in[130] , which utilizes infeed current, voltage, and impedance data measured at the remote ends of the transmission line by the Remote Terminal Units ,this scheme automatically adjusts its relay operational settings based on acquisition of remote end infeed data from the remote substation. In[131], both the original heap-based optimization (HBO) and a modified HBO of the algorithms were employed. These algorithms successfully addressed challenges in coordinating distance protection relays, and their performance was evaluated on a 400MW grid-connected microgrid.

Authors in [132] a scheme is suggested that relies on the Modified Complete Ensemble Empirical Mode Decomposition with Adaptive Noise technique. This algorithm serves as a supervisory scheme for determining the backup zone setting zone3 of the distance relay. Pilot superimposed impedance is proposed in this scheme and there is no requirement to send the voltage readings from the distant bus[133], bandwidth is saved while simultaneously increasing the data's dependability. Demonstration of the effect infeed has on the existing distance protection approach is discussed in[134], the authors also proposed a novel algorithm for distance relays that can adaptively modify for the influence of infeed by measuring phasors in synchronization. The model that analyses the hybrid system's response to asymmetrical faults involves real-time calculations of the equivalent impedance of the power grid and the current flowing through the fault point is discussed in [135]. Authors in[136] builds a prototype using an MCU (LPC2368_ARM7TDMI) for experimental purposes. This study also explores the impact of mutual coupling. Additionally, a Mho distance relay utilizing a phase comparator scheme is developed in [137, 138], The root-mean-square (RMS) of the positive sequence current within the faulty loop is contrasted with the TCSC terminal current. A phase comparator is suggested for the ground and phase distance elements, utilizing the positive sequence voltage as a polarized memory component. In the event of a fault occurring on the opposite side of the relay, the adaptive quadrilateral setting will transition to the third quadrant of the RX-plane in coordination with the other relays safeguarding the additional feeds from the same bus. The study [139] examines the adaptability of distance protection in response to fault conditions in an offshore wind farm connected via VSC-HVDC. It utilizes the power frequency component of the transmission line. In [140] dynamic frequency estimation-based adaptive protection scheme has been devised, employing a multiple signal classification approach to gauge the dynamic frequency. When the estimated frequency closely aligns with the fundamental frequency, the distance requirement is activated. Consequently, the regular distance protection remains unaffected by the frequency variation of the fault current. An adaptive distance protection scheme is developed in [141] the proposed method revolves around analyzing the influence of integration of largescale The proposed approach focuses on examining how Large-Scale RESs affect the changes in observed transmission line impedance, enabling accurate fault identification and localization. Additionally, the methodology factors in parameters such as

fault location, fault resistance, fault type, fluctuations in generation, and varying noise conditions when determining the phase angle of the fault loop current.

2.8 Machine learning approach in Power systems

2.8.1 Hybrid machine learning approaches.

Machine learning algorithms are gaining popularity in addressing challenges in the context of power systems engineering. However according to [142] there is a critical necessity for effective strategies to handle substantial volumes of data in order to facilitate sustainable electricity systems, especially with the incorporation of smart grid technologies. It stresses the significance of Big Data management and machine learning techniques in tackling the challenges posed by contemporary power systems. In [143] Artificial Neural Networks (ANN) are utilized to forecast the severity of line outages and the overall performance of the power system. This predictive ability enhances readiness and response strategies for potential system failures. The practical implications of this paper underscore the transformative capabilities of Big Data technologies in improving the efficiency, reliability, and sustainability of power systems. Authors in [144] has propose a hybrid deep learning methodology that integrates Deep Reinforcement Learning (DRL) with a Quantum Inspired Genetic Algorithm (QIGA) to tackle the Optimal Power Flow (OPF) challenge in hybrid renewable energy systems. model also minimized power loss to 1.85 MW and achieved a voltage deviation of 0.065, indicating improved stability and efficiency compared to traditional optimization algorithms. The model successfully reduced power loss to 1.85 MW and attained a voltage deviation of 0.065, demonstrating enhanced stability and efficiency in comparison to conventional optimization algorithms. Jumaili et.al [145] developed hybrid deep learning methodology that integrates Complex Value Neural Networks (CVNNs) and Long Short-Term Memory (LSTM) alongside Proportional Topology Optimization (PPTO) significantly improves fault detection and multiclass classification precision in power distribution systems. This approach surpasses both conventional and advanced techniques, achieving classification accuracies ranging from 98.22% to 99.83%. A hybrid deep learning model that integrates Multilayer Perceptron (MLP) and XGBoost classifiers to accurately predict the stability of smart grids within the Decentralized Smart Grid Control (DSGC) framework is proposed in [146]. The proposed hybrid model surpassed the performance of all individual models, attaining an impressive overall F1 score of 97.60%. It demonstrated exceptional capability in accurately

classifying both stable and unstable instances, with precision, recall, and accuracy metrics also reaching 97.60%. The comparison is done with regards to machine learning algorithms and the results are shown in table

model	Accuracy (%)	Precision (%)	Recall (%)	AUC(%)
Logistic regression	80.2	79.79	80.2	89
Random forest	92.2	92.22	92.2	99
Support Vector Classifier	96.10	96.10	96.1	98
Extreme Gradient Boosting	95	95	95	99
Hybrid (MLP +XGboost)	97.60	97.60	97.6	100

Hybrid models incorporating convolutional neural networks (CNN) have been created, including CNN-RNN, CNN-GRU, and CNN-LSTM in [147]. The findings reveal that the CNN-GRU model attained the highest accuracy rate of 93.92%, along with the lowest Mean Absolute Error (MAE) and Mean Squared Error (MSE) losses, recorded at 0.14 and 0.05, respectively. The CNN-LSTM and CNN-RNN models also demonstrated commendable performance, achieving accuracies of 93.05% and 92.85%, respectively. Rafi et.al in [148] proposes a unique hybrid model that combines Artificial Neural Networks (ANN) and Support Vector Machines (SVM) to detect transmission line faults with accuracy and precision. Hybrid model achieved 98% precision and 98.43% accuracy. In [149] The ICA-SVM algorithm was developed and tested on a 500kV 180km transmission line that was highly penetrated with solar PVs, simulated in MATLAB/Simulink. Simulations were conducted for different fault types, signal noise levels, and fault resistances. An accuracy of the ICA-SVM algorithm in determining the location of faults for the different scenarios was above 99.7%. The fault classification accuracy ranged between 99% and 100% for different levels of SNR. However, the method was only satisfactory for fault classification up to a SNR of 45dB and the transmission line is not compensated.

2.8.2 Challenges of implementation of ML based algorithms in real world network

In [150] it is mentioned that there isn't a single commercial relay that uses ML for either primary or backup protection at the time. This chapter delves into the complex challenges involved in integrating ML into power system protection applications. A significant challenge

is the limited interpretability of contemporary machine learning models. Specifically, intricate models such as deep neural networks are often regarded as "black boxes," which makes it difficult to understand the rationale behind their decision-making processes [151-153]. Another major issue in the implementation of machine learning (ML) for power system protection is the uncertainty surrounding its performance. Traditionally, the effectiveness of ML models is determined through processes of "testing and validation." However, it is essential to critically evaluate whether this conventional approach to testing is sufficient for vital applications like power system protection and control. For instance, an ML model that achieves a 99% accuracy rate during testing may appear impressive in various domains [154, 155] . According [156] the limited availability of high-quality data within the power system sector poses a significant obstacle to the advancement of data-driven techniques. Machine learning models thrive on high-quality data, as their effectiveness is directly influenced by the quality of the data utilized. The information produced by these sensors may include noise and exhibit imbalances, both of which can negatively impact model performance [157]. Moreover, the infrastructure required for efficient data collection frequently proves inadequate. In addition, despite the collection and storage of data, a significant portion remains unavailable to the broader research community because of security and privacy limitations. Compounding these challenges is the disparity between normal and abnormal data. Power systems predominantly function in a 'normal' state, with approximately 99.9% of the recorded data reflecting this stable condition. However, for the development of a resilient machine learning (ML) model, it is essential to incorporate data that represents abnormal or alert conditions. The scarcity of 'abnormal' data scenarios compels the model to frequently 'unlearn,' as it has limited opportunities to assimilate new information [158]. As a result, constructing an ML model based solely on real sensor data proves to be difficult. To address these challenges, it may be necessary to integrate real sensor data with simulated data, which could help mitigate issues related to data quality, accessibility, and imbalance. This strategy has the potential to enhance the model's capacity to predict and respond effectively to both normal and abnormal conditions within power systems. A further challenge arises from the presence of adversarial examples[159]. These are intentionally designed inputs that seek to mislead a neural network, resulting in erroneous classification of specific inputs[160]. The existence of adversarial examples presents a considerable hurdle for the effective implementation of machine learning in power system protection. Within the realm of power systems, an adversarial

example may manifest as a subtly altered input intended to provoke misclassification. In summary, the application of machine learning techniques for hardware implementation continues to pose challenges that necessitate additional research.

2.8.4 Summary

Hybrid methods have been explored for their application in power systems; however, the evaluation of protection systems remains unaddressed. These methods have demonstrated enhanced performance regarding accuracy. Nevertheless, a comparison conducted in one of the studies indicated that Support Vector Machines (SVM) outperformed all other techniques, with the exception of the hybrid machine learning approach. Although a significant amount of research and development has been documented thus far, many of these initiatives remain far from being implemented in practical applications. Therefore, it can be concluded that the application of machine learning technology in power system protection is still in its nascent phase.

2.9 Conclusion

The introduction of FACTS devices presents several challenges across multiple dimensions. These include the introduction of harmonics into the system, which can disrupt fault loop currents, as well as the torsional interaction and nonlinear and fluctuating characteristics inherent in these devices. Factors such as the Ferranti effect, the effects of switching operations and firing angles, and the potential rise in reactance observed by relays near zero capacitor crossings also need to be considered. Proper placement of these devices along the line is critical, as it impacts both transient and steady-state voltage and current signals, thereby affecting the performance of distance protection relays in fault detection, classification, and localization, due to modifications in the apparent impedance seen by the relay.

Various factors contribute to the malfunction of a Distance protection relay, including overreaching and under-reaching. To enhance the performance of distance protection relays in terms of accuracy and signal processing speed, schemes based on computational intelligence and diverse methodologies are recommended. These include control methods based on ANNs, Fuzzy Logic controllers, and PI controllers. Additionally, machine learning and data mining techniques, such as decision trees, Kalman filters, and adaptive Kalman filters,

along with various associated methods, are being explored. Furthermore, to effectively address technical challenges such as the impact of remote in feeds, out-of-step tripping during power swings, high-resistance faults, relay accuracy and speed, and the consequences of changing transformers and transmission lines, adaptive protection techniques are being employed. However, it is noteworthy that these techniques have yet to undergo testing in the presence of RESs on compensated transmission lines, and there is a lack of investigation into the impact of various compensation levels in the literature.

Moreover, limited information is available on methodologies involving time-frequency analysis and real-time evaluation at the point of integration where the line is compensated. The recognized impact of RES integration on the distribution network primarily focuses on enhancing frequency response and fault ride-through capabilities, as well as characterizing low inertia in RESs, without delving into the analysis of these phenomena in distance protection schemes. Researchers have explored the implementation of adaptive distance protection for transmission lines connected to wind farms, particularly those without compensated transmission lines. Although these methodologies have undergone extensive testing under various system operating conditions, they have yet to establish a solid foundation within the literature concerning the integration of RES into compensated transmission lines.

protection and resilience of renewable energy and HVDC network systems. Researchers can explore ways to enhance the protection philosophy of DC transmission networks.

Ensuring the reliable and safe operation of hybrid systems, which involve the integration of various energy sources and technologies, is paramount. Robust cybersecurity measures are essential for protecting hybrid systems, given their reliance on digital controls and communication networks. Continuous monitoring, meticulous maintenance, and rigorous testing are imperative to guarantee the sustained dependability and safety of these hybrid systems. The implementation of the DC optimal power flow (DC-OPF) approach may introduce capacity problems that trigger protective systems, data privacy, and cybersecurity issues. Therefore, studying the effects of DC-OPF implementation on protection systems is worthy of investigation. Furthermore, the Transmission Network Expansion Planning (TNEP) model offers significant benefits in terms of cost optimization and anticipating future energy requirements. However, it also presents numerous challenges related to complexity, data accuracy, compliance, initial expenditures, and the need for continuous adjustment to

evolving conditions. The protection system for the Transmission Network Expansion Project (TNEP) plays a crucial role in maintaining the stability and security of the transmission network. Hence, researchers should thoroughly examine the protection philosophy, considering the DC TNEP.

Chapter 3: A compensated Power system Network

3.1. Introduction

The conventional power system network consists of four fundamental components, as illustrated in figure 3.1: generation, transmission, distribution, and utilization. A vital aspect of power system engineering is the efficient transmission of electrical energy from generation sites to substations or end-users. Therefore, it is imperative for power system engineers to possess a comprehensive understanding of the mathematical models that describe this transmission process. To aid in the intricate calculations required, engineers utilize ABCD parameters in conjunction with a two-port model. To ensure the accuracy of this mathematical representation, transmission lines are categorized into three types: short, medium, and long transmission lines. The equations for calculating the ABCD parameters vary based on the length of the transmission line. This chapter focuses on the transmission line elements of the power system/network. A thorough comprehension of transmission line parameters is crucial for the effective operation, control, and development of protection systems within the power system. Mathematical models are employed to derive and articulate the parameters for each category. Figure 3.2 depicts the electrical equivalent circuit representation, while table 3.1 summarizes the ABCD parameters for the transmission line. These parameters are essential for determining the necessary transmit voltage Vs and current Is at the sending terminal (or power supply side) in relation to the voltage Vr and current Ir at the receiving terminal (or load side).

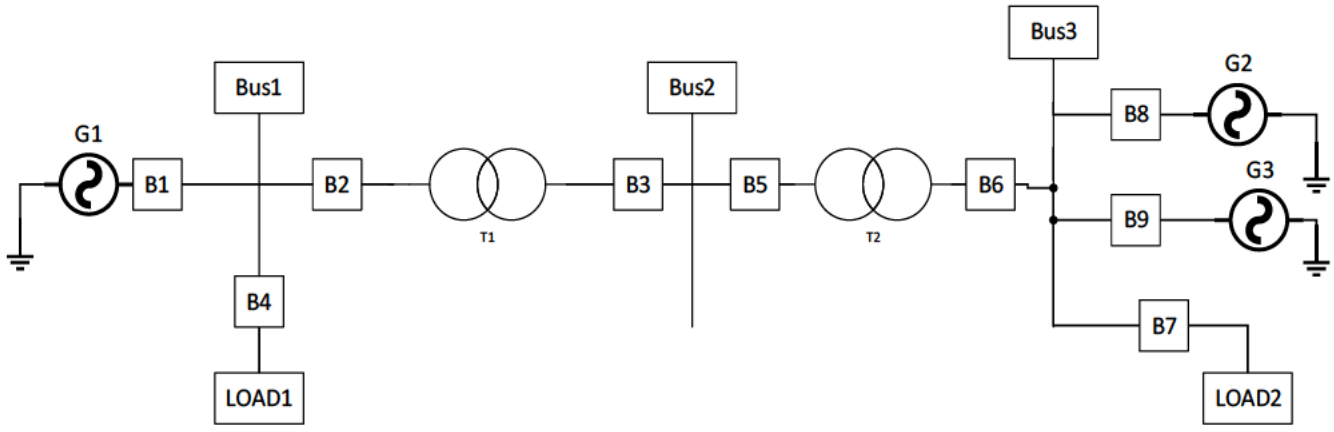

Figure 3. 1 Power system network topology

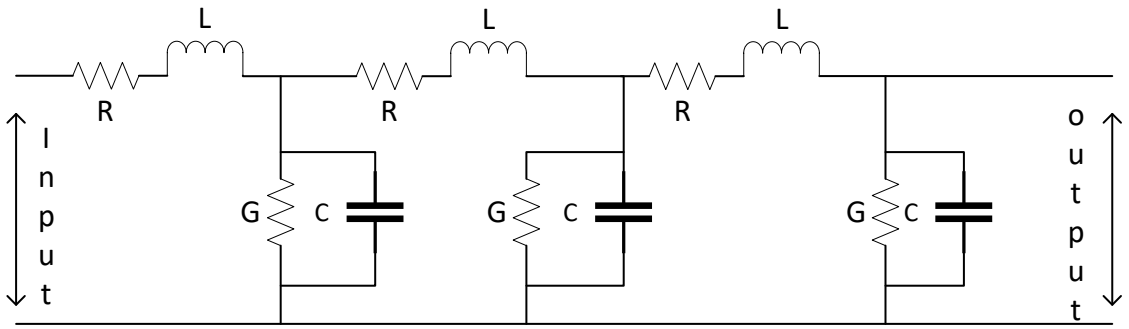

Figure 3. 2 Equivalent circuit representation of a transmission line

Table 3. 1The ABCD parameters of the transmission line can be tabulated as follows:

Parameter	Specification	units
A= $\frac{V_S}{V_R}$	Voltage Ratio	-
B: $\frac{V_S}{I_R}$	Short Circuit	Ω
C: $\frac{I_S}{V_R}$	Open Circuit	mho
D: $\frac{I_S}{I_R}$	Current ratio	-

An ABCD matrix is a 2x2 matrix consisting of complex numbers that defines the relationship between the input voltage and current and the output voltage and current at a designated frequency within a two-port network [161]. Authors in [162] the paper discusses the creation and implementation of a Virtual Lab aimed at measuring ABCD parameters within the context of a medium-length transmission line experiment. This innovative platform enables researchers to select appropriate components, input relevant values, and effectively simulate the medium-length transmission line in a hardware-oriented laboratory setting. The ABCD matrix is obtained from the line's responses under both open-circuit and short-circuit conditions, as determined through frequency domain calculations[163].

According to [164] A robust methodology for establishing transmission line models within solution domains is introduced. This approach streamlines the automatic selection of interconnect models and their associated analyses. Specifically, for a given acceptable threshold of modelling error, analysis domains are delineated to facilitate the automatic selection of models from the classical method of characteristics, a lumped modelling approach, and the state-based convolution technique within a simulation and analysis context. Importantly, this methodology is versatile and can be applied to a wide range of

model and analysis combinations, contingent upon the establishment of criteria for both accuracy and efficiency.

3.1.1 Short transmission line

A short transmission line is characterized as one that extends for less than 80 kilometres and operates at a relatively low voltage, specifically below 20 kV. Due to its limited reach, the influence of line capacitance is deemed insignificant and can be disregarded. As a result, the performance of short transmission lines is predominantly determined by their resistance and inductive reactance. The equivalent circuit model for this type of transmission line is depicted in figure 3.3 and is further explained by equations (2.1 to 2.3).

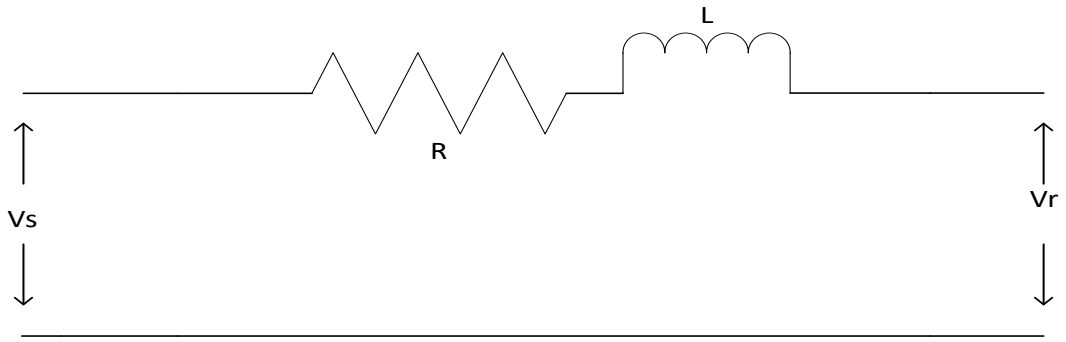

Figure 3. 3 Equivalent Circuit of a Short Line [165]

$$V_S = AV_R + BI_R \ . \qquad 3.1$$

$$I_S = CV_R + DI_R \ldots \qquad 3.2$$

Which can be further represented as

$$\begin{matrix} V_s \\ I_s \end{matrix} = \begin{bmatrix} A & C \\ B & D \end{bmatrix} \begin{matrix} V_R \\ I_R \end{matrix} \qquad 3.3$$

The mathematical model defined by the equivalent circuit, $V_s$and V_R denote the voltages at the sending and receiving ends, respectively, while I_s and I_R signify the currents at these terminals. Additionally, R and X correspond to the resistive and inductive components of the transmission line. The ABCD parameters for the short line are characterized by equations 3.4 to 3.7.

A=1 3.4

B=Z 3.5

C=0	3.6
D=1	3.7

3.1.2 Medium transmission line

Medium transmission lines are characterized by overhead cables that span distances ranging from 50 km to 150 km. The allowable voltage for these lines falls within the range of 20 kV to 100 kV. When examining medium transmission lines, three key lumped line constants—resistance, inductance, and capacitance—are considered. The ABCD parameters for a medium-length transmission line are determined by incorporating a lumped shunt admittance in conjunction with the series lumped impedance within the circuit. These lumped parameters can be depicted through three distinct models.

- Nominal **Π** representation (nominal pi model)
- Nominal **T** representation (nominal T model)
- End Condenser Method

Figure 3.4 illustrates a T-model representation of a transmission line, while () specifies the ABC parameters associated with the medium transmission line depicted in this T-model. Medium transmission lines are characterized by the use of lumped shunt admittance. In this configuration, the lumped series impedance is positioned centrally, with the shunt admittance equally divided and situated at both ends of the line. Figure 3.5 presents the nominal-π model of a medium-length transmission line. It is important to observe that this model employs a lumped line impedance approach, where the line impedance $\frac{z}{2}$ is distributed equally on both sides, and the lumped parallel admittance Y is located at the center of the line.

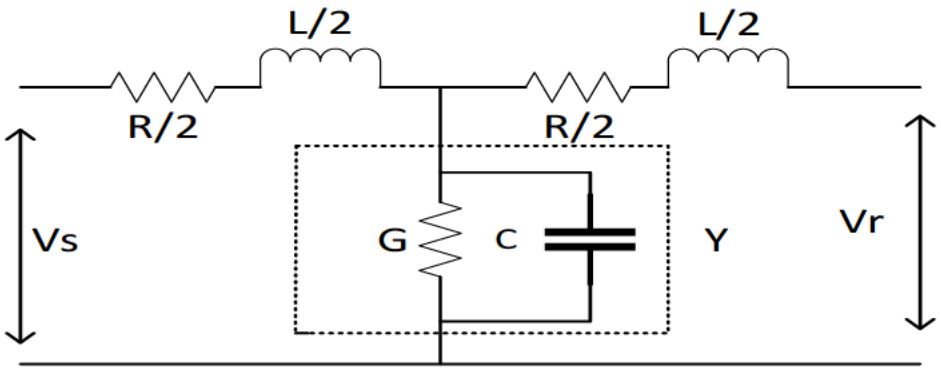

Figure 3. 4 The T-Model of a medium transmission line

The ABC parameters are defined by equation 3.8 to 3.11

$$A = 1 + \frac{YZ}{2} \quad 3.8$$

$$B = 1 + \frac{YZ}{4} \quad 3.9$$

$$C = Y \quad 3.10$$

$$D = A = 1 + \frac{YZ}{2} \quad 3.11$$

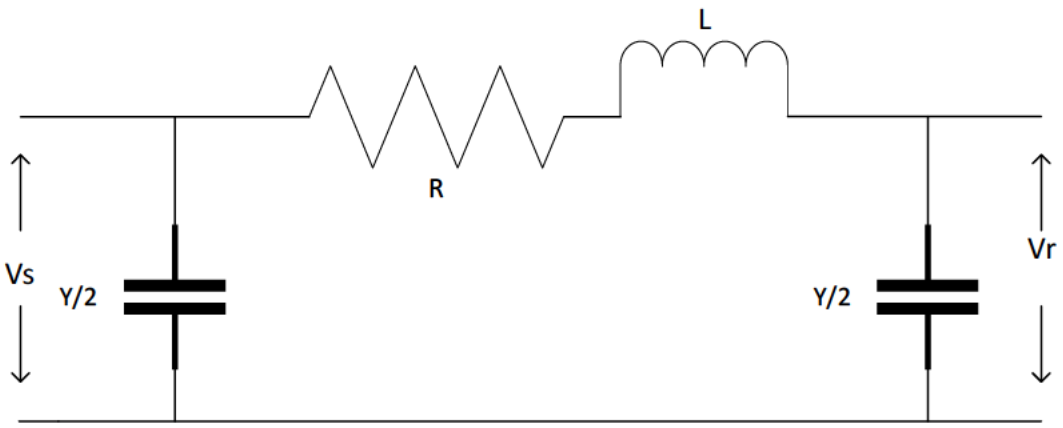

Figure 3. 5 The π -Model of a medium transmission line

3.1.3 Long transmission line

Long transmission lines are defined as overhead transmission lines that are longer than 150 km. These lines operate at a voltage greater than 100kV. Rigid methods are used to solve this sort of line's equations, and it is assumed that their line constants are spread uniformly along the length of the line. Figure 3.6 shows the equivalent π model of a long transmission line, for this model the ABCD parameters are defined using equation 3.12 to 3.15.

$$A = \cosh \gamma\, l. \quad 3.12$$

$$\mathrm{B} = Z_c \sinh \gamma l. \quad 3.13$$

$$C = \frac{1}{Z_c} \sinh \gamma l. \quad 3.14$$

$$D = \cosh \gamma l. \quad 3.15$$

Where γ is known as the propagation constant, Z is the series impedance and y is the admittance. Z' and Y' are defined by equation 3.16 – 3.17 and γ and Z_c are defined by equation 3.18 to 3.19

$$Z' = Z \frac{\sinh \gamma l}{\gamma l} \quad 3.16$$

$$Y' = Y \frac{\tanh \frac{\gamma l}{2}}{\frac{\gamma l}{2}} \quad 3.17$$

$$\gamma = \alpha + j\beta = \sqrt{ZY} \quad 3.18$$

$$Z_c = \sqrt{\frac{Z}{Y}} \quad 3.19$$

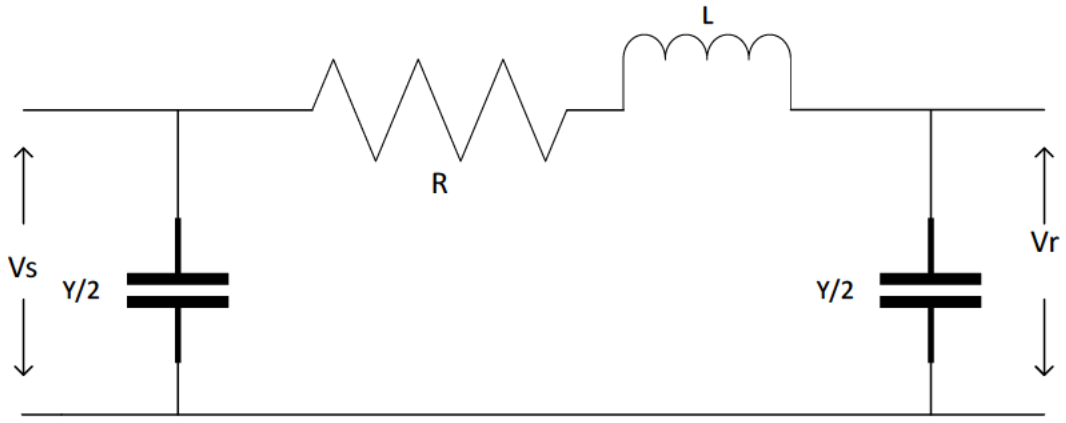

Figure 3. 6 Equivalent Pie Model of a long transmission line

Grasping the electrical properties of a power transmission system is vital for maintaining the dependable functioning of an electric power network. The accurate identification of parameters within a power grid is closely associated with multiple aspects of power system analysis, such as identifying and locating faults in both overhead transmission lines and underground cables, the precise parameterization of protective systems, comprehensive insulation coordination analysis, and an understanding of propagation characteristics, transient phenomena, and potential overvoltage's within the transmission framework. This expertise is critical for the design of effective surge protection systems. Furthermore, line parameters can be estimated through current and voltage readings obtained at the line's terminals.

These readings may be synchronized using phasor measurement units (PMUs) or derived from fault records captured by protective relays located at both the sending and receiving ends of the transmission lines. Although the theoretical basis for estimating transmission line parameters from synchronized measurements seems clear and accurate, practical execution demonstrates that this endeavour is significantly intricate, as evidenced by the limited methodologies reported in the technical literature. The effectiveness of various estimation techniques is affected by factors such as system characteristics, load profiles, line geometry, and system dynamics, whether in transient or steady-state conditions. As a result, each

estimation method is generally effective under particular operating conditions of the power system, and typically, only a select few parameters from the impedance and admittance matrices, represented as [Z] and [Y], respectively, can be estimated with a high level of precision. [166] .

3.2 Transmission line compensation

3.2.1 Introduction

Transmission line compensation is primarily divided into two fundamental types: shunt compensation and series compensation. The details of these categories will be discussed in the following subsections. This section discuss into details different techniques used for transmission line compensation

3.2.2 The principle of shunt compensation

An optimal compensator is characterized as lossless, which guarantees that the active power is maintained consistently at the sending end, midpoint, and receiving end. Utilizing the phasor diagram presented in Figure 3.7b, it is possible to ascertain the magnitudes of the voltage component as derived from Equation 3.20 and the current component as indicated in Equation 3.21 [29], The equivalent circuit is illustrated in Figure 3.7a. The voltage of the compensator, which is in phase with the midpoint voltage V_m, has an amplitude V that corresponds to the voltages at both the sending and receiving terminals. Consequently, it can be stated that $V_m = V = V_R = V_s$. The midpoint compensator effectively segments the transmission line into two separate parts, both parts has an impedance of $\frac{jX}{2}$ however they enable power transfer from the sending end to the middle there after from the middle to the receiving end.

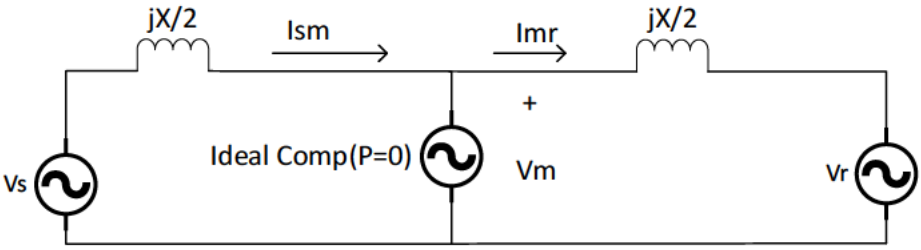

(a) Two Machine Power systems equivalent circuit

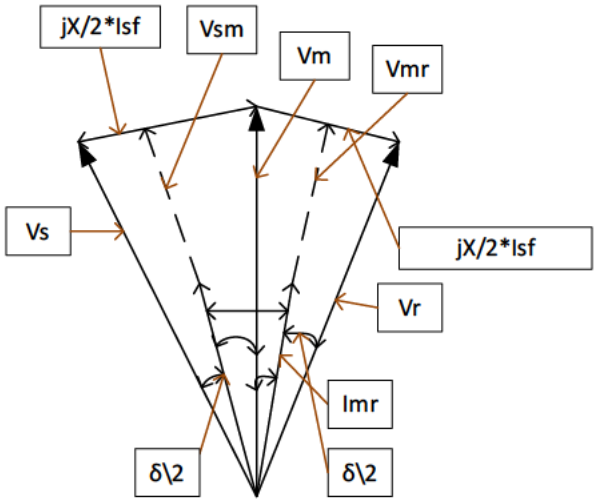

(b) Phasor diagram

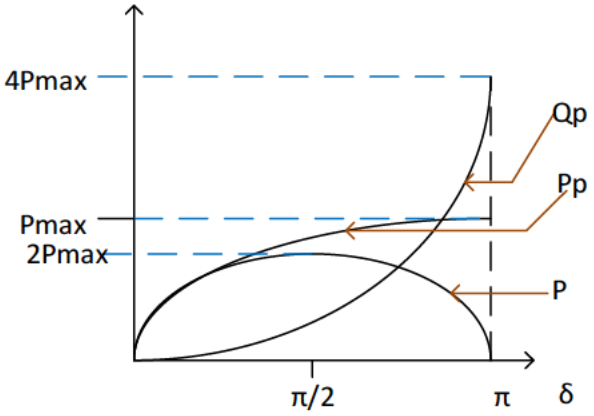

(c) Power against angle

Figure 3. 7 Ideal shunt compensator is connected at the midpoint of the transmission line

$$V_{sm} = V_{mr} = V\cos\frac{\delta}{4} \qquad 3.20$$

$$I_{sm} = I_{mr} = \frac{4V}{X}\sin\frac{\delta}{4} \qquad 3.21$$

There for the transmitted active Pp for shunt compensation is given by equation 3.22 and reactive power is given by equation 3.23.

$$P_P = VI\cos\frac{\delta}{4} \qquad 3.22$$

$$Q_p = \frac{4V^2}{X}\cos\frac{\delta}{2} \qquad 3.23$$

In [167] two-phase methodology that employs frequency response analyses is introduced, utilizing a 4780-bus model of the Nordic power system to assess controlled shunt compensations. The first phase focuses on evaluating the controllability of these compensations through long-distance frequency response assessments. The second phase involves determining the frequency responses of the transfer functions that connect bus

shunt susceptance to bus voltage magnitude for those buses that demonstrate notable controllability. This section further investigates various compensation strategies and their impacts on the stability and response of the power system network during fault conditions, while also delineating the voltage profile of a compensated network. The discussion below encompasses three types of shunt compensators.

3.2.2.1 Static VAR Compensator

A SVC consists of TCRs in parallel with one or more TSCs [168, 169]. The comprehensive arrangement of a SVC is depicted in Figure 3.8. The reactive components of the compensator are linked to the transmission line via a transformer, which functions to separate them from the total system voltage. A control mechanism is responsible for ascertaining the most effective timing for the engagement of the reactors.

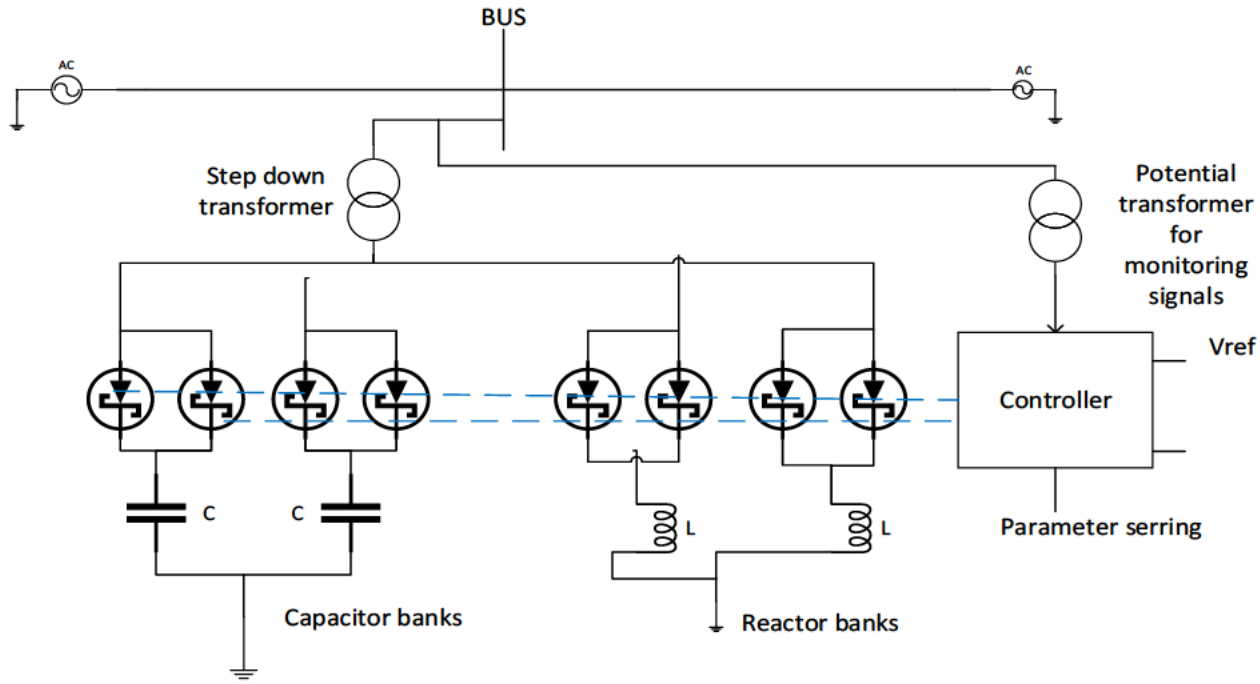

Figure 3. 8 Static VAR compensator

3.2.2.2 Thyristor-controlled reactor

A thyristor-controlled reactor (TCR) consists of a fixed reactor, usually air-cored, characterized by an inductance denoted as L, and a bidirectional thyristor switch, referred to as SW, as depicted in Figure 3.9 (a). The current traversing the reactor can be adjusted from zero (when the switch is open) to its maximum value (when the switch is closed) by varying the delay angle α associated with the thyristor's firing. The conduction angle of the thyristor switch is

represented by σ, where $\sigma = \pi - 2\alpha$. When α is set to 0, the switch remains continuously closed, thereby having no effect on the inductor current. If the activation of the switch is delayed by an angle α relative to the peak value of the supply voltage, denoted as V_m, the instantaneous inductor current can be expressed as a function of α, as shown in equation 3.24. It is essential to note that this condition varies within the interval $\alpha \leq \omega t \geq \pi - \sigma$, a relationship illustrated in Figure 3.9 (b). During the subsequent negative half-cycle, the signs of the terms in Equation 3.25 are inverted, enabling the calculation of the fundamental root-mean-square (rms) current of the reactor current, as well as the admittance expressed as a function of α, as indicated in equations 3.26.

$$I_L = \frac{Vm}{\omega t}(\sin \omega t - \sin \alpha) \quad 3.24$$

$$I_{FL} = \frac{V}{\omega L}(1 - \frac{2}{\pi}\alpha - \frac{1}{\pi}\sin 2\alpha) \quad 3.25$$

$$Y_{FL}(\alpha) = \frac{1}{\omega L}(1 - \frac{2}{\pi}\alpha - \frac{1}{\pi}\sin 2\alpha) \quad 3.26$$

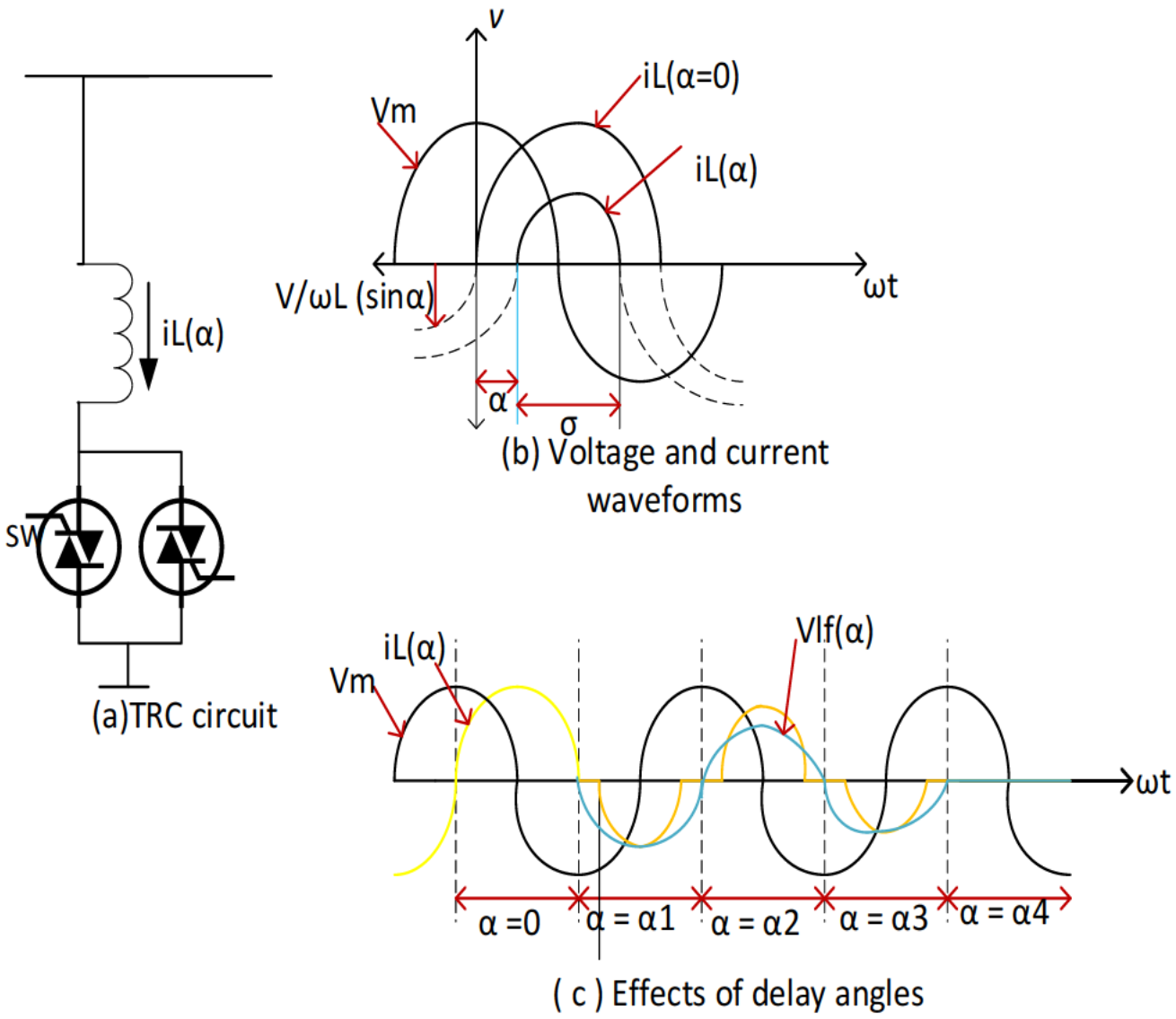

Figure 3. 9 Static Var Compensator configuration

3.2.2.3 Thyristor switched capacitor

Thyristor-switched capacitors (TSC) consist of a fixed capacitance C, a bidirectional thyristor switch SW, and a relatively small surge-limiting reactor L, as depicted in Figure 3.10. The functionality of the switch enables the capacitor to be either connected or disconnected from the circuit. Utilizing Kirchhoff's Voltage Law (KVL) in the Laplace domain, the supply voltage V_s can be articulated through equation 3.27, where V_{co} signifies the initial voltage across the capacitor. In the context of a sinusoidal supply, the instantaneous current as a function of time is represented by equation 3.28, with ω_n denoting the natural frequency of the LC circuit, and n is defined by equation 3.29

$$V_s = (L_s + \frac{1}{C_s}) * I_s + \frac{V_{co}}{S} \quad 3.27$$

$$i(t) = V_m \frac{n^2}{n^2-1}\ \omega C\ \cos(\omega t + \alpha) - \quad 3.28$$

$$n\omega C(V_{co} - \frac{n^2}{n^2-1}\ \sin\alpha) * \sin\omega_n t -$$

$$V_m \omega C \cos\alpha \cos\omega_n t$$

$$n = \sqrt{\frac{X_C}{X_l}} \quad 3.29$$

To obtain transient-free switching the following conditions must be satisfied: Condition1: $\cos\alpha = 0\ or\ \sin\alpha = 1$ Condition 2: $V_{co} = \frac{n^2}{n^2-1}$

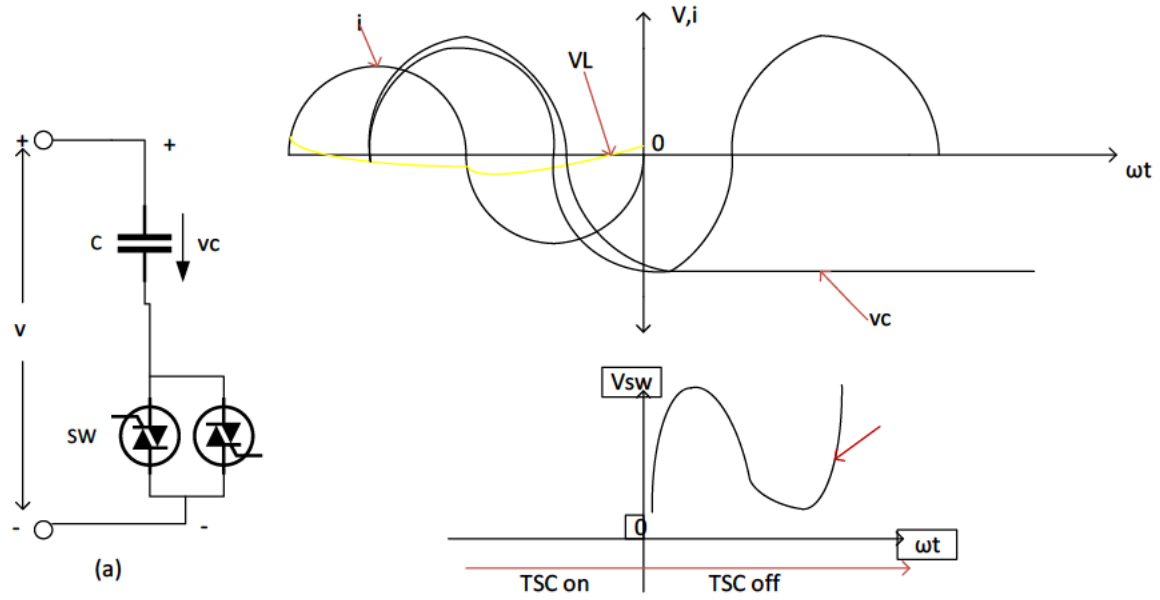

Figure 3. 10 Thyristor Switched Capacitor principle of operation

The initial condition specifies that the capacitor is activated when the supply voltage reaches its maximum. The following condition requires that the capacitor must achieve a voltage that surpasses the supply voltage prior to activation. Therefore, to maintain operation without transients, the steady-state current (when the TSC is closed) is described by equation 3.30. This goal can be accomplished with minimal transient interference if the TSC is engaged at times when the capacitor's residual voltage corresponds with the applied alternating current voltage. If this alignment is not achieved, switching transients will occur. These transients are a result of the nonzero rate of voltage change (dv/dt) at the switching moment, which, in the absence of a series reactor, would result in an instantaneous current of $i = C\ dv/dt$ flowing through the capacitor.

$$i(t) = V_m \frac{n^2}{n^2-1}\ \omega C\ \cos(\omega t + 90) - n\omega C(V_{co} - \frac{n^2}{n^2-1}\ \sin\alpha) * \sin\omega_n t \quad 3.30$$

3.3.3 The principle of series compensation

A voltage can be applied in series with the transmission line to regulate the current flow, which in turn influences the power transfer from the sending end to the receiving end. An ideal series compensator, denoted as the voltage source V_C, is positioned at the midpoint of the transmission line, as illustrated in Figure 3.11. The current traversing the transmission line is described by equation 3.31. The overall impedance is determined using equation 3.32, while the resistance is defined by equation 3.33. The total Active and Reactive power are calculated by equation 3.34 and equation 3.35 respectively

$$I = \frac{V_s - V_r - V_c}{jX_c} \quad 3.31$$

$$X_{eq} = X_s - X_{comp} = X\ (1 - r) \quad 3.32$$

$$r = \frac{X_{comp}}{X_c} \quad 3.33$$

$$P = \frac{V^2}{(1-r)X}\sin\delta \quad 3.34$$

$$Q = \frac{2V^2}{X} * \frac{r}{(1-r^2)}\ (1 - \cos\delta) \quad 3.35$$

The existence of considerable series reactive impedance in a long transmission line can restrict its power transmission capability. In such cases, the impedance introduced by a series compensating capacitor can mitigate some of the line's natural reactance, effectively reducing the transmission impedance as though the line had been physically shortened. A series compensator functions by injecting a voltage in series with the transmission line. The voltage applied in this manner is determined by the product of the variable impedance and the current flowing through it. When this voltage is in phase quadrature with the line current, the series compensator either supplies or absorbs variable reactive power exclusively. Consequently, the series compensator can be implemented as a variable impedance device (such as a capacitor or reactor) or as a power electronics-based variable source that operates at the fundamental frequency, as well as at sub-synchronous and harmonic frequencies, or a combination of these, to achieve the desired control strategy.

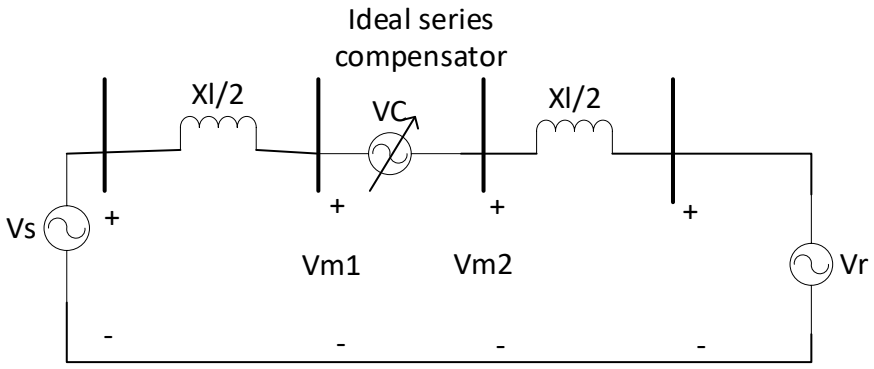

Figure 3. 11 A Series compensation

A voltage that is in quadrature with the line current is applied, leading to an increase in both the current and the power transmission capacity. Series compensation techniques can be further categorized as...

- Thyristor controlled series compensator
- Thyristor switched series compensator
- Forced Commutation -controlled series capacitor

3.3.3.1 Thyristor Switched series capacitor

A thyristor-switched series capacitor (TSSC) is composed of multiple capacitors connected in series, with each capacitor featuring a switch constructed from two antiparallel thyristors. The schematic diagram of this arrangement is depicted in figure 3.12a. The capacitor becomes active when the corresponding thyristor switch is in the off position, while it is bypassed when the switch is engaged. Consequently, when all switches are in the off state, the equivalent capacitance of the series configuration is determined by equation 3.36. Conversely, if all switches are simultaneously activated, the equivalent capacitance is effectively reduced to zero. Thyristors are naturally commutated, meaning they turn off when the current reaches zero. Therefore, capacitors can only be integrated into the circuit at the zero crossings of the line current, a method referred to as zero current switching (ZCS). This technique allows the capacitor to charge from zero to its maximum value during one half-cycle of the line current and to discharge back to zero in the subsequent half-cycle, resulting in a direct current offset voltage that corresponds to the amplitude of the alternating current capacitor voltage, as shown in Figure 3.12b. To mitigate the initial surge current through the switch and the associated transients, as outlined in equation 3.37, it is advisable to activate the thyristors for

bypassing only when the capacitor voltage is at zero. The presence of the DC offset and the condition of $V_C = 0$ may lead to a delay of up to one full cycle, thereby imposing a theoretical limit on the response time of the TSSC. Additionally, due to the di/dt limitations inherent to thyristors, practical implementations require the addition of a current-limiting reactor in series with the thyristor switch. This configuration can result in the development of a TCSC, which can substantially enhance the operational and performance attributes of the TSSC.

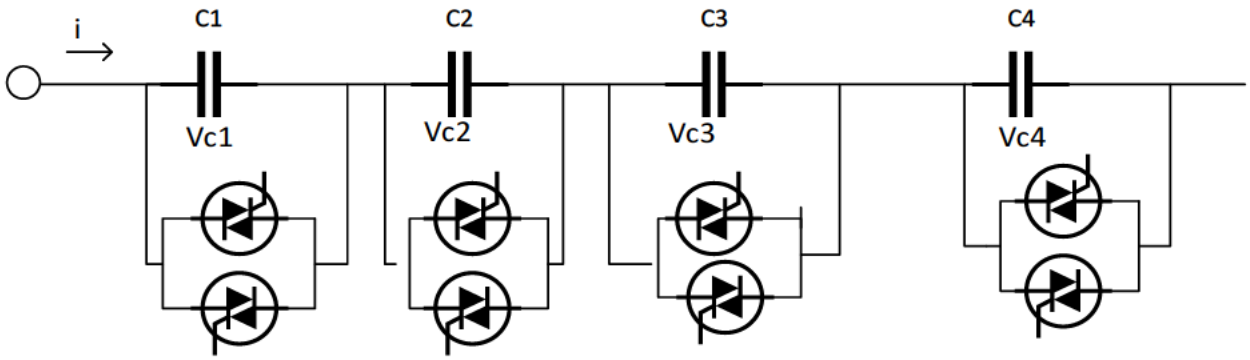

(a) Series connected Capacitors

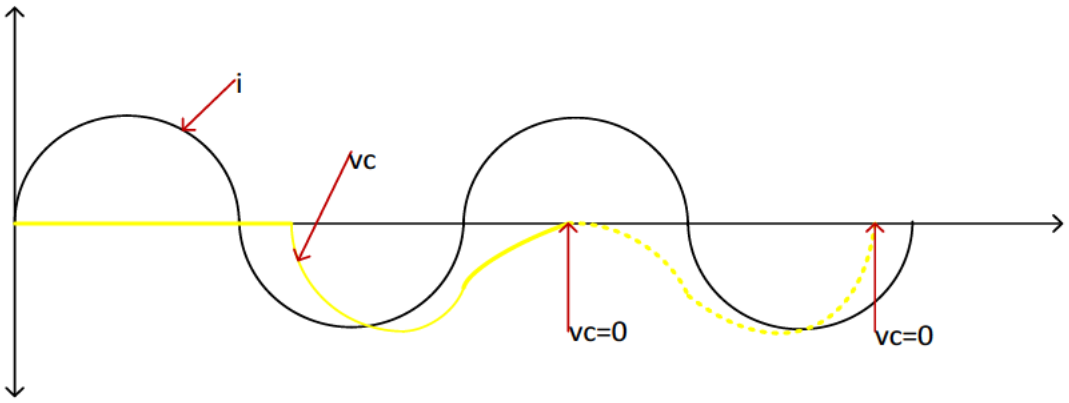

Figure 3. 12 Thyristor-switched series capacitor (TSSC)

$$C_{eq} = \frac{C}{m} \qquad 3.36$$

$$V_c = C\frac{dv}{dt} \qquad 3.37$$

3.3.3.2 Forced-Commutation-Controlled Series Capacitor

The forced-commutation-controlled series capacitor (FCSC) consists of a fixed capacitor that operates in conjunction with a forced-commutation device, which may take the form of a Gate Turn-Off (GTO), a Metal-Oxide-Semiconductor Controlled Thyristor (MCT), or an Insulated Gate Bipolar Transistor (IGBT). Figure 3.13 a provides a depiction of a GTO circuit configuration. This setup is similar to that of TCSC with the key difference being the

replacement of the bidirectional thyristor switch with a bidirectional forced-commutation device. When the GTO switch, referred to as SW, is closed, the voltage across the capacitor, labelled as V_c, is measured as zero. In contrast, when the switch is opened, the voltageV_c, attains its peak value. The switch enables the modulation of the alternating current (AC) voltage V_c, across the capacitor, depending on a predetermined line current i. Thus, by synchronously opening and closing the switch during each half-cycle in accordance with the AC system's frequency, the voltage across the capacitor can be effectively managed.

Figure 3.13 b illustrates the line current i alongside the capacitor voltage V_c, at a delay angle γ for both the positive and negative half-cycles. The capacitor voltage can be represented as a function of γ, as shown in equation 3.38. The GTO is activated whenever the capacitor voltage approaches zero and deactivated at a delay angle, which is measured relative to the peak of the line current or the zero crossing of the line voltage. The capacitor voltage V_c, at a delay angle γ for both positive and negative half-cycles indicates that the switch SW remains on from 0 to γ and off from $\pi - \gamma \; to \; \pi. For \; \gamma = 0$, the switch remains permanently open, resulting in no impact on the resultant capacitor voltage V_c,. If the switch's opening is delayed by an angle γ concerning the line current, this can be expressed in equation 3.40, while the capacitor voltage as a function of γ is articulated in equation 3.41. The waveforms of V_c corresponding to different values of γ1, γ2, γ3, and γ4 are illustrated in Figure 3.12c. Consequently, the FCSC serves as the dual of the TCR, and the fundamental capacitor voltage can be derived from equation 3.41, while the impedance as a function of γ is represented by equation 3.42.

$$\gamma = (0 \leq \gamma \geq \frac{\pi}{2}) \qquad 3.38$$

$$i = I_m \cos \omega t \qquad 3.39$$

$$V_c(t) = \frac{I_m}{\omega t}(\sin \omega t - \sin \gamma) \qquad 3.40$$

$$V_c(\gamma) = \frac{1}{\omega C}(1 - \frac{2}{\pi \gamma} - \frac{1}{\pi}\sin 2y) \qquad 3.41$$

$$X_c(\gamma) = \frac{V_c(\gamma)}{1} = \frac{1}{\omega C}(1 - \frac{2}{\pi \gamma} - \frac{1}{\pi} sin\, 2y) \qquad 3.42$$

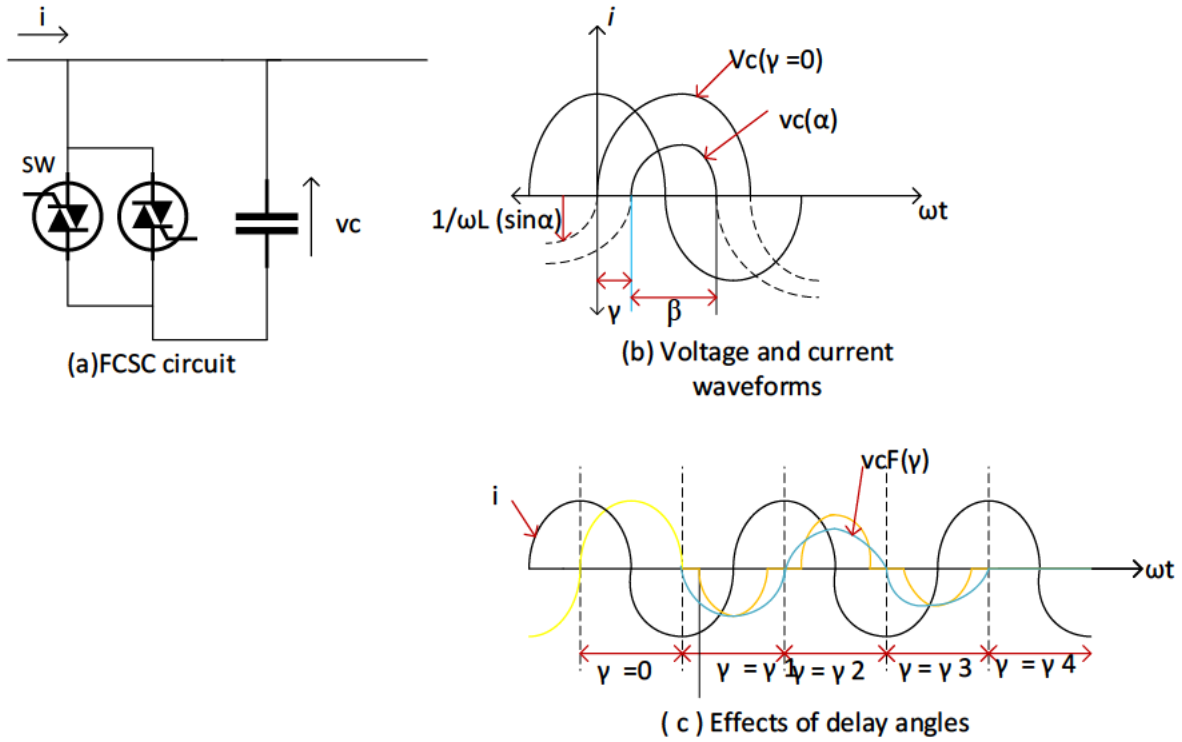

Figure 3. 13 Forced-Commutation-Controlled Series Capacitor

3.3.4 The Voltage Profile of a compensated transmission line

Expanding from the equivalent circuits used to determine the ABCD parameters of a transmission line, for a compensated transmission line the equivalent circuit is modified to figure 3.14. The first case to examine is that where the series capacitors are located at the middle of the transmission line. The efficacy of series compensation is enhanced when the series capacitors are positioned at the midpoint of the transmission line. This positioning is particularly crucial for extensive lines, given that the effectiveness is dependent on the length of the line. In the case of lines measuring 300 km or shorter, the improvement in effectiveness is relatively modest.

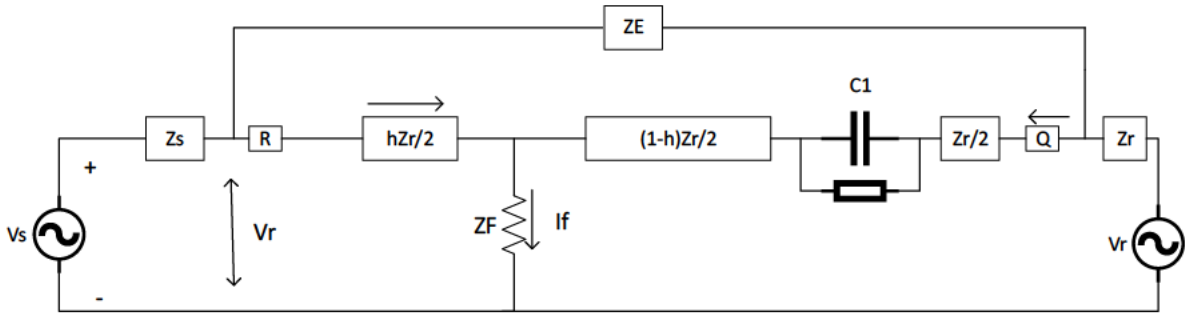

Figure 3. 14 Equivalent circuit of a transmission line compensated at the middle of the Line

Series compensated lines display a voltage profile characterized by a continuous variation with respect to distance, yet they demonstrate abrupt voltage transitions at the locations of the series capacitors. The voltage across each capacitor is contingent upon the current traversing the line at that specific point. In the case of an extended transmission line, the current behaves as a continuous function of distance, albeit with variations along the line's length. Consequently, in a lengthy line featuring multiple series capacitors, the voltage differential between two series capacitors may not be uniform. Figure 3.15 illustrates the relationship between the current magnitude detected at relay R and the position of the fault. In scenarios with minimal compensation, the current magnitude for faults situated to the left of the capacitor location closely resembles that of the uncompensated current magnitude. However, as the level of compensation increases, this similarity diminishes, albeit the variation remains relatively minor. For faults occurring beyond the capacitor bank, typical resonances emerge at higher compensation levels; nevertheless, the intensity of these resonant peaks is significantly lower compared to situations where capacitors are positioned at the line's extremities.

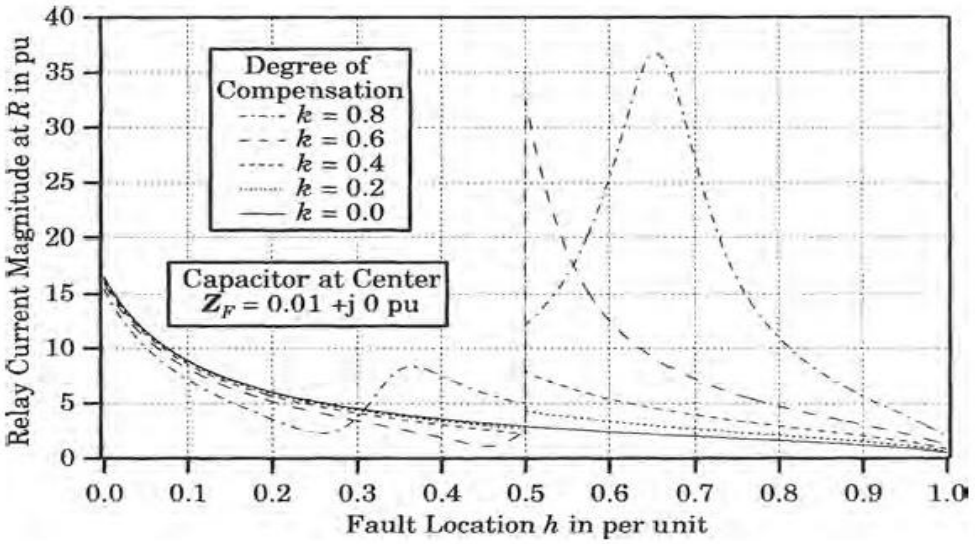

Figure 3. 15 The relationship between the current magnitude detected at relay R and the position of the fault

The relationship between relay voltage and fault location is illustrated in Figure 3.16, which highlights the voltage resonance observed at elevated levels of compensation. While the voltage peaks at point R are significantly higher than those of the uncompensated line, they do not reach the levels seen when capacitors are positioned at the line's terminals, as depicted in Figure 3.16 for reference. Figures 3.15 and 3.16 illustrate the magnitudes of

phasor current and voltage at various fault locations. At a compensation level of 0.6, a nascent resonant condition is observed, though it is not fully developed. Both current and voltage show an increase in magnitude; however, neither exhibits a well-defined resonant peak. This lack of smoothness in the resonance is due to the presence of the series capacitor, which disrupts the resonance pattern[170]. The complex phasor current and voltage for 60% series compensation are shown in Figure 3.17. As the fault location varies along the line, resonance is detected in both current and voltage.

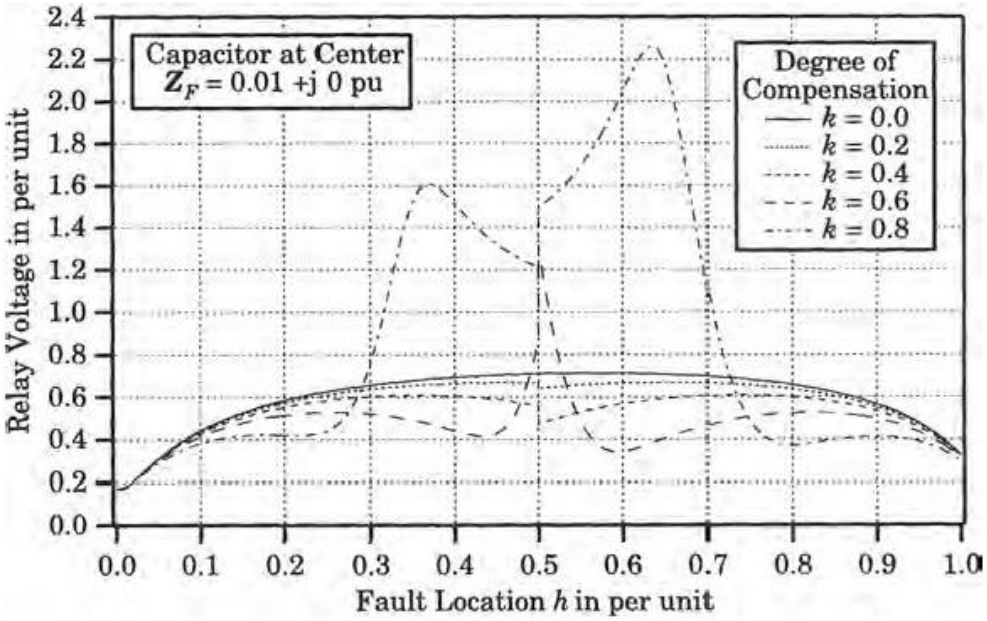

Figure 3. 16 The relationship between relay voltage and fault location

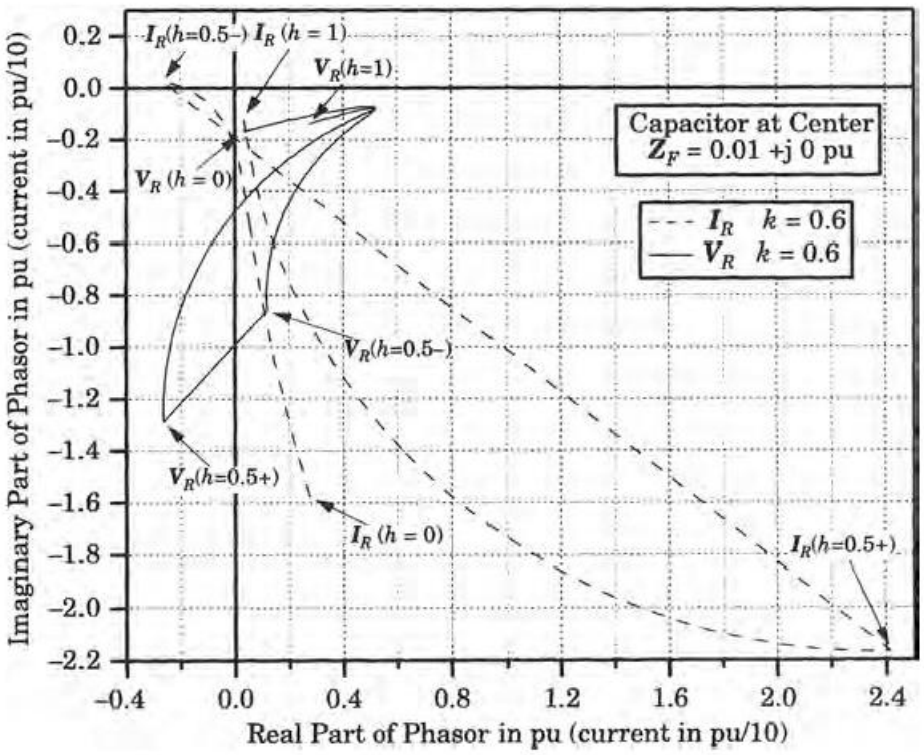

Figure 3. 17 The complex phasor current and voltage corresponding[170]

The complex phasor representations of current and voltage for a series compensation level of 60% are illustrated in Figure 3.17. This can be contrasted with Figure 3.16, which depicts the scenario involving capacitors positioned at the line's terminals. As the fault location shifts along the line, a resonance phenomenon emerges in both current and voltage; however, this is disrupted by the presence of the series capacitor, resulting in a significant alteration, particularly in the current. The change in voltage is noteworthy, as it transitions into the third quadrant. It is important to observe that at h = 0.5+, the current exhibits a leading behaviour relative to the voltage from the perspective of the relay at R. This unique situation is referred to as voltage inversion, a concept that will be examined in greater depth subsequently. This condition is applicable for faults located beyond the capacitor, extending to h = 0.55, at which point the real component of the voltage reverts to a positive value. When the compensation level is raised to 80%, the trajectories of the currents and voltages undergo a complete transformation, as depicted in Figure 3.18

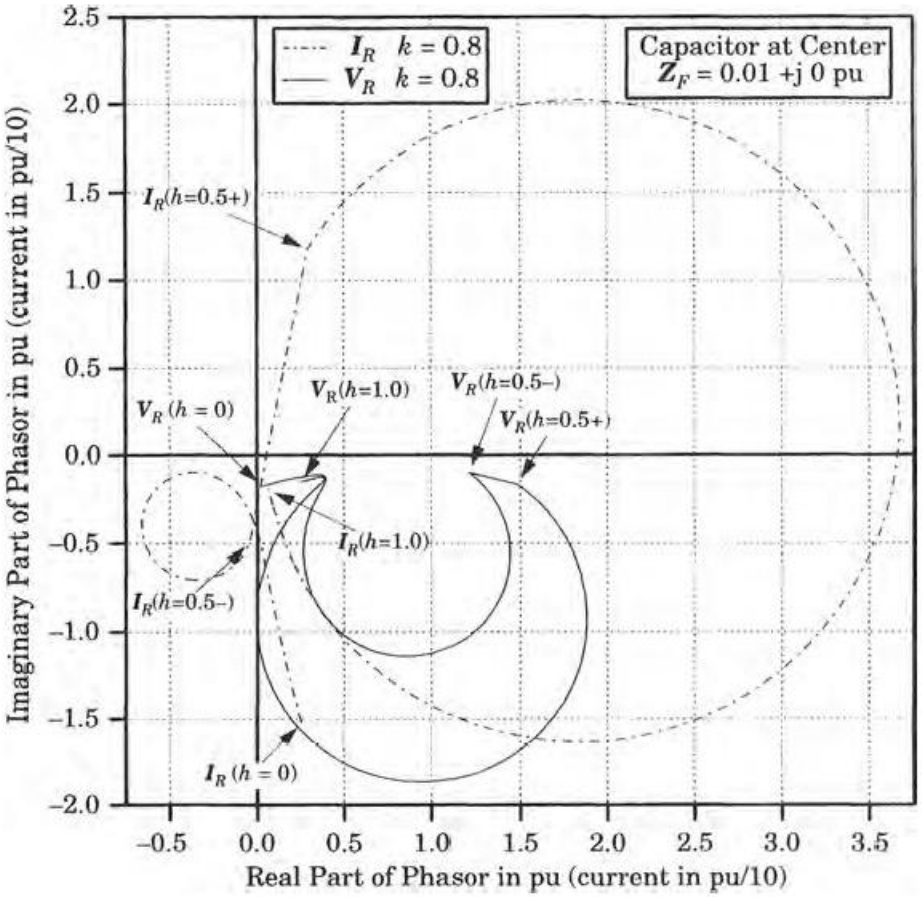

Figure 3. 18 the impact of the degree of compensation on current

In the context of this elevated compensation degree, the resonances are fully established in both current and voltage. Both parameters exhibit a minor resonance on the proximal side of the capacitor, yet they demonstrate a significantly pronounced resonance for faults located beyond the capacitor. It is important to note that the voltage does not reverse, in contrast to the behaviour observed at 60% compensation. Additionally, the current attains exceptionally high values and exhibits a leading characteristic. This phenomenon can be attributed to the substantial capacitive reactance. The impedance observed by the relay at point R is notably complex, as illustrated in Figure 3.18. Predominantly, the impedance resides within the nominal mho circle, suggesting that any standard line protection scheme will effectively identify the fault. However, for compensation levels exceeding 0.4, the impedance loci experience rapid and atypical variations as the fault traverses through the resonant conditions just beyond the centre of the line. The impedance tends to loop toward the origin during resonance, indicating that the relay significantly overreaches the actual fault location. Just past the resonant threshold, the impedance becomes negative, moving outside the

directional mho trip zone, but ultimately returns to the trip zone as the fault approaches the far end of the line. This behaviour implies that a conventional distance relay may not achieve accurate discrimination for all fault scenarios

3.4 The concept of resonance frequency

In a plain uncompensated power system, the main energy storage mechanism during faults is via magnetic flux, held in the loops and coils of the inductive elements such as overhead lines and transformers. From basic electrical theory, any single energy source produces exponential transients. Power Engineers recognise the exponential transient as being very common in faulted power systems [171]. The introduction of series capacitance provides the second alternative form of energy storage. This opens up the possibility of resonance between the capacitive and inductive forms. The critical parameter controlling the degree of resonance is the losses in the system. Analysis has proven that the losses incurred within the metal oxide varistor (MOV) can be significant [172] , The implementation results in a significant damping effect. Experimental findings indicate the presence of additional transient components across both high and low frequency ranges; nevertheless, these components do not prevail in the overall waveforms. The arrangement of the capacitor in series with the inductance of the transmission line forms a resonant circuit characterized by a resonant frequency, denoted as f_{RES}, as defined by equations 3.43 and 3.44. Any perturbation within the power system, whether resulting from a switching event or a fault, will induce oscillations in the power system at this subharmonic frequency.[6].

$$f_{RES} = \frac{1}{2\pi\sqrt{LC}} \qquad 3.43$$

$$f_{RES} = f_{nom}\sqrt{\frac{X_c}{X_l}} \qquad 3.44$$

3.5 The concept of Voltage and current Inversion

Consider a network shown in figure 3.19 (a), representing a 2-bus network system, suppose the fault is applied at point F the equivalent circuit of the system can be represented by figure 3.19(b), the current seen by the relay at bus M can be represented by equation 3.45.

$$I_R = \frac{V_S}{R + j(X_s + X_{LF} - X_C)} \qquad 3.45$$

Where X_{LF} lines inductive reactance during the fault, and X_C capacitive reactance by compensating the Line X_s is the source impedance. For conditions where $X_s + X_{LF} > X_C$ the current I_R will LAG the voltage V_s but when$X_s + X_{LF} < X_C$ the current will be inverted hence the current will now LEAD the voltage. This scenario is known and current inversion which has a direct impact on the impedance, also the bus voltage increases as shown in figure 3.21. The fault current that passes through the series capacitor during a current inversion typically exceeds the normal operating current of the series capacitor bank by a factor of six to seven times its rated capacity. This phenomenon induces a voltage drop across the power system that is largely in phase with the source voltage, leading to a resultant voltage that is lower than the source voltage throughout the power system[6]. Generally, the duration of a current inversion within a power system is less than one complete cycle of the system.

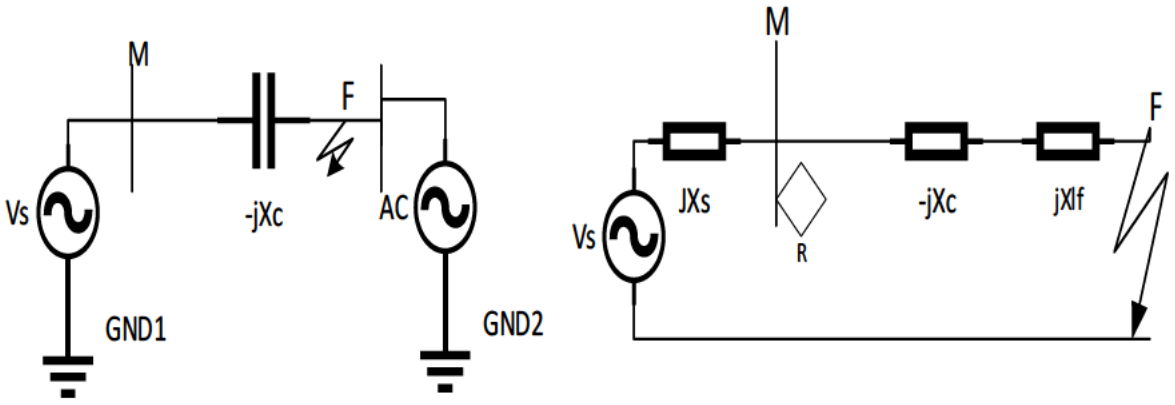

(a) Transmission line network (b) Equivalent circuits

Figure 3. 19 Compensated transmission network

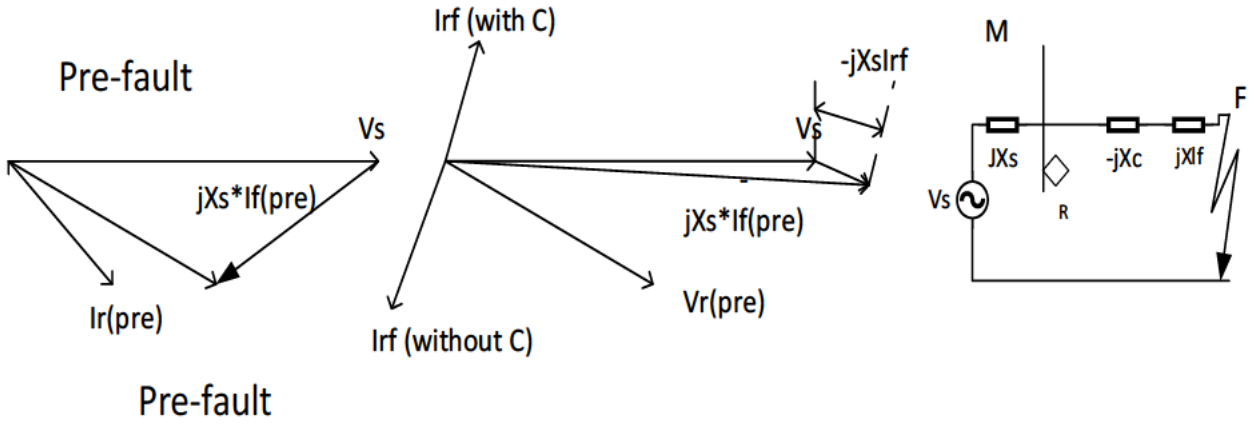

Figure 3. 20 the concept of current inversion

Voltage inversion in a compensated transmission line describes a situation in which the voltage phase angle at a specific measurement location undergoes a 180-degree shift during

a fault event this scenario can be graphically represented by figure 3.22, while equation 3.46 express the current seen by the relay during fault condition.V_R is defined by equation 3.47, it is importance to note that substituting 3.33 the voltage can be calculated using 3.48. Furthermore, under conditions where (i) $(i)X_c > X_{LF}\ or\ (ii)\ X_{LF} + X_S > X_c$ voltage will appear inverted relative to its normal state.

$$I_R = \frac{V_S}{R+j(X_s+X_{LF}-X_C)} \qquad 3.46$$

$$V_R = jI_R(X_{LF} - X_C) \qquad 3.47$$

$$V_R = \frac{V_S j(X_{LF}-X_C)}{j(X_s+X_{LF}-X_C} \qquad 3.48$$

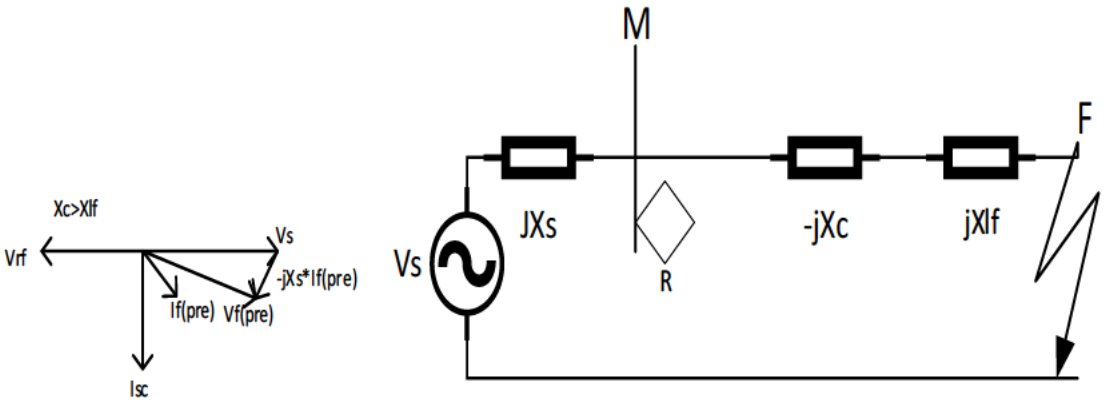

Figure 3. 21 The concept of Voltage inversion

This phenomenon is commonly observed when a series capacitor is employed for compensation, and the impedance from the fault site to the measurement point exhibits capacitive characteristics, while the overall system impedance retains its inductive nature. Such conditions can create challenges for protective relays, as they may misinterpret the direction of the fault. Key considerations regarding voltage inversion include the following, higher levels of series compensation on a transmission line can profoundly modify the impedance characteristics, resulting in a condition where the fault location is perceived as capacitive in relation to the relaying point, which can lead to a significant shift in the voltage phase.

- Effects on protection relays: Voltage inversion poses challenges for distance relays that are intended to ascertain fault direction, as these relays may misinterpret the inverted voltage as indicating a fault in the reverse direction.

- Dependence on fault location: The probability of voltage inversion is heightened when a fault occurs in proximity to the series capacitor, as the impedance between the fault and the measurement point tends to exhibit more capacitive behaviour.
- Strategies for mitigation: To counteract voltage inversion, specialized protection strategies are implemented, including the use of directional relays equipped with sophisticated algorithms capable of accommodating potential phase shifts resulting from compensation.

3.6 Conclusion

This section examines the mathematical formulation of transmission line compensation to elucidate its effects on parameters such as voltage and current, as well as the impedance perceived by the relay during the protection of a compensated line. Additionally, the concepts of voltage and current inversion are explored, particularly their influence on voltage and current behaviour. This analysis will contribute to a deeper understanding of the considerations necessary for designing an effective protection scheme for such networks. It is concluded that Series capacitors present two distinct challenges that complicate the relay logic's ability to accurately identify faults on the transmission line. Firstly, in the case of close-in faults, the occurrence of current or voltage inversions leads to a reduction in the apparent impedance, placing it within the fourth quadrant. Although this scenario does not impair the directional sensing capabilities of the relay logic, it results in the fault being situated outside the conventional trip zone. The second challenge arises from current inversions that shift the apparent impedance into the second quadrant of the impedance plane. This phenomenon is often associated with resonant conditions, which can push the relay's apparent impedance beyond the standard trip zone limits, thereby compromising the accuracy of the directional measurement. Voltage and current inversions are evidently more probable at elevated levels of compensation, and their severity increases when end-of-line capacitors are utilized. In contrast, capacitors positioned at the centre of the system exhibit different characteristic

Chapter 4 Renewable Energy Integration

4.1 Introduction

Renewable energy systems are integrated into the electrical grid at multiple scales, ranging from large-scale implementations (megawatt capacity at the transmission level) to smaller-scale applications (kilowatt capacity at the distribution level). This section specifically focuses on the integration of wind energy at the bulk level. The primary emphasis is on the system's response to various events, particularly concerning modifications in protection mechanisms. It is widely recognized that the fundamental characteristic of wind and solar energy is their dependence on weather conditions, which inherently introduces uncertainty and unpredictability. To mitigate the effects of this intermittency, renewable energy systems, such as wind and photovoltaic power systems, must provide support to the grid [173] The architecture of the renewable energy plant is illustrated in Figure 4.1, where the energy sources may include either solar panels or wind turbines.

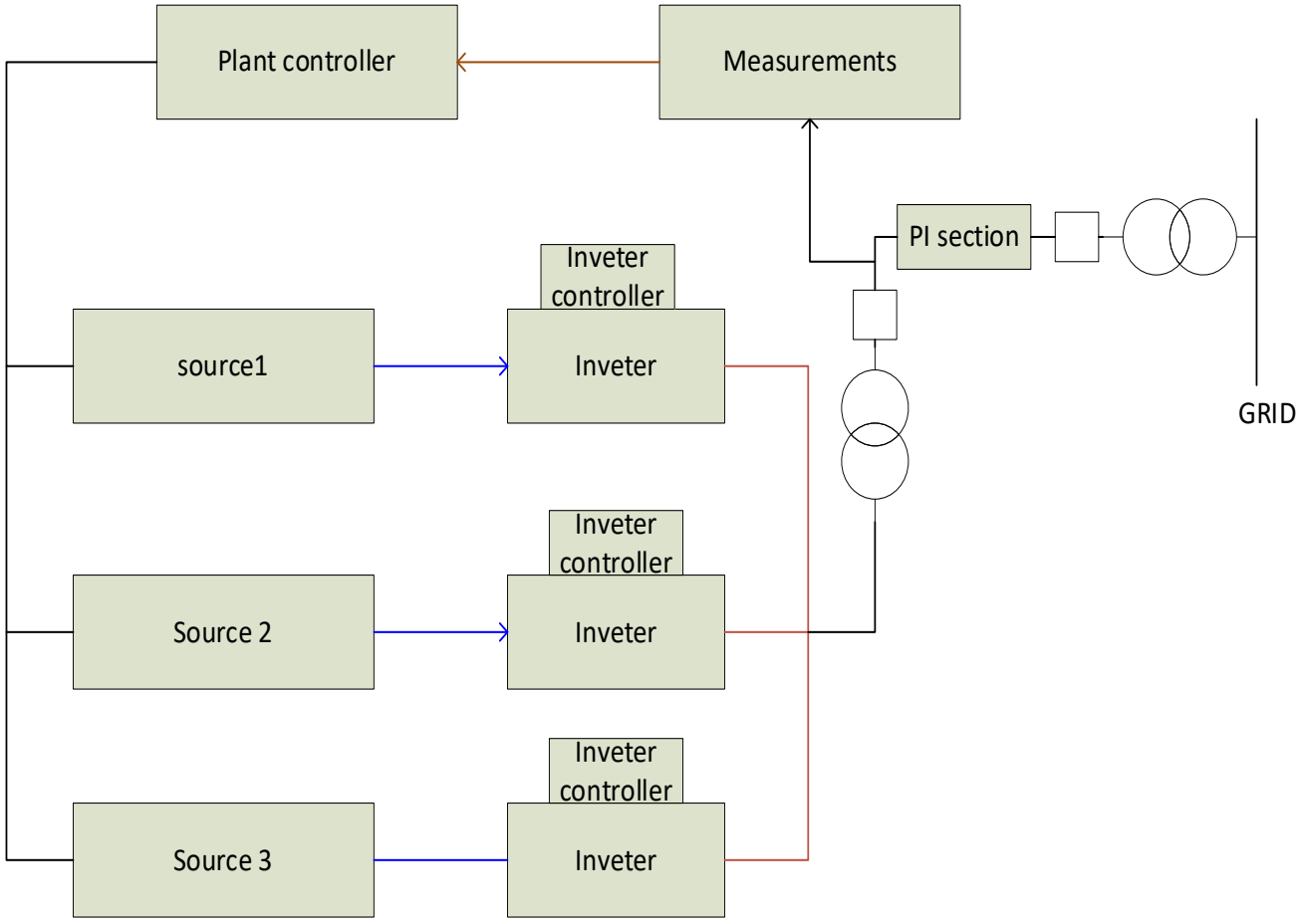

Figure 4. 1 The renewable Plant architecture

The Ideal close loop setup of the system is shown in figure 4.2., where there is an interaction between the GRID and RESs parameters. Controls plays a crucial role in stabilizing the systems. The sections below will discuss the important parameters and technologies used in renewable energy integration to maintain the stability of the grid at different fault scenarios.

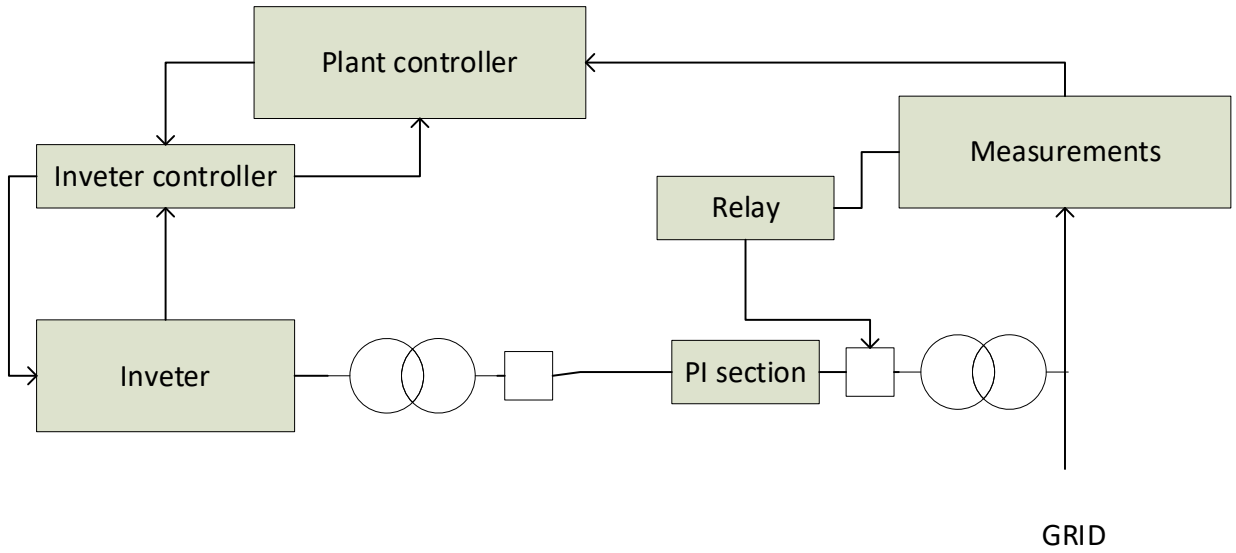

Figure 4. 2 The close loop setup of a RESs grid connected Plant

4.2 PV model design and integration

The schematic representation of a grid-connected PV system is illustrated in Figure 4.3, highlighting the fundamental components of the system. The process of selecting an appropriate converter from the available options, while considering various circumstances and criteria, may result in ambiguity.

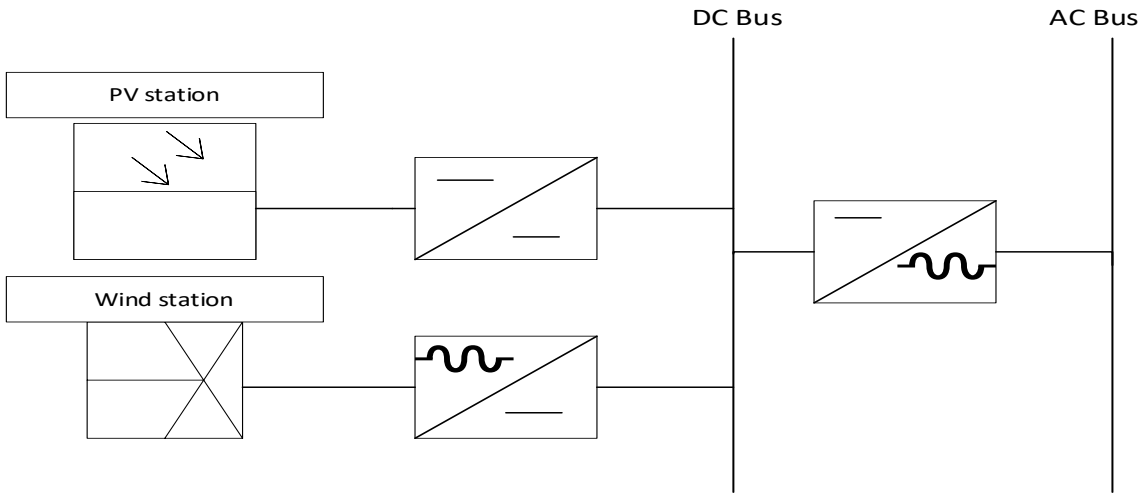

Figure 4. 3 network topology of a grid integrated network

4.2.1 PV Module design

The initial aspect to consider in the design of a PV system is the modelling of a PV module which is shown in figure 4.4 . Manufacturers provide the parameters of PV modules based on Standard Test Conditions, which are defined as a temperature of 25 °C and solar radiation of 1000 W/m². However, in many instances and locations, the conditions outlined by STC are not met. This discrepancy arises because solar radiation typically falls below 1000 W/m², and the operating temperature of the cells often exceeds 25 °C. Such variations lead to a decrease in the output power of the PV module. The photocurrent can be expressed by equation 4.1.

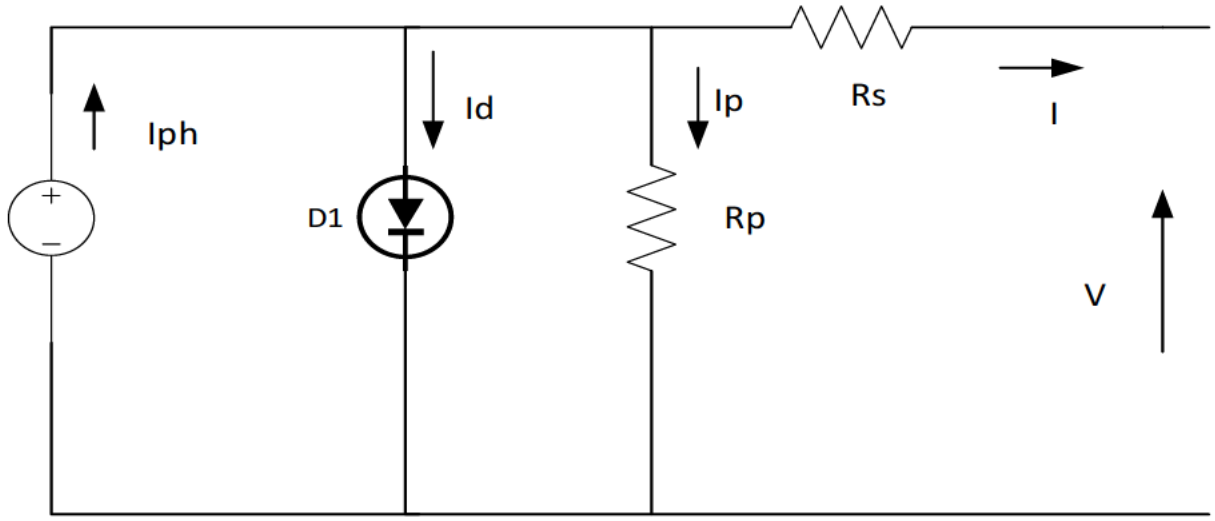

Figure 4. 4 Ideal circuit of PV cell

$$I_{ph} = [I_{SC} + K_i(T - 298)\frac{Ir}{1000}] \qquad 4.1$$

T is the operating temperature I_{sc} is the short circuit current and I_r is the solar irradiation. The I_{rs} is expresses as equation 4.2 which is the module reverse saturation, q and K are equal to 1.6x10^{-19} and 1.308x10^{-23}. V_{oc} is the open circuit voltage while the siries connected cells are represented by N_s. I_0 (saturation current) varies according to equation 4.3

$$I_{rs} = [\frac{I_{SC}}{e^{\frac{qV_{oc}}{N_S KnT}}}] \qquad 4.2$$

$$I_O = I_{rs}[\frac{T}{T_r}]^3 e^{[(\frac{1}{T}-\frac{1}{T_r})\frac{qEgo}{nK}]} \qquad 4.3$$

In equation 4.3 T_r is the nominal temperature at which is 298.15K, E_{go} is the band gap energy of the semiconductor and is a constant value of 1.1eV. The output current module is

expressed as equation 4.4 where V_t is calculated by equation 4.5 and equation 4.6 represent the shunt current.

$$I = N_p I_{ph} - N_p I_o e^{\left[\frac{\frac{V}{N_S}+I\frac{R_S}{N_p}}{nV_t}-1\right]} - I_{sh} \quad 4.4$$

$$V_t = \frac{kT}{q} \quad 4.5$$

$$I_{sh} = \frac{V\frac{N_p}{N_S}+IR_{sh}}{R_{sh}} \quad 4.6$$

PV parallel modules are represented by N_p, R_s and R_{sh} are series and shunt resistance respectively and diode thermal voltage is expressed as V_t. The parameters of PV module referenced from a manufacture's datasheet is shown in each equation is model in MATLAB Simulink to create a subsystem of the PV module.

4.2.2 Wind turbine design

The comprehensive configuration of the wind energy system employed in this study is illustrated in Figure 4.5 in this section wind turbine, drive train, generator model and pitch angle controller will be discussed while the power conversion will be discussed in a separated section.

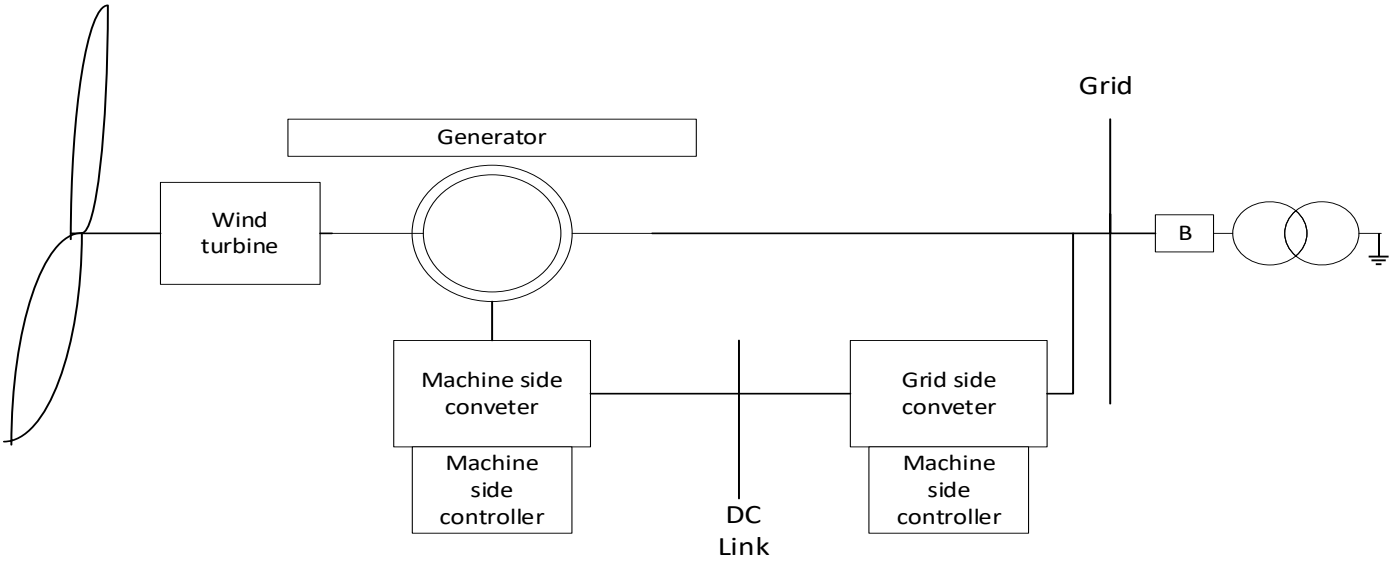

Figure 4. 5 The wind energy conversion system

The Mechanical output power extracted (P_m) from the wind turbine is determined by 4.7 where V is the wind speed, A is the wind turbine area swept by the rotor, ρ is the wind density

which is normally a constant of 1.225Kg/m^3, C_p is the power co-efficient dependent on the tip speed ratio (λ) and the blade pitch angle (β) the coefficient of power is defined by 4.8 and A is determined using 4.9 where R represents the radius of the blade in meters (m).

$$P_m = 0.5C_p(\lambda, \beta).\rho.A.V^3 \quad 4.7$$

$$C_p(\lambda, \beta) = C_1(C_2\frac{1}{\gamma} - C_3\beta - C_4\beta^x - C_5)e^{-C\frac{1}{6\gamma}} \quad 4.8$$

$$A = \pi R^2 \quad 4.9$$

Theoretically the value of power coefficient is assumed to be 0.593 however practically even for well-designed wind turbines the value ranges between $0.35 \leq C_p \geq 0.45$. and $C_1 to\ C_6$ are constants $C_1 = 0.5$, $C_2 = 116, C_3 = 0.4, C_4 = 0, C_5 = 5\ and\ C_6 = 21$. Gamma ($\gamma$)is defined by 4.10 and the tip speed lambda(λ) is defined by 4.11. where ω_m is the angular velocity of the Rotor. The rotor toque is determined by 4.12.

$$\frac{1}{\gamma} = \frac{1}{\lambda - 0.08\beta} - \frac{0.035}{1+\beta^3} \quad 4.10$$

$$\lambda = \frac{\omega_m R}{v} \quad 4.11$$

$$T_m = \frac{P_m}{\omega_m} \quad 4.12$$

An alternative model of wind turbine is examined by [174]. Wind turbines can be categorized into two primary design models based on the orientation of their rotational axis: Horizontal Axis Wind Turbines (HAWT) and Vertical Axis Wind Turbines (VAWT). The VAWT, also known as the Darrieus rotor, is named after its creator [175]. HAWTs are particularly effective in harnessing the maximum amount of wind energy throughout different times of the day and across various seasons, and their blades can be adjusted to mitigate the impact of high wind storms. The kinetic energy rate of change defines the power (P) expresses as equation 4.13, the flow rate is described by 4.14 and hence the power equation can be simplified as equation 4.15.

$$P = \frac{dE}{dt} = \frac{1}{2}\frac{dm}{dt}\ {v_m}^2 \quad 4.13$$

$$\frac{dm}{dt} = \rho A V_\omega \quad 4.14$$

$$P = \frac{1}{2}\rho A {V_\omega}^2 \quad 4.15$$

The mechanical power, denoted as Pw, that is extracted by the rotor blades in watts, is determined by the difference between the wind power upstream and downstream, as expressed in equation 4.15. In this context, $V_u \, and \, V_d$ represent the velocities of the wind upstream and downstream, respectively. It will be demonstrated subsequently that these two velocities contribute to the blade tip speed ratio. Furthermore, the expression for mechanical power can be streamlined into equation 4.16, which is ultimately encapsulated in equation 4.17.

$$P_w = \frac{1}{2}\rho A(V_u - V_d)^2 \qquad 4.15$$

$$P_w = \frac{1}{2}\rho A[\frac{v_u}{2}(V_u - V_d)^2 + \frac{v_d}{2}(V_u - V_d)^2] \qquad 4.16$$

$$P_w = \frac{1}{2}\rho A(V_u)^2 C_p \qquad 4.17$$

The power generated by a turbine is influenced by several factors, including the rotor blade area, wind velocity, and the power coefficient. Adjustments to the turbine's output power can be made by modifying the rotor system's area and the flow conditions, which underpins the control system's functionality. The power coefficient (Cp) is optimized at a specific tip speed ratio (λ), which is unique to each turbine's design. By varying the pitch angle (β), one can derive performance curves that illustrate the optimal operational range for a given turbine. An example of such a performance curve is depicted in figure..., where the pitch angle values range from 0° to 240°.

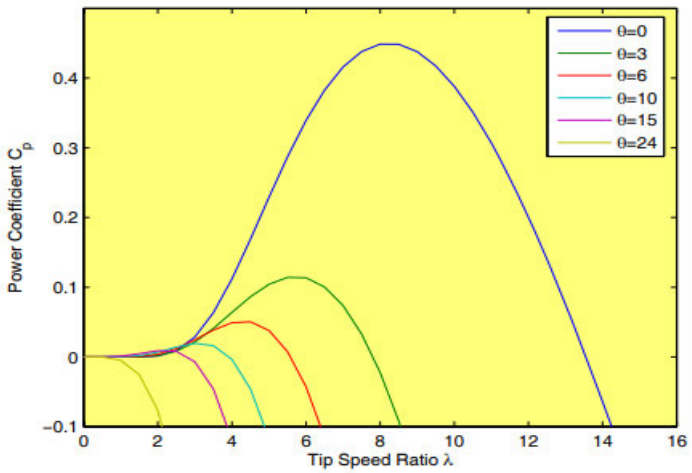

Figure 4. 6 Wind energy conversion system performance curve

The data presented in figure 4.6 illustrates that adjusting the pitch of the turbine blades leads to a decrease in the coefficient of performance (Cp), dropping from approximately 40% at a pitch angle of 0 degrees to around 10% when the pitch angle is increased to 30 degrees. This adjustment is advantageous as it effectively regulates the power output of a variable wind speed turbine, such as the one under consideration, when wind speeds exceed the rated threshold. The moment of inertia is of paramount importance due to its significantly high value. Consequently, the wind turbine should be regarded as a "speed source." This characterization adheres to the mechanical relationship delineated in equations 4.18 and 4.19, where $T_{wt}\ and\ T_{em}$ represent the torques of the wind turbine and the electromagnetic system, respectively, with f denoting the total viscous friction coefficient.

$$\Delta T = T_{wt} - T_{em} = j\frac{d\Omega}{dt} + f\Omega \qquad 4.18$$

$$\Omega = \frac{1}{j}\int(\Delta t - fn)dt \qquad 4.19$$

The drive transmission system of a wind power turbine primarily consists of a turbine-generator assembly and a gearbox. The predominant source of inertia within this system is attributed to the turbine-generator unit, while the inertia of the gearbox is considered negligible due to the minimal impact of the gear teeth. Consequently, the drive transmission can be conceptualized as a combination of two substantial components linked by a shaft, which incorporates both the inertia and the elements of the shaft itself. The mathematical representation of the drive transmission is articulated through equations 4.20 to 4.24, where T_t denotes turbine torque, T_{sh} represents shaft torque, ω_t signifies turbine speed, K_{ss} is a constant, K_d is another constant, and T_m refers to the mechanical torque generated, which is constrained by aerodynamic factors to enhance energy capture.

$$T_t - T_{sh} = 2H_t\frac{d\omega_t}{dt} \qquad 4.20$$

$$\frac{w_t - w_r}{w_{base}} = \frac{d\theta_{sta}}{dt} \qquad 4.21$$

$$T_{sh} = \theta_{sta}K_s + K_d(\omega_t - \omega_r) \qquad 4.22$$

$$T_{base} = \frac{P_{nom}}{w_{base}} \qquad 4.23$$

$$T_m = T_{base}T_{sh} \qquad 4.24$$

Wind Power Plants (WPPs) are typically situated in isolated regions characterized by limited distribution network connections. Consequently, the Short Circuit Capacity (SCC), the size of

the WPP, and the ratio of short circuit impedance angle (X/R) play crucial roles in maintaining the voltage stability of a distribution system that incorporates WPPs. According to [176] The calculation of the Short Circuit Current can be performed utilizing equation 4.25, while the Short Circuit Ratio is determined through equation 4.26, which pertains to the power output from the wind farm in each respective test system. V_{rated} is the nominal voltage of the distribution feeder, I_{SC} is the short circuit current and P_{wind} is the amount of power generated.

$$SCC = \sqrt{3} V_{rated} I_{SC} \quad 4.25$$

$$SRC = \frac{SSC}{P_{wind}} \quad 4.26$$

4.3 Power conversion circuits

Static power electronic devices that transform direct current (DC) into alternating current (AC) at the specified output voltage and frequency are referred to as inverters. Inverters can be categorized into two primary types: voltage source inverters (VSIs) and current source inverters (CSIs). Within the entire system, the inverter serves as the core component. Consequently, this section will explore various configurations of inverters. The fundamental building block of the system is illustrated in figure 4.7, which primarily includes an energy source (such as photovoltaic or wind energy) connected to voltage VSCs and subsequently linked to the grid through a filter. The specific controller, located at a designated point within the system, regulates current, voltage, as well as active and reactive power.

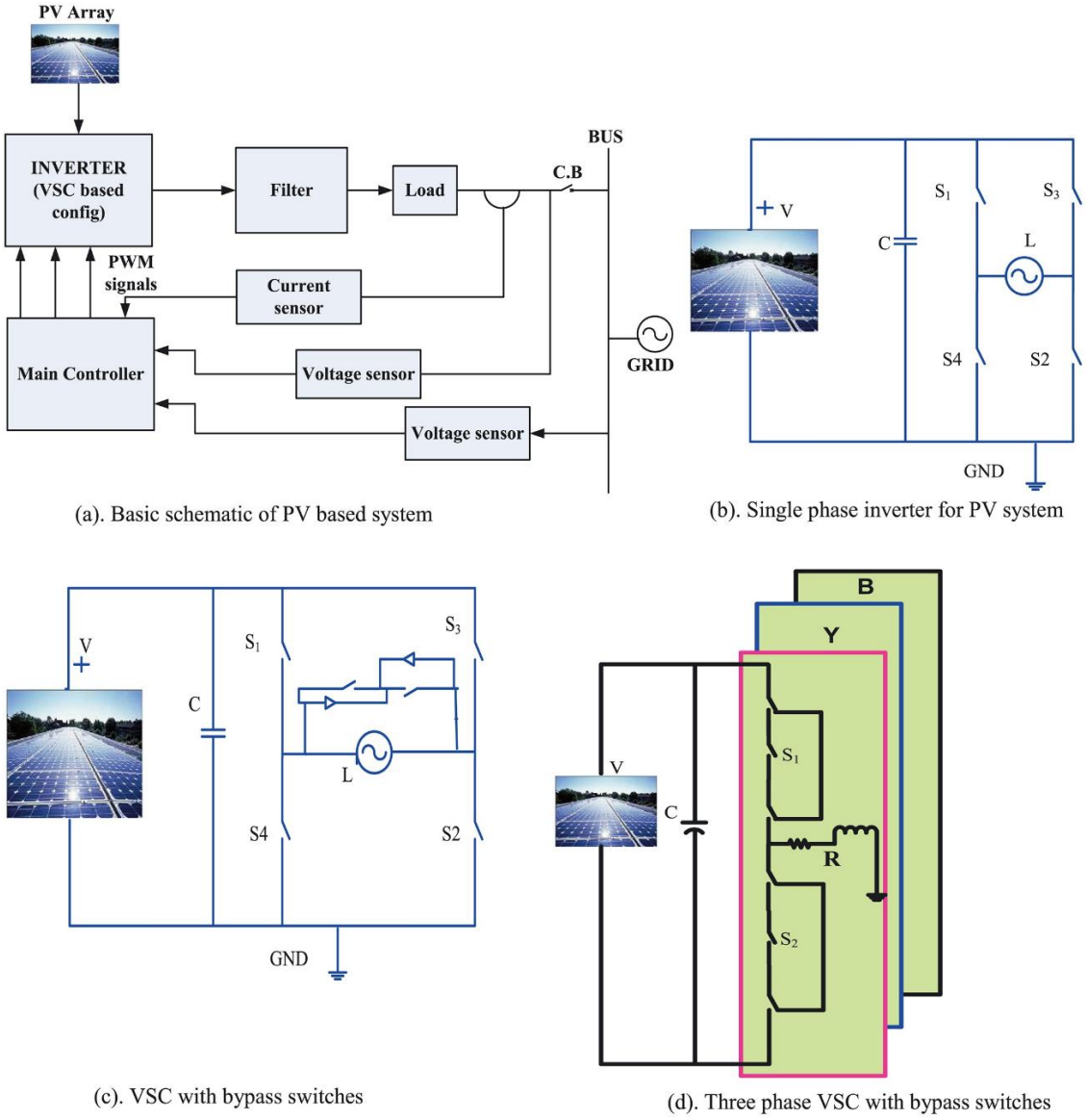

Figure 4. 7 The basic concept of power conversion in renewable energy[177]

The fundamental schematic of an inverter is illustrated in Figure 4.7 (b). It comprises four switches, which may be either metal-oxide-semiconductor field-effect transistor (MOSFETs) or IGBTs, depending on the power capacity requirements. For applications involving low power capacity and high-frequency operation, MOSFETs are typically favoured as the semiconductor switch; conversely, IGBTs are preferred for higher power applications. The input voltage from the PV cell is directed to a DC–DC converter, which stabilizes the direct current using a buck-boost converter. The output voltage from the converter is subsequently fed into the inverter, where it is transformed into an AC voltage waveform. This waveform is then filtered to achieve a sinusoidal form. Understating the mathematical formulation of

these power conversion circuit is crucial for design purposes the following section describes them into details and these mathematical models are further implemented in MATLAB to understand the dynamics of renewable energy integration int protection schemes. In order to implement stand alone or combined renewable energy sources which is to be interconnected with electrical grid, the DC-DC and DC-AC converter topologies must be implemented in the system

4.3.1 DC-DC converters

To enhance the efficiency of power conversion, DC–DC converters are utilized in the initial phase for the extraction of electric power. This section provides a comprehensive mathematical modelling of various types of DC–DC converters, including Buck–Boost, Cuk, and SEPIC converters. Furthermore, it also introduces the state-space mathematical modelling of these converters, which is instrumental in the design of controllers for various non-isolated DC–DC converter configurations. The circuits illustrated in Figure 4.8 depict the operational states of the power converter. These configurations are instrumental in formulating the model of an ideal power converter. The circuit corresponding to equation 4.38 is applicable when the converter switch is in the 'on' position, whereas the circuit associated with equation 4.39 is relevant when the switch is in the 'off' position. Equations 4.27 through 4.30 pertain to both figures, while equations 4.31 and 4.32 specifically apply to Figure 4.8b.

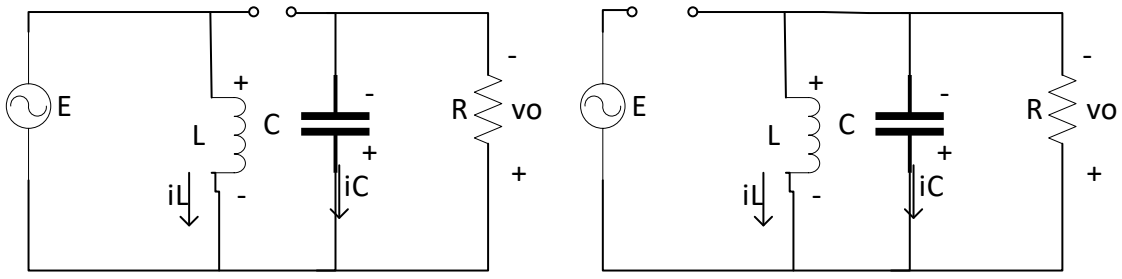

(a) On position (b) off position

Figure 4. 8 Buck Boost converter configuration

$$\mathrm{J_u} = 1(q_L) = \frac{1}{2} L {q_L}^2 \qquad 4.27$$

$$\mathrm{U_u} = 1(q_C) = \frac{1}{2C} L {q_C}^2 \qquad 4.28$$

$${F_{qC}}^{u=1} = 0 \qquad 4.29$$

$$F_{qL}{}^{u=1} = E \quad 4.30$$

$$D_u = 1(q_C) = Rq_C{}^2 \quad 4.31$$

$$D_u = 0(q_L, q_C) = \frac{1}{2}R(q_L + q_C)^2 \quad 4.32$$

J is the circuit kinetic energy, which is caused for stored energy in the power inductor; u is the potential energy related to the stored energy in the capacitor; D represents elements that generate heat not reusable for the device; and F represents all the signals that excite the system in such a way that its state of operation has changed. The D and F terms are defined as generalized forces. Using the energy expressions in the Euler–Lagrange formalism, the ideal converter dynamical model is given by equation 4.33 and 4.34.

$$L\frac{d}{dt}iL = (1-u)V_c + uE \quad 4.33$$

$$C\frac{d}{dt}V_c = -(1-u)i_L + \frac{1}{R}V_c \quad 4.34$$

The output of photovoltaic systems is typically low. To effectively integrate this PV system with the electrical grid, it is essential to gradually elevate the output to the necessary level while ensuring that the voltage remains stable. Consequently, a boost converter should be positioned between the photovoltaic system and the DC grid. Recent studies have introduced an innovative DC-DC converter topology designed to achieve a tenfold increase in input voltage, as illustrated in figure 4.9 [178]. The DC/DC Converter topology described below is engineered to attain a significant voltage gain while minimizing voltage stress on the power switch. This is accomplished through the integration of coupled inductors and a switched capacitor. Additionally, the converter is designed to simultaneously accommodate three distinct types of renewable energy sources[179]. It enables the extraction of maximum power from all connected sources, facilitating effective voltage regulation at the output. This regulation is achieved through the operation of inductors L1 and L2, along with the control of switches S1, S2, and S3 at varying switching frequencies. When L1 is connected to the energy sources, it allows for energy storage in L2. By appropriately activating one of the two switches, both inductors can be configured in series to deliver power to the load, thus ensuring a high voltage gain[180].

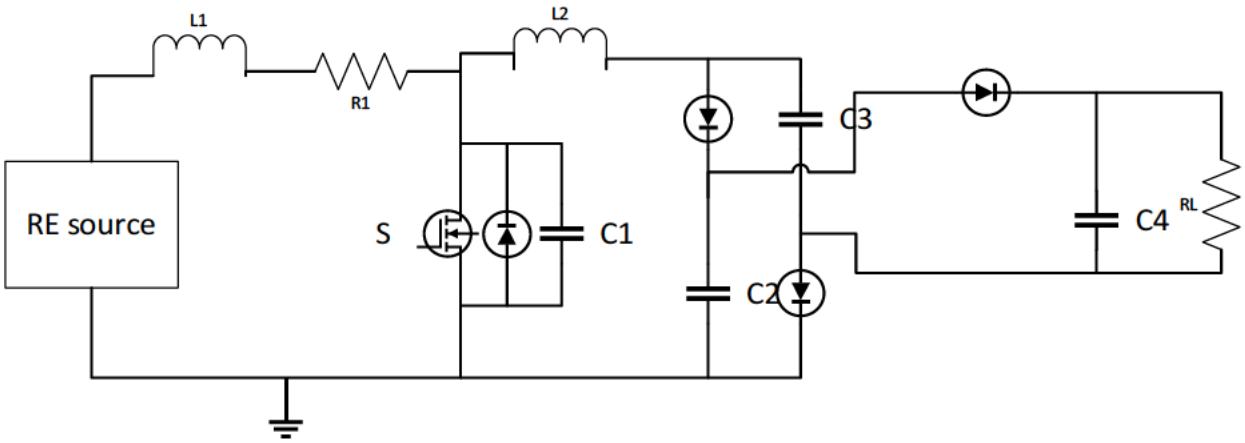

Figure 4. 9 DC-DC Network topology

The most common DC-DC converters are Multi-input and single output multiport (MISO), these converters are characterised by having the capability handle different sources connected at a time and can delivers the constant DC voltage to bus. Figure 4.10 illustrates the basic configuration of a MISO topology.

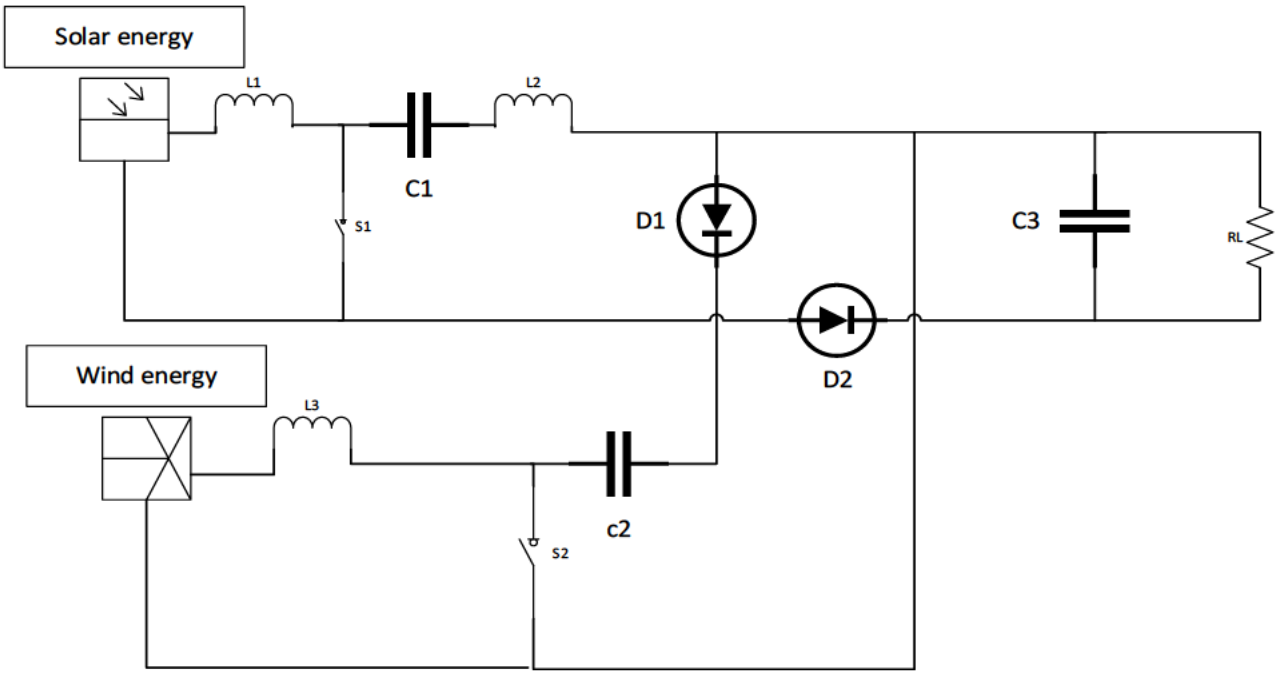

Figure 4. 10 Multi-input and single output multiport DC to DC converter topology

The MIMO topology encompasses both Cuk and SEPIC converter configurations. The load is powered by utilizing both input sources either concurrently or independently [8]. This topology offers several significant advantages, including the capability of both sources to implement Maximum Power Point Tracking (MPPT) techniques, the elimination of the need for an input filter, and the ability to function in both boost and Cuk converter modes. Additionally, it is noteworthy that the output voltage polarity is opposite to that of the input

sources [10]. When the output voltage is generated from the solar panels, Diode D2 remains continuously activated, while the corresponding switch S1 and Diode D1 are engaged. During this period, the converter operates as a Cuk converter, and the voltage gain is described by equation 4.35. In this context, V_o and V_{PV} are the panels input and output voltages respectively, d1 is the duty cycle of the switch S1. The voltage gain can be expressed as equation 4.36.

$$\frac{V_O}{V_{PV}} = \frac{D_1}{1 - D_1} \quad 4.35$$

$$\frac{V_O}{V_W} = \frac{D_2}{1 - D_2} \quad 4.36$$

The output voltage delivered to the load RL is influenced by the modulation of the Ton and Toff parameters of the switches within this configuration. In the initial operational mode, Source-1 provides power to the load by activating switches Sp1 and S2 while deactivating Sp2. When treating Source-1 as a voltage source, the voltage gain can be expressed as equation 4.37, where T represents the switching period and d1 denotes the duty cycle of switch Sp1. Conversely, when Source-2 is engaged in supplying the load, switches Sp2 and S1 are activated, while S2 remains deactivated. Consequently, the voltage gain in this scenario can be articulated as equation 4.38.

$$V_O = \frac{2V_1}{1-D_1}[1 + \sqrt{1 + \frac{8L_a}{R_o T(1-D_1)^2}} \quad 4.37$$

$$V_O = \frac{2V_2}{1-D_2}[1 + \sqrt{1 + \frac{8L_a}{R_o T(1-D_1)^2}} \quad 4.38$$

The specified values of inductors and capacitors prevent the addition of the input sources.

4.3.2DC-AC converters

DC-AC inverters can be categorized into two primary types: Pulse Width Modulation (PWM) inverters and Multilevel Modulation inverters. Among these, PWM inverters, which include VSI and CSI are the most widely utilized[181]. The recent surge in the incorporation of renewable energy sources into the electrical grid has resulted in a heightened deployment of converters across various technologies, including wind turbines, photovoltaic systems, fuel cells, energy storage systems, and FACTS devices. Simultaneously, the substantial power

requirements of renewable energy systems require ongoing research and the continuous advancement of effective control methodologies. Figure 4.11 illustrates a three-phase two-level AC/DC converter. This converter comprises three IGBT bridges linked to the grid, accompanied by a choke that includes inductors L and resistors R. On the DC side, converters that operate purely resistively demonstrate greater efficiency, thereby improving power quality and transient stability [182].

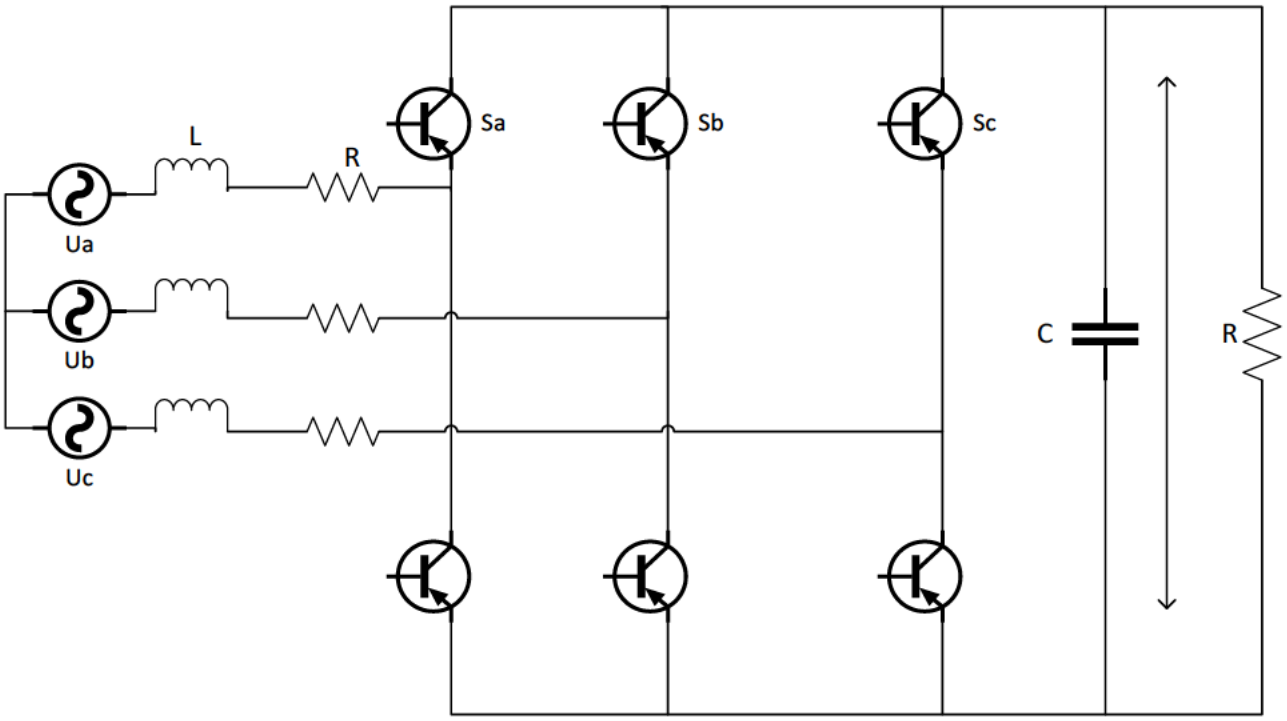

Figure 4. 11 The schematic diagram of an AC/DC converter

The phase voltages are identified as $Ua, Ub, and\ Uc$, while the corresponding phase currents are denoted as $ia, ib, and\ ic$. The direct current output voltage is referred to as Udc, with R and L representing the source resistance and inductance, respectively. A smoothing capacitor, indicated as C, is connected across the load to reduce ripple effects. The mathematical model is developed based on the switching scheme of the rectifier. Initially, the switches Sa and Sć are activated. The sequence then advances to Sć and Sb, followed by Sb and S'c, and continues in this pattern. Equations 4.39 to 4.40 illustrate the relationships among the voltages, currents, and the fundamental components L and Cs

$$\begin{bmatrix} u_a \\ u_b \\ u_c \end{bmatrix} = L\frac{d}{dt}\begin{bmatrix} i_a \\ i_b \\ i_c \end{bmatrix} + R\begin{bmatrix} i_a \\ i_b \\ i_c \end{bmatrix} + V_{dc}\begin{bmatrix} s_a \\ s_b \\ s_c \end{bmatrix} \qquad 4.39$$

$$C\frac{dV_{dc}}{dt} = \sum_{k=a}^{c} i_k S_k - i_L \qquad 4.40$$

4.3.3 Voltage source converters

A diverse array of voltage source converters (VSC) is currently available. The advent of the insulated-gate bipolar transistor (IGBT) has significantly enhanced the popularity of three-phase VSCs, which are now widely utilized across various applications. Among the notable types of three-phase VSC converters are the diode clamped (NPC), flying capacitors (FCs), and cascaded H-bridge (CHB) configurations, to name a few [183]. These converters are classified as multi-level converters and are based on the two-level converter depicted in figure 4.12. This figure illustrates a simplified circuit diagram of a three-phase, two-level voltage source converter, which comprises six switches, designated as s1 through s6, each associated with an antiparallel free-wheeling diode. The switches can be realized using either IGBT or IGCT devices, depending on the specific power and voltage requirements of the converter. In renewable energy systems, this type of converter is typically connected to an electric grid, enabling the efficient transfer of power generated by the generator to the grid.

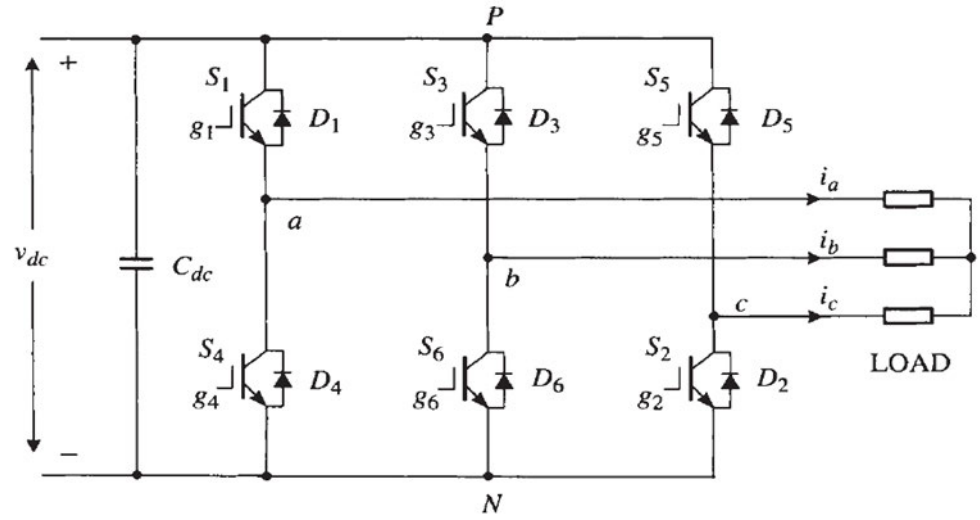

Figure 4. 12 The simple two-level converter configuration

The converter is referred to as a 2-level converter due to its capability to operate at two distinct voltage levels, namely VDC and −VDC, on the AC side. This converter facilitates bidirectional power transfer between the DC side and the three-phase AC system [184]. The control mechanism employed for the converter utilizes pulse width modulation (PWM) as its

switching strategy. The terminal voltages on the AC side of the ideal converter are characterized by equations 4.41 and 4.42, which pertain to phases a, and b, respectively, where m(t) represents a balanced three-phase modulation signal

$$V_{ta} = m_a(t)\frac{V_{DC}}{2} \qquad 4.41$$

$$V_{tb} = m_b(t)\frac{V_{DC}}{2} \qquad 4.42$$

Figure 4.13 illustrates the connection of the VSC converter to both the grid and a DC source, alongside the current-controlled real and reactive power controller. The control mechanism operates within the dq-frame. This setup enables the converter to manage power flow using straightforward PI controllers as compensators. To facilitate this control, seven measurements are required, including phase voltages, phase currents, and the DC voltage, with the DC current also being monitored[185]. These measurements are subsequently transformed into the dq-frame and input into the compensators, which adjust either the currents id and iq or the V_{DC} to align with a specified reference value. The compensator then generates the modulation signals in the dq-frame.

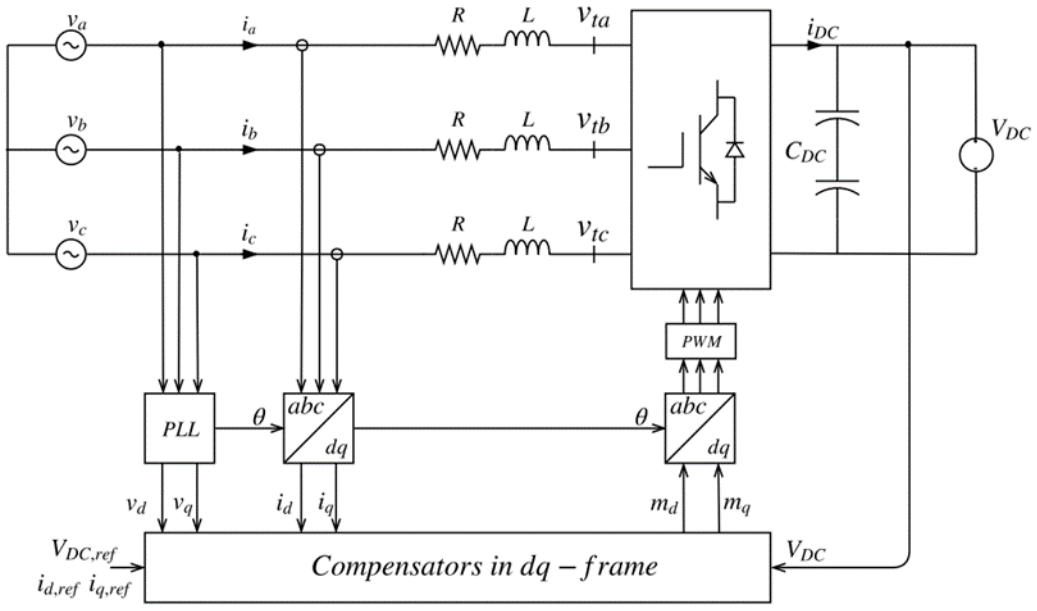

Figure 4. 13 Schematic diagram of a current-controlled real-/reactive-power controller in dq-frame.

With this it is possible to control active and reactive power flow of the converter. It also shows the current controlled real/reactive power controller. The control is performed in the dq-frame. With this configuration the converter can regulate the power flow with simple PI

controllers as compensators. Seven measurements are needed for the control, phase voltages, phase currents and the DC voltage. It is also good to monitor the DC current. These are then transformed into the dq-frame and fed into the compensators which either regulates the currents id and iq or VDC to a reference value. The compensator then returns the modulation signals in dq-frame[186]. If the AC system is assumed to be ideal with a balanced sinusoidal three-phase source which has a constant frequency, the dynamics from of figure 4.15 can be described by equation 4.43-4.45

$$L\frac{di_a}{dt} = v_{ta} - v_a - Ri_a \qquad 4.43$$

$$L\frac{di_b}{dt} = v_{tb} - v_b - Ri_b \qquad 4.44$$

$$L\frac{di_c}{dt} = v_{tc} - v_c - Ri_c \qquad 4.45$$

To achieve the desired power output in a three-phase voltage source converter (VSC) system, it is essential to implement a closed-loop compensator for effective control [187] ,
To regulate a current $i(t)$ at a reference value $i(t)_{ref}$ ref within a three-phase system, it is essential to recognize that this current represents a sinusoidal signal that must be accurately followed. Consequently, the sinusoidal signals from a balanced three-phase system can be transformed into a DC signal, thereby facilitating a more straightforward control design. The mathematical representation of a balanced three-phase sinusoidal system is provided in equations 4.46-4.48 [188]

$$\hat{V}_a(t) = \hat{V}\cos(\omega t + \theta_o) \qquad 4.46$$

$$\hat{V}_b(t) = \hat{V}\cos(\omega t + \theta_o - \frac{2\pi}{3}) \qquad 4.47$$

$$\hat{V}_c(t) = \hat{V}\cos(\omega t + \theta_o - \frac{4\pi}{3}) \qquad 4.48$$

In the event that the quantities pertain to voltages, $V_{a,b,c}$ represent the phase voltages, while V̂ denotes the peak values. The initial phase angle is indicated by θ_0 . The time response of the phases is illustrated in figure 4.16. This system can also be characterized by a space vector, which is a complex function of time. In its polar representation, it is expressed by equation 4.49.

$$\vec{v}(t) = \frac{2}{3}(v_a(t) + e^{j\frac{2\pi}{3}}v_b(t) + e^{j\frac{4\pi}{3}}v_c(t) \qquad 4.49$$

The phase-lock-loop (PLL) is used to transform $V_{abc} to\, V_{dq}$ and dynamically adjust the rotational of the $dq - frame$ and to keep v_q at zero. Hence the space vector is written as equation 4.50 and further simplified to equation 4.51 and 4.52. The block diagram of a PLL is shown in figure 4.14. By choosing $\theta(t) = \omega t + \theta_0$ the desired result of keeping $v_q = 0$ is obtained.

$$\vec{V}(t) = \hat{V} e^{j(\omega+\theta_0)} \qquad 4.50$$

$$v_d = \hat{V} \cos(\omega t + \theta_0 - \theta(t)) \qquad 4.51$$

$$v_q = \hat{V} \sin(\omega t + \theta_0 - \theta(t)) \qquad 4.52$$

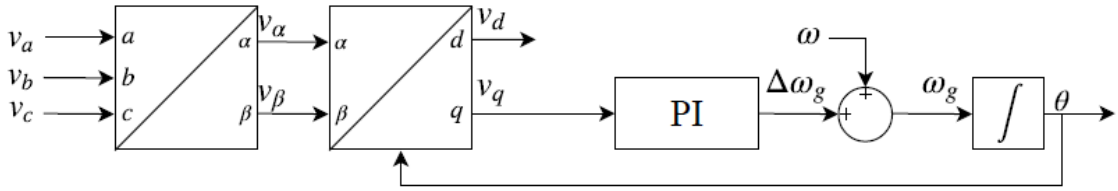

Figure 4. 14 the block diagram of the PLL

The input signal v_q is fed into the PI controller which outputs the angular frequency deviation $\Delta\omega. \omega = 2\pi f$ is then added to this which is finally integrated into θ As which can be formulated by equation 4.53

$$\theta = \int \omega_g dt = \omega + \int \Delta\omega_g dt \qquad 4.53$$

The extensive versatility of the dq-current controller presents significant incentives to explore and suggest alternative regulatory frameworks that can address the axis coupling challenges associated with renewable integrated systems[189]. This provides some advantages over ABC-frame because , d- and q-components are DC variables which result in an easy controllability simple PI compensators can be used in the control loop[190]. In [191] The control of the d and q axis inverter currents is achieved through the implementation of two proportional-integral (PI) controllers. This approach is effective because the parameters of both the grid and the inverter are converted into dq components, resulting in the d and q axis inverter currents being represented as direct current (DC) values. The role of the PI controller is to eliminate the steady-state error, ensuring that the reference currents$I_d \& I_q$ align precisely with the actual currents produced by the inverter. According to [188] the output

voltage of inverter according to the mathematical model of grid- connected inverter is given by equation 4.54 and 4.55.

$$U_d = L\frac{di_d}{dt} + Ri_d - \omega Li_q + e_d \qquad 4.54$$

$$U_q = L\frac{di_q}{dt} + Ri_d + \omega Li_q + e_q \qquad 4.55$$

Where $U_d$and U_q are the dq components of the park transformation of inverter output voltage. $e_d$and e_q are the dq components of the park transformation of the grid voltage.

4.4 Conclusion

This chapter has examined the mathematical framework associated with renewable energy sources. It encompassed the generation sources, energy conversion processes, and their regulation. Power electronics components play a vital role in ensuring system stability and managing both active and reactive power outputs. Furthermore, this analysis provides valuable insights into the essential steps and parameters necessary for modelling a renewable integrated system. The research aims to investigate the effects of integrating renewable energy into a compensated network, a topic that will be elaborated upon in Chapter 6 (methodology). The next chapter discusses the theoretical formulation of a fault detection, classification and location in the context of power systems network

Chapter 5: Fault Detection and Classification

5.1 Introduction

Series compensation enhances the efficiency of transmission voltage, a critical aspect to consider, as technical challenges often arise during its operation, particularly concerning low and high voltage conditions. The fault identification mechanism for series compensation is influenced by the nature of the fault and the variations in fault voltages, which can be represented as a positive sequence, alongside changes in fault current, also expressed as a positive sequence. Most fault classification methodologies analysed rely on specific values, whether they pertain to phasor voltage or current, which are derived from measurements taken by voltage and current transformers located at substations or conversion points. This process is essential for gathering data through transformers connected to the terminal ends of sub-transmission or transmission lines. This chapter examines fault detection techniques applicable to compensated transmission lines and proposes a novel fault detection and classification scheme utilizing machine learning. The efficacy of this scheme is evaluated based on accuracy and misclassification rates across various fault types, including single-phase to ground (L-G), double-phase (L-L), double-phase to ground (L-L-G), and three-phase faults (L-L-L). Initially, current and voltage signals are sampled, and these sampled data points are forwarded to a feature extraction module. This module extracts relevant features utilized by the fault detector, classifier, and locator. The outputs consist of the identified fault type and its location, as determined by the fault classifier and locator, respectively. This chapter primarily emphasizes the mathematical formulation underlying these schemes. A crucial aspect of fault identification schemes is the extraction of features from the signal. This section discusses various components of the protection scheme, including sampling methods, data sampling, feature extraction, fault detection classification, and fault location

5.2 Sampling / signal processing

Numerous signal processing techniques have been explored for the purpose of identifying faults in transmission lines. These techniques include the discrete Fourier transform (DFT), Hilbert-Huang transform (HHT), principal component analysis (PCA), wavelet transform (WT), Hilbert transform (HT), and Gabor transform (GT). The following section describes each of these schemes from a critical viewpoint. In the event of a fault occurring within the power

system, the resulting fault signal can be characterized as a synthesis of a steady-state sinusoidal component and an exponentially decaying DC component. Consequently, this relationship can be articulated mathematically as represented in equation 5.1

$$x_f(t) = X_0 e^{-t/\tau} + X \cos(\omega t + \emptyset) \qquad 5.1$$

In this context, X_0 is the DCC amplitude, while τ signifies the time constant associated with this amplitude. Is the magnitude of the sinusoidal component, with the phase shift ϕ on signal $xf(t)$, ω corresponds to the angular frequency. The kth sample of $xf(t)$ is therefore shown by equation 5.2

$$x_f(k) = X_0 e^{k\lambda\Delta t} + X \cos(\delta k + \emptyset) \qquad 5.2$$

Where $\Delta t = \frac{1}{f_s}$ is the sampling interval, N denotes samples/cycle, $\lambda = \frac{-1}{\tau}$, $s = \omega\Delta t$ and $t = n\Delta t$. The first-order Taylor series expansion indicates that, equation 5.2 can be expressed as equation 5.3.

$$X_f(k) = X_0 + \lambda k\Delta t + X\cos(\delta k + \phi) \qquad 5.3$$

Should this expansion take place at a central point $Xf\ (k)$, the samples on the left and right sides can be represented by equations 5.4 and 5.5, respectively. The summation of equations 5.4 and 5.5 results in equation 5.6

$$X_f(k-n) = X_0 + \lambda(k-n)\Delta t + X\cos(\delta(k-n) + \phi) \qquad 5.4$$

$$X_f(k+n) = X_0 + \lambda(k+n)\Delta t + X\cos(\delta(k+n) + \phi) \qquad 5.5$$

$$X_f(k-n) + X_f(k+n) = 2X_f(k)\cos(n\delta) + 2(X_0 + \lambda k\Delta t)(1 - \cos(n\delta)) \qquad 5.6$$

If n is a small integer, then for highf_s, $\cos(\omega n\Delta t) = \cos(s\delta)\ and\ is\ almost\ equals\ to\ 1$. Hence, equation (above) can be approximated as equation 5.7 and 5.8

$$X_f(k-n) + X_f(k+n) \approx 2X_f(k) \qquad 5.7$$

$$X_f(k) \approx \frac{X_f(k-n)+X_f(k+n)}{2} \qquad 5.8$$

5.2.1. Fourier transform (FT)

The Fourier Transform (FT), including its fast variant known as the Fast Fourier Transform (FFT), has been utilized across numerous applications, demonstrating significant effectiveness. However, it is important to acknowledge the following limitations associated with its use [192].

- The concept of time is absent in the Fourier transform, presenting challenges when attempting to apply this theory to power systems that depend on signals propagating over time.
- The application of window limitation is not feasible when the signal experiences rapid or even minor fluctuations, particularly during transitional phases [193].

The Fourier transform, denoted as $F(w)$, and its computationally efficient counterpart, the fast Fourier transform F_k(F_k), are articulated in equations 5.9 and 5.10, respectively. Here, k and n represent integers that correspond to the number of samples. In 1946, Dennis Gabor introduced an innovative methodology to address the limitations of the FFT. His approach utilized a tripartite representation of signals to tackle the temporal resolution issue. Additionally, to overcome the constraints associated with windowing, he advocated for the application of multiple windows instead of relying on a single window and the Short-Time Fourier Transform (STFT) is represented by equation 5.11.

$$F(w) = \int_{-\infty}^{\infty} f(t) e^{-i\omega t}\, dt \qquad 5.9$$

$$F_k = \sum_{n=0}^{N-1} x_n e^{-\frac{j2\pi kn}{N}} \qquad 5.10$$

$$STFT\{f(t)\}(\tau, \omega) = F(\tau, \omega) = \int_{-\infty}^{\infty} f(t) w(t-\tau) e^{-i\omega t}\, dt \qquad 5.11$$

The Short-Time Fourier Transform (STFT), while effective in addressing certain challenges and yielding satisfactory results, exhibits limitations in particular contexts, notably in the analysis of power system signals. To mitigate these identified deficiencies, wavelet transforms have been proposed as viable alternatives to the traditional methods

5.2.2 Wavelength transform

The Wavelet Transform has attracted considerable attention and is currently extensively applied in the domains of image and speech processing [194-197]. The mother wavelet is

described by equation 5.12 Where $a, b\epsilon\mathbb{R}\ \&\ \psi_{ab}$ is the wavelength $\psi_{ab}{}^{*}$represents its complex conjugate.

$$CWT(a,b) = \langle f, \psi_{a,b} \rangle = \quad 5.12$$
$$\frac{1}{\sqrt{a}} \int_{-\infty}^{\infty} f(t).\psi_{a,b}(\frac{t-b}{a})\, dt$$

Fourier transforms represent signals as a combination of waves with varying frequencies, whereas wavelet transforms depict signals through wavelets that differ in both scale and position[194]. Wavelet analysis relies on two primary equations: the scaling function ϕ(t) and the wavelet function ψ(t), as articulated in equations 5.13 and 5.14. These functions represent two-scale difference equations derived from a selected scaling function, commonly referred to as the mother wavelet. They possess characteristics that fulfil the criteria outlined in equations 5.15 and 5.16.

$$\psi(t) = \sqrt{2} \sum_k h_k \psi(2t-k) \quad 5.13$$
$$\psi(t) = \sqrt{2} \sum_k g_k \psi(2t-k) \quad 5.14$$
$$\sum_{k=1}^{N} h_k = \sqrt{2} \quad 5.15$$
$$\sum_{k=1}^{N} h_k h_{k+2\iota} = 1\ if\ \iota = 0, 0\ if\ \iota \mathcal{E} Z,\ \ \iota \neq 0 \quad 5.16$$

The sequences h_k and $g_k$are indicative of discrete filters that address each equation presented in 5.17. The scaling and wavelet functions serve as prototypes for a category of orthonormal basis functions, as described in equation 5.18.

$$gk = (-1)^k h_{N-1-k} \quad 5.17$$
$$\varphi_{j,k}(t) = 2^{\frac{j}{2}} \varphi\left(2^j t - k\right); j, k \in z \quad 5.18$$

The parameter j governs the dilation or compression of the function with respect to both time scale and amplitude. Meanwhile, the parameter k is responsible for the translation of the function in the temporal domain. The variable z represents the set of integers. After establishing a wavelet system, it becomes possible to express a function f(t) in terms of the basic functions, as illustrated in equation 5.19.

$$f(t) = \sum_{\iota \in z} c(\iota) \varphi_\iota(t) + \sum_{j=0}^{j-1} d(j,k) \varphi_{jk}(t) \quad 5.19$$

Where the coefficients $c(l)$ and $d(j,k)$ are calculated by inner product of equation 5.20 and 5.21 respectively.

$$c(\iota) = \langle \varphi_t \iota | f \rangle = \int f(t)\varphi_t(t)dt \qquad 5.20$$

$$d(j,k) = \langle \varphi_t \iota | f \rangle = \int f(t)\varphi_{jk}(t)dt \qquad 5.21$$

The expansion coefficients $c(l)$ serve to approximate the original signal with a resolution of one point for every 2^j points of that signal. In contrast, the coefficients $d(j,k)$ capture the details of the original signal across various resolution levels. Both $c(l)\ and\ d(j,k)$ can be derived through direct convolution of the signal samples $f(t)$ with the coefficients h_k and g_k which are specific to the selected mother wavelet

5.3 Feature extraction

The process of feature selection is referred to feature engineering which is defined as the process of using domain knowledge to transform the most relevant variable from raw data when creating a predictive model using machine learning of statistic model. The main goal of feature extraction is to improve the performance of machine learning algorithms. The process can be simplified as shown in 5.1**,** the whole process is then divided into two subsections namely Selection and extraction. Selection is the technique used to find the smaller subset on many dimensional (set of features) datasets to create a data model. The complexity depends on data sample (N), the number of inputs (d) and the selected demission (k), it is therefore simplified as technique of finding k features of d dimension that give the most information and discard (d-k) dimension. There are three main methods under supervised models on feature selection which are filter methods, wrapper methods and embedded methods and one method for unsupervised mode which is data dimension criteria.

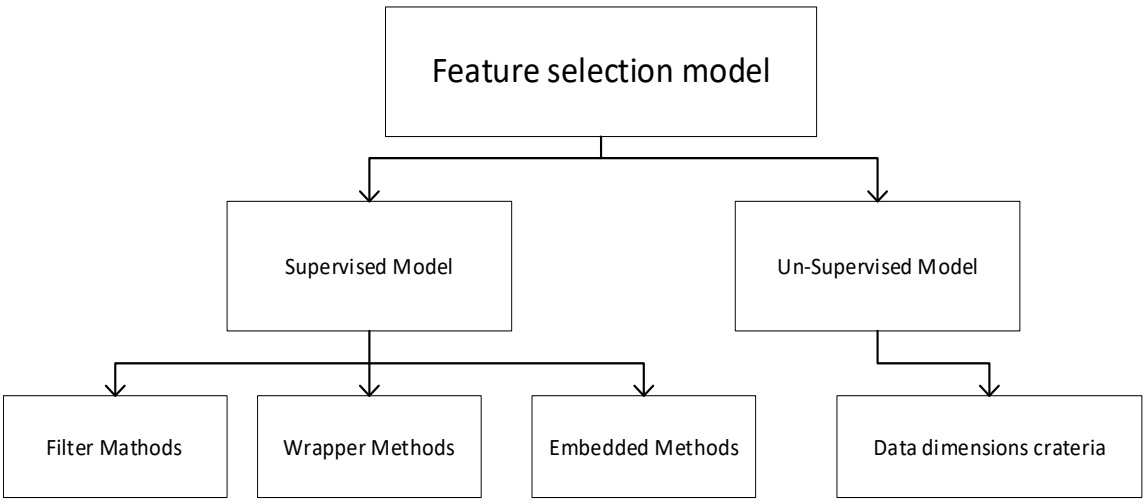

Figure 5. 1 Feature selection model

The current and voltage signals inherently encompass all necessary information; however, it is often challenging to translate these raw signals into a structured framework of rules and criteria that can effectively interpret the underlying messages they convey. This challenge highlights the utility of feature extraction techniques, which are designed to extract pertinent information while minimizing the influence of variability within the system under investigation. By employing appropriate feature extraction methods, researchers can enhance their understanding of fault classification and localization issues, thereby addressing these challenges in a more systematic and effective manner. Additionally, reducing the dimensionality of the data can enhance the performance of certain algorithms utilized in classification or localization tasks, yielding more precise and reliable outcomes in a timely fashion. This section will outline various methods employed for feature extraction, accompanied by detailed examples of their applications. Furthermore, a concise overview of fault detection methods, which heavily relies on the feature extraction process, will be provided at the conclusion of this section. The foundation of most detection and classification techniques is a well-curated dataset of fault features. Ideally, this set of relevant features should be compact and computationally efficient. In practical applications, however, relevant features are often obscured by redundancy and noise, making it essential to extract this information in a cost-effective manner without compromising the integrity of the valuable data[198].

5.3.1 Fourier Transform (FT)

The Fourier Transform (FT) decomposes an input signal into its constituent frequencies represented by various sinusoids. This method is particularly effective and straightforward when applied to static signals. However, accurately conveying information becomes problematic for transient or nonstationary signals, as some characteristics may be obscured during the transition from the frequency domain back to the time domain. The mathematical representation of the FT for a signal $x(t)$ is provided in equation 5.22, which can be succinctly summarized in equation 5.23, illustrating the inner product between the signal $x(t)$ and the complex sinusoid $e^{j2\pi ft}$

$$x(f) = \int_{\infty}^{-\infty} x(t)e^{j2\pi ft}dt \qquad 5.22$$

$$x(f) = x(t)e^{j2\pi ft} \qquad 5.23$$

5.3.2 Wavelet Transform

The Wavelet Transform (WT) facilitates the attainment of both time and frequency resolution for a given signal by localizing various frequency components in time. In the WT process, the input signals undergo translation—referring to shifts along the time axis—and dilation, which involves the expansion of the wavelet. This manipulation transforms the signal into a different representation that reveals its structure over time and scale, as illustrated in figure 5.2. The wavelet transform assesses the correlation between the input signal and a scaled and translated version of the 'mother wavelet,' which is characterized by a finite duration and a zero mean[172].

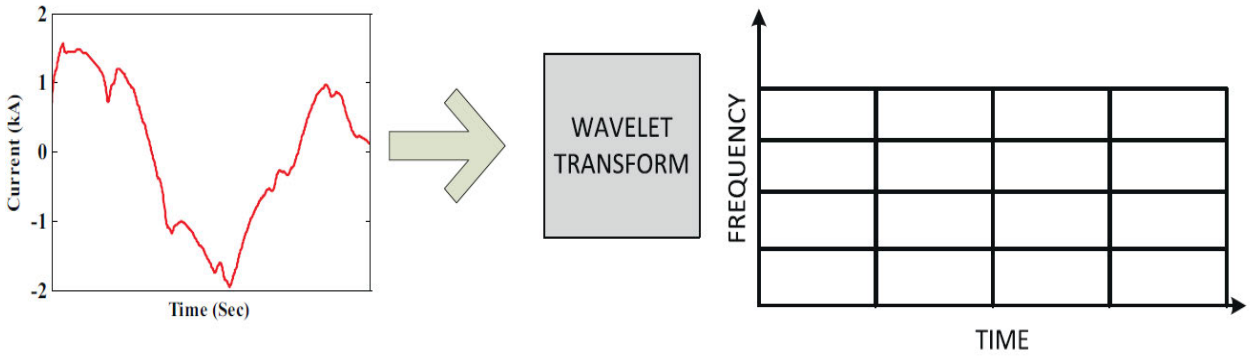

Figure 5. 2 The concept of wavelength transforms

Nonstationary signals are decomposed into low-frequency and high-frequency components, known as approximation and detail coefficients, respectively, which demonstrate a diverse array of resolution scales[199]. The system employs filters that possess a range of cut-off frequencies, enabling the analysis and observation of a signal at various levels of resolution. [200]. The wavelet transform employs high-pass filters to examine the high-frequency components of a signal, while low-pass filters are utilized to analyse the low-frequency components [201]. According to [202] Two stages of decomposition are performed. Initially, the signal is divided into components A1 and D1, as illustrated in figure 5.3. In the subsequent stage of decomposition, A1 is further broken down into A2 and D2. Following this process, the energy is computed from the detailed coefficients, which is mathematically expressed in equation 5.24, where x(t) represents the signal and E signifies the energy over a specified time interval (ta, tb).

$$E(t_a, t_b) = \int_{t_a}^{t_b} (|x(t)|)^2 dt \qquad 5.24$$

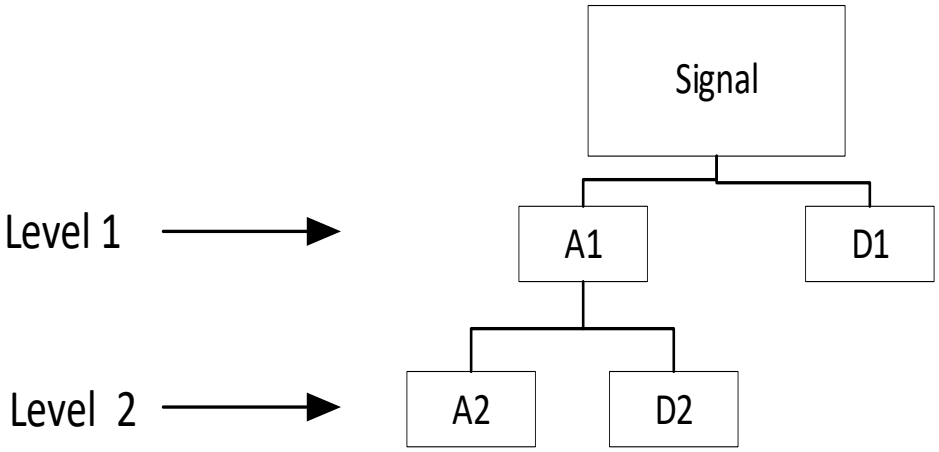

Figure 5. 3 Two levels of decomposition

The technique of feature selection plays a critical role in ensuring precise fault detection and classification. Features are extracted from faulty signals utilizing discrete wavelet transform. In this study, the input is determined based on features that include the peak values of wavelet coefficients. High-frequency signals present in the fault current significantly influence these features. To capture these high-frequency signals, the signals are decomposed to the second level[202]. Subsequently, the differential wavelet energy (DWE) is calculated by subtracting the wavelet energy content of one cycle post-fault from that of one cycle pre-fault, and the absolute value is taken, expressed mathematically as: DWE = abs (WE (one cycle

post-fault) – WE (one cycle pre-fault)). The DWE values observed in the faulted phases are notably higher in comparison to those in other phases of the network being analysed. The main aim of feature extraction is to provide the significant information for the classifier to classify the type of event through the features calculated, using standard deviation (SD) and energy values. The detailed information of this is discussed as follows. The SD is defined as the statistical measure of variation or dispersion that exists in the original signal and is given as equation 5.25

$$SD = \sqrt{\frac{1}{n-1}[\sum_{t=1}^{n}(x_i - \vec{x})^2} \qquad 5.25$$

Where $\vec{x} = \frac{1}{n} = \sum_{i=1}^{n} x_i$, x represent the data vector and n is the number of elements in x. To test the effectiveness of the proposed classifier, this work uses another approach to calculate features based on the energy of the decomposed current signal. The spectral energy of the decomposed signal can be obtained using equation 5.26, n denotes the quantity of detailed coefficient levels, while x signifies the data vector. To derive the features, a moving window encompassing one complete cycle of the current wavelet coefficient is utilized, from which the features are extracted for the purpose of training the classifiers.

$$E = \sum_{t=1}^{n} |x_i|^2 \qquad 5.26$$

5.3.3 S-transform

This method was originally developed for the analysis of geophysical signals and serves as a tool for time-frequency analysis. Like other techniques in this domain, the S-transform allows for the observation of a signal's energy distribution across both time and frequency domains. It builds upon the principles established by wavelet and short-time Fourier transforms. The S-transform utilizes a Gaussian window function whose width inversely correlates with frequency, thereby eliminating the necessity of selecting a specific window function and overcoming the constraints associated with fixed window widths. Furthermore, the phase spectrum corresponding to each frequency component in the S-transform's time-frequency representation is intricately connected to the original signal, enabling the extraction of more distinctive features for fault analysis. Consequently, the S-transform is capable of capturing

frequency information at specific moments within a designated frequency band, as well as the amplitude information of the signal at particular frequencies. By integrating the wavelet transform with a phase factor, the S-transform effectively combines the strengths of both methodologies, thereby enhancing their respective characteristics.

5.3.4 The Principal component analysis (PCA)

The dimensionality reduction process can be divided into two primary steps: feature selection and feature extraction. Feature selection may utilize methods such as embedded, filter, or wrapper techniques, while feature extraction commonly employs principal component analysis (PCA)[203]. The primary objective of PCA is to diminish the dimensionality of high-dimensional datasets by linearly projecting the data onto a lower-dimensional space, thereby minimizing the reconstruction error associated with this projection. The benefits of employing PCA include[204]:

- An optimal representation of high-dimensional observations within a reduced space;
- The transformation of original variables into new, linearly independent variables, facilitating easier data interpretation

In order to develop an intuition for PCA, an essential condition for applying Principal components (PCs) is centring the variables of the data matrix X, this operation converts original variables into new ones[205]. Given the n × p data matrix X, where n represents the number of observations and p the number of variables, the p × p variance-covariance matrix S contains the variances of the p variables in its diagonal elements and the covariance in the elements outside the diagonal. Variance is a measure of variability. It quantifies how disperse the observations of one variable are. Covariance measures how two variables change together. If both variables vary together in the same direction, then the covariance is positive. On the other hand, if they vary in opposite direction, the covariance is negative[206]. If the variables are uncorrelated, which means no-linear dependency, the covariance is zero. The general expression for the variance –covariance matrix is given by equation 5.27.

$$S = \frac{1}{n}\sum_{i=1}^{n}(x_1 - \bar{x})'(x_2 - \bar{x}) \qquad 5.27$$

Where xi is a 1 × p vector corresponding to the i observation and $\bar{x}$ is the 1 × p mean vector which contains the mean of each one of the p variables. Additionally, eigenvalues and

eigenvectors of the S matrix are the basis for obtaining the PCs In general, the PCs scores can be calculated with equation 5.28 where U is the p × p matrix of coefficients (column eigenvectors of S sorted in accordance to the eigenvalues) necessary for computing the n × p matrix Y which contains the PCs scores of original data[207].

$$\gamma = X * V \qquad 5.28$$

The data exhibit a distribution along a primary axis represented by the U-axis, while the secondary axis, denoted as the V-axis, is orthogonal to U. When the U–V axis system is positioned at the mean of the data, it facilitates a bidirectional representation. [208]. The transformation of the X–Y coordinate system into the U–V coordinate system results in the de-correlation of the data. The directions represented by U, V, and others are referred to as the principal components, as illustrated in figure 5.4.

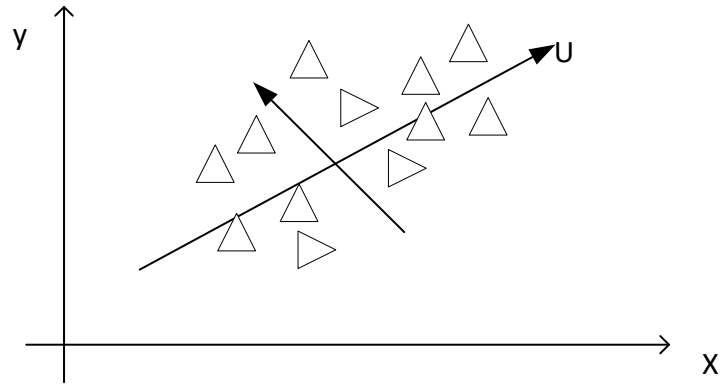

Figure 5. 4 Distributed data set and direction of variation of data

PCA uses the mean and standard deviation to form covariance matrix of a multidirectional data set and, from there, finds out eigenvalues and eigenvectors of the covariance matrix. To develop a PCA algorithm

Step1: //A distributed data set is obtained with m variables and n observations $[X]_{n*m}$

Step2: //Find the mean (μ) and variance (σ) of

Step3: //Form data adjust matrix XA by normalizing (autoscaling) X matrix; scaling XA to zero mean and unit variance using equation 5.29

$$[A]_{XN} = [X_i - {}^{\mu_i}/_{\varrho_i}] \qquad 5.29$$

Step4: //Calculate covariance matrix$[A]_{m*m}$, then Calculate Eigenvectors and Eigenvalues of the covariance matrix. There are two methods that can be used which are using direct analysis and using singular value decomposition (SVD)

Method 1 Using direct axis: in this method

- Eigenvalues: By finding the roots of the characteristic equation (CE)
  - Determinant of $(A - \lambda I) = 0$, where $I = m * m$ identity matrix and this CE has m roots,
- Eigenvector: If λ is an eigenvalue, there exists a vector e such that: $(Ae = \lambda e)$, where e is called an eigenvector associated with the eigenvalue λ
  - Formation of Feature Vector: Arrange eigenvectors in the descending order of eigenvalues.
  - Feature vector $= (eigv_1, eigv_2, \dots, eigv_m)$
    - i.e Feature vector$(e_1, e_2, \dots, e_m)$
- The principal components are constructed as a linear transformation of X by described by T below
  - $T = E^T X$, where $T = [t_1, t_2, \dots\dots, t_m]^T$
    - where $t_1, t_2, \dots\dots, t_m$ are the PCs of X in the descending order of variance
  - /Row Feature Vector: Matrix with the eigenvectors in the columns transposed
  - //Row Data Adjust: Mean-adjusted data transposed
  - //Final data or principal component scores (PCS) PCS ¼ Row Feature Vector Row Data Adjust

Method 2: Using singular value decomposition (SVD)

- //A being symmetrical, it can be computed via the singular value decomposition (SVD), determined by
  - $A = E^T - \lambda E$, where $E^T E = E E^T = I$
    - Where I is the identity matrix, $\lambda = diag(\lambda_1, \lambda_2, \dots\dots \lambda_m)$ is the $eigenvalue\ matrix$ with elements in a decreasing order of magnitude, and $E = (e_1, e_2, \dots\dots\dots, e_m)$ is the eigenvector matrix corresponding to eigenvalues of λ
    -

5.4 Fault Detection and Classification

5.4.1 Introduction

The identification, categorization, and localization of defects within power systems can be significantly enhanced through the application of machine learning (ML) methodologies [17,18]. The figure 5.5 summarises the concept of these ML, the highlighted (supervised ML) is related to this research work. Unlike traditional approaches, deep learning (DL) algorithms operate end-to-end, eliminating the necessity for a dedicated feature extractor. Techniques such as convolutional neural networks (CNNs) and recurrent neural networks (RNNs) are capable of autonomously learning features directly from raw data, thereby removing the need for manual feature engineering. The capacity of DL models to derive hierarchical representations from data enhances their flexibility and proficiency in recognizing intricate patterns and relationships within defect data. Furthermore, these models are particularly adept at managing nonlinear and non-stationary data due to their ability to learn and predict nonlinear dynamics. DL algorithms have demonstrated effective performance in defect classification across various fields, including image analysis, audio processing, and sensor data evaluation. As a result, DL methodologies present considerable advantages over traditional fault classification techniques by automating feature extraction, capturing complex fault patterns, adapting to new fault scenarios, minimizing data pre-processing requirements, and effectively scaling to large datasets. However, it is important to note that DL approaches typically demand substantial computational resources when analysing intricate datasets or training extensive models. The training process often benefits from the use of high-performance graphics processing units (GPUs) or specialized hardware accelerators. Sufficient computational resources are also essential for efficiently analysing input data during the inference phase, where the trained model is employed for real-time classification. In this section different machine learning based fault detection and classification schemes are discussed.

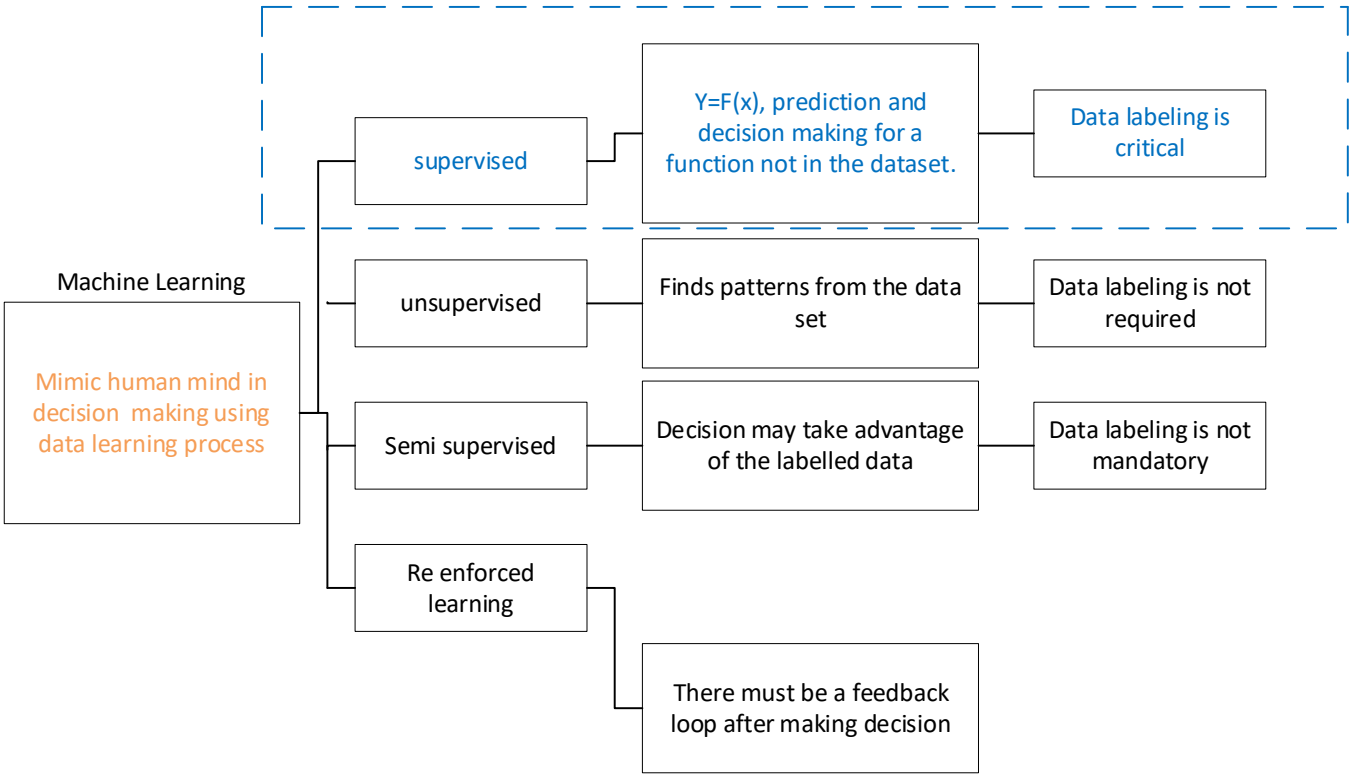

Figure 5. 5 The concept of ML

5.4.2 KNN classifier development classifier

The nearest neighbour algorithm represents a category of instance-based learning methods wherein the function is approximated in a localized manner, with all computational efforts deferred until the classification stage. This technique is regarded as one of the most fundamental and straightforward classification methods, particularly in scenarios where there is minimal or no prior knowledge regarding the data distribution. The k-nearest neighbour's (kNN) algorithm offers several advantages, including its resilience to noisy training data, effectiveness with large datasets, the absence of a dedicated training phase, and its capacity to model complex relationships. However, it also presents certain challenges, such as the difficulty in determining the optimal number of neighbour's and its limited applicability in high-dimensional spaces, which can result in reduced computational efficiency, increased data sparsity, and substantial storage requirements [209].

The selection of an appropriate distance metric remains uncertain, and the associated computational expenses are notably substantial. K-NN is a supervised learning algorithm applicable to both regression and classification tasks. This method aims to ascertain the correct class for a given test instance by measuring the distance between the test instance

and all training data points. Subsequently, it identifies the K nearest points to the test instance. KNN is recognized as a fundamental and straightforward classification approach, especially in scenarios where there is limited or no prior understanding of the data distribution. The strengths of KNN include its resilience to noisy training data, effectiveness with extensive training datasets, the absence of a formal training phase, and its capacity to model complex relationships with relative simplicity. Conversely, the algorithm is not without its drawbacks, including the challenge of selecting the optimal number of neighbour's, difficulties encountered in high-dimensional spaces that can lead to diminished computational efficiency, increased sparsity of data, and significant storage demands. Furthermore, the ambiguity surrounding the choice of a suitable distance metric persists, alongside the potential for high computational costs.[210].

The KNN algorithm assesses the likelihood that a given test data point is associated with the classes represented by 'K' training data points, ultimately selecting the class with the highest probability. In regression scenarios, the output is determined by calculating the mean of the 'K' training points that have been selected. Depending on the chosen value of K and the distance metrics employed, KNN can be further classified into categories such as Fine KNN, Medium KNN, Coarse KNN, Cosine KNN, Cubic KNN, and Weighted KNN. The distinct features of each KNN variant are detailed in Table 5.1 [211]. The efficacy of the proposed KNN classifier is evaluated using a range of K values, specifically 1, 10, and 100, alongside various distance metrics, including Euclidean, cosine, and cubic distances. In the context of weighted KNN, the classification decision is determined by applying a weighting function derived from the Euclidean distance measurement.

Table 5. 1The classification of KNN classifiers

Classifier type	K value	Distance function	Distance (d)=
Fine, Medium, Course	1, 10, 100 respectively	Euclidean distance	$\sqrt{\sum_{i=1}^{n}(P_i - q_i)^2}$
Cosine KNN	100	Cosine distance	$\frac{\bar{P}\bar{Q}}{\lvert\vec{P}\rvert\lvert\vec{Q}\rvert}$

Cosine KNN	10	Cubic Distance	$(\sum_{i=1}^{m}\|p_1 - q_i\|^3)^{\frac{1}{3}}$
Weighted KNN	10	Distance weighting and Euclidean distance	$w = \frac{1}{d^2}$

5.4.3 Artificial Neural Network classifiers

5.4.3 Artificial Neural Network classifiers

Certain classification tasks necessitate the prediction of multiple class labels, indicating that class labels or membership are not mutually exclusive. Such tasks are commonly known as multi-label classification. In this context, each input sample may yield zero or more labels as outputs, which are generated concurrently. The underlying assumption is that the output labels depend on the input data. This study utilizes numerical values of three-phase voltages and currents to predict various types of faults, including single-phase faults and single-phase-to-ground faults within three-phase systems. Neural networks typically consist of three layers, as illustrated in figure 5.6.

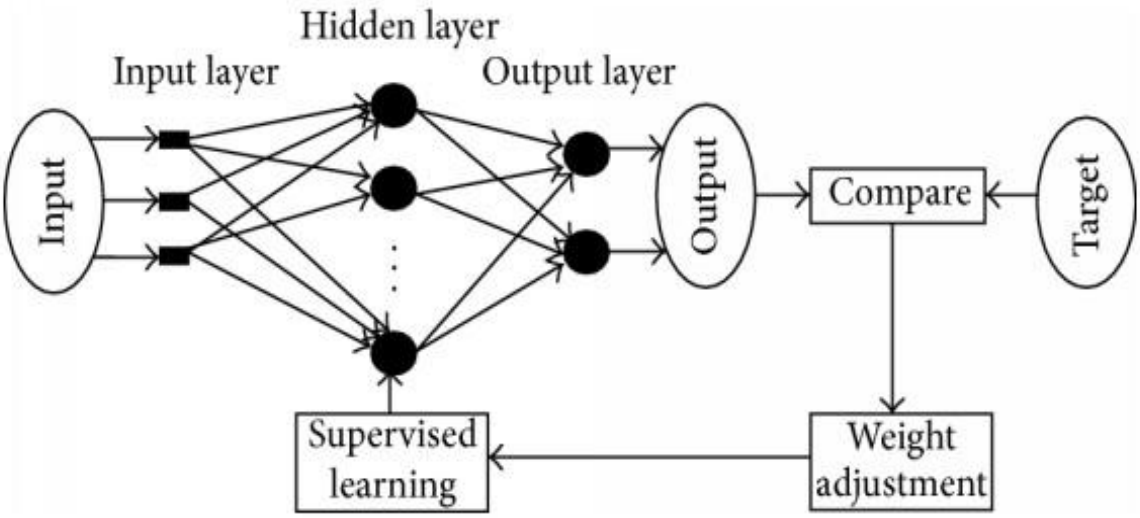

Figure 5. 6 The ANN layers

Artificial neural networks (ANNs) are sophisticated mathematical constructs designed to emulate the processing capabilities of the human brain. They consist of basic units referred to as artificial neurons, which are organized into layers. In the case of ANNs featuring a single layer of neurons, the input, represented as a vector of features$x' = x_1, \ldots\ldots\ldots\ldots\ldots\ldots, x_n)$, is processed within the neuron using weights denoted by ω_i, where i ranges from 1 to n. This

processing yields a value z, which is subsequently transformed into the final output y through a specific function ($\varphi, \gamma = \varphi(z)$. (ϕ, γ = ϕ(z)). The entire process can be summarized as equation 5.28, z is the result of processing the n-inputs of x_i through the weights $(\omega_1, \ldots., \omega_n)$: b is called bias attempt to imitate the human filter. This is achieved by processing the affine function described in equation 5.29. The bias can be considered analogous to a weight $b = w0$ for an initial input $x_0 = 1$, thus allowing the processing of inputs within a neuron to be interpreted as a linear function described by equation 5.30

$$z = (\omega_1, \ldots., \omega_n), \begin{pmatrix} x_1 \\ \cdots \\ x_n \end{pmatrix} + b = \sum_{i=1}^{n} \omega_i x_i + b = \omega^t . x + b \ldots\ldots 1 \quad 5.28$$

$$z = \sum_{i=1}^{n} \omega_i x_i + b = \omega^t . x + b. \quad 5.29$$

$$z == (b = \omega_0, \omega_1, \ldots., \omega_n), \begin{pmatrix} x_{0=1}, x_1 \\ \cdots \\ x_n \end{pmatrix} + b = \sum_{i=1}^{n} \omega_i x_i + b = \omega^t . x + b \ldots\ldots 2 \quad 5.30$$

For ANNs with more than one layer (MLP multilayer perceptron), let us consider the previous process as a mathematical function on the inputs: $y = F^1(x_1, \ldots, x_n), x = \phi(\omega^1 x + b^1)$. The generalization for multilayers is simple: inputs entering a neuron become outputs after adequate processing inside (mostly, a linear combination of inputs as seen), which are sent as inputs to other neurons (the propagation of information from one layer to the next is known as feed-forward). Mathematically a multilayer perceptron can be defined as a function $F: \mathbb{R}^n \rightarrow \mathbb{R}^m$, is characterized as $an\ n-L-m-perceptron$, where n represents the number of inputs, L denotes the number of hidden layers, and m indicates the number of outputs. The function takes the form equation 5.31 for affine functions $\mathrm{f_i(x)} = \omega^{\mathrm{i}}\mathrm{x} + \mathrm{b^i}$, one has the linear multilayer perceptron expressed as equation 5.32

$$F(x) = \phi(F_L(f_{L-1}(\ldots f_1(x)))), for\ x^t = (x_1, \ldots, x_n). \quad 5.31$$

$$F(x) = \phi(\omega^L \ldots (\omega^2 (\omega^1 x + b^1) + b^2) \ldots + b^L) \quad 5.32$$

5.4.4 Support Vector Machine Classifiers

One prominent classifier encountered in the study of machine learning is the Support Vector Machine (SVM). This algorithm ranks among the most widely utilized classification techniques within the field. In this section, we will explore the mathematical principles underlying SVM

in the context of classification problems, examine its class classification process, and understand how it generates predictions. Support Vector Machines are presently considered a robust method for supervised learning, as they focus on determining a hyperplane that optimally separates two adjacent classes[212]. This optimization is essential for reducing the generalization error associated with the classification model. In Figure 5.7, The classes are organized in a linear fashion, with the margin defined as the distance from the decision boundary to the nearest training samples. This margin is determined by support vectors, which play a crucial role in defining the classification functions. In situations where data points are grouped in such a way that linear separation is not possible, they can be mapped into a higher-dimensional space, allowing for linear separation via a hyperplane [213].

N-dimensional inputs denoted as $x_i = (i = 1,2,3, \dots, m)$, m indicates the total number of samples in either class one or class two, are assigned labels yi=1 for the first class and $yi = 1$ for the second class. In cases where the data can be separated linearly, a hyperplane defined by $f(x) = 0$ is established to distinguish the two classes, as articulated in equation 5.33

$$f(x) = \omega^T x + b = 0 \qquad 5.33$$

ω denotes the n-dimensional vector, while b signifies the intercept term. The hyperplane that distinguishes the two vectors is determined by their respective positions and adheres to the constraints $f(x) \geq 0$ where $yi = 1$ and $f(x) \leq -1$ where $yi = -1$, thereby establishing a functional margin as described in equation 5.34.

$$y_i f(x_i) = y_i(\omega^T x_i + b) \geq 1, for\ i = 1,2,3, \dots, m \qquad 5.34$$

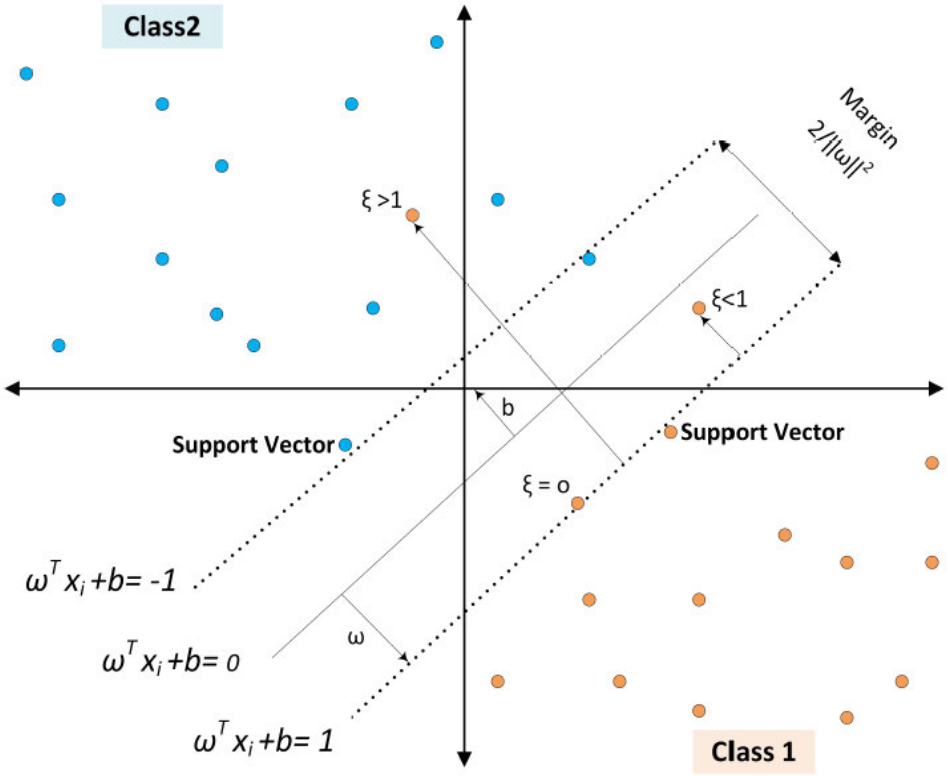

Figure 5. 7 Maximum margin classification with Support Vector Machines.

The optimal separating hyperplane is characterized as the hyperplane that maximizes the distance between itself and the nearest data point, as depicted in Figure 5.7. The geometric margin is calculated as$\frac{1}{2}\|\omega\|^2$. To incorporate noise, the variable ζ_i is introduced as a slack variable, while $C_i$serves as an error penalty. The determination of the optimal hyperplane is achieved by solving a convex quadratic optimization problem, represented by equations 5.35 to 5.37.

$$\min_{\omega,b} \frac{1}{2}\|\omega\|^2 + C\sum_{i=1}^{m}\zeta_i \qquad 5.35$$

$$s.t.\, y_1 = (\omega^T x_i + b) \geq 1 - \qquad 5.36$$

$$\zeta_i \;\; and i = 1,2,3,\ldots,m$$

$$\zeta_i \leq 0, for\; i = 1,2,3,\ldots,m \qquad 5.37$$

In equation 5.33, the minimization of $\|\omega\|$ is synonymous with minimising. Equation 5.34, describes the quadratic programming problem which is formalized into Lagrange formula by incorporating both objective functions$\min_{\omega,b} \frac{1}{2}\|\omega\|^2$ and $(\omega^T x_i + b) \geq 0$. It is then possible to formulate from the Lagrange equation 5.38

$$\min_{\alpha} \omega(\alpha) = \sum_{i=1}^{m} \alpha_i - \frac{1}{2} \sum y_i y_j \alpha_i \alpha_j \langle x_i, x_j \rangle \quad 5.38$$

Subject to the constraints $0 \leq \propto_i \leq C \; and \; i = 1,2,3, \ldots, m$, the equation $\sum \alpha_i y_i = 0$ must hold. To determine the values ofα_i, it is necessary to solve the dual Lagrange problem. In the context of a two-class problem derived from SVM, the decision boundary can be expressed as follows, utilizing the kernel function $K(\vec{x}^{(i)}, \vec{x})$ for a new pattern $\vec{x}^{(i)}$ (intended for classification) and the training pattern as outlined in equation 5.39.

$$D_x = \sum_{i=1}^{m} \alpha_i y^{(i)} K\left(\vec{x}^{(i)}, \vec{x}\right) + b \quad 5.39$$

the values of $\alpha_i, s,$ are all set to zero, except for those corresponding to the support vectors. The kernel function employed for SVM is the Radial Basis Function (RBF), which is articulated in equation 5.40.

$$K(x_i j_i) = e^{-\|x_i - x_j\|^2 / \sigma^2} \quad 5.40$$

5.4.5 Extreme learning machine

Extreme Learning Machine (ELM) represents an innovative learning algorithm tailored for single layer feedforward neural networks (SLFNs), characterized by its superior learning speed compared to conventional feedforward methods. Support Vector Machines (SVMs), initially developed for binary classification tasks, have undergone various adaptations to accommodate multiclass classification scenarios. Notable extensions include the One-Versus-One (OVO) and One-Versus-Rest (OVR) approaches. The subsequent section will elucidate the mathematical frameworks underpinning both the OVO and OVR SVM methodologies

For OVO a training dataset is presented as indicated in equation 5.41, where$x_i \; and \; y_i$ i are defined in equations 5.42 and 5.43, respectively. Here, the class index of x_i is denoted, and k represents the total number of classes. The One-Versus-One approach formulates a model as described in equation 5.44, with each model being trained using data from two distinct classes. To address the training data from the i_{th} and the j_{th} classes, the problem is articulated through equation 5.45.

5.41

$$x_i = [x_{i1};\; x_{i2}; \ldots\ldots\ldots\ldots\ldots x_{in}]$$

$$y_i \in [1, \ldots\ldots\ldots\ldots\ldots\ldots, k] \quad 5.42$$

$\frac{k(k-1)}{2}$ ……..(n) 5.43

Minimize$\frac{1}{2}\sum_{m=1}^{N}\sum_{n=1}^{N} y_m y_n K(x_m x_n)\alpha^{ij}{}_m \alpha^{ij}{}_n \sum_{m=1}^{N}\alpha^{ij}{}_m$……..[84] 5.44

Subjected to $\sum_{m=1}^{N} y_m \alpha^{ij}{}_m = 0,\ 0 \leq \alpha^{ij}{}_m \geq C$ 5.45

In this context, $C > 0$ represents the penalty parameter, while $K(x_m x_n)$ denotes the kernel function. Upon resolving the optimization problem (o), one obtains (n) decision functions. Classification is performed utilizing the "Max Wins" strategy, as outlined in equation 5.46. If the test instance x is classified as belonging to the i_{th} class, the vote for that class is incremented by one; conversely, if it is classified as belonging to thei_{th} class, the vote for the i_{th} class is increased by one as indicated by equation 5.47-5.48. No votes are recorded if the test instance does not belong to either the i_{th} or i_{th} class. Consequently, the test data x will be assigned to the class that receives the highest number of votes.

Minimize $\frac{1}{2}\sum_{m=1}^{N}\sum_{n=1}^{N} y_m y_n K(x_m x_n)\alpha^{i}{}_m \alpha^{i}{}_n - \sum_{m=1}^{N}\alpha^{i}{}_m$…… {1 5.46

Subjected to $\sum_{m=1}^{N} y_m \alpha^{i}{}_m = 0,\ 0 \leq \alpha^{i}{}_m \geq C$ 5.47

$:= arg \max_{i=1\ldots,k} \sum_{n=1}^{N} y\alpha^{i}{}_m K(x_m x) + ıb^2$ 5.48

5.4.6 Classification accuracy and analysis

The evaluation of classifiers is conducted to gauge their performance, employing a confusion matrix to derive specific metrics. A critical measure of performance is accuracy, which reflects the degree of correctness in classifications. Additional metrics utilized include recall and precision [41], with their definitions provided by equation 5.49 to 5.52.

$accuracy = \frac{TP+TN}{d} * 100\%$ 5.49

$Precision = \frac{TP}{TP+FP} * 100\%$ 5.50

$specificity = \frac{TN}{TN+FP} * 100\%$ 5.51

$sensitivity = \frac{TP}{TP+FN} * 100\%$ 5.52

TP denotes the count of True Positive classifications, reflecting the number of instances that are accurately identified as belonging to the “x” category by the classifier. FN represents the count of False Negatives, which are instances that should be classified as “x” but have been misclassified into another category. The True Negatives, indicated by TN, represent the

number of instances that correctly do not belong to class “x” and have been classified as such. FP signifies the count of False Positives, which are instances erroneously classified by the model as belonging to class “x” when they do not actually belong to that category. The variable d represents the total number of samples in the test set. An additional metric often utilized alongside these classifications for evaluating classifier performance is the confusion matrix, also known as the contingency table. This matrix offers a clear and straightforward method for summarizing classification results. It illustrates binary classification scenarios through a two-by-two matrix format.

5.5 Fault Locations

5.5.1 Introduction

This section provides a brief overview of the concept of fault location in transmission lines. While the focus of this study is limited to detection and classification, it is essential to address this topic briefly, as it constitutes a fundamental component of protection schemes

5.5.2 Traveling wave refraction methods

The initial phase in the formulation of the proposed algorithm involves evaluating the relationship between the harmonic frequencies produced by the TCSC and the traveling waves detected by relays during a fault occurrence. For illustration, let us examine a transmission line equipped with a TCSC, as depicted in Figure 5.8. It is widely recognized that following a fault event, two traveling waves propagate in opposing directions along the transmission line. Typically, the voltage at any designated point "x" along the transmission line can be expressed by equation 5.53 [214].

$$V_x = V\_e^{-x\gamma} + Ve^{+x\gamma} \qquad 5.53$$

Where γ denotes the propagation coefficient of the transmission line, , Ve^{+xy} signifies the voltage of the incident wave, while Ve^{-xy} indicates the voltage of the reflected wave originating from the remote end. As illustrated in Figure 5.7, in the scenario of a fault occurring between the local end and the TCSC (case 1), the traveling waves reach the relay (R) at the local end with minimal disturbance. This situation does not present significant challenges for conventional traveling wave relays. Conversely, in the event of a fault occurring

between the TCSC and the remote end (case 2), the traveling waves encounter an impedance change at the TCSC terminals prior to reaching relay (R). This alteration can lead to distortion and modification of the traveling waves as they arrive at the local end. The reflection coefficient at the transition point is expressed as equation 5.54

$$\rho_v = \frac{V_- e^{+x\gamma}}{V_- e^{-x\gamma}} = \frac{Z_x - Z_o}{Z_x + Z_o} \qquad 5.54$$

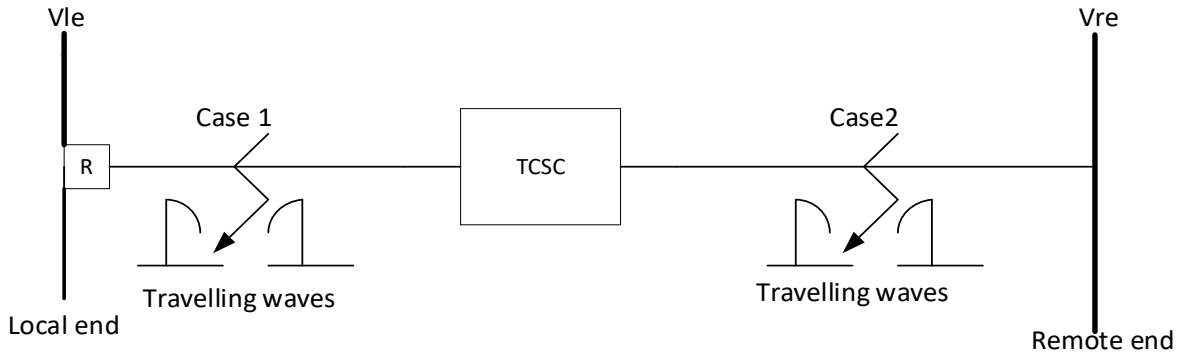

Figure 5. 8 The concept of Travelling waves in a TCSC Network

In this context, Z_x represents the impedance of the TCSC, while Z_o denotes the characteristic impedance of the transmission line. The reflection and refraction coefficients serve as analytical tools to assess the modifications that the TCSC introduces to the characteristics of traveling waves as they reach the relay (R) at the local end during a fault condition. It is observed that the magnitude of these traveling waves diminishes to approximately one-third of its initial value after a specific time constant. This duration is considered excessively long to exert any meaningful influence on the magnitudes of traveling waves utilized in high-speed relaying applications. Consequently, when the thyristors are in an open state, the traveling waves pass through the TCSC with minimal attenuation. Key parameters for system analysis include line voltage, length, inductance, zero-sequence impedance, and compensation capacitance.

According to [215] To comprehend the interaction between traveling waves and the TCSC, it is essential to examine both scenarios: open and closed states. When the thyristors are in the open state, specifically for the time interval $0 \leq t < \alpha$, the high-frequency impedance encountered by the traveling waves is described by equation 5.55. Consequently, the reflection coefficient can be determined using equation 5.56

$$Z_{x(s)} = Z_0 \frac{1}{S\frac{C_{TCSC}C_F}{C_{TCSC}+C_F}} \quad 5.55$$

$$\rho_v = \frac{1}{2Z_0 C_{E(S)}+1} \quad 5.56$$

The term C_E denotes the equivalent capacitance for bothC_{TCSC} andC_F , while s represents the variable in the Laplace transform. By converting ρ_v into the time domain, it can be expressed through equation 5.57. When the thyristors are in a closed position. The performance of the TCSC closely resembles that of the earlier scenario. The high-frequency impedance encountered by the traveling waves reaching the terminals is described by equation 5.58, and the final expression for the reflection coefficient is provided in equation 5.59

$$\rho_v = e^{-\tau t} = e^{-2Z_o C_E t} \quad 5.57$$

$$Z_{x(s)} = Z_o + \frac{1}{SC_F} + \frac{\frac{1}{sC_{TCSC}} sL_{TCSC}}{\frac{1}{sC_{TCSC}} + sL_{TCSC}} \quad 5.58$$

$$\rho_V = \frac{s^2 B+1}{s^3 A+s^2 B+sC+1} \quad 5.59$$

Where: A=$2Z_o L_{TCSC} C_{TCSC} C_F$

B=$L_{TCSC}(C_{TCSC} + C_F)$

C= $2Z_o C_F$

The linear circuit is characterized by the state variable vector x, which includes the inductor current as represented in equation 5.60 and the capacitor voltage as outlined in equation 5.61. When these equations are expressed in state-space form, they are reformulated as indicated in equation 5.62.

$$\dot{x} = A_1 x + B_1 V_g \quad 5.60$$

$$y = C_1 x \quad 5.61$$

$$A_1 = \begin{bmatrix} -\frac{R_{ON}}{L} & 0 \\ 0 & -\frac{1}{RC} \end{bmatrix}, B_1 = \begin{bmatrix} \frac{1}{L} \\ 0 \end{bmatrix}, x = \begin{bmatrix} i_L \\ V_c \end{bmatrix} \quad 5.62$$

5.6 Conclusion

This chapter focused on the principles of fault detection, classification, and localization through an examination of the mathematical formulations associated with various models. The traditional mathematical frameworks analysed include the Fourier transform and wavelength transforms, while more sophisticated methodologies involve Principal Component Analysis (PCA), Support Vector Machines (SVM), and Artificial Neural Networks (ANN). These mathematical frameworks provide the essential groundwork for the development of machine learning detection and classification strategies, as described in the methodology section, which elaborates on the formulation of the simulation model pertinent to this research before its testing and implementation in MATLAB. The subsequent chapter is organized into three distinct models, each addressing the specific objectives outlined in the first chapter.

Chapter 6 Methodology

6.1 The impact of compensation in transmission line.

A standard transmission line is illustrated in Figure 6.1, which represents a power system network linking points A and B. This line facilitates the transfer of electrical power from the generator station to the load located at the receiving end bus bar. The relationships between the sending voltage V_s and the receiving voltageV_R are articulated in Equations 6.1 and 6.2 respectively, which depend on the angular difference δ between the voltages at the respective bus bars. By replacing an ideal lossless transmission line with a real transmission line that incurs losses, the transmitted power can be determined using Equations 6.3 and 6.4. In this context, X_t denotes the nominal series reactance of the line, as outlined in Equation 6.5.

$$V_s = V_s \angle \delta \quad 6.1$$

$$V_R = V_R \angle 0 \quad 6.2$$

$$P = \frac{V_R V_S}{X_t} \sin \delta \quad 6.3$$

$$Q = \frac{V_R V_S \cos \delta - V^2}{X_t} \quad 6.4$$

$$X_t = X_s + X_l \quad 6.5$$

Initially the study a two-line bus system is modelled in MATLAB Simulink shown in figure 6.3. The objective is to examine the performance of the system when subjected to different faults including single phase to ground (L-G), double line(L-L), double line to ground (L-L-G) and three phase faults (L-L-L). The system model is a 300km, and segmented to two equal parts (150kM) as shown in figure 6.2 . Table 6.1 shows the data of the segmented transmission line.

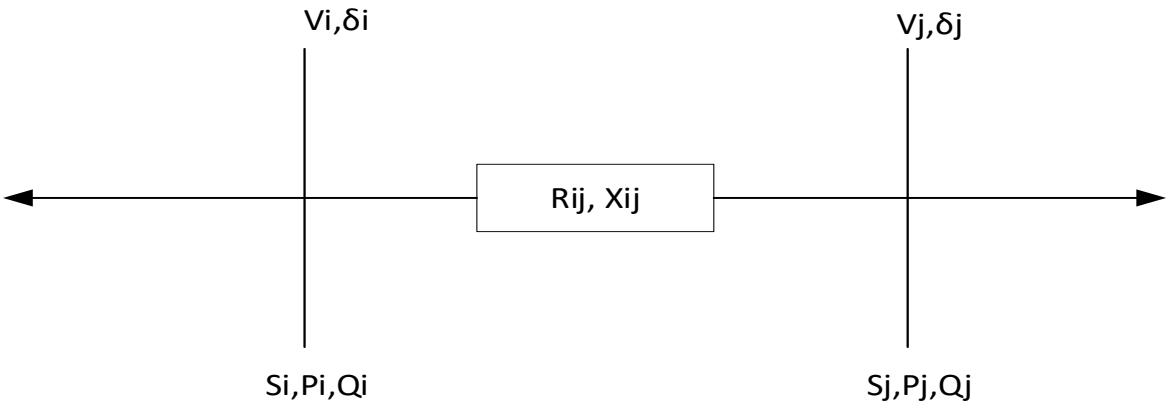

Figure 6. 1Transmission line single line diagram

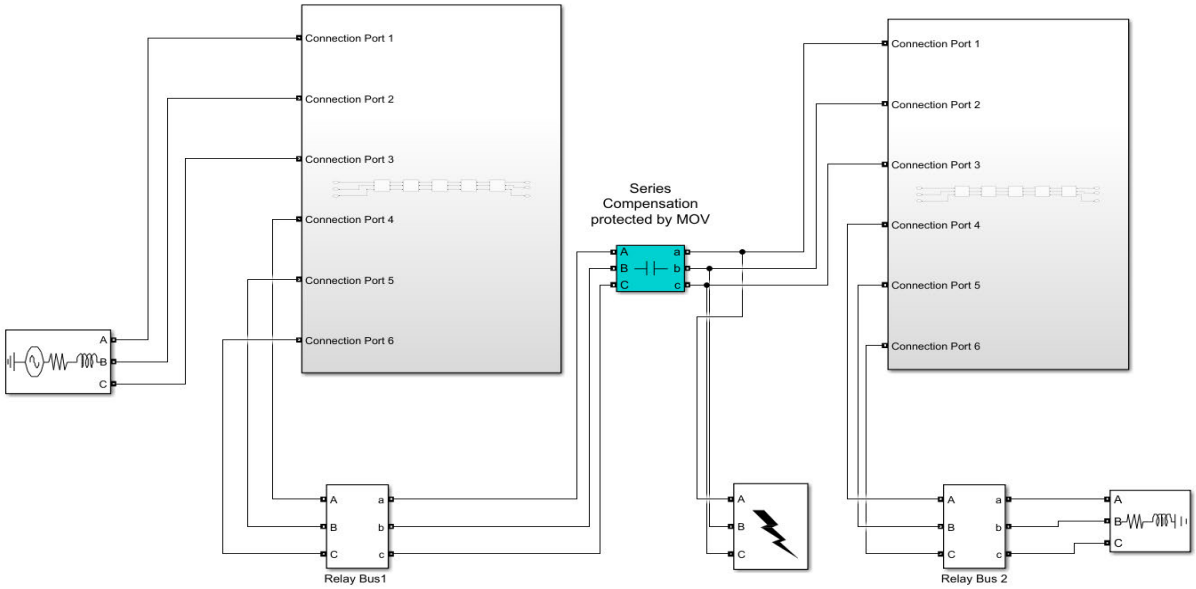

Figure 6. 2 Model of a two-bus system

Table 6. 1 Transmission line parameters

parameter	Values
Length	300km
Nominal Frequency	50 Hz
Voltage	765kV
Line resistance	0.01273Ω/km
Line Inductance	0.9337mH/km
Line capacitance	12.74nF/km
Zero sequence resistance	0.03864Ω/km
Zero sequence inductance	4.1264mH/km

Zero sequence capacitance	7.75nF/km

The Metal-Oxide Varistor (MOV) becomes conductive when the instantaneous phase voltage of the Series Capacitor Bank surpasses a specified maximum threshold. Consequently, the MOV is capable of conducting current only during certain segments of the positive and negative half cycles of the SCB voltage waveform. This behaviour results in a nonlinear correlation between the instantaneous MOV current (i) and the voltage (v). Furthermore, while the MOV is in a conductive state, the relationship between (i) and (v) does not adhere to a linear model; instead, it follows an exponential function. To analyse the relationship between the voltage and the current flowing through the MOV during fault conditions, equation 6.6 to 6.12 are employed with reference to phase A, and it is essential to recognize that the same methodology applies to phases B and C.

$$V_{ca} = V_g + k_1 I_{na,a} \quad 6.6$$

Where $I_{na,a}$can be represented by equations (6.7) or (6.8). Equation (6.9) represents the transmission line current. When we substitute equations 6.8 and 6.9 the current to series capacitor including MOV can be represented by equation 6.10. Assuming 1/K1=A and Vg/K1=B, current is then by equation 6.11 and the voltage by equation 6.12

$$I_{na,a} = (\frac{V_{ca} - V_g}{K_1}) \quad 6.7$$

$$I_{na,a} = V_{ca} j\omega C \quad 6.8$$

$$I_{na} = I_{na,a} - I_{na,c} \quad 6.9$$

$$I_{na} = V_{ca}\left(\frac{1}{K_1} - j\omega C\right) - \frac{V_g}{K_1} \quad 6.10$$

$$I_{na} = AV_{ca} - B \quad 6.11$$

$$V_{ca} = \rho I_{na} + \gamma \quad 6.12$$

The Metal-Oxide Varistor (MOV) serves as a protective measure against overvoltage for the capacitor. This protective arrangement includes a capacitor bank, a bank of metal-oxide varistors, a triggered bypass air gap, a damping reactor, and a bypass switch, as illustrated in Figure 6.4. In the event of high transient voltages, the MOV limits the voltage to a safe threshold and converts the excess energy into heat, thereby safeguarding the circuit components from overvoltage and preventing potential damage to the system. A notable challenge associated with this system is the nonlinear characteristics of the MOV. The total

reactive impedance of the line at 0% compensation is determined using equation 6.13, which employs positive sequence inductance. For varying levels of compensation, defined as a specific percentage reduction of the transmission line's inductive reactance through the addition of capacitive reactance, the necessary impedance is calculated using equation 6.14, while the total capacitance required is specified by equation 6.15

$$X_t = 2\pi f L_1 \qquad 6.13$$

$$X_c = (required\ compensation\ level\ \%)X_t \qquad 6.14$$

$$C = \frac{1}{2\pi f X_c} \qquad 6.15$$

The necessary MOV protection level to safeguard the capacitors is established at 2.5 times the nominal voltage of the capacitors, which is defined at a line current of 2 kA rms. Consequently, equation (6.16) specifies the voltage that must be achieved for adequate protection

$$V_p = 2 * 2000 * X_c * \sqrt{2} \qquad 6.16$$

Furthermore, the line is compensated with series capacitor protected by an MOV and this model is implemented on the previous model of a transmission line compensation is varied in 3 intervals 50%, 100% and 120% to further investigate the impact of different levels of compensation. The MOV model is shown in figure 6.3.

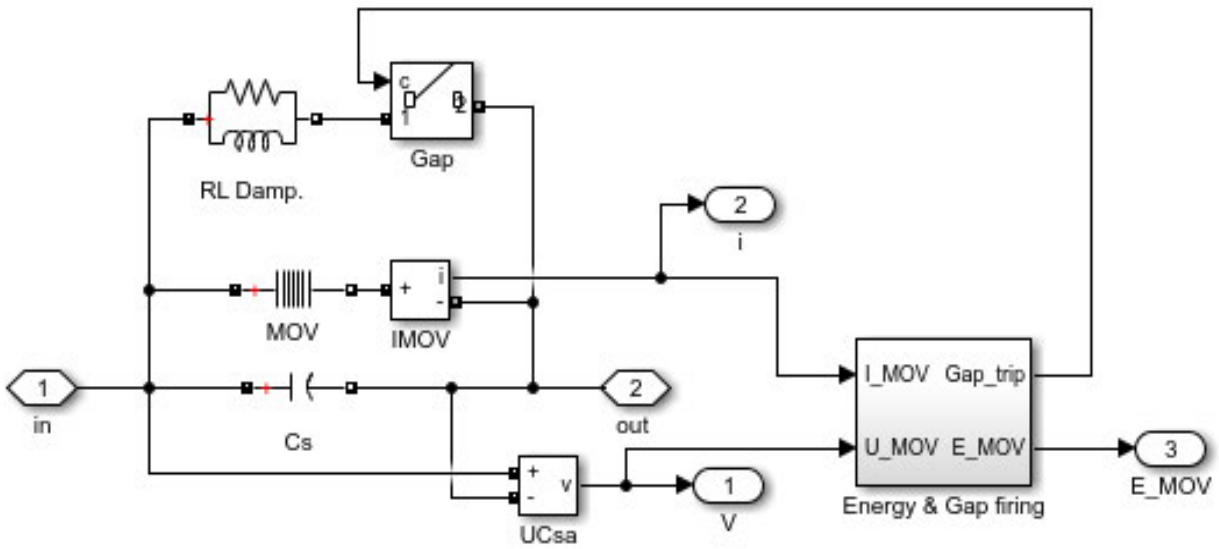

Figure 6. 3 The SIMULINK MOV model

6.2 The implementation on an IEEE-9 Bus system

6.2.1 Load flow analysis

A bus is defined as any node where multiple components, such as electric generators and transmission lines, are interconnected. In the field of electrical engineering, the bus is associated with four key parameters: currents, potential difference, phase angle, and both active and reactive power[209]. Analyzing load flow is crucial for planning and ensuring the stable operation of the system. Such analyses utilize systematic and analytical methods to assess the various voltages at the bus, phase angles, and the flow of reactive and active power across different branches of the load, including generators and transformers, once steady state is achieved. In load flow analysis, two variables are predetermined while the remaining two must be calculated. Buses are classified into three distinct types based on the particular quantity under examination: generation bus, load bus, and slack bus.

In P-V buses, the voltage magnitude associated with the generated voltage and the true or active power P, as per its rating, is defined. The voltage magnitude is kept constant at a predetermined level by the injection of reactive power. It is necessary to calculate the reactive power generation Q and the phase angle δ of the voltage. These buses are connected to generators, which means that the power generation at these locations is regulated by a prime mover, while the terminal voltage is managed through the excitation of the generator. Maintaining a constant input power via turbine-governor control, alongside ensuring a stable bus voltage through the use of an automatic voltage regulator, allows us to define constant values for and P_i at $V_i$these buses. Consequently, these buses are commonly designated as P-V buses. It is important to recognize that the reactive power provided by the generator, denoted as Q_i, is contingent upon the configuration of the system and cannot be predetermined. Additionally, it is necessary to determine the unknown angle δi associated with the bus voltage.

The slack bus in a power system plays a crucial role in managing the active and reactive power within the network, either absorbing or supplying it as needed. Notably, this bus does not support any load. At the slack bus, both the voltage magnitude and phase angle are defined, with the phase angle typically set to zero. The active and reactive power associated with this bus is generally calculated through the resolution of relevant equations. In load flow analysis, this bus is conventionally designated as bus number 1. It serves as the angular reference point

for all other buses in the system. The flow of real and reactive power between two voltage sources is determined by the angular difference between them; thus, the specific angle of the slack bus itself is not critical. Nevertheless, it establishes the baseline against which the angles of all other bus voltages are referenced, which is why the angle of the slack bus is commonly assigned a value of 0°. Additionally, it is presumed that the voltage magnitude at this bus is known. IEEE-9 bus system shown in figure 6.4 complexity and real-world applicability make it a benchmark for power system analysis and optimization. This section describes a method for IEEE-9 bus load flow and dispatch analysis.

RRR

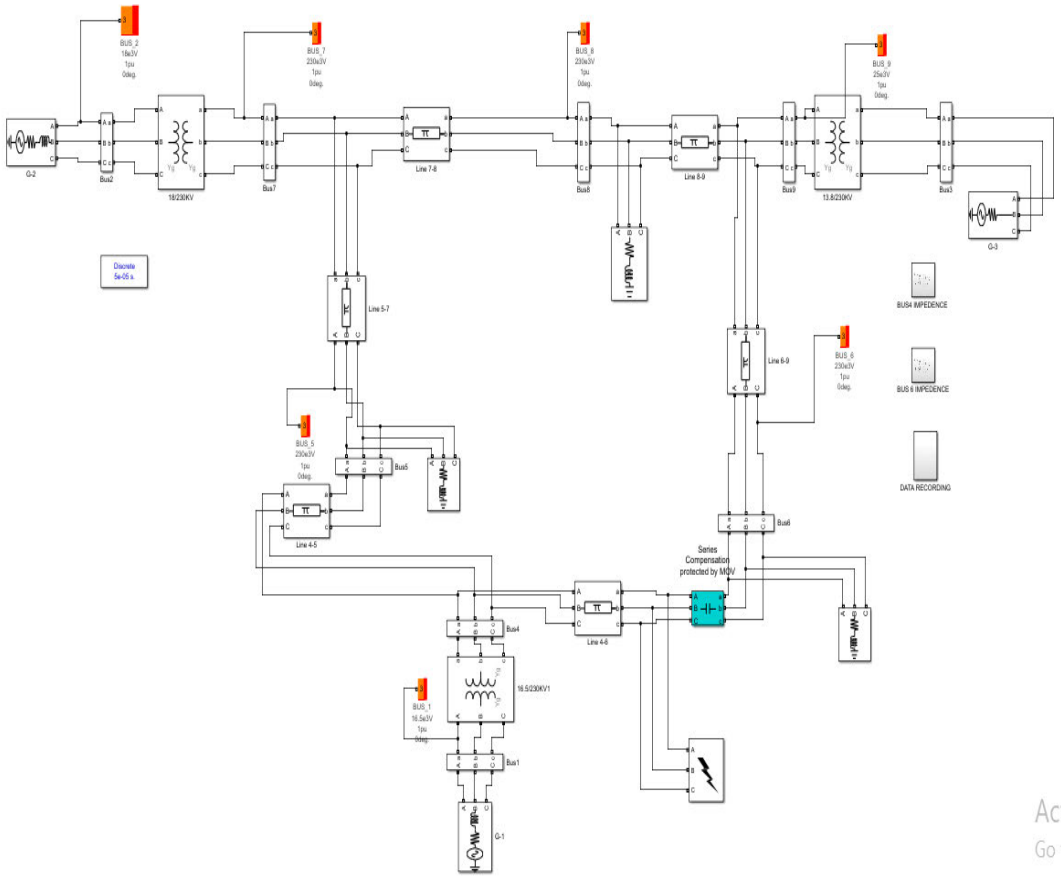

Figure 6. 4 IEEE 9 bus system model in MATLAB SIMULINK

Load dispatch analysis focuses on optimizing the allocation of generators to satisfy load requirements, while load flow analysis is concerned with identifying the steady-state operational parameters, such as voltage levels, phase angles, and power flows. In load flow analysis, the Newton-Raphson method is employed iteratively to calculate bus voltages,

thereby ensuring both system stability and adherence to voltage constraints. Evaluating line flows and losses provides insights into the overall performance of the system. A critical aspect of the solution methodology involves determining the polar angle of the voltage at PQ buses and the polar voltage angles at PV buses, as outlined in equation 6.17.

$$S_i = P_i + jQ_i = V_i \sum_{k=1}^{n} V_{ik} V_k \qquad 6.17$$

On further disintegration the above equation can be separated as sum of two individual equations of active power and reactive power which can be expressed as shown in equation 6.18 and 6.19 respectively.

$$P_i = V_i V_{ii} Y_{ii} \cos \emptyset_{ii} + \sum_{k=1}^{n} V_i V_k V_{ik} \cos(\delta_i - \delta_k - \emptyset_{ik}) \qquad 6.18$$

$$Q_i = V_i V_{ii} Y_{ii} \cos \emptyset_{ii} + \sum_{\substack{k=1 \\ K \neq 1}}^{n} V_i V_k V_{ik} \sin(\delta_i - \delta_k - \emptyset_{ik}) \qquad 6.19$$

Utilizing the appropriate tools, construct the specified IEEE system model in MATLAB Simulink as illustrated in figure 6.5. Subsequently, the load flow analysis is conducted. The load flow study for a 9-bus system, employing the Newton-Raphson iterative solution method, is elaborated upon in chapter 7.

6.3 Fault Detection and classification

6.3.1 Data Sampling

This research work uses voltage (V) and current (I) signals collected at the relay bus during different types of faults as described in data collection section above. The data set are numerical values of (V) and (I), and the categorical data representing each fault scenario shown in Table 6.2 while figure 6.5 shows a sample of current signals and figure 6.6 voltage signals

Table 6. 2 : Fault type representation

Fault type	code
No fault	0000
L-G	1001
L-L	0110
L-L-G	1011
L-L-L	1110
L-L-L-G	1111

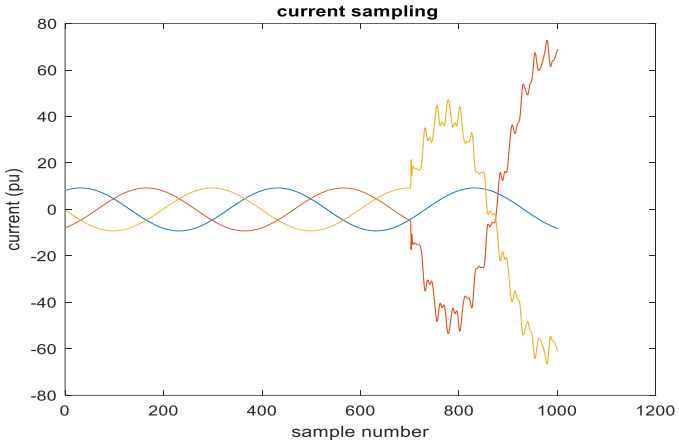

Figure 6. 5 Graphical representation of sample current signal

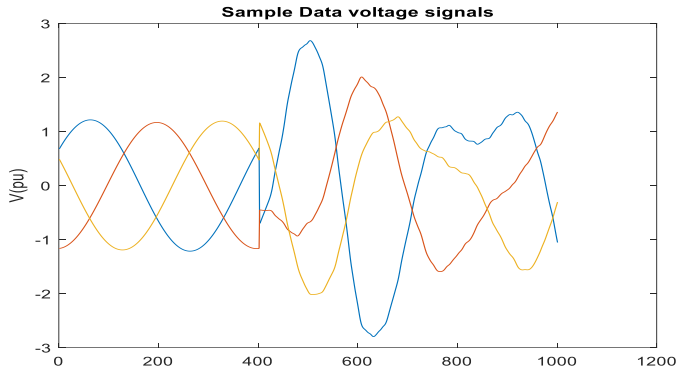

Figure 6. 6 Graphical representation of voltage signals

The data that has been gathered is organized into a numerical table. It is crucial to emphasize that the chosen data represents a sample from the time preceding the fault and during the fault itself; data following the fault's occurrence has been excluded from this selection. The table includes voltage and current signals, which serve as the input signals for the fault detection classifier, specifically the three-phase instantaneous voltage and current signals.

Subsequently, features were extracted from the voltage (V_a, V_B, V_C), and current. I_a, I_b, I_c, signals. This process is illustrated in Figure 6.7 the process can be summarised as figure 6.5

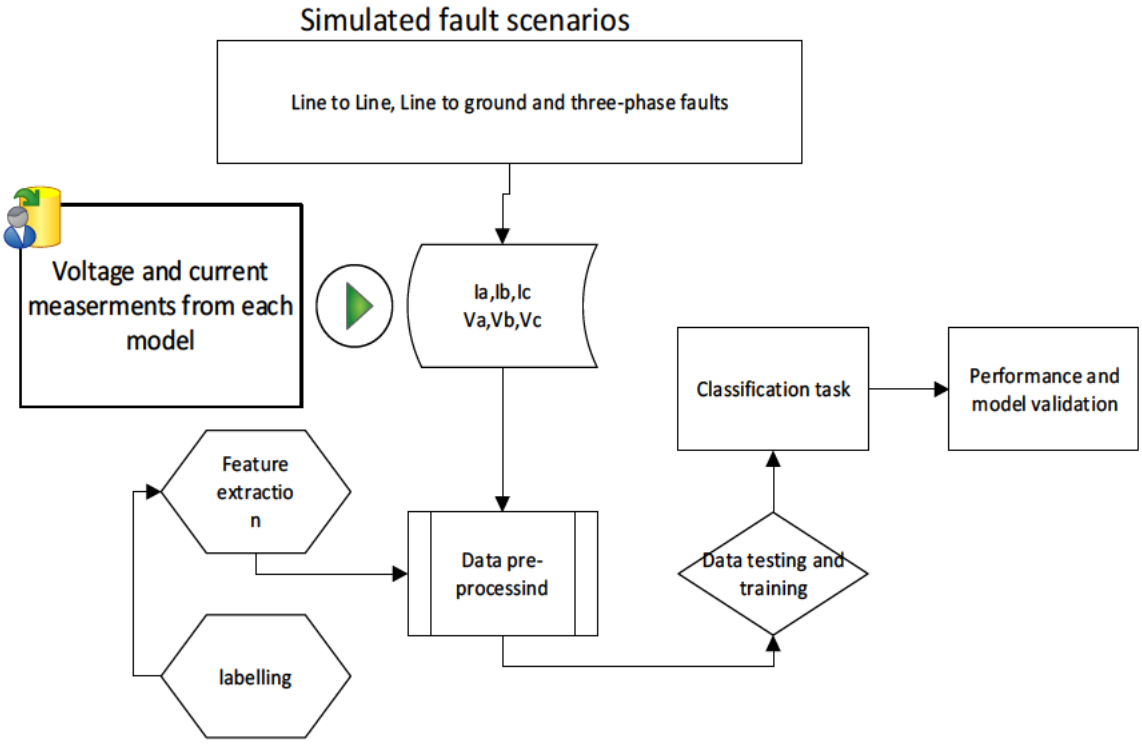

Figure 6. 7 A Sample model of Machine learning based protection scheme

6.3.2 Feature Extraction

Faults events in transmission lines creates transient disturbances to current and voltage signals. In this study Dimensional reduction is used for feature extraction to preprocess raw data before implementing classification process. Feature extraction is normally used when the raw data is large, after the simulation within 1sec the dataset is more to 1000000, during data preprocessing the date is still large hence the need for feature extraction. To develop a PCA algorithm please refer to section 5.3.4.

6.3.3 Fault detection and classification models

The increasing advancement of power systems and smart grids necessitates the implementation of sophisticated fault diagnosis methodologies to mitigate unwanted disruptions and financial losses. A critical component of these systems is the transmission lines. This research explores the application of contemporary machine learning techniques for the detection and classification of faults within a compensated transmission line model,

which was established in the preceding section. Utilizing the MATLAB platform, this study develops and simulates three distinct algorithms for fault detection and classification specifically tailored for compensated transmission lines. Initially, data is gathered from an IEEE 9-bus system featuring series compensation on line 4-6. Subsequently, feature extraction is performed using principal component analysis (PCA), followed by the deployment of fine K-nearest neighbours (KNN), Medium Neural Network (MNN), and quadratic support vector machine (QSVM) classifiers. A thorough performance evaluation is conducted, focusing on the accuracy of each classifier in identifying and categorizing various types of faults. Figure 6.8 summarises the selection criteria for the classifiers used.

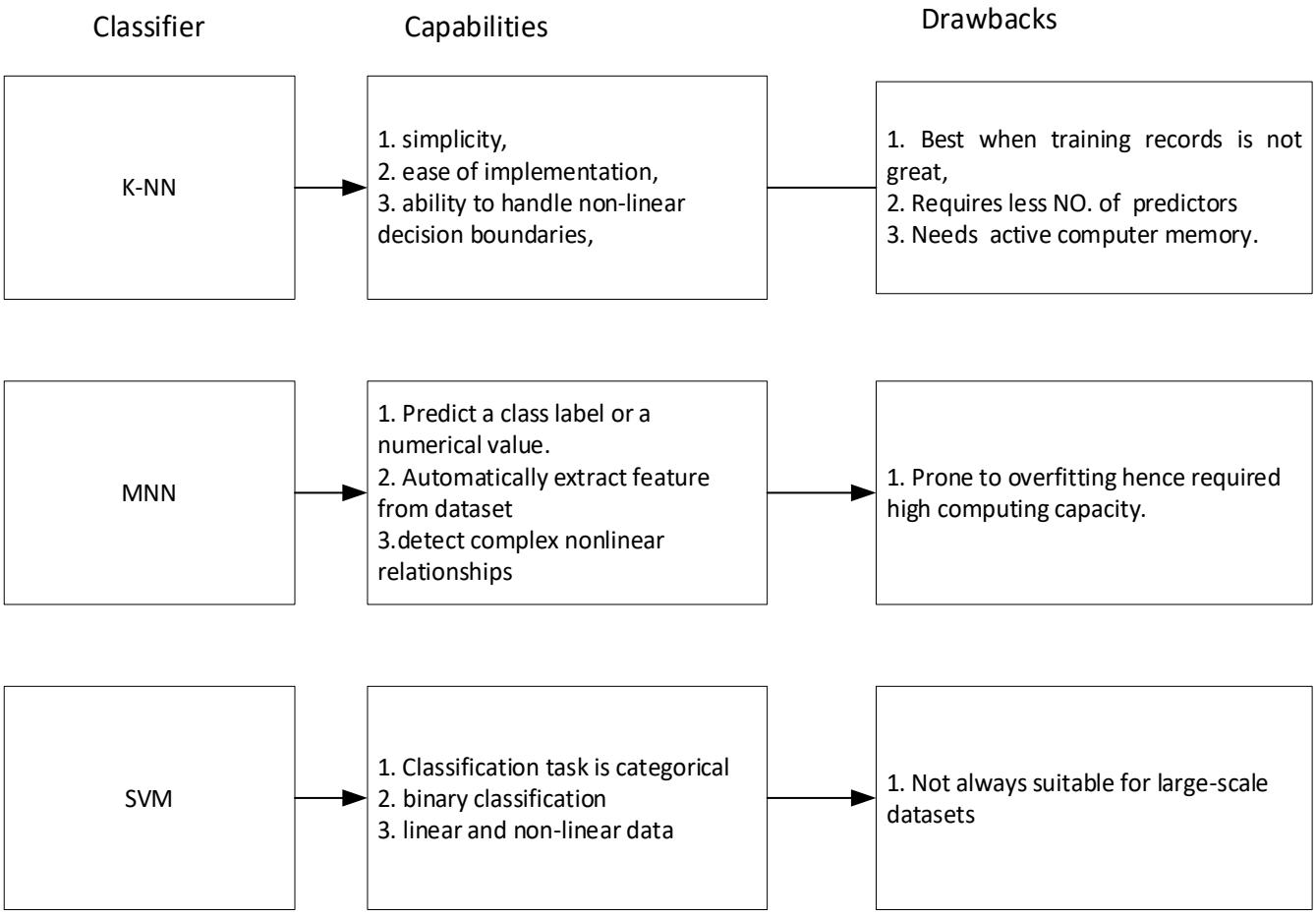

Figure 6. 8 Classifier selection criteria

6.3.3.1 KNN Classifier

For this research there is a need to be able to define similarity measure in the data space. In $\mathbb{R}^q$, the Minkowsink metric (P-norm) is applied as equation 6.21 [216].

$$\left[\left[X_{'} - X_j\right]\right]^P = \left(\sum_{i=1}^{n} \left|(x_i)_{'} - (x_i)_j\right|^p\right)^{1/p} \qquad 6.21$$

The expression aligns with the Euclidean distance when *p* equals 2. In alternative data spaces, it is essential to select appropriate distance functions. The detrimental distance in $\mathbb{Z}^q$ is considered. For binary classification, the label set $\gamma = \{1, -1\}$ is employed, and the K-nearest neighbours (KNN) algorithm is articulated through equation 6.22.

$$f_{KNN} = \begin{cases} 1\ if\ \sum_{i \in N_k(x)_{'}} \Upsilon_1 \geq 0 \\ -\ if\ \sum_{i \in N_k(x)_{'}} \Upsilon_1 < 0 \end{cases} \qquad 6.22$$

The neighbourhood size *K* and with the set of indices $N_k(x)_{'}$ of the K-nearest patterns. The choice of K defines the locality of KNN. For K = 1, little neighbourhoods arise in regions, where patterns from different classes are scattered [217]. The efficacy of the k-NN model can be assessed through various metrics. A widely utilized parameter for this evaluation is the average accuracy, which is articulated by the equation 6.23. In this context, TP represents true positives, TN denotes true negatives, FP signifies false positives, and FN indicates false negatives. The subscript i corresponds to a specific category, while l represents the total number of categories [218].

$$average\ accuracy = \sum_{i=1}^{l} \frac{TP_i + TN_i}{TP_i + FN_i + FP_i + TN_i} / l \qquad 6.23$$

6.3.3.2 Medium Neural Network

The procedure of adjusting weights and biases to reduce errors is referred to as backpropagation (BP) algorithms. In the context of machine learning, the error function E_ω ,commonly known as the cost or loss function, along with the scale factor ∈, identified as the learning rate, play crucial roles. E_ω quantifies the discrepancy between the outputs of the artificial neural network (ANN), denoted as (y), and the target value $(\hat{y})$ One specific measure of error is the mean square error, which is articulated in equation 6.24. Furthermore, equations 6.25 to 6.26 illustrate the Root Mean Square Error (RMSE), which is employed to

eliminate the constant during gradient computation, as well as the mean bias error (MBE) and the mean absolute error (MAE), respectively

$$MSE = \frac{1}{n}\sum_{i=1}^{n}(y_i - \hat{y}_i)^2 \quad 6.24$$

$$RMSE = \sqrt{\frac{1}{n}\sum_{i=1}^{n}(y_i - \hat{y}_i)^2} \quad 6.25$$

$$\text{MAE} = \frac{1}{n}\sum_{i=1}^{n}|y_i - \widehat{y_i}| \quad 6.26$$

The GDM algorithm is used to minimize the error, it the weights co-ordinates are described by $y(\omega_i) = \varphi\sum_{i=0}^{n}(\,(y_i - \hat{y}_i)^2$ there for the MSE can be re-described by equation 6.27. The partial derivative of MSE is represented by equation 6.28, this applies for a case where the activation function φ is assumed to be being the identity of function,

$$MSE = \frac{1}{n}\sum_{i=1}^{n} y(\omega_i) - \widehat{y_i})^2 = \quad 6.27$$

$$\frac{1}{n}\sum_{i=1}^{n}(\varphi\sum_{i=0}^{n}(\omega_i.x_i - \widehat{y_i})^2$$

$$\frac{\partial}{\partial\omega_i}SE = y(\omega_i - \hat{y}_i)\varphi'(z).x_i \quad 6.28$$

For a particular case where the activation function is equal to the identity function, the learning algorithm results in s specific error function. Convergence of the method is ensured following this method

$if\ \ map\ f:\mathbb{R}\to\mathbb{R}\ is\ called\ a\ Lipschitz\ function\ that\ exist\ for\ \ k\in\mathbb{R}, k >$ $0particulary.when\ 0\le k<1, f\ is\ called\ contraction$ the function is described by equation 6.29. for the construction to be continuous the function is described by equation 6.30

$$|f(x) - f(y)| \le k|x - y|, \forall x, y \in \mathbb{R} \quad 6.29$$

$$|\nabla f(x) - \nabla f(y| \le k|x - y|, \forall x.u \in \mathbb{R} \quad 6.30$$

The subsequent theorem delineates the criteria pertaining to the error that must be satisfied to guarantee convergence.

$convergence\ of\ gradient)\ suppose\ the\ fuction\ E:\mathbb{R}^n\to$ $\mathbb{R}\ is\ convex\ differentiable\ and\ k-$

$smooth. Then\ if\ we\ run\ gradient\ descent\ for\ a\ r\ iterations\ with\ a\ fixed\ step\ size\ t \leq \frac{1}{k}, it\ will\ yeald\ a\ solution\ E^{(r)}\ which\ satisfies$ equation 6.31

$$E\left((\omega^{(r)}\right) - E(\omega^*) \leq \frac{|\omega^{(o)} - \omega^8|}{2fr} \qquad 6.31$$

$E(\omega^*)$ represents the minimum value, indicating that the gradient descent method is assured to converge.

6.3.3.3 Quadratic Support vector machine (QSVM)

The objective of Support Vector Machines (SVM) is to identify a hyperplane that maximizes the geometric margin $\{x_i y_i\}_{i\ =\ 1}^{\ n}$, ,for a linearly separable dataset. The minimum geometric margin is articulated in equation 6.32

$$y(w, b) \coloneqq \min_{x_{iD}} \frac{|x_i{}^T w + b|}{\|w\|_2} \qquad 6.32$$

The goal expands to finding $(w, b) s.t.$ which separates the data and maximize$\gamma(w, b)$ which is defines as equation 6.33 and the s.t. is defined in equation 6.34

$$\max_{w,b} \gamma(w, b) \qquad 6.33$$

$$S.T\ \forall_{i,} \gamma(w^T, x_2 + b) \geq 0 \qquad 6.34$$

When we plug in the definition of $\gamma(w, b)$ the geometric margin can be summarized as equation 6.35 and 6.36

$$\max_{w,b} \frac{1}{\|w\|_2}\ , \min_{x_2} |w^T x_1 + b) \geq 0 \qquad 6.35$$

$$S.T\ \forall_{2,} \gamma_1(w^T, x_2 + b) \geq 0 \qquad 6.36$$

It is important to note that margin and hyperplane is scale invariant for and (w, b), it can be always be scaled by some constant to have equation 6.37.

$$\min_{x_2} |w^T, x_2 + b| = 1 \qquad 6.37$$

Without the loss of generality, the focus is on (w, b) pairs with $\min_{x_2} |w^T, x_2 + b| = 1$, constrains can be further simplifier to equation 6.38 to 6.40.

$$\min_i \left\| w \right\|_2^2 \qquad 6.38$$

$$S.T\ \forall_{2,} \gamma_1(w^T, x_2 + b) \geq 0 \qquad 6.39$$

$$\min_{x_2} |w^T, x_2 + b| = 1 \qquad 6.40$$

Where $\gamma_1(w^T, x_2 + b) \geq 0$ is an optimal function margin of (w, b) pair, points where $(w^T, x_2 + b) = 1$ are called support vectors.

6.4 Renewable integration

The incorporation of RERs into electrical grids presents considerable challenges related to the reliability and stability of the grid. This integration also affects the operation of protection schemes within networks that experience renewable energy penetration. In this section, the addition of PV systems and wind farms to the grid will be examined to assess the influence of RESs on the efficacy of the established fault detection and classification mechanisms. Critical factors to consider when integrating wind energy into the grid include ensuring stable grid operation, designing effective controllers, and responding appropriately to various operational scenarios. The primary objective of this research is to analyze the effects of grid integration on protection schemes; therefore, the PV and wind farms will be modelled and incorporated into the compensated network. Detailed discussions regarding these models can be found in sections 6.4.1 and 6.4.2. The concepts outlined in Chapter 5 will be utilized and implemented in MATLAB, with references made to relevant equations from that chapter. The system will undergo testing under various fault scenarios to assess its performance in terms of accuracy and response time. The subsequent sections will outline the comprehensive methodology employed to design these systems using MATLAB software.

6.4.1 Generating mechanism

6.4.1.1 PV Module design

The current-voltage (I-V) characteristic shown in figure 6.9, of the modules is derived from the Shockley equation of a diode, while also incorporating additional parameters to more accurately represent the measured data from the PV array. The parameters of PV modules are provided by manufacturers based on Standard Test Conditions (STC), which include a temperature of 25 °C and solar radiation of 1000 W/m². However, these conditions are rarely met in real-world scenarios. Typically, solar radiation falls short of 1000 W/m², and the operating temperature of the cells often exceeds 25 °C. This discrepancy leads to a decrease in the output power of the PV module.

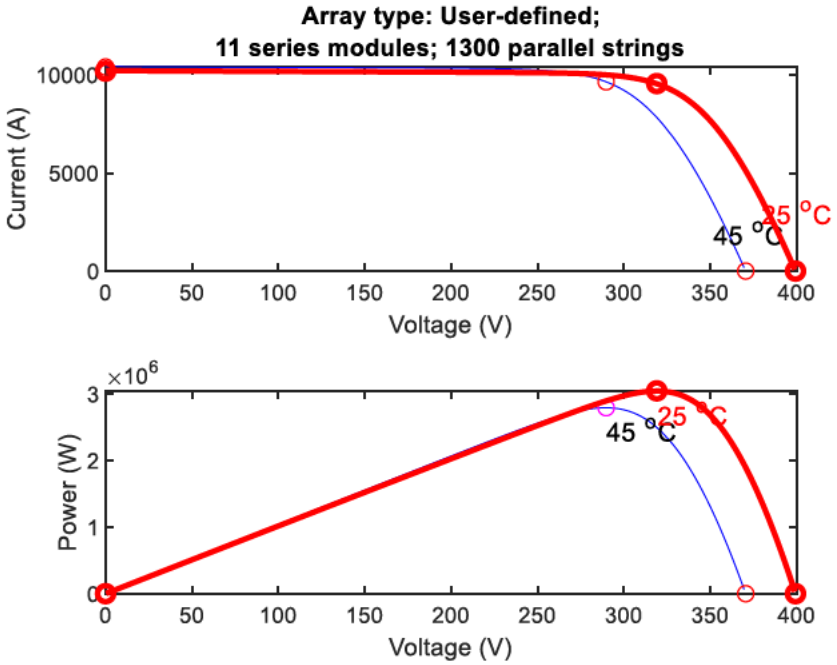

Figure 6. 9 The voltage–current characteristic equation of a solar cell is provided as a module photo-current

6.4.1.2 Wind Turbine design

The Wind Turbine block functions as a model of a wind turbine that converts the kinetic energy of wind into mechanical rotational energy. These turbines harness wind energy to produce electricity. The advancement of wind turbines focuses on enhancing efficiency, reliability, and cost-effectiveness for each unit, while the development of wind farms is concerned with the optimal arrangement of multiple turbines to maximize energy capture. This block can be employed to simulate both individual wind turbines and complete wind farms. It facilitates the examination of turbine performance, electricity generation, and the interactions within a wind farm, as well as the influence of different turbine geometries, configurations, control algorithms, and layout designs on the overall performance and energy output of the wind farm. Users are able to specify the incoming wind velocity and the collective blade pitch as input parameters, with the capability to output the thrust applied to the turbine. Additionally, the effects of thrust and inertia can be integrated into the model. The block can be parameterized using either tabulated power and thrust coefficients or coefficients related to air foil lift and drag. When configured to use tabulated data for power and thrust coefficients, the block calculates the coefficients of power and torque based on the provided tables.

$C_p = tablelookup(\beta_{Ref}, \lambda_{Ref}, C_{p,Ref}, \beta, \lambda_{Smooth}, interpolation = linear, extrapolation = nearest)$

$C_T = tablelookup(\beta_{Ref}, \lambda_{Ref}, C_{T,Ref}, \beta, \lambda_{Smooth}, interpolation = linear, extrapolation = nearest)$

Where the reference pitch angle and tip speed ratio is represented by β_{Ref} and, λ_{Ref} is the respectively. $C_{p,Ref}$ and$C_{T,Ref}$ are the power coefficient table and Thrust coefficient table parameters, respectively, λ_{Smooth} is the smoothed tip speed ratio. Equation 6.41 is used to define the basis of the instantaneous tip speed ratio. Where R is ω is the differential angular velocity and V is the is the incident air velocity on the rotor. This value is the physical signal input port V.

$$\lambda = \frac{R\omega}{V} \quad 6.41$$

The smoothed version of the instantaneous tip speed ratio equation is defined by equation 6.38, where V_{Thr} is the wind velocity threshold parameter, the power and thrust equations are defined by equation 6.42 and 6.44 respectively.

$$\lambda_{Smooth} = \frac{R\omega V}{(V^2 + V^2{}_{Thr})^2} \quad 6.42$$

$$power = \frac{1}{2} C_p \rho A V^3 = T.\omega \quad 6.43$$

$$Thrust = \frac{1}{2} C_r \rho A V^2 \quad 6.44$$

Where ρ represents the air density, A denotes the area of the circle covered by the turbine blades, with A calculated $as\ \pi r^2$. To connect the block parameters to the mechanical power rating of the wind turbine, it is essential to evaluate the turbine's power at the peak power coefficient and the rated wind speed. The rated power is associated with the block parameters as outlined in equation 6.45, whereC_{pmax} signifies the peak power coefficient, the highest value found in the Power coefficient table, $C_P(\beta, \lambda)$. V_{rated} indicates the rated wind speed, which typically ranges from 10 to 15 m/s. Wind turbine controller designs may modify their strategy at this wind speed to ensure the maintenance of rated power.

$$P_{rated} = \frac{1}{2} C_{pmax} \rho A V^2 \quad 6.45$$

Furthermore, the block uses numerically smoothed equations for the thrust, power, and torque, such that they are defined by equations 6.46-6.49. The wind turbine characteristics is shown in figure

$$P = \frac{1}{2} A C_p |V|^3 \quad 6.46$$

$$T_{smooth} = \begin{cases} 0 & if\ \omega < -\omega_{Thr} \\ \frac{P}{\sqrt{\omega^2 + \omega_{Thr}{}^2}} & if \omega > 0 \end{cases} \quad 6.47$$

$$P_{smooth} = T_{smooth}(t) \quad 6.48$$

$$Thrust_{smooth} = \frac{1}{2} C_r \rho A (V^2 + V^2{}_{Thr}) \quad 6.49$$

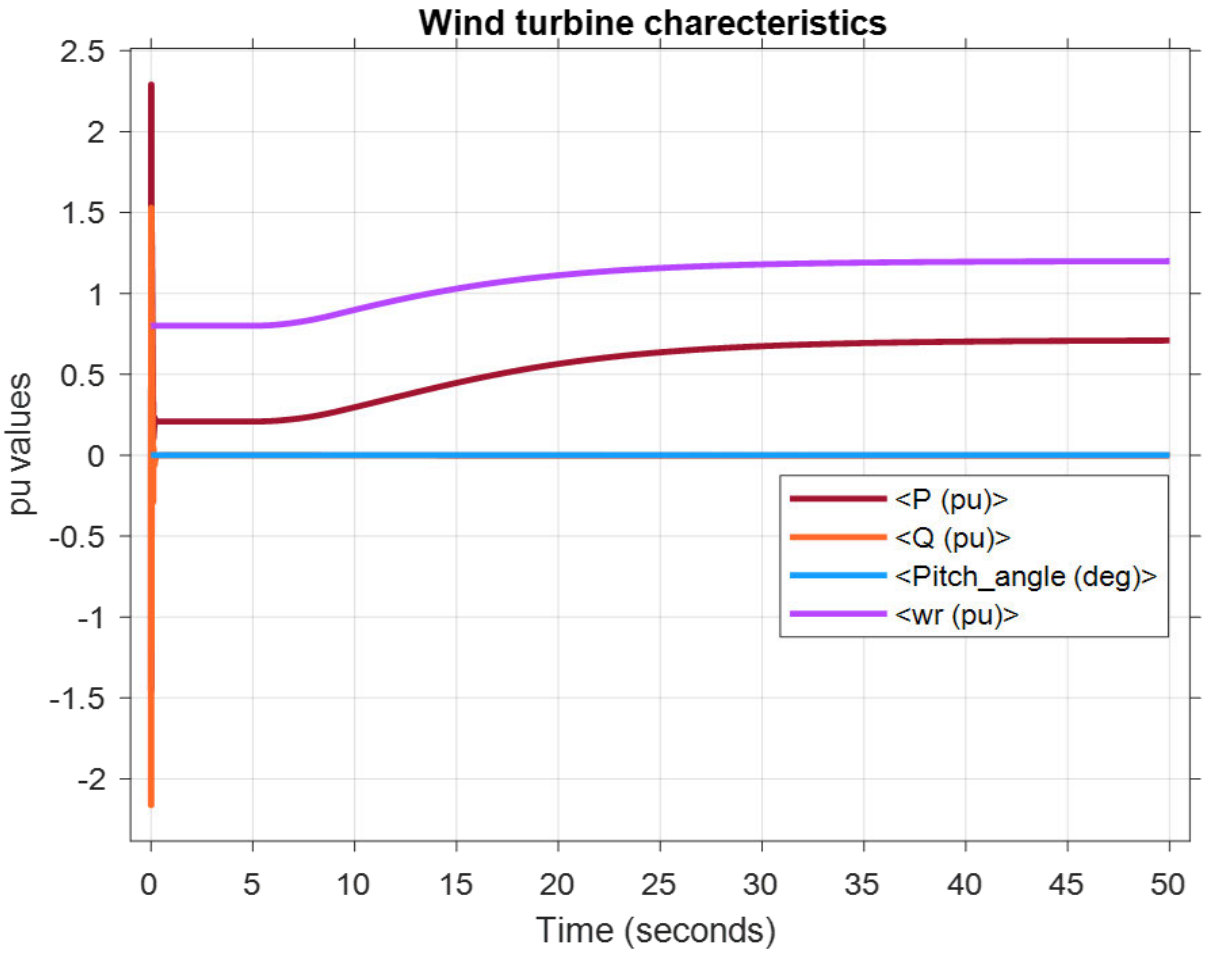

Figure 6. 10 the wind turbine characteristic

The double Fed induction generator (DFIG) shown in figure 6.11 is used, its present numerous benefits, including a lower converter rating, cost-effectiveness, and diminished losses, all contributing to enhanced efficiency. Additionally, they facilitate the straightforward

implementation of power factor correction strategies, support variable speed operation, and provide capabilities for active and reactive power control across four quadrants. The equivalent circuit of a DFIG in a general reference frame that rotates at a synchronous angular speed of ω is illustrated in. The stator and rotor voltages $V_s \; and \; V_R$ in the synchronous reference frame are expressed by equations 6.50 and 6.53 respectively while equations 6.48 and 6.49 represents the flux linkages. while table 6.1 show the specification as implemented in MATLAB.

$$V_s = R_s I_s + \frac{d\omega_s}{dt} + j\omega_s \lambda_s \qquad 6.50$$

$$V_R = R_r I_r + \frac{d\lambda_r}{dt} + j(\omega_s - \omega_r)\lambda_r \qquad 6.51$$

$$\lambda_s = L_s I_s + L_m(I_s + I_r) \qquad 6.52$$

$$\lambda_r = L_r I_r + L_m(I_s + I_r) \qquad 6.53$$

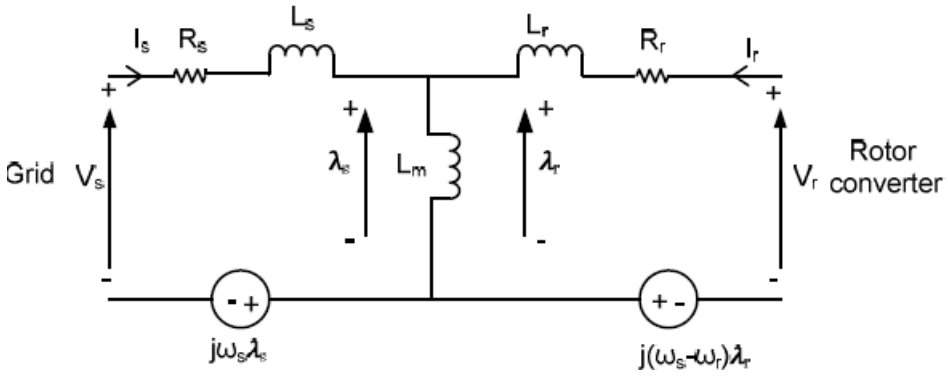

Figure 6. 11 The equivalent circuit of a DFGI

6.4.3 Power conversion circuits

6.4.3.1 PV controller

To develop an effective control system, it is essential to possess an accurate model of the buck-boost converter. This study employs the transfer function model derived from the state-space averaging technique for the buck-boost converter. The open-loop transfer function model of the uncompensated system is formulated based on the mathematical representation of the buck-boost converter, and the controller is designed utilizing frequency domain analysis[219]. The operation of the buck-boost converter circuit can be categorized into two distinct modes: DCM and CCM. he critical value of the inductor, denoted as LC, can

be articulated through Equation 1. When the inductor value L falls below this critical threshold LC, the buck-boost converter operates in DCM. Conversely, if L exceeds LC, the converter functions in CCM. MATLAB scripts have been created to compute the critical values of L and C for both operational modes, grounded in the principles of the buck-boost converter. The critical value of L is determined using Equation 6.54, where T signifies the switching cycle of the transistor Q, as illustrated in figure 6.12.

$$L_c = (1 - DRT) \qquad 6.54$$

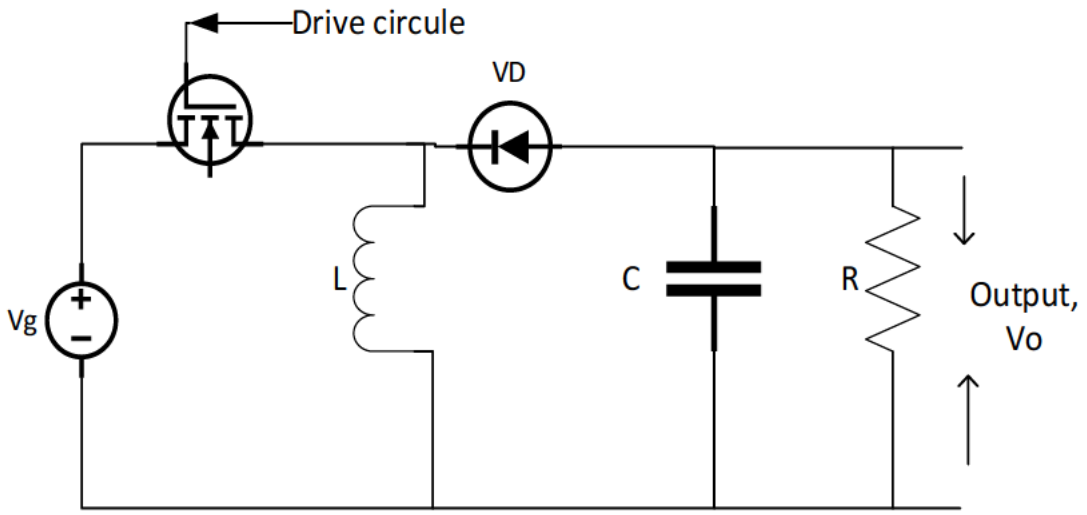

Figure 6. 12 The buck-boost converter configuration

The output voltage is defined by equation 6.56, which enables it to be either lower or higher than the input voltage, contingent upon the duty ratio. Specifically, when the duty ratio (D) is less than 0.5, the output voltage will be lower than the input voltage. Conversely, if D is greater than or equal to 0.5, the output voltage will exceed the input voltage. In this context, V_g represents the input voltage, while α denotes the duty ratio. The Ripple Voltage is computed using equation 6.57.

$$V_o = \frac{D}{1-D} V_g \qquad 6.56$$

$$\frac{\Delta V_o}{V_0} = \frac{DT}{CR} \qquad 6.57$$

In CCM, the operation of a buck-boost converter can be categorized into two distinct phases within each switching cycle. In the first phase, referred to as mode 1, the diode VD is reverse-biased while the transistor Q is activated. Consequently, the input current is directed through the inductor L and the transistor Q, resulting in an increase in the inductor current as energy is stored in the inductor. Simultaneously, the capacitor C provides power to the load R, as

illustrated in Figure 6.13. In the subsequent phase, known as mode 2, the transistor Q is deactivated, allowing the current that was previously flowing through the inductor L to now circulate through L, C, VD, and the load R. During this phase, the inductor continues to play a crucial role in the energy transfer process. Using Middlebrook models the Mode 1 operating is While the switch Q is in open position [219]. Applying Kirchhoff's voltage law (KVL), the inductor current, capacitor voltage are described as equations 6.58 and 6.59 respectively

$$\frac{di_L}{dt} = -i_L \frac{(R_{on}+r_L)}{L} + \frac{V_g}{L} \qquad 6.58$$

$$\frac{dV_c}{dt} = -\frac{V_c}{RC} \qquad 6.59$$

6.4.3.2 Wind controller

The active and reactive power supplied by the DFIG to the grid is regulated through the management of the rotor currents DFIG [220-222].The operation rotor side controller is showing in figure 6.13,

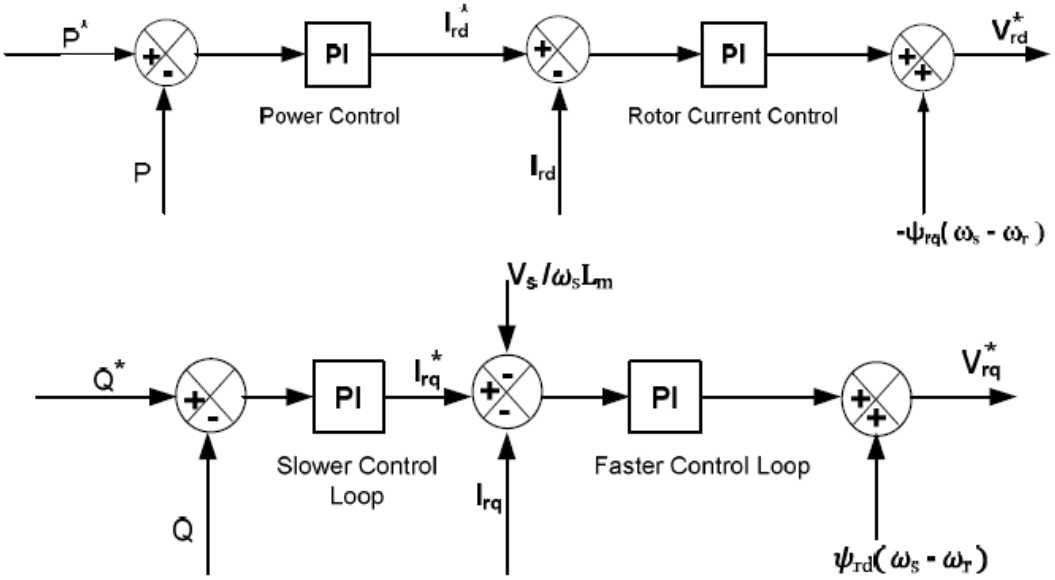

Figure 6. 13 Rotor side controller topology

In the context of Stator Voltage Orientation (SVO), and assuming the resistive voltage drop across the stator is negligible, the active and reactive powers for both the stator and rotor are quantified as equations 6.60 to 6.63, respectively. These equations clearly indicate that the power delivered to the grid can be adjusted by altering the components of the rotor current. Furthermore, the management of these rotor current components can be effectively achieved through the application of vector control methodologies.

$$P_s = 1.5\frac{L_m}{L_s+L_m} * V_{sd}I_{rd} \quad 6.60$$

$$Q_s = 1.5\frac{V_s}{L_s+L_m}(\frac{V_{sd}}{\omega_s} + L_m I_{qr}) \quad 6.61$$

$$P_r = 1.5(V_{rd}I_{rd} + V_{rq}I_{rq}) \quad 6.62$$

$$Q_r = 1.5(V_{rq}I_{rd} + V_{qd}I_{rq}) \quad 6.63$$

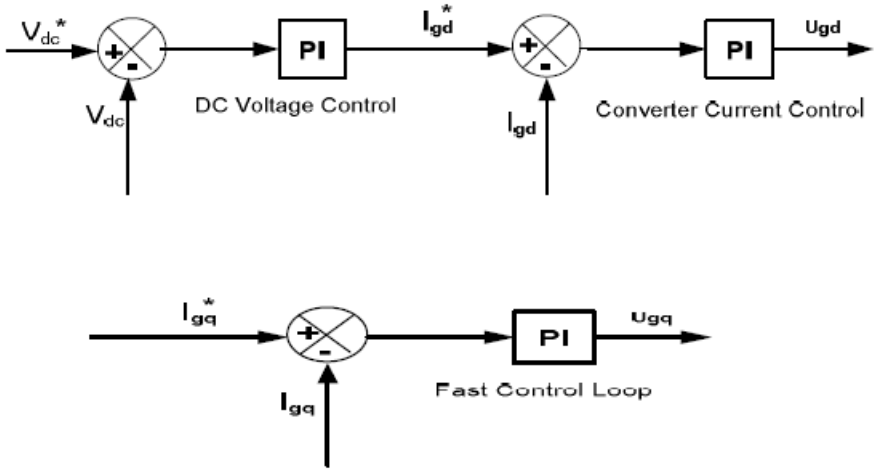

Figure 6. 14 The Grid side converter of a DFIG based wind energy system.

The grid-side converter illustrated in figure 6.14 is engineered to uphold a stable DC link voltage, independent of the direction of power flow from the rotor. To ensure this voltage stability, it is essential to incorporate a bidirectional converter within the rotor side circuit. When the system operates below synchronous speed, this converter acts as a rectifier; conversely, when operating above synchronous speed, it functions as an inverter. This dual functionality guarantees that all power generated is delivered to the grid at a uniform DC link voltage.

6.4.4 Maximum Power Tracking

6.4.4.1 PV

Photovoltaic (PV) power generation is significantly influenced by environmental factors and weather conditions, including solar irradiance and ambient temperature. Due to the reliance on a singular control condition, any variations in the external environment can lead to inaccuracies in the initial response of the converter duty cycle when employing the traditional Maximum Power Point Tracking (MPPT) incremental conductance algorithm, resulting in

erroneous assessments. To enhance the efficiency and cost-effectiveness of PV systems, an advanced incremental conductance algorithm for MPPT control strategy has been implemented[223]. The complete configuration of the MPPT algorithm is illustrated in Figure 6.15 within the MATLAB Simulink environment.

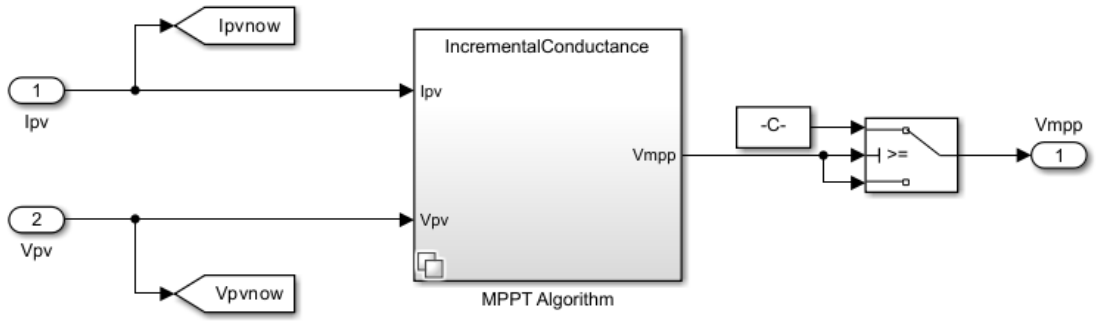

Figure 6. 15 The MPPT algorithm in Simulink

According to [223] the conventional algorithm can be confused when the solar irradiation increases. The authors proposed a new and improved algorithm. The proposed algorithm is shown in the flow chart in figure 6.16. When the irradiance changes, the current and voltage will be affected accordingly. This algorithm thus uses the instantaneous changes of current and voltage of PV modules. This research as adopted this improved algorithm.

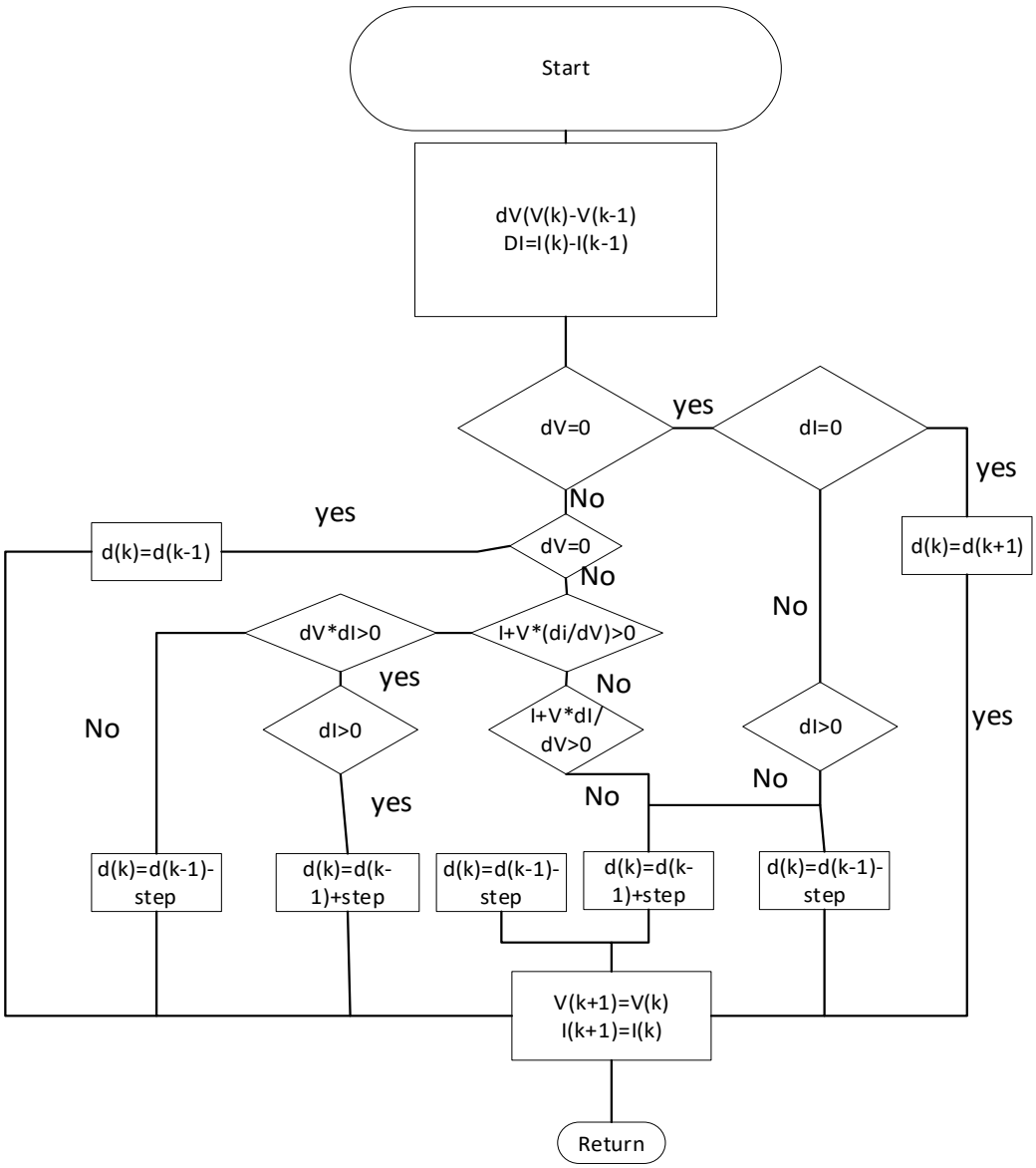

Figure 6. 16 The incremental conductance algorithm for MPPT of a PV system

6.5 Conclusion

In summary the integrated network system as shown in figure 6.17 compromises of a renewable energy intergraded into a compensated line with a series capacitor (TSCS) protected by an MOV. The total renewable energy is 12MW system which compromises of 3MW PV and 9MW Wind system. This final model is implemented in MATLAB and subjected to different faults, voltage and current signals are collected to develop a Machine learning based fault detection and classification scheme as done for a compensated line.

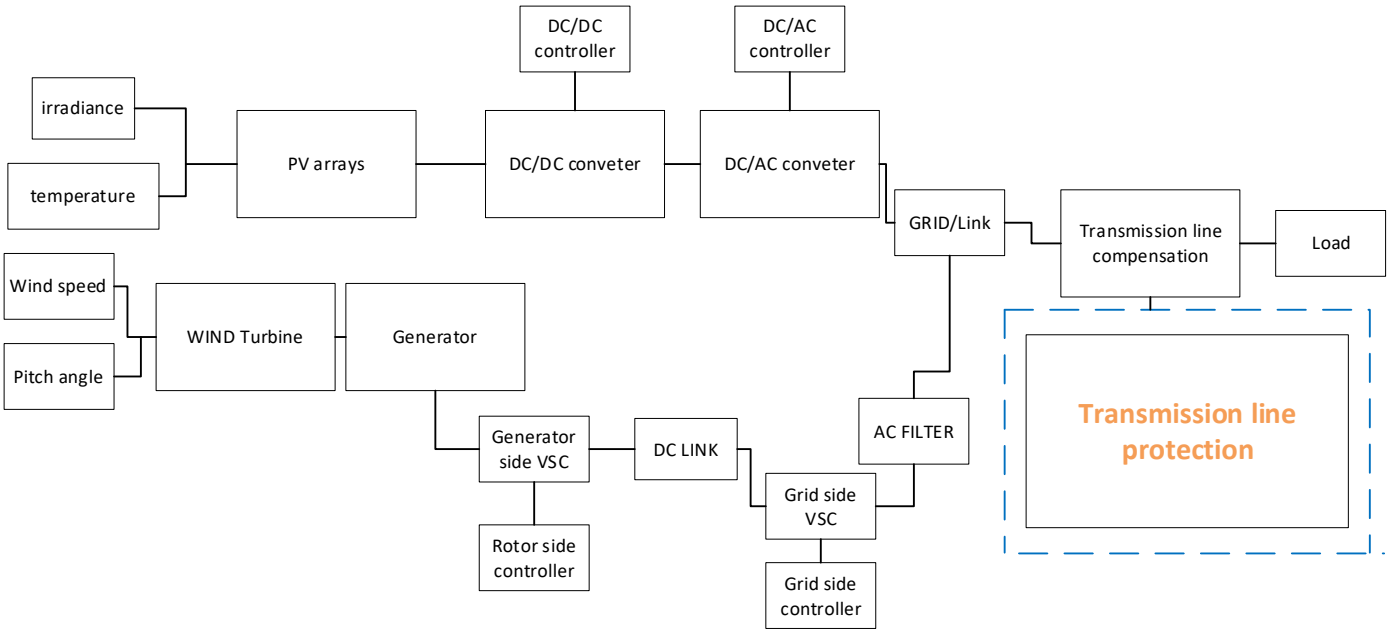

Figure 6. 17 The compete model of Renewable Energy system integrated into a compensated line

Chapter 7 Results and discussions

7.1 The impact of transmission line compensation

The model of a transmission line shown I figure 6.2 is implemented in MATLAB Simulink, with the line parameter in table 6.1. The series compensation model as shown in figure 6.3 is implemented in each phase and the parameters are used as per equation 6.13 to 6.16. This section discussed the results for each model used to investigate the impact of transmission line compensation in the impedance response. Firstly, the results for the compensated network without faults is discussed in order to make reference point. Furthermore, different types of faults are applied to see their impact if the network is uncompensated, and lastly the levels of different compensation are tested to further investigate the impact. The results are discussed in section 7.1.1 to section 7.1.4, while the application of machine learning to assess the impact of transmission line compensation is discussed in section 7.1.5

7.1.1 Normal Network without faults

This section examines the RX response of the compensated network in the absence of a fault. The graph illustrates that as compensation increases, the normal impedance decreases, shifting towards the capacitive region, The capacitive region is characterised by the positive values of the impedance X. Initially, when the network is uncompensated, as shown in Normal graph (3), the reactive impedance is higher, but it diminishes as the level of compensation rises. This trend is evident in Normal impedance (2), which corresponds to a 50% compensation level, and further illustrated by (1), which represents a 100% compensation level. It is crucial to note that the overall impedance perceived by the relay is influenced regardless of whether a fault is present. The Relay may maloperates should the impedance falls within the pre-set impedance zone.

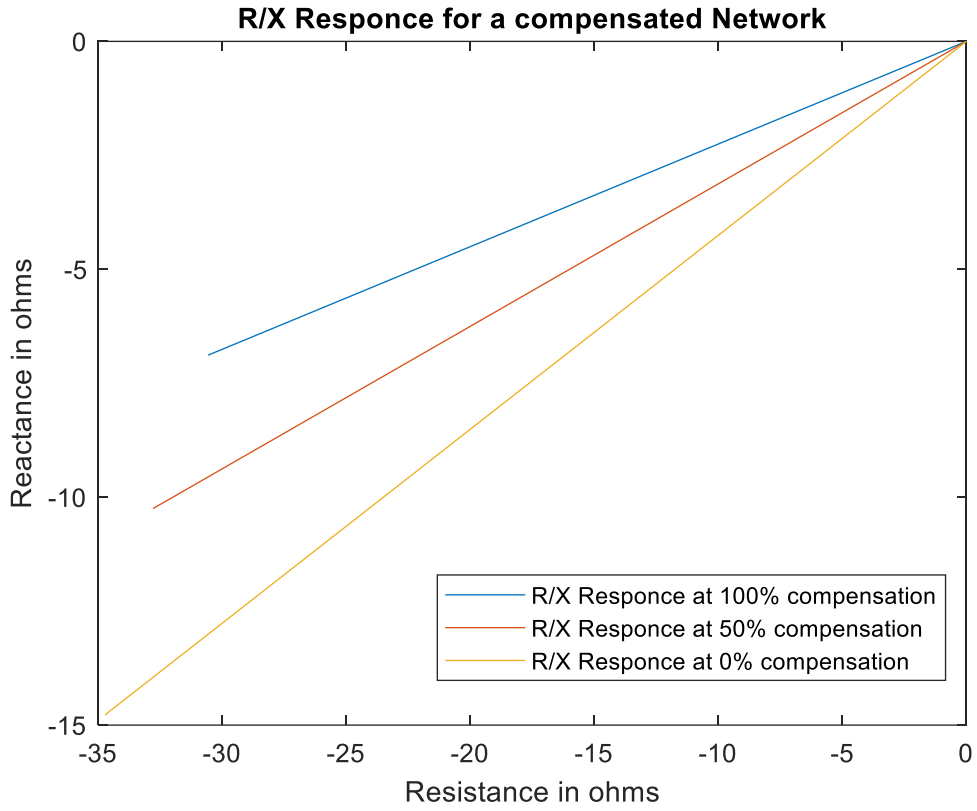

Figure 7. 1 The RX Plane when no fault is applied

7.1.2 Three phase faults (L-L-L) applied to the network

Figure 7.2 (a) illustrates the R/X response of an uncompensated transmission line subjected to a three-phase fault (L-L-L). The data indicates that the reactive impedance ranges from -j60 to j60 ohms, with a primary emphasis on the resistance, which is approximately 30 ohms. Figure 7.2 (b) depicts the impedance response of a compensated network across various compensation levels. To further analyse the effects of transmission line compensation, a comparison of these two graphs is conducted. It is observed that each graph have shifted further into the capacitive region on the R/X plane, with the reactance becoming increasingly inductive as the compensation level rises. The impedance experienced by the relay is associated with the data presented in both graphs a and b. This comparison leads to the conclusion that such changes may result in the maloperation of traditional distance protection relays.

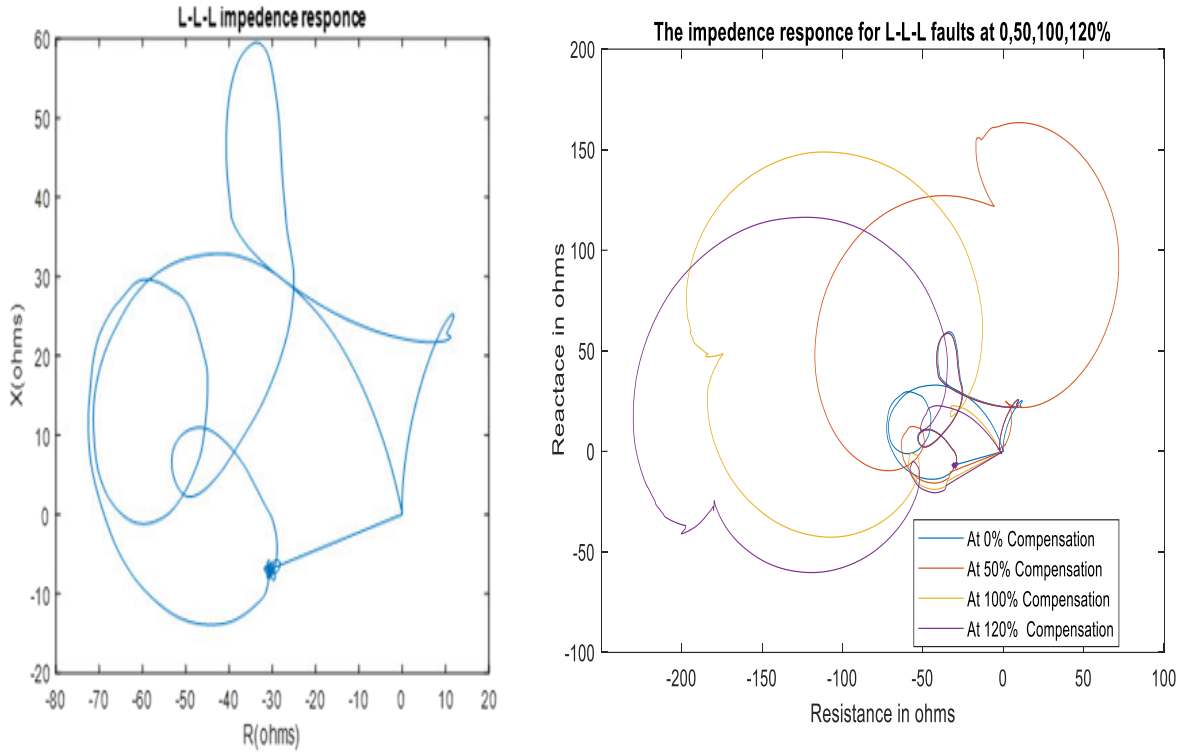

(a) L-L-L response for uncompensated line (b) L-L-L response for a compensated line

Figure 7. 2 The impedance response during a L-L-L fault

7.1.3 Double phase faults (L-L) applied to the network

The impedance response is further examined in the context of a double phase fault, specifically in a line-to-line (LL) scenario, where a notable shift towards the capacitive region is observed. The results for an uncompensated system are illustrated in Figure 7.3(a) while (b) are results for a compensated line at different levels. In this instance, at 100% compensation, the graph exhibits a more capacitive nature, consistent with the observations made in Figure 7.2(b). Additionally, while the resistance perceived by the relay has altered, it can be inferred that the overall impedance is also influenced.

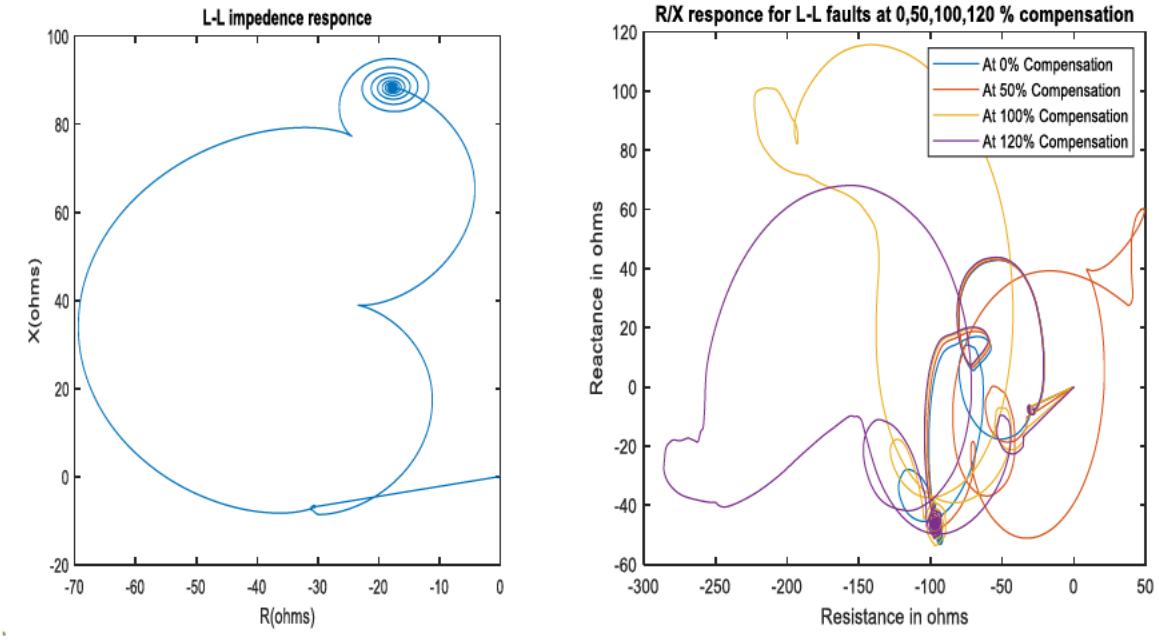

(a) L-L response for uncompensated line (b) L-L response for a compensated line

Figure 7. 3 The Impedance Response for L-G faults

7.1.4 Line to ground fault applied to the network

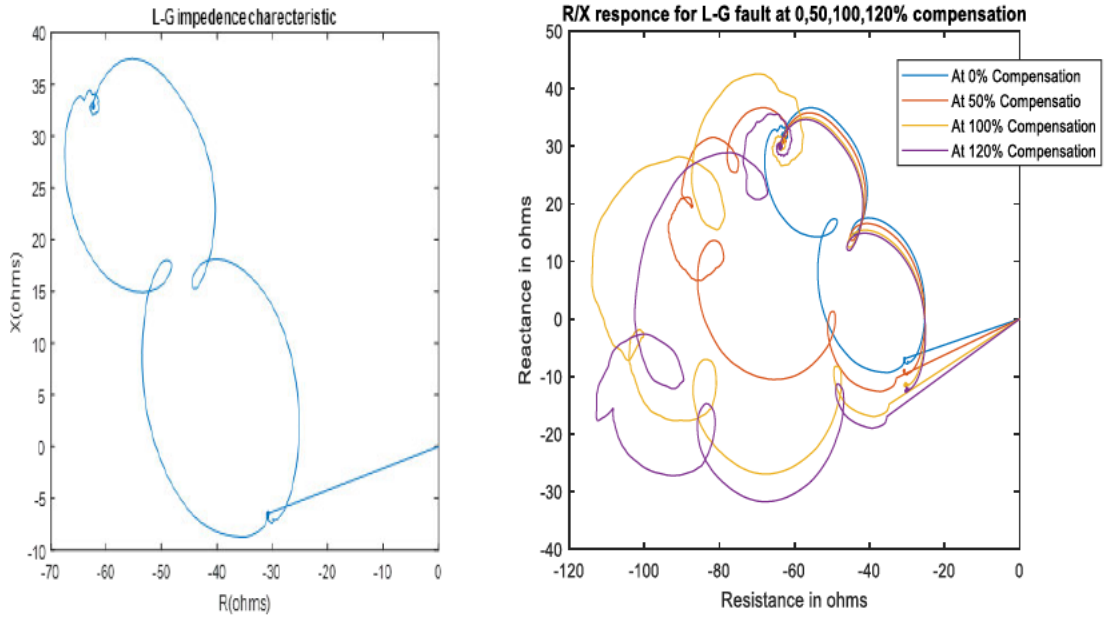

(a) L-G response for uncompensated line (b) L-G response for a compensated line

Figure 7. 4 The impedance response for a L-G Fault

From figure 7.4 (a) and (b) the shift is observed more on the resistance; however the result did shift a bit towards a capacitive region.

7.1.5 Using Machine learning based to analyze the impact of transmission line compensation

The analysis presented in Figure 7.5 illustrates the machine learning evaluation of the effects of a 50% compensated transmission line. The results indicate that the model misclassified 0.1% of instances with no faults, 0.1% for line-to-ground (L-G) faults, 2.6% for line-to-line-to-ground (L-L-G) faults, 0.1% for line-to-line (L-L) faults, 40.8% for line-to-line-to-line (L-L-L) faults, and 59.9 % for line-to-line-to-line-to-ground (L-L-L-G) faults. These findings suggest that the network is predominantly influenced by three-phase faults. In comparison, the performance for other fault types shows slight variations when contrasted with an uncompensated line. At 100% compensation, the network's performance faces additional challenges, as evidenced by the data in Figure 7.5. The misclassification rates at this level of compensation are recorded as 0% for no faults, 0% for L-G faults, 2.6% for L-L-G faults, 0% for L-L faults, 1.2% for L-L-L faults, and 3.4% for L-L-L-G faults.

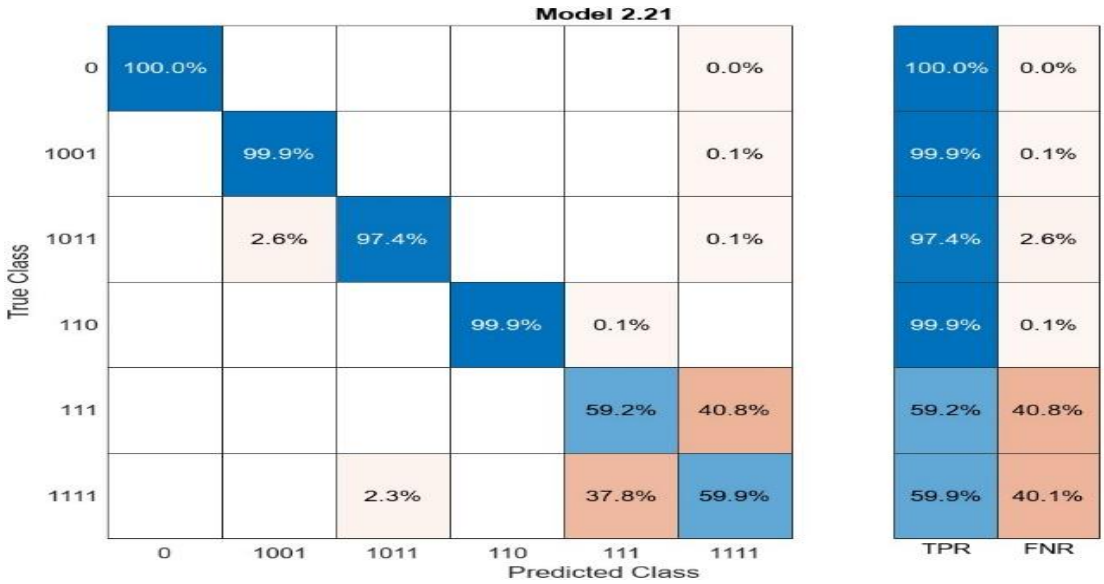

Figure 7. 5 Machine learning analysis of the impact of transmission line for a 50% compensated line

The True Positive Rate (TPR) indicates how often a model correctly predicts positive outcomes, while the False Negative Rate (FNR) represents the percentage of correct predictions for negative outcomes. It is evident with the 40.8% and 59.9% that the network is highly affected with the application of three phase faults The performance of the network is further compromised at full compensation, as illustrated in Figure 7.6. The misclassification

rates are as follows: 0% for no faults, 7.8% for line-to-ground (L-G) faults, 12.9% for line-to-line-to-ground (L-L-G) faults, 8.5% for line-to-line (L-L) faults, 28.2% for line-to-line-to-line (L-L-L) faults, and 86.9% for line-to-line-to-line-to-ground (L-L-L-G) faults.

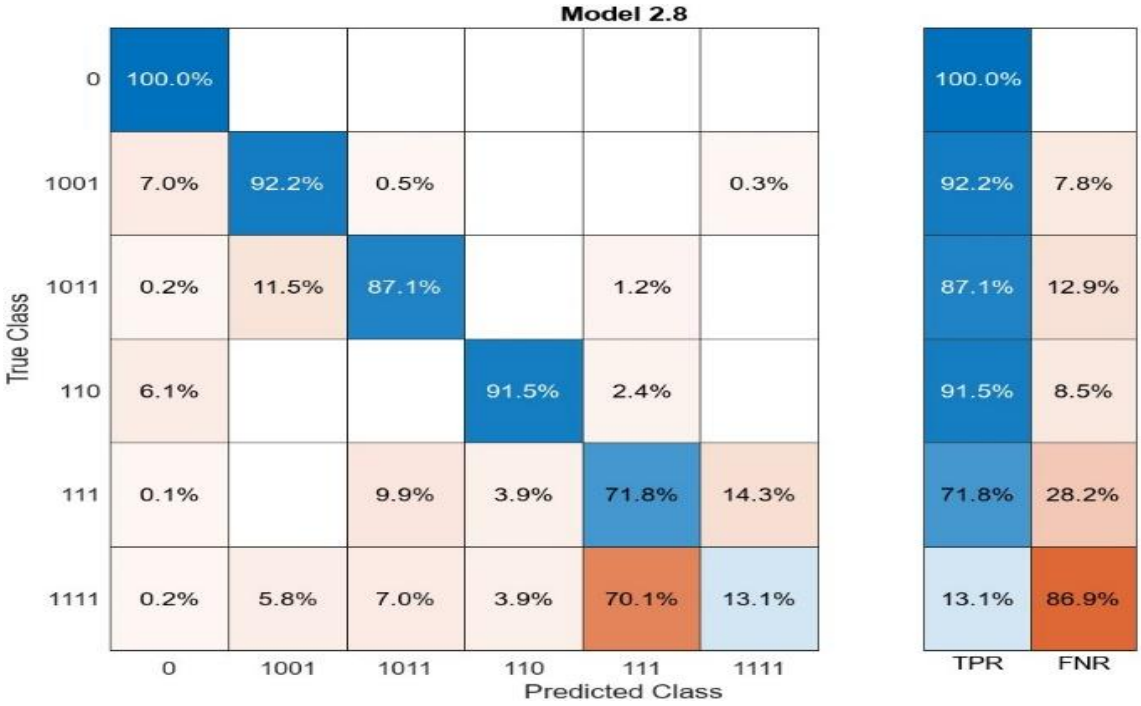

Figure 7. 6 Machine learning analysis of the impact of transmission line for a 100% compensated line

The influence of transmission line compensation on impedance response is analyzed, highlighting its significance in fault detection and classification through machine learning techniques. The findings indicate that the incorporation of capacitive reactance alters the impedance perceived by the relay, thereby affecting its overall performance and accuracy. Consequently, it is advisable for protection engineers to consider these effects when designing protection schemes for such networks.

7.2 Load flow analysis on a 9-bus system

A model of a 9-bus system as developed in section 6.2 is also implemented in MATLAB Simulink, with the compensation between line 4-6. Investigating load flow is essential for the effective planning and maintenance of system stability. Such investigations employ systematic analytical techniques to evaluate various parameters, including bus voltages, phase angles, and the active and reactive power traversing different branches of the load, such as generators and transformers, once a steady state is reached. Load Flow Analysis

represents one such analytical approach. It plays a vital role in planning, economic scheduling, operational efficiency, and the distribution of power among various sources. In this study, load flow analysis is conducted prior to the installation of renewable energy sources, utilizing the Gauss-Seidel Method to assess bus voltages, power angles, active power, and reactive power. While further analyses could be performed, this study is constrained by specific limitations. Figure 7.7 shoes the voltage magnitudes at each bus while figure 7.8 and 7.9 show the active and reactive power respectively.

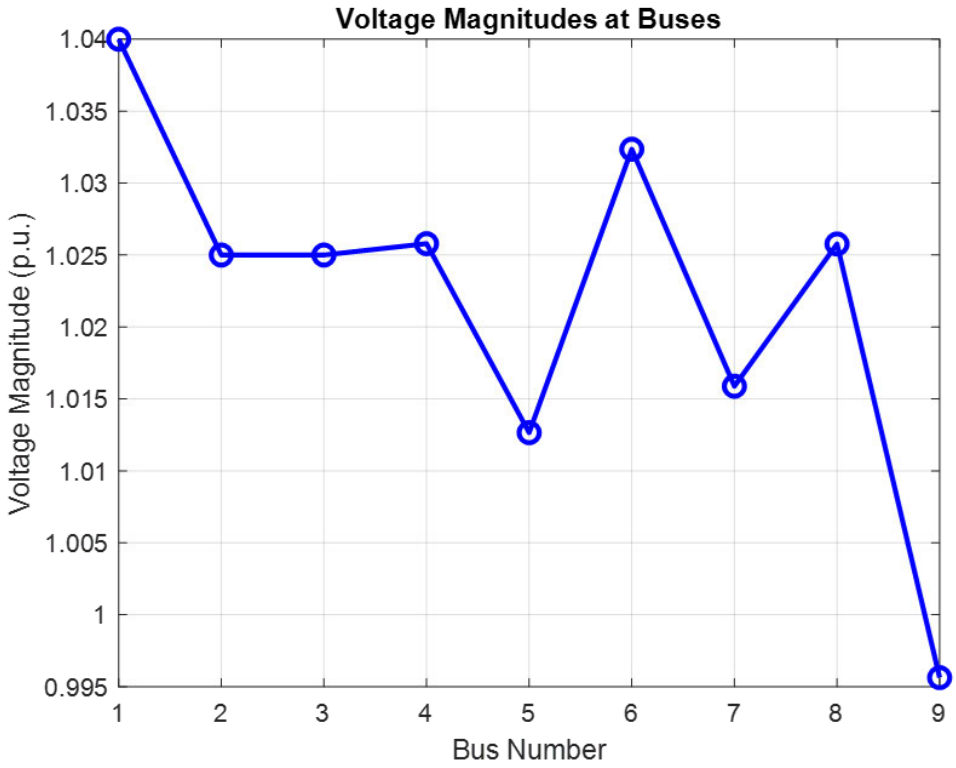

Figure 7. 7 Voltage Magnitudes at all bussed

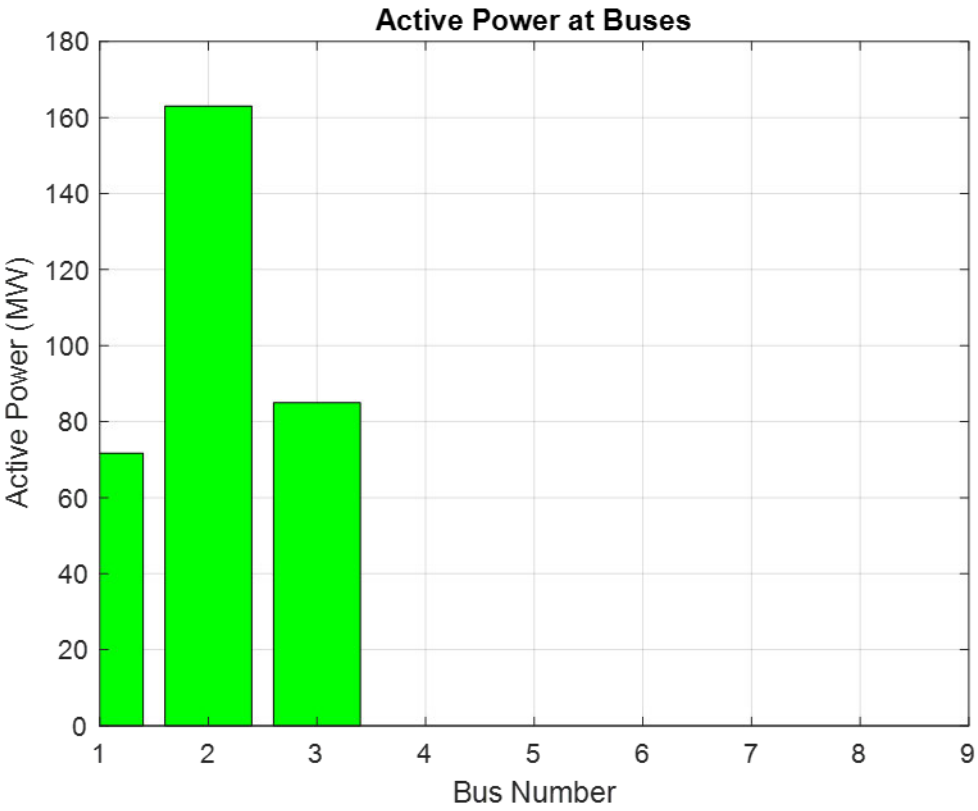

Figure 7. 8 The reactive power at each bus

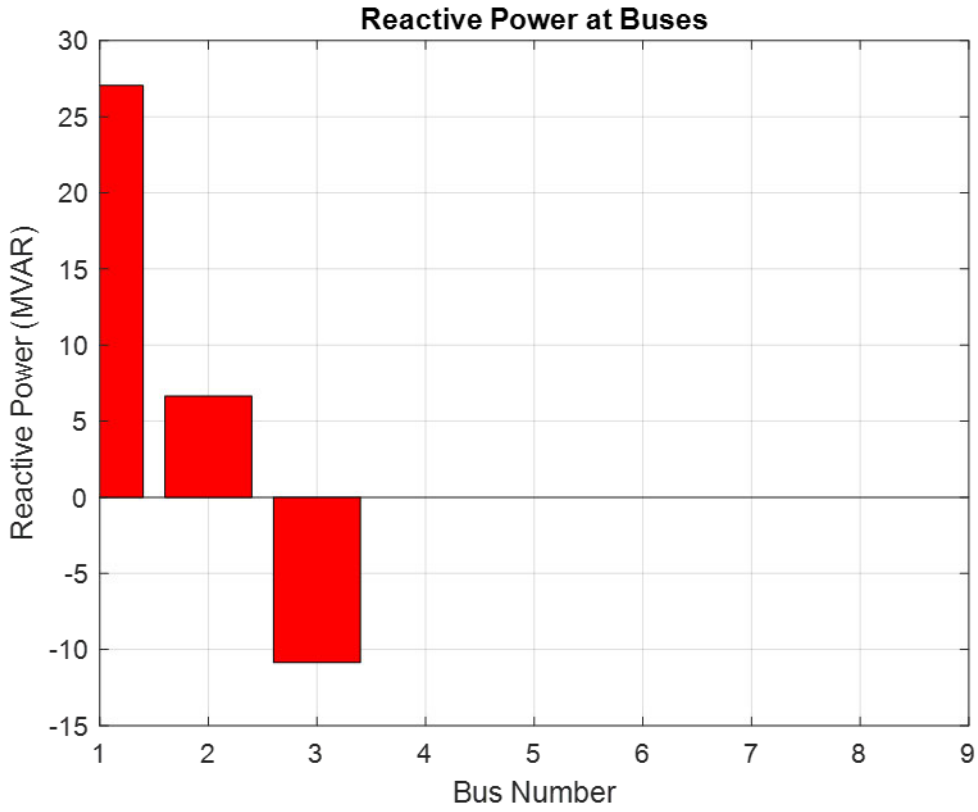

Figure 7. 9 The Reactive power at each bus

7.3 Machine learning fault classification and detection scheme

In this section, as per the discussion in section 6.3.1 the raw voltage and currents data than was selected and prepossessed for the three selected classifiers as discussed in figure 6.8 for testing and validation. The main focus is to investigate the performance of these classifiers in terms of accuracy and speed. It is also important to note that only detection and classification is covered in this study. The performance matrices include confusion matrix, ROC curve and precision recall curve for each model the results are discussed below.

7.3.1 The Compensated Transmission network

Amongst the tested classifier the KNN was the least performing, this classifier has a challenge in classifying three phase faults as evident in figure 7.7 below. The misclassification percentage for the L-L-L faults is 33.9% and for the L-L-L-G faults it is 34.2%, however in can be noted for all other faults the classifier is the best amongst the three. The overall performance of this classifier is 89.9%

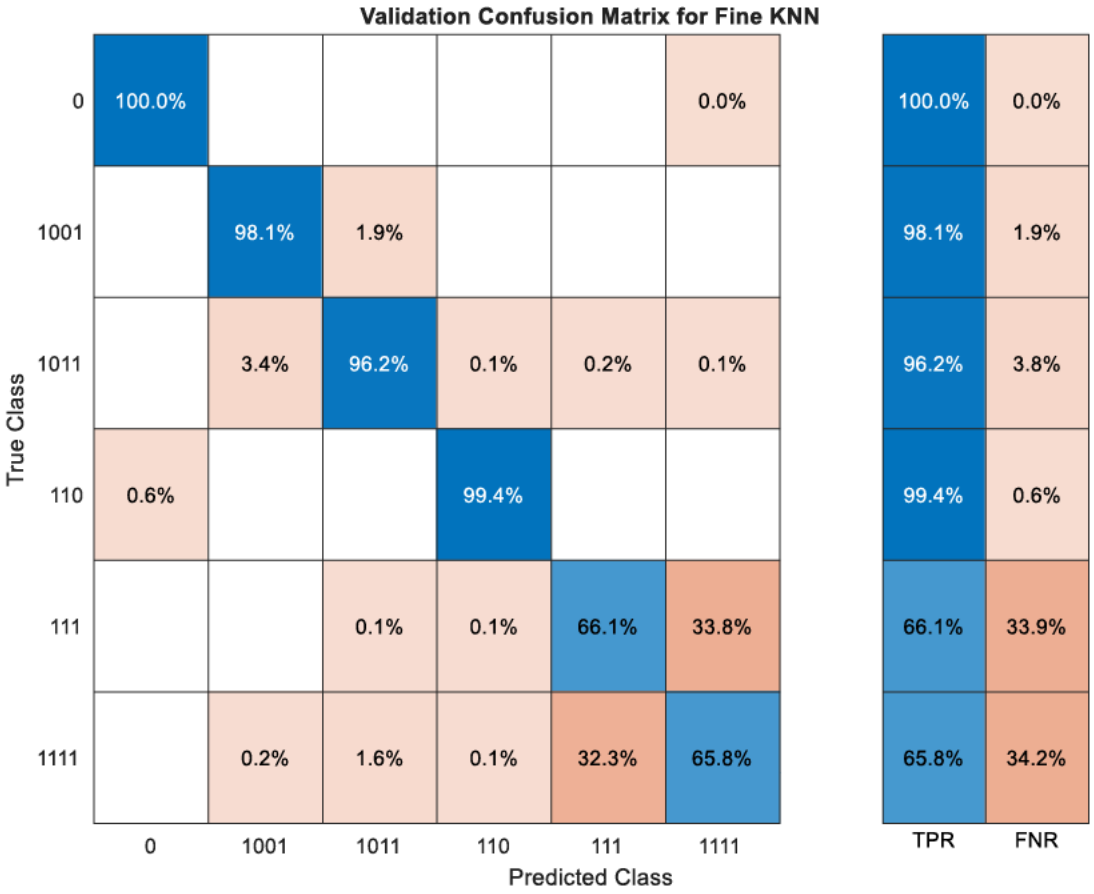

Figure 7. 10 Fine KNN Classification results

The receiver operating characteristic ROC curve illustrates the relationship between the true positive rate (TPR) and the false positive rate (FPR) across various classification score thresholds, as determined by the selected classifier. The Model Operating Point represents the specific false positive rate and true positive rate associated with the threshold employed by the classifier for categorizing an observation. For instance, a false positive rate of 0.1 signifies that the classifier erroneously classifies 10% of the negative class observations as belonging to the positive class. Conversely, a true positive rate of 0.85 indicates that the classifier accurately identifies 85% of the positive class observations as positive. Figure 7.8 shows the ROC curve for a fine KNN classifier while table 7.1. The area under the curve (AUC) represents the integral of the receiver operating characteristic (ROC) curve, specifically the true positive rate (TPR) in relation to the false positive rate (FPR), evaluated from FPR = 0 to FPR = 1. The AUC serves as an indicator of the classifier's overall effectiveness. AUC values range from 0 to 1, with higher values signifying superior classifier performance. It is essential to compare different classes and trained models to assess their performance variations on

the ROC curve. The AUC for this particular classifier is presented in Table 7.1. The results indicate that the classifier continues to face challenges in accurately classifying the three phases

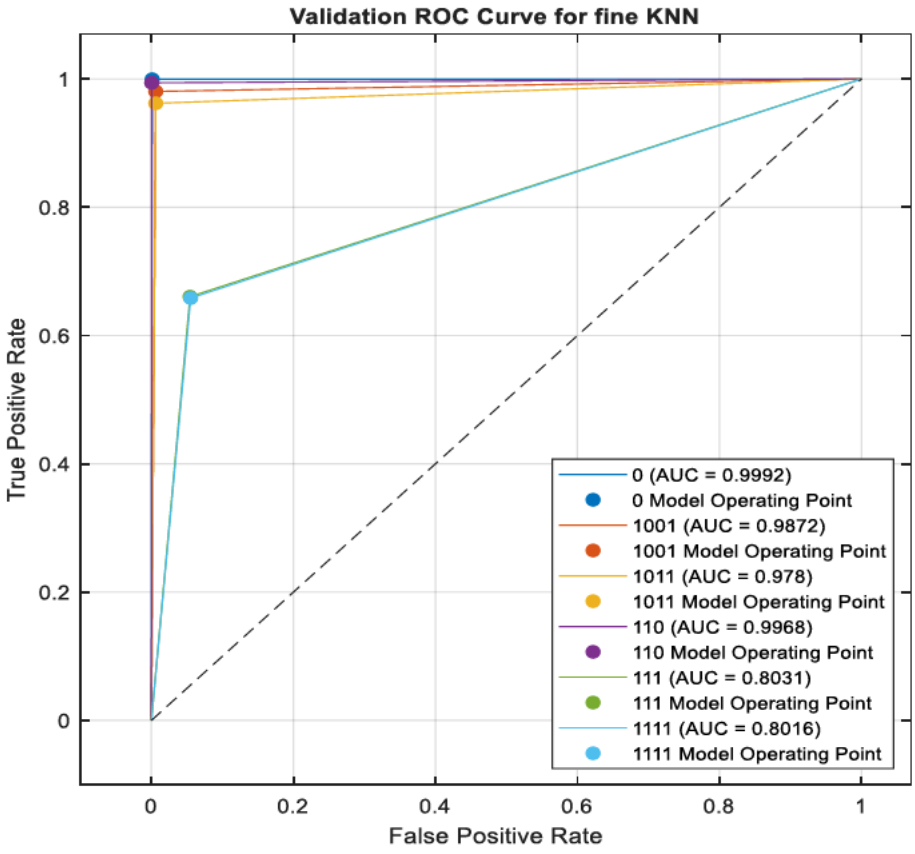

Figure 7. 11 Fine KNN ROC results

The precision-recall curve illustrates the relationship between positive predictive value (precision) and the true positive rate (recall) across various classification score thresholds, as determined by the selected classifier. The Model Operating Point represents the precision and true positive rate (TPR) associated with the threshold employed by the classifier for categorizing an observation. For instance, a precision of 0.85 signifies that 85% of the instances identified as positive are indeed true positives. Similarly, a true positive rate of 0.85 indicates that the classifier accurately classifies 85% of the observations belonging to the positive class. Figure 7.9 shows the Precession recall for a KNN) it is still evident that the performance of this classifier is challenged during three phase faults.

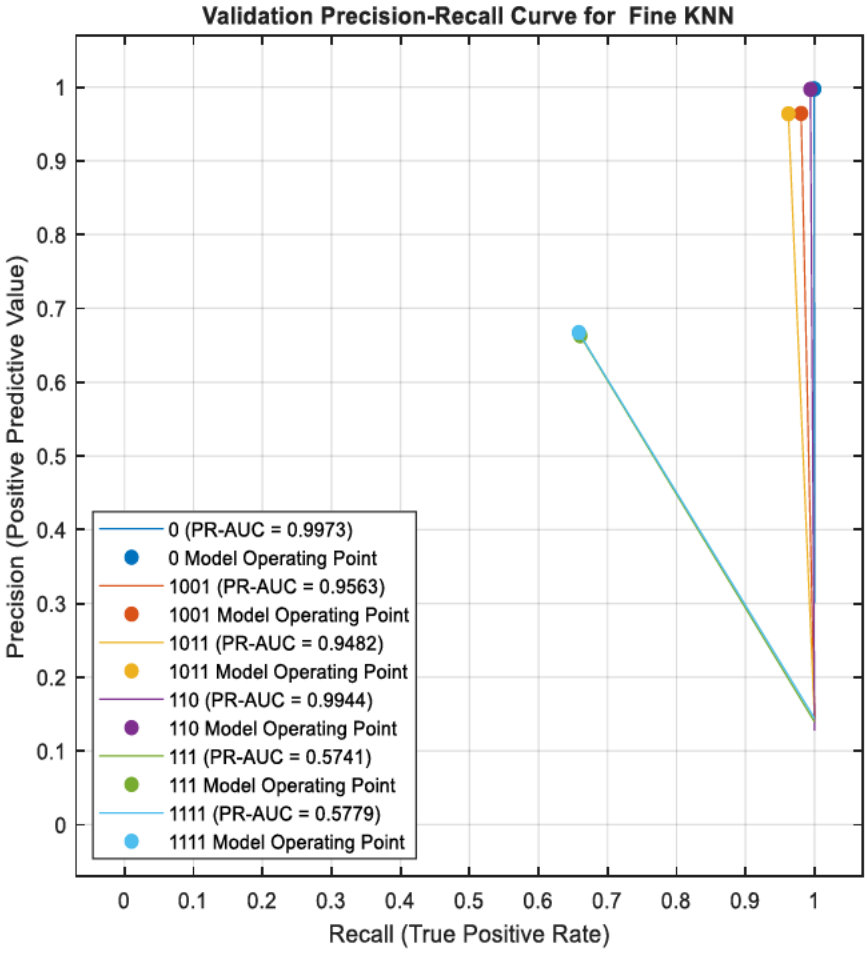

Figure 7. 12 Fine KNN precision-recall curve

The second classifier that demonstrated superior performance was the Medium Neural Network (MNN) classifier, achieving an overall accuracy of 93.4%. Nevertheless, in the context of single and double phase faults, the K-Nearest Neighbours (KNN) classifier surpassed the MNN. Performance results for the MNN are illustrated in Figures 7.8 through 7.10. Notably, Figure 7.8 indicates a significant enhancement in Precision Rate (PR) and False Negative Rate (FNR), particularly concerning the three-phase fault, which was a critical issue identified with the first classifier. The accuracy has dropped from 33.9% to 3.5% on three phase faults and from 34.2% to 56%.

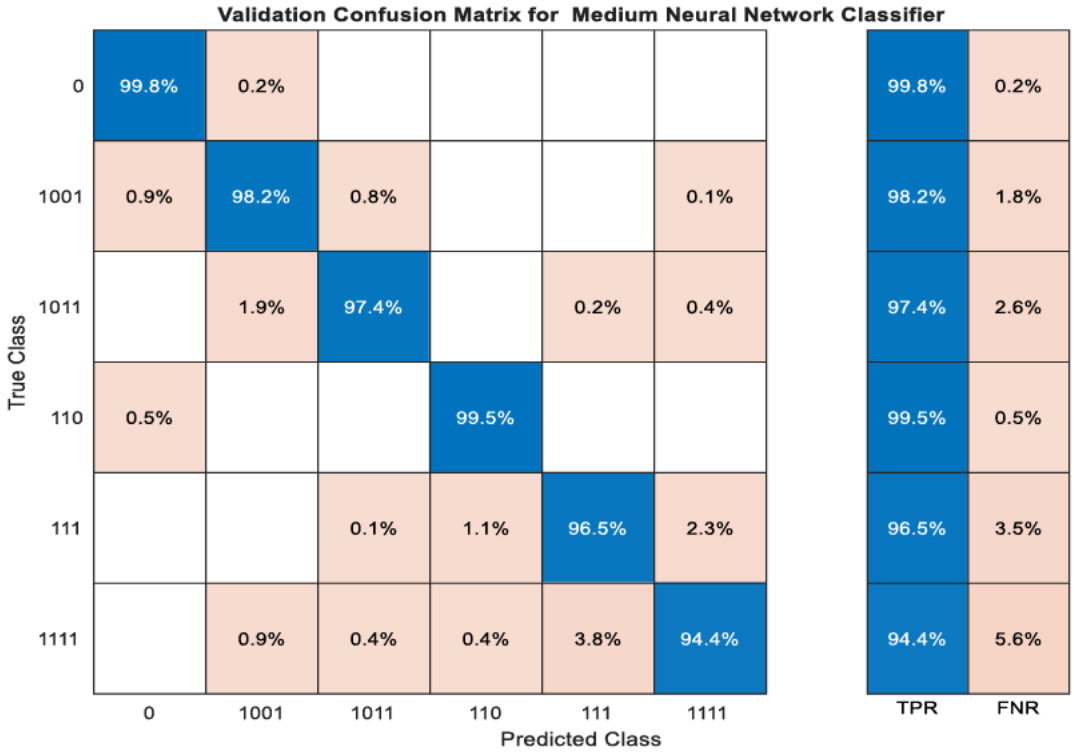

Figure 7. 13 MNN Classification results

Figure 7.11 presents the ROC curve for an MNN classifier, highlighting a significant improvement in the model's operating point for both L-L-L and L-L-L-G faults, with increases from 0.5741 to 0.8015 and from 0.5779 to 0.8031, respectively. Additionally, Figure 7.2 depicts the precision-recall metrics for the MNN classifier, further indicating that its performance surpasses that of the K-NN classifier

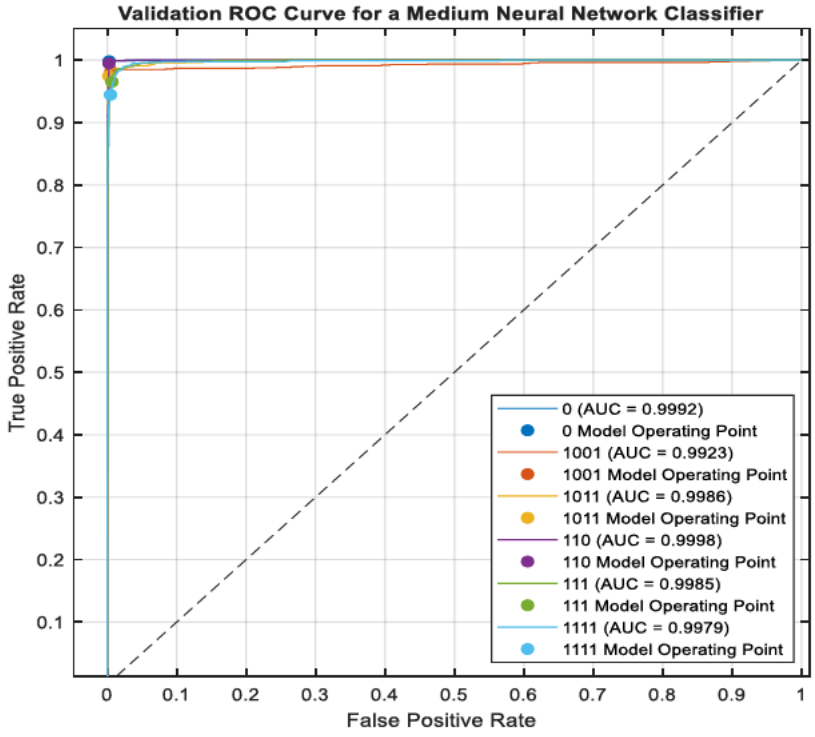

Figure 7. 14 MNN classifier ROC curve

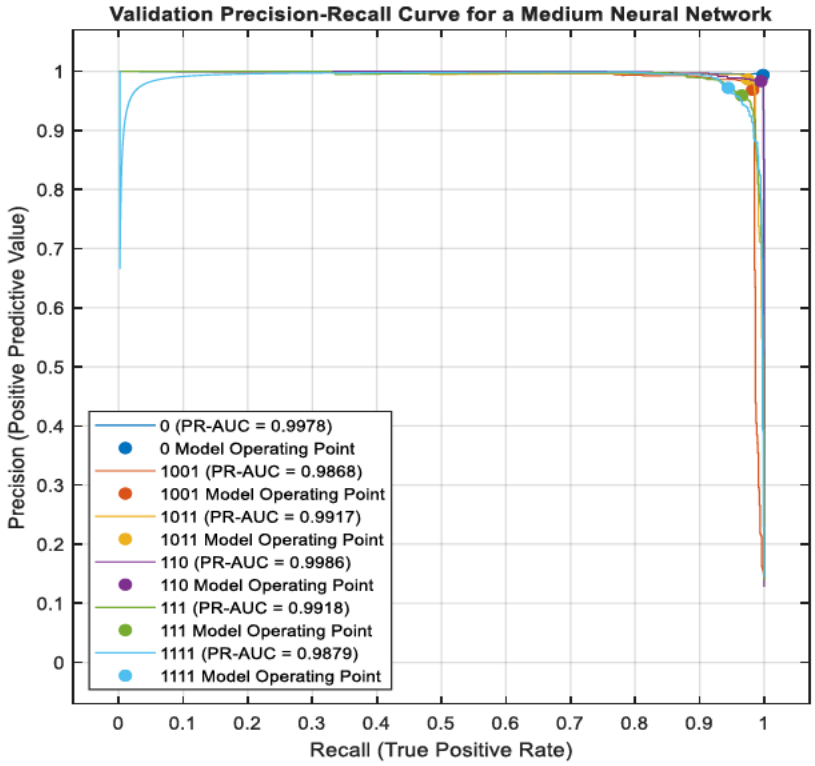

Figure 7. 15 MNN Precision recall curve

In figure 7.13 the accuracy performance of a T quadratic Support Vector Machine (SVM)is shown. This classifier emerged as the most effective classifier, achieving a perfect accuracy of 100% for both line-to-ground (L-G) and line-to-line (L-L) faults. In contrast, it recorded 1.2% for line-to-line-to-line (L-L-L) faults and 1.3% for line-to-line-to-line-to-ground (L-L-L-G) faults in the context of three-phase faults. When compared to the Multi-Layer Neural Network (MNN), which achieved a misclassification of 1.2% and 1.8% for these fault types, the K-Nearest Neighbours (KNN) classifier demonstrated superior performance specifically for L-L-G faults. Overall, the quadratic SVM attained a performance rate of 99.3%. Additionally, the ROC and Precision-recall Curve QSVM is shown in figure 7.16 and 7.17 respectively. This shows an improve overall performance for the SQVM classifier as compared to the two previous classifiers. This is also observed in the all performance indexes.

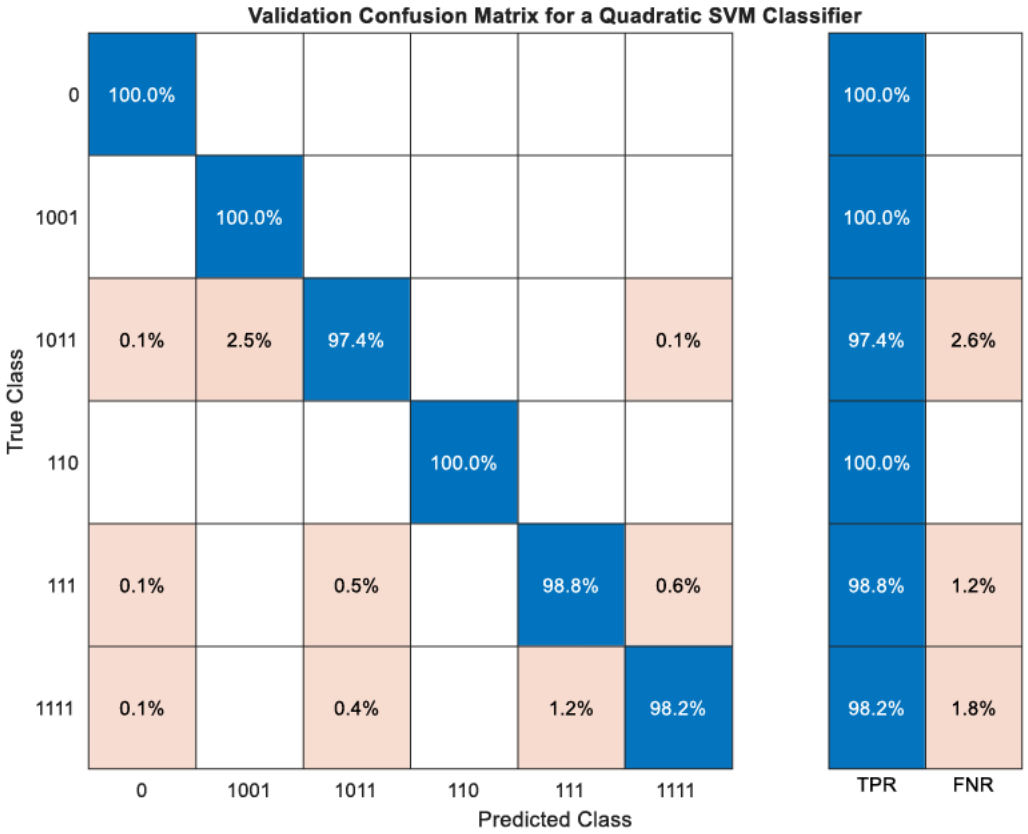

Figure 7. 16 QSVM Classification results

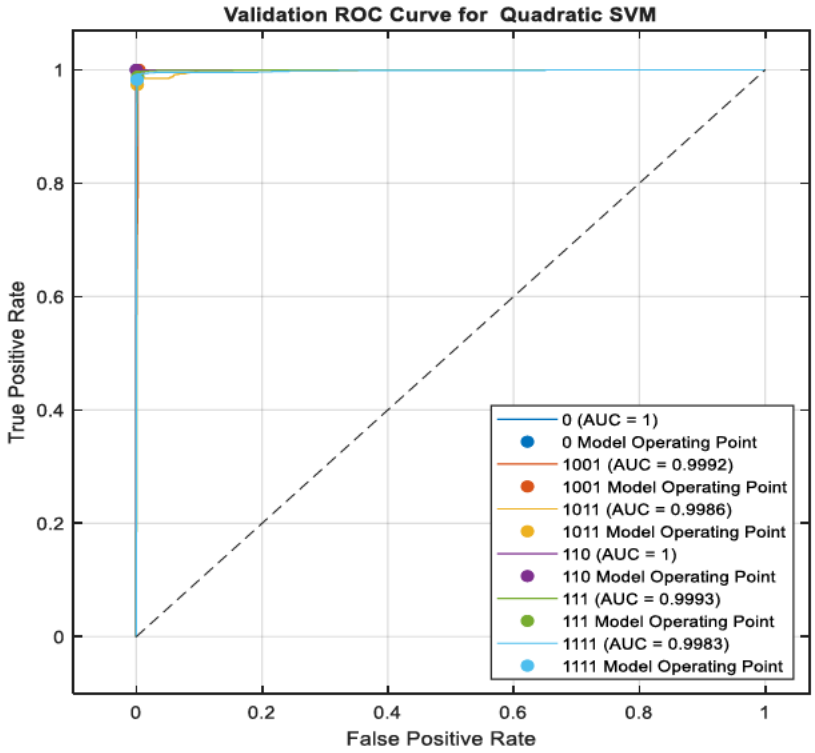

Figure 7. 17 QSVM ROC curve

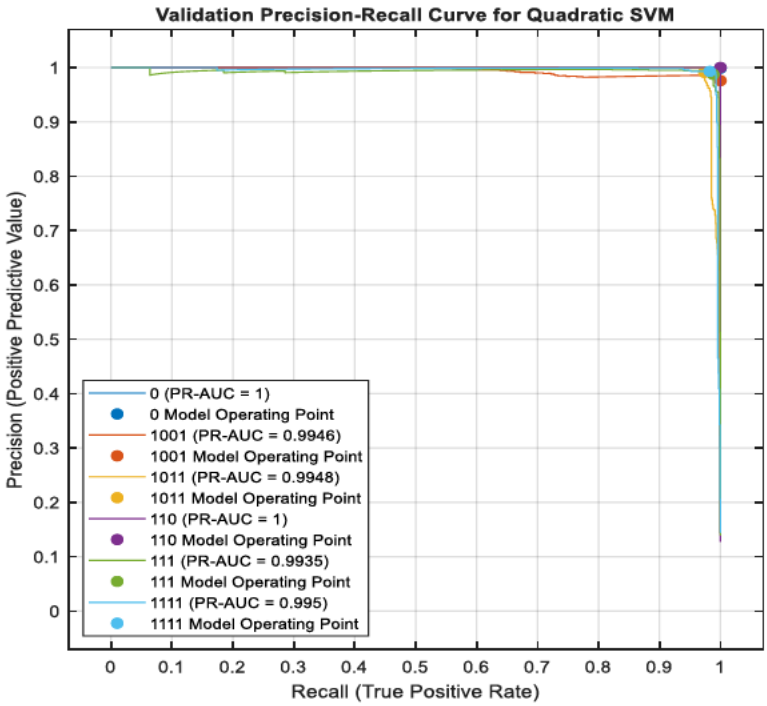

Figure 7. 18 QSVM Precision-recall curve

7.3.2 Performance summary

This research investigated the potential of employing machine learning technologies to tackle challenges within protection schemes, particularly concerning compensated transmission lines. While transmission line compensation presents an opportunity to enhance energy availability, the nonlinear characteristics of the devices used pose significant challenges for protection schemes. Therefore, it is essential to explore the application of machine learning techniques to address fault detection and classification issues in compensated transmission lines. Each classifier exhibits both strengths and weaknesses; for instance, the fine KNN classifier achieves a lower overall accuracy of 88.9%, yet it is particularly affected by three-phase faults while performing well for other fault types. This limitation was addressed in the SQVM classifier. The summary of three classifiers is presented in table 7.1 below. Future research endeavors could focus on developing a fault location scheme based on machine learning, as well as testing various system dynamics such as power swings, among other considerations. The graphical representation comparing three classifiers is shown in figure 7.17 and 18 Respectively. In figure 7.18 the speed of these classifiers is compared.

Table 7. 1 performance comparison of classifier for a compensated network

classifier	No-Fault	L-G	L-L-G	L-L	L-L-L	L-L-L-G
Fine KNN	100	98.1	97.9	99.4	33.9	34.2
MNN	99.8	98.2	97.4	99.6	96.5	94.4
SQVM	100	100	97.4	100	98.8	98.2

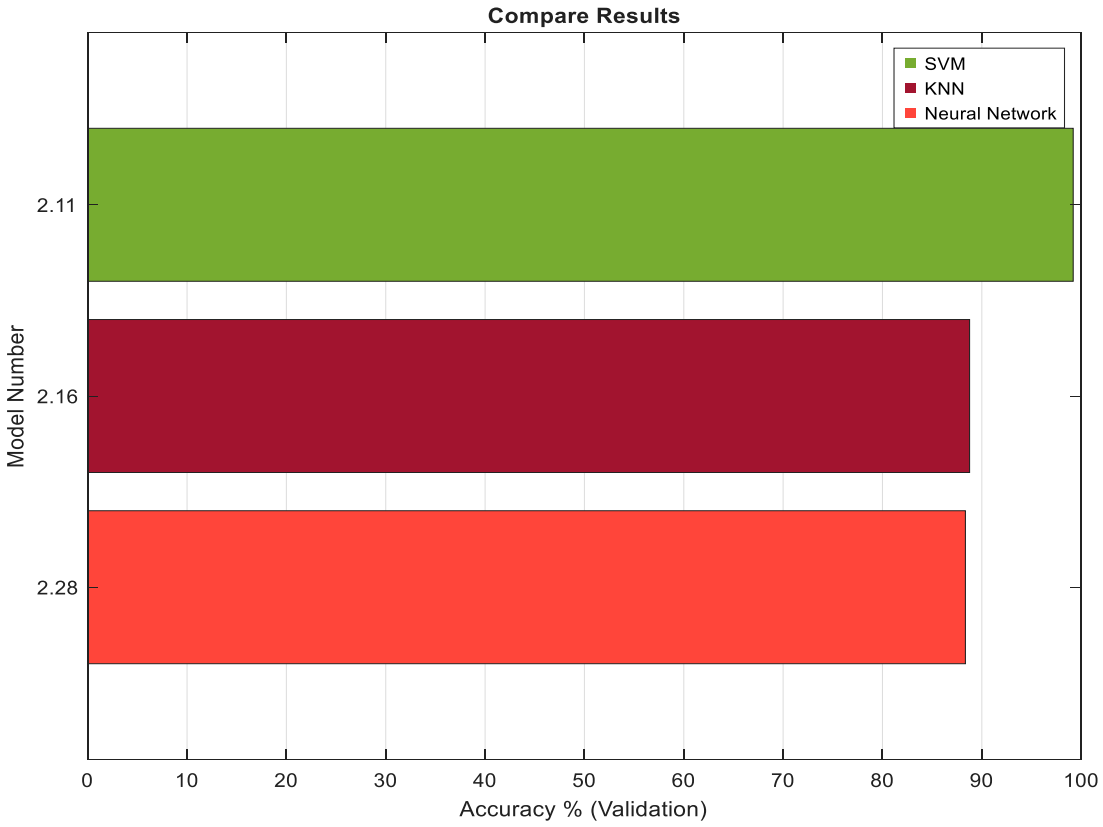

Figure 7. 19 Accuracy comparison for three classifiers

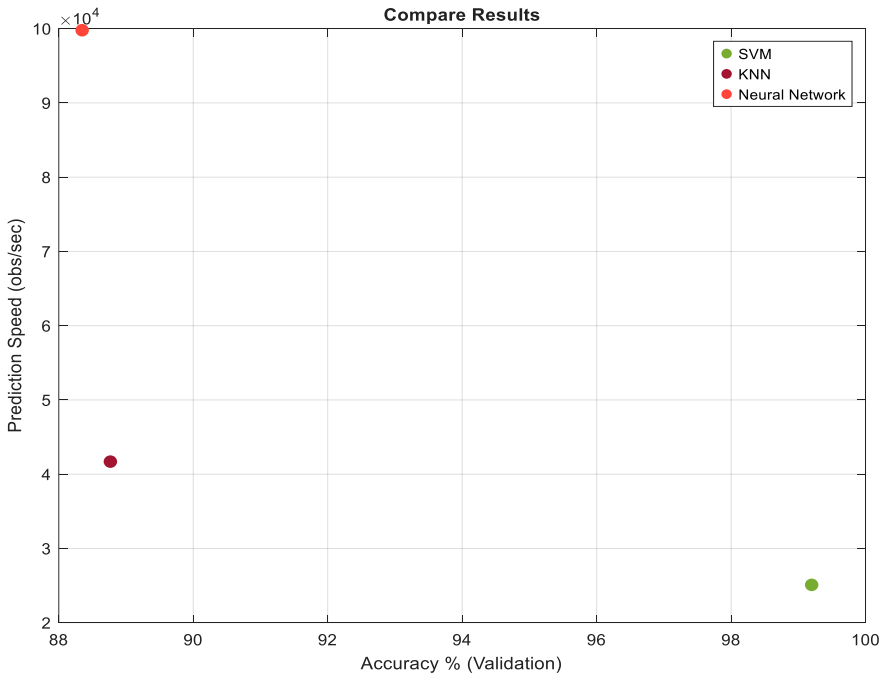

Figure 7. 20 Prediction speed comparison for three classifiers

7.4 The impact of renewable energy integration

7.4.1 Power output

The models of Wind and PV modelled in chapter 5Renewable energy sources were added into a compensated transmission line, the total power is 12MW which compromises of 3MW PV and 9M wind energy. Figure 7.18 shows the V-I and V-P characteristic of the integrated PV system. Figure 7.19 shows the output reactive active power of the wind energy conversion system (WECS) while the active power is shown for figure 7.20. it is important to note that the performance of converters is not discussed in this report, however it was important to show the intergraded power into the compensated network. Each system was developed and tested individually and later integrated to the compensated line.

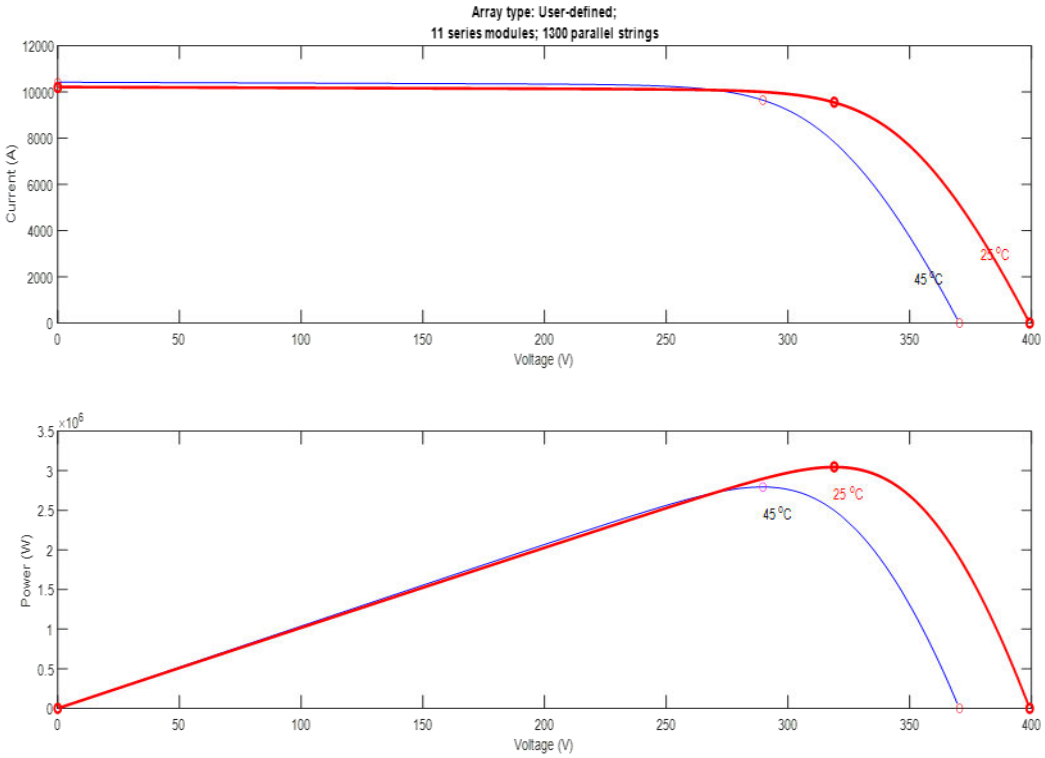

Figure 7. 21 The output power curve of a PV energy system

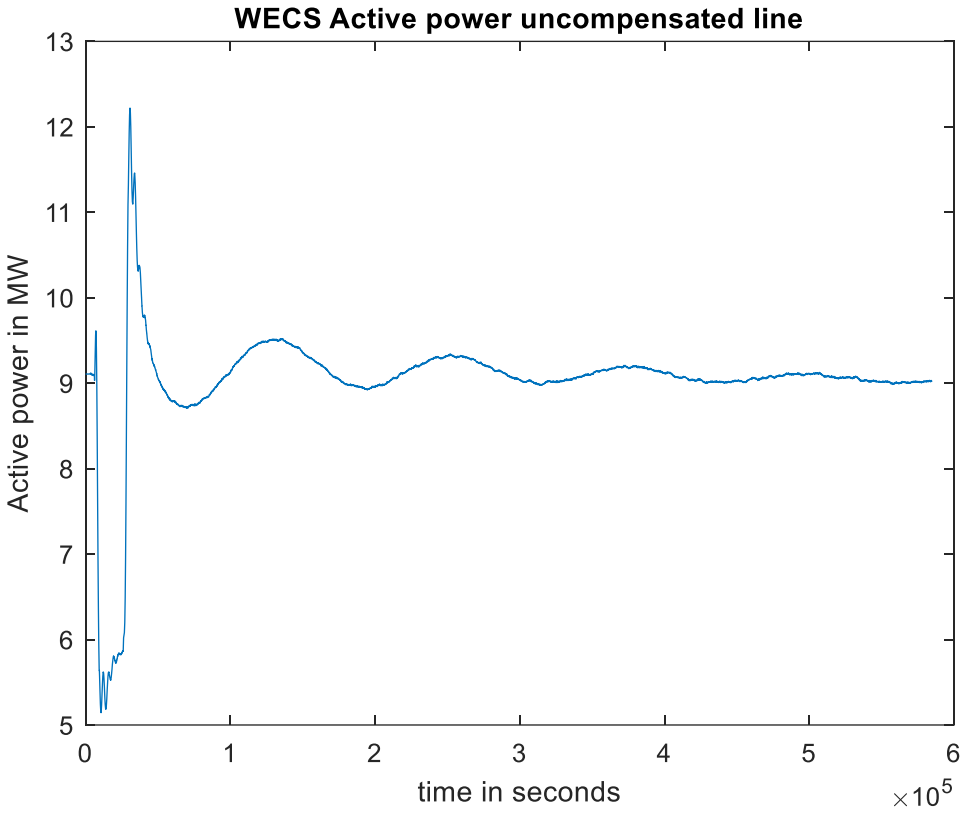

Figure 7. 22 The output active Power of Wind Energy conversion system (WECS)

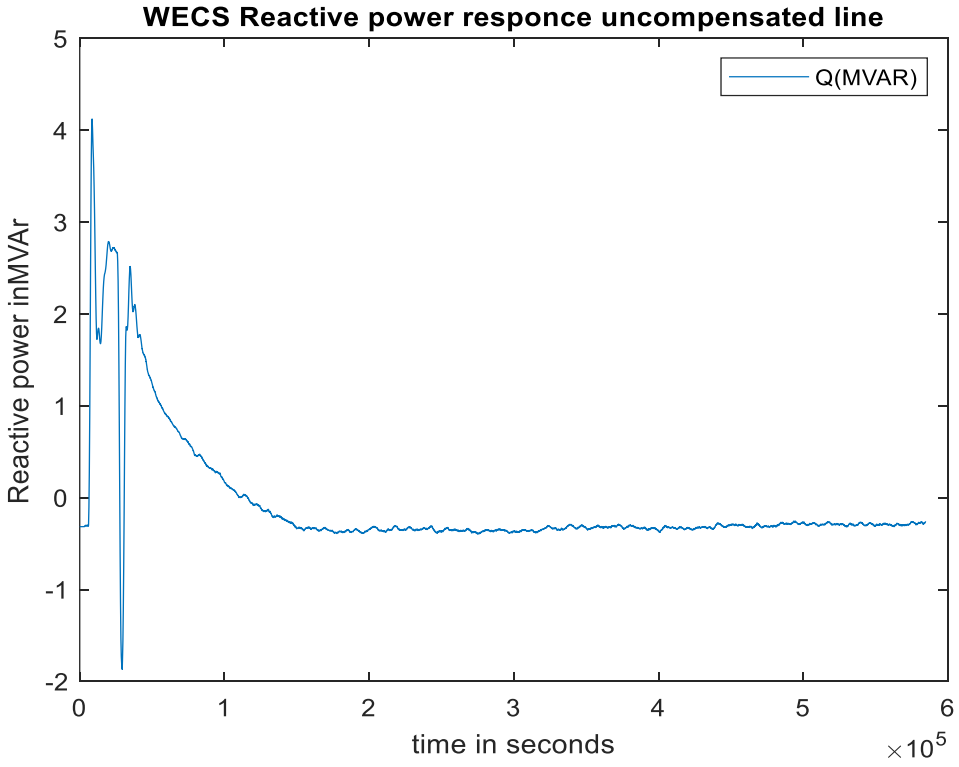

Figure 7. 23 The output Reactive Power of Wind Energy conversion system (WECS)

7.4.2 Detection and Classification Schemes with Renewable energy integrated

The three classifiers discussed in section 7.3 are assessed in the context of integrating renewable energy into the network. An initial analysis is performed to evaluate the impact of this integration on the developed models. The classifiers undergo optimization to improve the overall performance with the renewable energy integrated. The SQVM is chosen for its proven effectiveness in the compensated network before the introduction of renewable energy. Figure 17.21 illustrates the classification outcomes of a K-NN Classifier following the addition of 12MW of renewable energy to the previous model (Compensated Transmission Line). A comparison for the performance of the K-NN classifier is simplified in table 7.2. Furthermore, the ROC curve is shown in figure 7.22. while the comparison is on table 7.3.

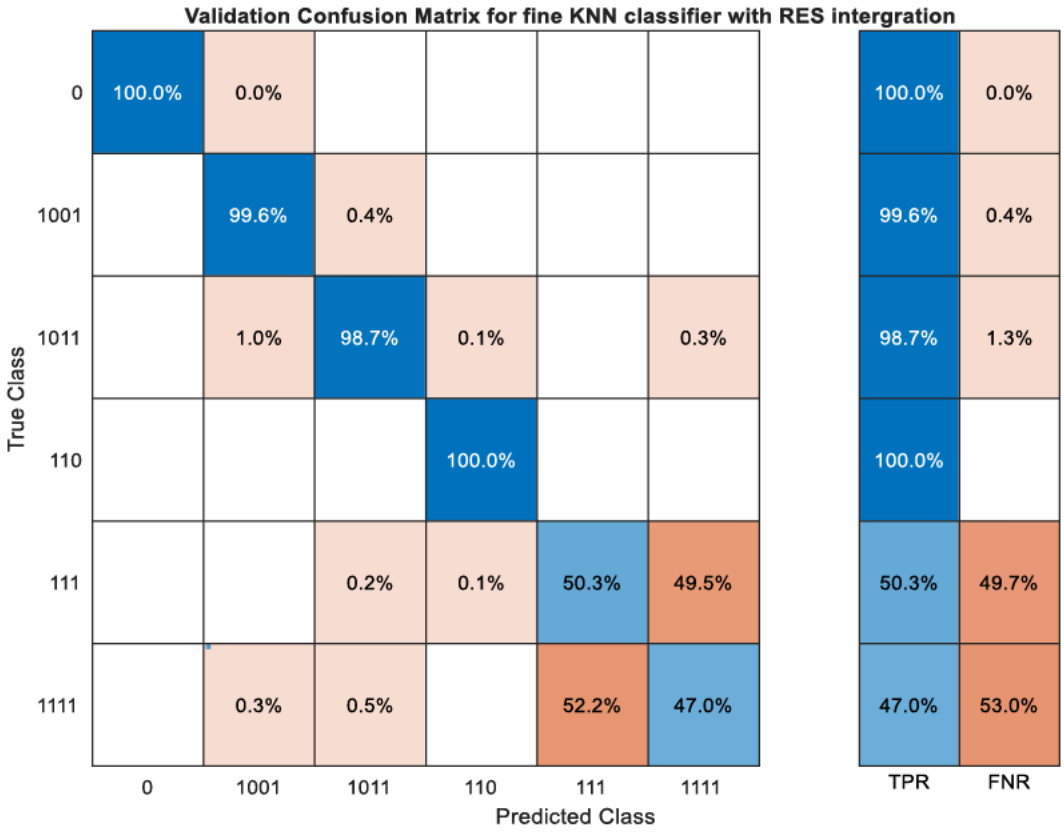

Figure 7. 24 The Classification results of K-NN classifier with Res integrated

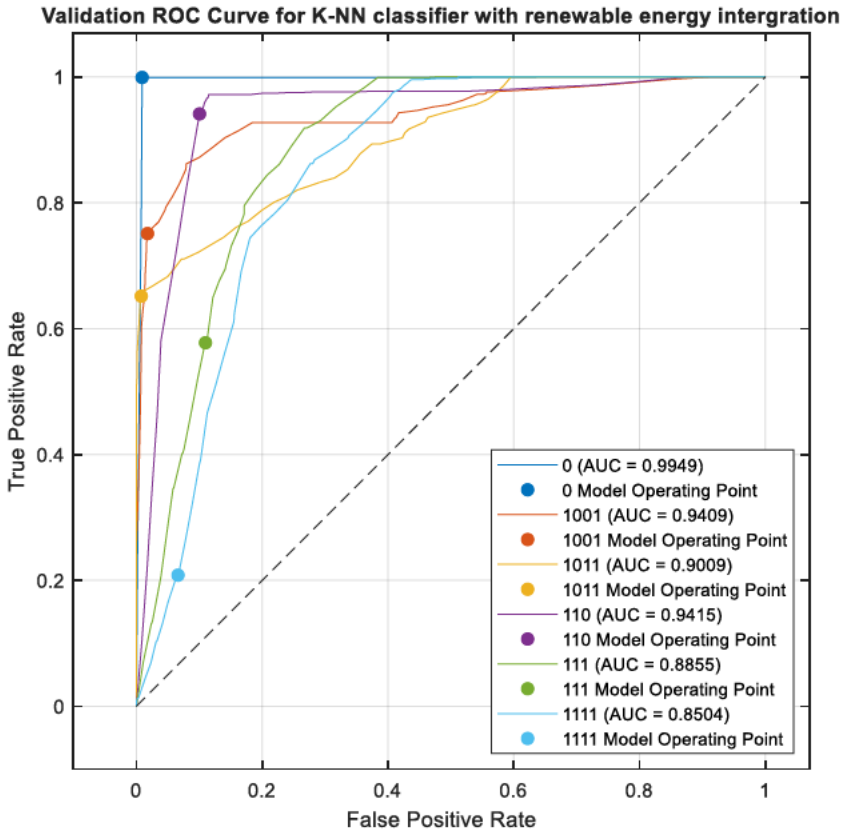

Figure 7. 25 The ROC curve of K-NN classifier with RES integrated

Table 7. 2 Comparison of Classification results for a K-NN classifier

Network	No-Fault	L-G	L-L	L-L	L-L-L	L-L-L-G
No RES	100	98.1	96.2	99.4	66.1	65.8
With RES	100	99.6	98.7	100	50.7	47.0

Table 7. 3 Comparison of ROC curve results for K-NN Classifier

Network	No-Fault	L-G	L-L	L-L	L-L-L	L-L-L-G
No RES	0.9992	0.9872	0.9780	0.9968	0.8031	0.8016
With RES	0.9949	0.9409	0.9009	0.9415	0.8855	0.8504

Figure 7.23 illustrates the classification outcomes of an MNN classifier following the addition of 12MW of renewable energy to the previous model (Compensated Transmission Line). A comparison for the performance MNN classifier is simplified in table 7.4. Furthermore, the ROC curve is shown in figure 7.24. while the comparison is on table 7.5.

Table 7. 4 Comparison of Classification results for an MNN classifier

Network	No-Fault	L-G	L-L	L-L	L-L-L	L-L-L-G
No RES	99.8	98.2	97.4	99.5	96.5	94.4
With RES	100	99.7	98.9	100	80.7	80

Table 7. 5 Comparison of ROC curve results for MNN Classifier

Network	No-Fault	L-G	L-L	L-L	L-L-L	L-L-L-G
No RES	0.9978	0.9923	0.9986	0.9998	0.9985	0.9979
With RES	0.9962	0.9804	0.9794	0.9847	0.9042	0.8747

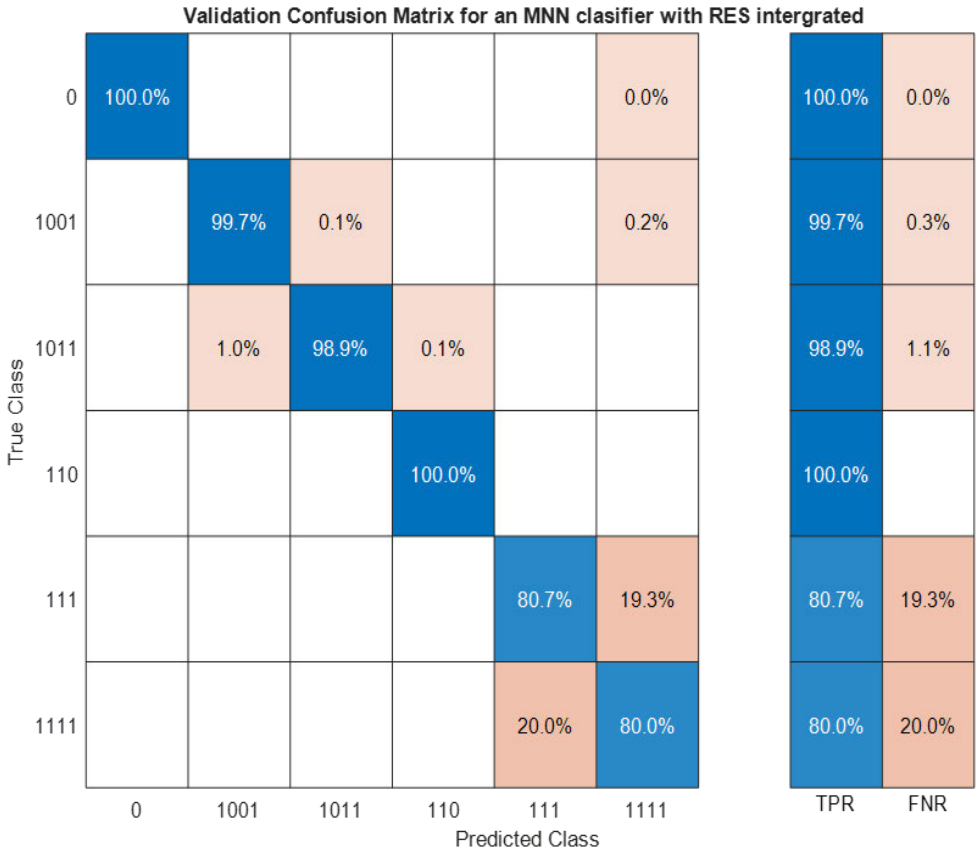

Figure 7. 26The Classification results of MNN Classifier with RES integrated

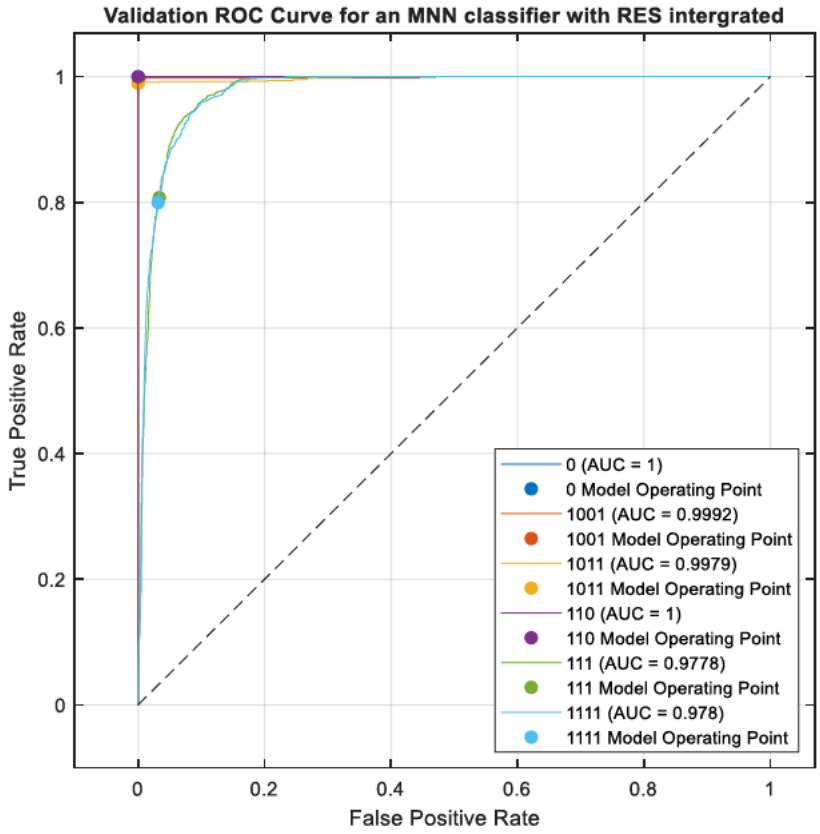

Figure 7. 27The ROC curve of MNN classifier with RES integrated

Figure 7.28 illustrates the classification outcomes of an SQVM classifier following the addition of 12MW of renewable energy to the previous model (Compensated Transmission Line). A comparison for the performance SQVM classifier is simplified in table 7.6. Furthermore, the ROC curve is shown in figure 7.26. while the comparison is on table 7.7.

Table 7. 6 Comparison of Classification results for an SQVM classifier

Network	No-Fault	L-G	L-L	L-L	L-L-L	L-L-L-G
No RES	100	100	97.4	100	98.8	98.2
With RES	99.8	98.3	97.8	98.6	98.5	98.2

Table 7. 7 Comparison of ROC curve results for SQVM Classifier

Network	No-Fault	L-G	L-L	L-L	L-L-L	L-L-L-G
No RES	1	0.9946	0.9948	1	0.9935	0.995
With RES	1	0.9992	0.9979	1	0.9778	0.9780

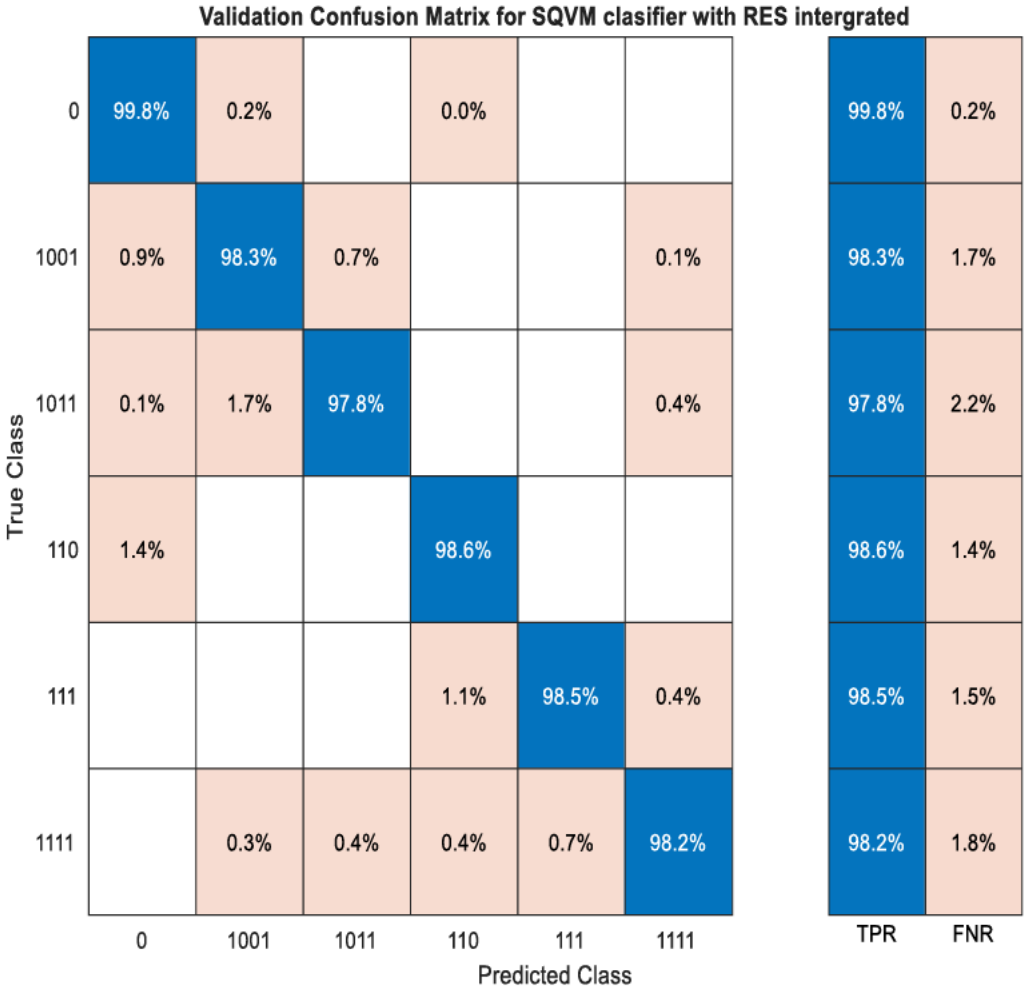

Figure 7. 28 The Classification results of QSVM Classifier with RES integrated

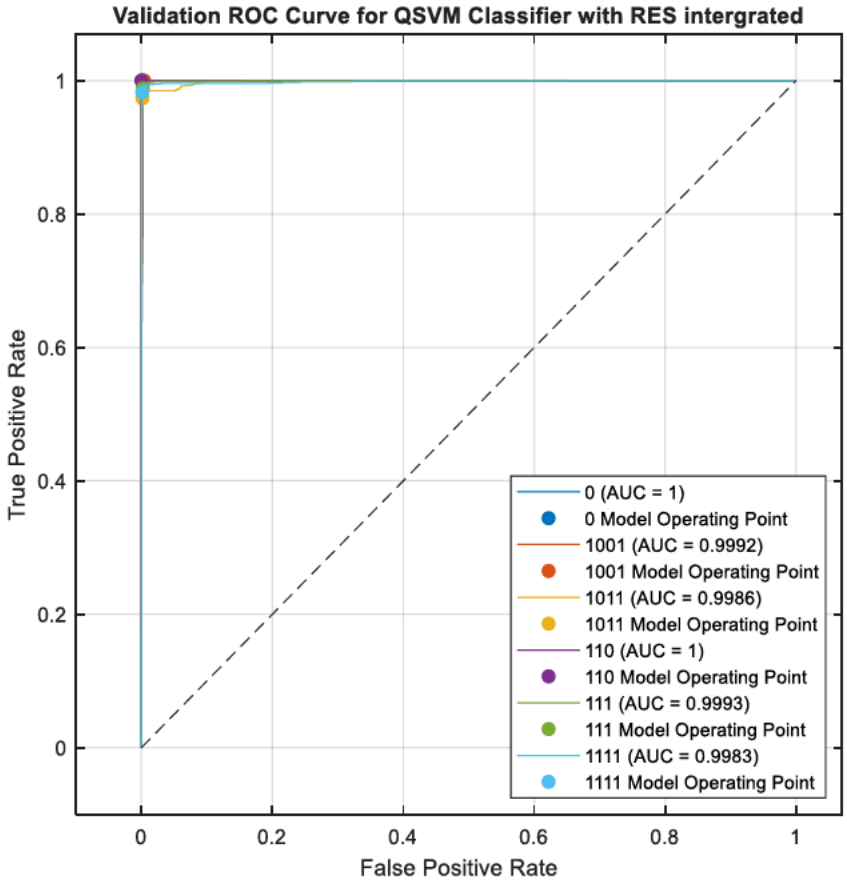

Figure 7. 29The ROC curve of QSVM classifier with RES integrated

Chapter 8 Conclusion and Recommendations

8.1 Conclusion

This research investigates the efficacy of a power systems network utilizing two methodologies aimed at reducing the disparity between energy supply and demand. The methodologies under consideration include transmission line compensation and the integration of renewable energy sources. Both approaches pose considerable challenges to the conventional protection systems currently in place. The models employed in this study are executed using MATLAB. A segment of the network characterized as a compensated transmission line is examined to evaluate the effects of this methodology. An analysis in the R/X plane is conducted, focusing on the impedance perceived by the relay under various fault conditions. The findings indicate that the implementation of compensation tends to shift the impedance into the capacitive domain, which may lead to maloperation of the relay, as the functioning of distance relays is contingent upon the impedance detected by the relay. Additionally, three machine learning-based classification techniques are developed for the compensated scenario. The performance of these classifiers is ranked from 1 to 3, utilizing performance metrics such as accuracy, ROC curves, and precision-recall curves. The SQVM classifier demonstrated the highest overall performance; however, each classifier exhibited specific advantages and disadvantages depending on the type of fault encountered.

A 12MW renewable energy system has been integrated, comprising 9MW from wind sources and 3MW from PVs systems. To evaluate the effects of incorporating sources RES into a compensated transmission network, the three classifiers previously utilized in the network analysis are employed once again. A comparative analysis is conducted for two scenarios: one without renewable energy and the other with its integration. The results indicate that while the ranking of the classifiers remains consistent, the accuracy diminishes in the presence of RES. Specifically, the overall performance of the fault detection and classification scheme for a compensated transmission line with renewable energy integration is recorded at 97.3%, compared to 99.2% in the absence of RES.

The objectives specified in the first section have been successfully met. The initial model created to evaluate the influence of compensation on the impedance response of transmission lines has confirmed that it indeed impacts the transmission line's performance. Additionally, the incorporation of renewable energy sources (RES) has further influenced the

effectiveness of the protection system, particularly regarding accuracy and response time, in alignment with the hypothesis. While the use of machine learning techniques has the potential to enhance the protection system's performance, the need for substantial computing power remains a significant challenge in increasing the speed of the classifiers.

8.2 Recommendations

Rigorous testing of the network topology under various system dynamics is essential to ensure both speed and accuracy. Additionally, the utilization of internet of things (IoT) technology presents several challenges, including real-time situational awareness, rapid and precise fault localization, fault detection, fault classification, cost reduction, and condition-based maintenance. These challenges can be addressed through the implementation of a wireless sensor network IoT for monitoring and managing transmission and distribution lines. Advancements in IoT offer improved methods for overcoming protection challenges and implementing smart grid policies. Further research can explore the impact of RES on protection systems, particularly in scenarios where underground cables are utilized at the point of connection, considering their unique characteristics. Various aspects such as fault detection and localization, fault clearance, ground fault protection, cable thermal protection, communication and coordination, maintenance and testing, and cybersecurity can be investigated within the context of digital protection schemes. Moreover, the integration of renewable energy networks into High Voltage Direct Current (HVDC) systems requires a comprehensive approach encompassing cybersecurity measures, physical security measures, resilient monitoring, and response systems. Establishing an effective collaboration framework among government agencies, energy providers, technology vendors, and cybersecurity experts is crucial. Further more the practical implementation for the developed scheme is recommended which may include using real time digital simulator (RTDS) . The application of Hybrid machine learning approaches to improve the performance of the protection in terms of speed and also in terms of reliability is recommended.

References

[1] K. Kant and O. H. Gupta, "DC Microgrid: A Comprehensive Review on Protection Challenges and Schemes," *IETE Technical Review,* pp. 1-17, 2022.

[2] U. B. Parikh, B. Das, and R. Maheshwari, "Fault classification technique for series compensated transmission line using support vector machine," *International Journal of Electrical Power & Energy Systems,* vol. 32, no. 6, pp. 629-636, 2010.

[3] M. Shwehdi and S. R. Mohamed, "Proposed smart DC nano-grid for green buildings—A reflective view," in *2014 International Conference on Renewable Energy Research and Application (ICRERA)*, 2014: IEEE, pp. 765-769.

[4] M. S. Alam, F. S. Al-Ismail, A. Salem, and M. A. Abido, "High-level penetration of renewable energy sources into grid utility: Challenges and solutions," *IEEE Access,* vol. 8, pp. 190277-190299, 2020.

[5] M. T. Hoq, J. Wang, and N. Taylor, "The impact of current inversion on line protection in high voltage transmission lines with series compensation," in *2019 Nordic Workshop on Power and Industrial Electronics (NORPIE)*, 2019: IEEE, pp. 1-7.

[6] E. Bakie, C. Westhoff, N. Fischer, and J. Bell, "Voltage and current inversion challenges when protecting series-compensated lines—A case study," in *2016 69th Annual Conference for Protective Relay Engineers (CPRE)*, 2016: IEEE, pp. 1-14.

[7] L. A. Pilotto, A. Bianco, W. F. Long, and A.-A. Edris, "Impact of TCSC control methodologies on subsynchronous oscillations," *IEEE transactions on Power Delivery,* vol. 18, no. 1, pp. 243-252, 2003.

[8] M. Adamiak and R. Patterson, "Protection requirements for flexible AC transmission systems," in *International Conference on Large High Voltage Electric Systems*, 1992, vol. 2, pp. 34/206-34/206.

[9] M. A. Bhaskar and A. Indhirani, "Impact of FACTS devices on distance protection in transmission system," in *2014 IEEE National Conference on Emerging Trends in New & Renewable Energy Sources and Energy Management (NCET NRES EM)*, 2014: IEEE, pp. 52-58.

[10] S. Mishra, S. Gupta, and A. Yadav, "Study on factors affecting distance protection scheme of UPFC compensated transmission lines," in *2020 First International Conference on Power, Control and Computing Technologies (ICPC2T)*, 2020: IEEE, pp. 143-148.

[11] M. Khederzadeh, "Power quality impacts of series and shunt compensated lines on digital protective relays," in *International Conference on Power Systems Transients*, 2003: Citeseer.

[12] M. M. Keramat and M. H. Fazaeli, "The new adaptive protection method for the compensated transmission lines with the series capacitor in a high share of wind energy resources by using PMU data," in *7th Iran Wind Energy Conference (IWEC2021)*, 2021: IEEE, pp. 1-6.

[13] H. F. Habib, C. R. Lashway, and O. A. Mohammed, "A review of communication failure impacts on adaptive microgrid protection schemes and the use of energy storage as a contingency," *IEEE Transactions on Industry Applications,* vol. 54, no. 2, pp. 1194-1207, 2017.

[14] K. Cheruiyot, E. Lengaram, and M. Siteleki, "South Africa's Energy Landscape Amidst the Crisis: Unpacking Energy Sources and Drivers with 2022 South African Census Data," *Sustainability,* vol. 16, no. 2, p. 682, 2024.

[15] O. M. Akinbami, S. R. Oke, and M. O. Bodunrin, "The state of renewable energy development in South Africa: An overview," *Alexandria Engineering Journal,* vol. 60, no. 6, pp. 5077-5093, 2021.

[16] D. o. Energy, "Integrated resource plan for electricity 2010–2030," *Government Gazette,* vol. 551, no. 34263, 2011.

[17] Eskom. "Just Energy Transition (JET) - Eskom." www.eskom.co.za/about-eskom/just-energy-transition-jet/ (accessed 23/06/2024, 2024).

[18] N. W. Ndlela and I. E. Davidson, "Power planning for a smart integrated African super-grid," in *2022 30th Southern African Universities Power Engineering Conference (SAUPEC)*, 2022: IEEE, pp. 1-6.

[19] Eskom. "Current installed Renewable Energy Capacity." https://www.eskom.co.za/dataportal/renewables-performance/renewable-statistics/ (accessed 23/06/2023, 2024).

[20] E. Mukoni, "Grid-connected Hybrid Energy System Modeling and Optimization Study for Green Hydrogen Production in South Africa," 2023.

[21] Eskom. "Hourly Renewable Generation." https://www.eskom.co.za/dataportal/renewables-performance/hourly-renewable-generation/ (accessed 23/06/2024, 2024).

[22] a. I. R. C. Department of Environment Affairs (DEA). "Phase 2 strategic environmental assessement for wind and solar pv energy in south africa." https://redzs.csir.co.za/ (accessed 23/06/2024, 2024).

[23] H. Zenk and A. S. Akpinar, "PI, PID and fuzzy logic controlled SSSC connected to a power transmission line, voltage control performance comparison," in *4th International Conference on Power Engineering, Energy and Electrical Drives*, 2013: IEEE, pp. 1493-1497.

[24] D. Murali, M. Rajaram, and N. Reka, "Comparison of FACTS devices for power system stability enhancement," *International Journal of Computer Applications,* vol. 8, no. 4, pp. 30-35, 2010.

[25] N. Mithulananthan, C. A. Canizares, J. Reeve, and G. J. Rogers, "Comparison of PSS, SVC, and STATCOM controllers for damping power system oscillations," *IEEE transactions on power systems,* vol. 18, no. 2, pp. 786-792, 2003.

[26] A. L. Ara, A. Kazemi, and S. N. Niaki, "Modelling of Optimal Unified Power Flow Controller (OUPFC) for optimal steady-state performance of power systems," *Energy conversion and Management,* vol. 52, no. 2, pp. 1325-1333, 2011.

[27] P. Kumkratug and M. Haque, "Versatile model of a unified power flow controller in a simple power system," *IEE Proceedings-Generation, Transmission and Distribution,* vol. 150, no. 2, pp. 155-161, 2003.

[28] V. Vittal, N. Bhatia, and A. Fouad, "Analysis of the inter-area mode phenomenon in power systems following large disturbances," *IEEE Transactions on Power Systems,* vol. 6, no. 4, pp. 1515-1521, 1991.

[29] S. Chawla, S. Garg, and B. Ahuja, "Optimal location of series-shunt FACTS device for transmission line compensation," in *2009 International Conference on Control, Automation, Communication and Energy Conservation*, 2009: IEEE, pp. 1-6.

[30] M. Puka, N. Hobdari, L. Gjini, and M. Qemali, "Impact of shunt compensation in improving voltage level of overhead transmission lines," 2015.

[31] F. Z. Peng, H. Akagi, and A. Nabae, "A new approach to harmonic compensation in power systems-a combined system of shunt passive and series active filters," *IEEE Transactions on industry applications,* vol. 26, no. 6, pp. 983-990, 1990.

[32] J. Shi, "Comparison of MCT and IGBT for power electronics applications," UNSW Sydney, 1995.

[33] N. Sahadat, S. Hossain, A. Rahman, S. T. Atique, and M. Touhiduzzaman, "Power Quality Improvement of Large Power System Using a Conventional Method," *Engineering,* vol. 3, no. 8, p. 823, 2011.

[34] M. T. Hoq, J. Wang, and N. Taylor, "Impact of high levels of series compensation on line distance protection," 2020.

[35] M. Abasi, M. Joorabian, A. Saffarian, and S. G. Seifossadat, "A Comprehensive Review of Various Fault Location Methods for Transmission Lines Compensated by FACTS devices and Series Capacitors," *Journal of Operation and Automation in Power Engineering,* vol. 9, no. 3, pp. 213-225, 2021.

[36] S. Biswas and P. K. Nayak, "State-of-the-art on the protection of FACTS compensated high-voltage transmission lines: a review," *High voltage,* vol. 3, no. 1, pp. 21-30, 2018.

[37] N. B. Kadandani and Y. A. Maiwada, "An overview of facts controllers for power quality improvement," *The International Journal Of Engineering: And Science (IJES),* vol. 4, no. 9, pp. 9-17, 2015.

[38] A. Sunny and V. Janamala, "Available Transfer Capability (ATC) enhancement & optimization of UPFC shunt converter location with GSF in deregulated power system," in *2016 International Conference on Circuit, Power and Computing Technologies (ICCPCT)*, 2016: IEEE, pp. 1-5.

[39] S. Biswas and P. K. Nayak, "A fault detection and classification scheme for unified power flow controller compensated transmission lines connecting wind farms," *IEEE Systems Journal,* vol. 15, no. 1, pp. 297-306, 2020.

[40] M. Riahinasab, M. Dehghani, A. Fathollahi, and M. R. Behzadfar, "A brief Overview of the Application of Unified Power Flow Controller in Power Systems," *International Journal of Smart Electrical Engineering,* 2023.

[41] C. RIVERA S, A. Messina, D. OLGUÍN S, and D. RUIZ V, "Analysis of Subsynchronous Torsional, Interactions with SVCs," *Electric Power Components and Systems,* vol. 31, no. 5, pp. 467-481, 2003.

[42] S. Bhowmick, *Flexible ac transmission systems (FACTS): Newton power-flow modeling of voltage-sourced converter-based controllers*. CRC Press, 2018.

[43] I. Y. Fawzy, M. A. Mossa, A. M. Elsawy, and A. A. Z. Diab, "Enhancing the Performance of Power System under Abnormal Conditions Using Three Different FACTS Devices," *International Journal of Robotics and Control Systems,* vol. 4, no. 1, pp. 1-32, 2024.

[44] S. Gupta and R. Tripathi, "FACTS modelling and control: Application of CSC based STATCOM in transmission line," in *2012 Students Conference on Engineering and Systems*, 2012: IEEE, pp. 1-5.

[45] S. Gangolu, S. Sarangi, and R. Mohanty, "Relay algorithm for STATCOM compensated line using differential current ratio," *International Journal of Electrical Power & Energy Systems,* vol. 155, p. 109473, 2024.

[46] C. D. Prasad, M. Biswal, and P. Ray, "Line protection in presence of high penetration of wind energy: a review on possible solutions," *Electrical Engineering,* pp. 1-13, 2024.

[47] J. Song, S. Oh, J. Lee, J. Shin, and G. Jang, "Application of the first replica controller in korean power systems," *Energies,* vol. 13, no. 13, p. 3343, 2020.

[48] S. M. Hashemi, M. T. Hagh, and H. Seyedi, "High-speed relaying scheme for protection of transmission lines in the presence of thyristor-controlled series capacitor," *IET Generation, Transmission & Distribution,* vol. 8, no. 12, pp. 2083-2091, 2014.

[49] T. Sidhu and M. Khederzadeh, "TCSC impact on communication-aided distance-protection schemes and its mitigation," *IEE Proceedings-Generation, Transmission and Distribution,* vol. 152, no. 5, pp. 714-728, 2005.

[50] Y. G. Paithankar and S. Bhide, *Fundamentals of power system protection*. PHI Learning Pvt. Ltd., 2022.

[51] Y. Jacome and C. Henville, "Setting Out-of-Step Blocking or Tripping Using Dynamic Simulations," *Schweitzer Engineering Laboratories: Pullman, WA, USA,* 2011.

[52] D. A. Tziouvaras and D. Hou, "Out-of-step protection fundamentals and advancements," in *57th Annual Conference for Protective Relay Engineers, 2004*, 2004: IEEE, pp. 282-307.

[53] Q. Arooj and U. A. Khan, "Improving the Efficiency of Transmission Line by Using 48-Pulse Smart Power Flow Controller," in *2021 16th International Conference on Emerging Technologies (ICET)*, 2021: IEEE, pp. 1-6.

[54] P. K. Singh and A. K. Dahiya, "Analysis Modelling & Simulation of VSC based D-Statcom for Reactive VAR Compensation," in *2018 International Conference on Current Trends towards Converging Technologies (ICCTCT)*, 2018: IEEE, pp. 1-6.

[55] R. S. Dhekekar and N. Srikanth, "ANN Controlled VSC with Harmonic Reduction for VAR Control of Transmission Line," *International Journal of Power Electronics and Drive Systems,* vol. 2, no. 1, p. 76, 2012.

[56] F. M. Albatsh, B. Ismail, L. J. Awalin, I. Alhamrouni, S. Ahmad, and K. Naidu, "Implementation of UPFC based on fuzzy logic controller to resolve power quality issues in transmission network," in *2017 6th International Conference on Electrical Engineering and Informatics (ICEEI)*, 2017: IEEE, pp. 1-6.

[57] M. Chethan and R. Kuppan, "A review of FACTS device implementation in power systems using optimization techniques," *Journal of Engineering and Applied Science,* vol. 71, no. 1, p. 18, 2024.

[58] B. T. Ooi *et al.*, "Mid-point siting of FACTS devices in transmission lines," *IEEE Transactions on Power Delivery,* vol. 12, no. 4, pp. 1717-1722, 1997.

[59] S. Biswas and P. K. Nayak, "A new approach for protecting TCSC compensated transmission lines connected to DFIG-based wind farm," *IEEE Transactions on Industrial Informatics,* vol. 17, no. 8, pp. 5282-5291, 2020.

[60] M. Amroune, M. Zellagui, T. Bouktir, and A. Chaghi, "Optimal Placement of TCSC to Improve Voltage Stability Limit Considering Impacts on Setting Zones of Distance Protection Relays," *Acta Electrotehnica,* vol. 55, no. 1-2, pp. 10-18, 2014.

[61] S. Das, B. K. Panigrahi, and P. K. Jaiswal, "Qualitative assessment of power swing for enhancing security of distance relay in a TCSC-compensated line," *IEEE Transactions on Power Delivery,* vol. 36, no. 1, pp. 223-234, 2020.

[62] J. Zakonjšek, B. S. Palki, R. K. Aggarwal, and R. Krebs, "Protection, Control and Monitoring of Series Compensated Networks," *CIGRE, Working Group B5. 10,* 2010.

[63] D. Korot, P. Marken, and L. Bock, "The next fifty years of series capacitors—And the last eighty-six," in *2014 IEEE PES T&D Conference and Exposition*, 2014: IEEE, pp. 1-5.

[64] M. T. Hoq and N. Taylor, "Distance Protection of Series Capacitor Compensated Lines: Practical Considerations, Industrial Status and Development," *Electricity,* vol. 2, no. 2, pp. 168-186, 2021.

[65] D. Tzelepis *et al.*, "Impact of synchronous condensers on transmission line protection in scenarios with high penetration of renewable energy sources," 2020.

[66] N. Sa-ngawong and I. Ngamroo, "Intelligent photovoltaic farms for robust frequency stabilization in multi-area interconnected power system based on PSO-based optimal Sugeno fuzzy logic control," *Renewable Energy,* vol. 74, pp. 555-567, 2015.

[67] C. A. Hill, M. C. Such, D. Chen, J. Gonzalez, and W. M. Grady, "Battery energy storage for enabling integration of distributed solar power generation," *IEEE Transactions on smart grid,* vol. 3, no. 2, pp. 850-857, 2012.

[68] N. Kakimoto, S. Takayama, H. Satoh, and K. Nakamura, "Power modulation of photovoltaic generator for frequency control of power system," *IEEE Transactions on Energy Conversion,* vol. 24, no. 4, pp. 943-949, 2009.

[69] H. Xin, Y. Liu, Z. Wang, D. Gan, and T. Yang, "A new frequency regulation strategy for photovoltaic systems without energy storage," *IEEE Transactions on Sustainable Energy,* vol. 4, no. 4, pp. 985-993, 2013.

[70] P. Zarina, S. Mishra, and P. Sekhar, "Exploring frequency control capability of a PV system in a hybrid PV-rotating machine-without storage system," *International Journal of Electrical Power & Energy Systems,* vol. 60, pp. 258-267, 2014.

[71] H. Alatrash, A. Mensah, E. Mark, G. Haddad, and J. Enslin, "Generator emulation controls for photovoltaic inverters," *IEEE Transactions on Smart Grid,* vol. 3, no. 2, pp. 996-1011, 2012.

[72] S. I. Nanou, A. G. Papakonstantinou, and S. A. Papathanassiou, "A generic model of two-stage grid-connected PV systems with primary frequency response and inertia emulation," *Electric Power Systems Research,* vol. 127, pp. 186-196, 2015.

[73] W. K. Ntuli, G. Sharma, and M. Kabeya, "Study of Fault Ride-Through Capability of Doubly Fed Induction Generator Based Wind Turbine," in *2022 30th Southern African Universities Power Engineering Conference (SAUPEC)*, 2022: IEEE, pp. 1-6.

[74] X. Liang and C. Andalib-Bin-Karim, "Harmonics and mitigation techniques through advanced control in grid-connected renewable energy sources: A review," *IEEE Transactions on Industry Applications,* vol. 54, no. 4, pp. 3100-3111, 2018.

[75] T. D. Reddy, J. R. Dash, and P. Agarwal, "A New Control Strategy of a Single Stage PV System for Providing Frequency Support to the Power Grid," in *2023 IEEE IAS Global Conference on Emerging Technologies (GlobConET)*, 2023: IEEE, pp. 1-5.

[76] V. Gevorgian, Y. Zhang, and E. Ela, "Investigating the impacts of wind generation participation in interconnection frequency response," *IEEE transactions on Sustainable Energy,* vol. 6, no. 3, pp. 1004-1012, 2014.

[77] H. D. Tafti *et al.*, "Adaptive power system frequency support from distributed photovoltaic systems," *Solar Energy,* vol. 257, pp. 231-239, 2023.

[78] B.-I. Crăciun, T. Kerekes, D. Séra, and R. Teodorescu, "Frequency support functions in large PV power plants with active power reserves," *IEEE Journal of Emerging and Selected Topics in Power Electronics,* vol. 2, no. 4, pp. 849-858, 2014.

[79] Q. Peng, Z. Tang, Y. Yang, T. Liu, and F. Blaabjerg, "Event-triggering virtual inertia control of PV systems with power reserve," *IEEE Transactions on Industry Applications,* vol. 57, no. 4, pp. 4059-4070, 2021.

[80] C. Seneviratne and C. Ozansoy, "Frequency response due to a large generator loss with the increasing penetration of wind/PV generation–A literature review," *Renewable and Sustainable Energy Reviews,* vol. 57, pp. 659-668, 2016.

[81] M. Alam, K. Muttaqi, and D. Sutanto, "A novel approach for ramp-rate control of solar PV using energy storage to mitigate output fluctuations caused by cloud passing," *IEEE Transactions on Energy Conversion,* vol. 29, no. 2, pp. 507-518, 2014.

[82] Q. Xu, H. Wen, Y. Zhu, and X. Li, "An adaptive ramp-rate control for photovoltaic system to mitigate output fluctuation," in *2019 IEEE PES Asia-Pacific Power and Energy Engineering Conference (APPEEC)*, 2019: IEEE, pp. 1-5.

[83] S. Patel, M. Ahmed, and S. Kamalasadan, "A novel energy storage-based net-load smoothing and shifting architecture for high amount of photovoltaics integrated power distribution system," *IEEE Transactions on Industry Applications,* vol. 56, no. 3, pp. 3090-3099, 2020.

[84] `234567890-\/*+*-, "Mitigation of solar PV intermittency using ramp-rate control of energy buffer unit," *IEEE Transactions on Energy Conversion,* vol. 34, no. 1, pp. 435-445, 2018.

[85] G. Bao, H. Tan, K. Ding, M. Ma, and N. Wang, "A novel photovoltaic virtual synchronous generator control technology without energy storage systems," *Energies,* vol. 12, no. 12, p. 2240, 2019.

[86] M. H. Marzebali, M. Mazidi, and M. Mohiti, "An adaptive droop-based control strategy for fuel cell-battery hybrid energy storage system to support primary frequency in stand-alone microgrids," *Journal of Energy Storage,* vol. 27, p. 101127, 2020.

[87] T. Yang, K.-T. Mok, S.-C. Tan, C. K. Lee, and S. Y. Hui, "Electric springs with coordinated battery management for reducing voltage and frequency fluctuations in microgrids," *IEEE Transactions on Smart Grid,* vol. 9, no. 3, pp. 1943-1952, 2016.

[88] Y. Zhu, H. Wen, and G. Chu, "Active power control for grid-connected photovoltaic system: A review," *2020 IEEE/IAS Industrial and Commercial Power System Asia (I&CPS Asia),* pp. 1506-1511, 2020.

[89] H. D. Tafti, G. Konstantinou, J. E. Fletcher, L. Callegaro, G. G. Farivar, and J. Pou, "Control of distributed photovoltaic inverters for frequency support and system recovery," *IEEE Transactions on Power Electronics,* vol. 37, no. 4, pp. 4742-4750, 2021.

[90] H. Ma and B. Chowdhury, "Working towards frequency regulation with wind plants: combined control approaches," *IET Renewable Power Generation,* vol. 4, no. 4, pp. 308-316, 2010.

[91] M. E. Zarei, D. Ramirez, M. Prodanovic, and G. Venkataramanan, "Multivector model predictive power control for grid connected converters in renewable power plants," *IEEE Journal of Emerging and Selected Topics in Power Electronics,* vol. 10, no. 2, pp. 1466-1478, 2021.

[92] V. Kumar, V. Sharma, and R. Naresh, "Leader Harris Hawks algorithm based optimal controller for automatic generation control in PV-hydro-wind integrated power network," *Electric Power Systems Research,* vol. 214, p. 108924, 2023.

[93] Y. Liu, H. Wang, X. Wang, G. Guo, and H. Jing, "Control Strategy and Corresponding Parameter Analysis of a Virtual Synchronous Generator Considering Frequency Stability of Wind Power Grid-Connected System," *Electronics,* vol. 11, no. 18, p. 2806, 2022.

[94] J. Liu and J. Liu, "Modeling and Calculation of Grid Frequency Support Effect and Transient Energy Demand of a Virtual Synchronous Generator," in *2022 International Power Electronics Conference (IPEC-Himeji 2022-ECCE Asia)*, 2022: IEEE, pp. 2334-2339.

[95] Q. Peng, Y. Yang, T. Liu, and F. Blaabjerg, "Coordination of virtual inertia control and frequency damping in PV systems for optimal frequency support," *CPSS Transactions on Power Electronics and Applications,* vol. 5, no. 4, pp. 305-316, 2020.

[96] M. M. Kabsha and Z. H. Rather, "Adaptive Control Strategy for Frequency Support From MTDC Connected Offshore Wind Power Plants," *IEEE Transactions on Power Electronics,* vol. 38, no. 3, pp. 3981-3991, 2022.

[97] A. Azamian, B. Rezaeealam, T. Ghanbari, and E. Rokrok, "Improved Low Voltage Ride-through Capability of PV Connected to the Unbalanced Main Grid," *Journal of Solar Energy Research,* vol. 8, no. 1, pp. 1326-1344, 2023.

[98] M. Firouzi and G. Gharehpetian, "Improving fault ride-through capability of fixed-speed wind turbine by using bridge-type fault current limiter," *IEEE Transactions on Energy Conversion,* vol. 28, no. 2, pp. 361-369, 2013.

[99] R. Sitharthan, C. Sundarabalan, K. Devabalaji, S. K. Nataraj, and M. Karthikeyan, "Improved fault ride through capability of DFIG-wind turbines using customized dynamic voltage restorer," *Sustainable cities and society,* vol. 39, pp. 114-125, 2018.

[100] A. Falehi and M. Rafiee, "Enhancement of DFIG-wind turbine's LVRT capability using novel DVR based odd-nary cascaded asymmetric multi-level inverter," *Engineering science and technology, an international journal,* vol. 20, no. 3, pp. 805-824, 2017.

[101] T. K. Roy, M. Mahmud, and A. Oo, "Nonlinear backstepping controller design for improving fault ride through capabilities of DFIG-based wind farms," in *2018 IEEE Power & Energy Society General Meeting (PESGM)*, 2018: IEEE, pp. 1-5.

[102] E. Bekiroglu and M. D. Yazar, "Improving fault ride through capability of DFIG with fuzzy logic controlled crowbar protection," in *2022 11th International Conference on Renewable Energy Research and Application (ICRERA)*, 2022: IEEE, pp. 374-378.

[103] M. S. Alam, M. A. Y. Abido, A. E.-D. Hussein, and I. El-Amin, "Fault ride through capability augmentation of a DFIG-based wind integrated VSC-HVDC system with non-superconducting fault current limiter," *sustainability,* vol. 11, no. 5, p. 1232, 2019.

[104] V. Telukunta, J. Pradhan, A. Agrawal, M. Singh, and S. G. Srivani, "Protection challenges under bulk penetration of renewable energy resources in power systems: A review," *CSEE journal of power and energy systems,* vol. 3, no. 4, pp. 365-379, 2017.

[105] V. Kale and S. Khond, "Adaptive Overcurrent Protection Scheme for Distribution Network Integrated With Distributed Energy Resources," in *2022 IEEE International*

Conference on Power Electronics, Drives and Energy Systems (PEDES), 2022: IEEE, pp. 1-5.

[106] H. Shah, J. Chakravorty, and N. G. Chothani, "Protection challenges and mitigation techniques of power grid integrated to renewable energy sources: A review," *Energy Sources, Part A: Recovery, Utilization, and Environmental Effects,* vol. 45, no. 2, pp. 4195-4210, 2023.

[107] R. Dubey, S. R. Samantaray, and B. K. Panigrahi, "Simultaneous impact of unified power flow controller and off-shore wind penetration on distance relay characteristics," *IET Generation, Transmission & Distribution,* vol. 8, no. 11, pp. 1869-1880, 2014.

[108] Y. Fang, K. Jia, Z. Yang, Y. Li, and T. Bi, "Impact of inverter-interfaced renewable energy generators on distance protection and an improved scheme," *IEEE Transactions on Industrial Electronics,* vol. 66, no. 9, pp. 7078-7088, 2018.

[109] N. George and O. Naidu, "Distance protection issues with renewable power generators and possible solutions," in *16th International Conference on Developments in Power System Protection (DPSP 2022)*, 2022, vol. 2022: IET, pp. 373-378.

[110] A. Hooshyar, M. A. Azzouz, and E. F. El-Saadany, "Distance protection of lines emanating from full-scale converter-interfaced renewable energy power plants—Part II: Solution description and evaluation," *IEEE Transactions on Power Delivery,* vol. 30, no. 4, pp. 1781-1791, 2014.

[111] C. Wang, G. Song, and J. Tang, "Protection performance of traditional distance relays under wind power integration," 2016.

[112] X. Chen, X. Yin, and Z. Zhang, "Impacts of DFIG-based wind farm integration on its tie line distance protection and countermeasures," *IEEJ Transactions on Electrical and Electronic Engineering,* vol. 12, no. 4, pp. 553-564, 2017.

[113] Y. Chen, M. Wen, X. Yin, Y. Cai, and J. Zheng, "Distance protection for transmission lines of DFIG-based wind power integration system," *International Journal of Electrical Power & Energy Systems,* vol. 100, pp. 438-448, 2018.

[114] S. Kumar, A. Gupta, and R. K. Bindal, "Power quality investigation of a grid tied hybrid energy system using a D-STATCOM control and grasshopper optimization technique," *Results in Control and Optimization,* vol. 14, p. 100368, 2024.

[115] J. Ma, W. Zhang, J. Liu, and J. S. Thorp, "A novel adaptive distance protection scheme for DFIG wind farm collector lines," *International Journal of Electrical Power & Energy Systems,* vol. 94, pp. 234-244, 2018.

[116] H. Sadeghi, "A novel method for adaptive distance protection of transmission line connected to wind farms," *International Journal of Electrical Power & Energy Systems,* vol. 43, no. 1, pp. 1376-1382, 2012.

[117] A. Jodaei, Z. Moravej, and M. Pazoki, "Effective protection scheme for transmission lines connected to large scale photovoltaic power plants," *Electric Power Systems Research,* vol. 228, p. 110103, 2024.

[118] C. D. Prasad, M. Biswal, and A. Y. Abdelaziz, "Adaptive differential protection scheme for wind farm integrated power network," *Electric Power Systems Research,* vol. 187, p. 106452, 2020.

[119] A. A. R. Mohamed, H. M. Sharaf, and D. K. Ibrahim, "Enhancing distance protection of long transmission lines compensated with TCSC and connected with wind power," *IEEE Access,* vol. 9, pp. 46717-46730, 2021.

[120] J. Ma, W. Ma, Y. Qiu, and J. S. Thorp, "An adaptive distance protection scheme based on the voltage drop equation," *IEEE Transactions on Power Delivery,* vol. 30, no. 4, pp. 1931-1940, 2015.

[121] A. Ghorbani, M. Khederzadeh, and B. Mozafari, "Impact of SVC on the protection of transmission lines," *International Journal of Electrical Power & Energy Systems,* vol. 42, no. 1, pp. 702-709, 2012.

[122] A. R. Singh and S. S. Dambhare, "Adaptive distance protection of transmission line in presence of SVC," *International Journal of Electrical Power & Energy Systems,* vol. 53, pp. 78-84, 2013.

[123] A. A. Girgis, A. Sallam, and A. K. El-Din, "An adaptive protection scheme for advanced series compensated (ASC) transmission lines," *IEEE Transactions on Power Delivery,* vol. 13, no. 2, pp. 414-420, 1998.

[124] R. Dubey, S. R. Samantaray, B. K. Panigrahi, and V. G. Venkoparao, "Data-mining model based adaptive protection scheme to enhance distance relay performance during power swing," *International Journal of Electrical Power & Energy Systems,* vol. 81, pp. 361-370, 2016.

[125] A. Ghorbani, "An adaptive distance protection scheme in the presence of phase shifting transformer," *Electric Power Systems Research,* vol. 129, pp. 170-177, 2015.

[126] H. Lin, K. Sun, Z. H. Tan, C. Liu, J. M. Guerrero, and J. C. Vasquez, "Adaptive protection combined with machine learning for microgrids," *IET generation, transmission & distribution,* vol. 13, no. 6, pp. 770-779, 2019.

[127] H. Mehrjerdi and A. Ghorbani, "Adaptive algorithm for transmission line protection in the presence of UPFC," *International Journal of Electrical Power & Energy Systems,* vol. 91, pp. 10-19, 2017.

[128] S. Paladhi and A. K. Pradhan, "Adaptive distance protection for lines connecting converter-interfaced renewable plants," *IEEE Journal of Emerging and Selected Topics in Power Electronics,* vol. 9, no. 6, pp. 7088-7098, 2020.

[129] U. Uzubi, A. Ekwue, and E. Ejiogu, "An adaptive distance protection scheme for high varying fault resistances: Updated results," *Scientific African,* vol. 9, p. e00528, 2020.

[130] U. Uzubi, A. Ekwue, and E. Ejiogu, "Adaptive distance relaying: Solution to challenges of conventional protection schemes in the presence of remote infeeds," *International Transactions on Electrical Energy Systems,* vol. 30, no. 5, p. e12330, 2020.

[131] M. Abdelhamid, S. Kamel, E. M. Ahmed, and E. B. Agyekum, "An adaptive protection scheme based on a modified heap-based optimizer for distance and directional overcurrent relays coordination in distribution systems," *Mathematics,* vol. 10, no. 3, p. 419, 2022.

[132] F. Dewangan and M. Biswal, "An adaptive time–frequency approach based secured back-up distance protection scheme for system stress conditions," *Sustainable Energy, Grids and Networks,* vol. 31, p. 100732, 2022.

[133] M. Khoshbouy, A. Yazdaninejadi, and T. G. Bolandi, "Transmission line adaptive protection scheme: A new fault detection approach based on pilot superimposed impedance," *International Journal of Electrical Power & Energy Systems,* vol. 137, p. 107826, 2022.

[134] S. Bharathidasan, M. Sankar, and S. Akash, "Adaptive Distance Protection for Smart Grids with Infeed Compensation using Synchronized Phasor Measurements," in *2022 International Conference on Smart Generation Computing, Communication and Networking (SMART GENCON)*, 2022: IEEE, pp. 1-10.

[135] C. Chao, X. Zheng, Y. Weng, Y. Liu, P. Gao, and N. Tai, "Adaptive distance protection based on the analytical model of additional impedance for inverter-interfaced renewable power plants during asymmetrical faults," *IEEE Transactions on Power Delivery,* vol. 37, no. 5, pp. 3823-3834, 2021.

[136] H. Teimourzadeh, B. Mohammadi-Ivatloo, and M. Shahidehpour, "Adaptive protection of partially coupled transmission lines," *IEEE Transactions on Power Delivery,* vol. 36, no. 1, pp. 429-440, 2020.

[137] G. M. Abo-Hamad, D. K. Ibrahim, E. Aboul Zahab, and A. F. Zobaa, "Adaptive mho distance protection for interconnected transmission lines compensated with thyristor controlled series capacitor," *Energies,* vol. 14, no. 9, p. 2477, 2021.

[138] B. M. Raju and S. Ashok, "Adaptive quadrilateral setting for distance protection of feeder connecting renewable energy," in *2021 IEEE Kansas Power and Energy Conference (KPEC)*, 2021: IEEE, pp. 1-6.

[139] F. Peng, H. Gao, W. Miao, X. Feng, B. Xu, and Y. Wu, "Analysis of Fault Characteristics and Distance Protection Adaptability for VSC-HVDC-Connected Offshore Wind Farms," in *2023 5th Asia Energy and Electrical Engineering Symposium (AEEES)*, 2023: IEEE, pp. 572-577.

[140] B. Li, Y. Sheng, J. He, Y. Li, Z. Xie, and Y. Cao, "Improved distance protection for wind farm transmission line based on dynamic frequency estimation," *International Journal of Electrical Power & Energy Systems,* vol. 153, p. 109382, 2023.

[141] A. Jodaei and Z. Moravej, "Fault Detection and Location in Power Systems with Large-Scale Photovoltaic Power Plant by Adaptive Distance Relays," *Iranica Journal of Energy & Environment,* vol. 15, no. 3, pp. 265-278, 2024.

[142] Y. Guo, Z. Yang, S. Feng, and J. Hu, "Complex power system status monitoring and evaluation using big data platform and machine learning algorithms: a review and a case study," *Complexity,* vol. 2018, no. 1, p. 8496187, 2018.

[143] P. Venkatesh and N. Visali, "Evaluation and Improvement of Power System Security with the Application of Machine Learning," *El-Cezeri,* vol. 11, no. 1, pp. 48-57, 2024.

[144] G. Gurumoorthi, S. Senthilkumar, G. Karthikeyan, and F. Alsaif, "A hybrid deep learning approach to solve optimal power flow problem in hybrid renewable energy systems," *Scientific Reports,* vol. 14, no. 1, p. 19377, 2024.

[145] F. S. M. Al-Jumaili and M. U. Onat, "Hybrid Deep Learning Approach for Accurate Detection and Multiclass Classification of Broken Conductor Faults in Power Distribution Systems," *IEEE Access,* 2024.

[146] L. Aliyeva and N. Abdullayev, "Hybrid Deep Learning Approach Towards Smart Grid Stability Prediction," in *2024 IEEE 8th Energy Conference (ENERGYCON)*, 2024: IEEE, pp. 1-5.

[147] F. M. Almasoudi, "Enhancing power grid resilience through real-time fault detection and remediation using advanced hybrid machine learning models," *Sustainability,* vol. 15, no. 10, p. 8348, 2023.

[148] M. A. I. Rafi, M. R. Sohan, M. H. Nadid, T. S. Rafa, and A. Jawad, "Enhancing Power Transmission Line Fault Detection with a Hybrid ANN-SVM Machine Learning Model: A Comparative Study," in *2024 International Conference on Advances in Computing, Communication, Electrical, and Smart Systems (iCACCESS)*, 2024: IEEE, pp. 1-6.

[149] S. K. Mramba, D. P. M. Musau, and D. A. M. Nyete, "Development of a Traveling Wave-based Protection Scheme for Power Systems with High Penetration of Renewable Energy Sources using a Hybrid Independent Component Analysis-Support Vector Machine Algorithm," *Available at SSRN 4650529,* 2024.

[150] G. Porawagamage, K. Dharmapala, J. S. Chaves, D. Villegas, and A. Rajapakse, "A review of machine learning applications in power system protection and emergency control: opportunities, challenges, and future directions," *Frontiers in Smart Grids,* vol. 3, p. 1371153, 2024.

[151] Z. Aghababaeyan, M. Abdellatif, L. Briand, and M. Bagherzadeh, "Black-box testing of deep neural networks through test case diversity," *IEEE Transactions on Software Engineering,* vol. 49, no. 5, pp. 3182-3204, 2023.

[152] B. Zaker, G. Gharehpetian, M. Mirsalim, and N. Moaddabi, "PMU-based linear and nonlinear black-box modelling of power systems," in *2013 21st Iranian Conference on Electrical Engineering (ICEE)*, 2013: IEEE, pp. 1-6.

[153] G. Rojas-Dueñas, J.-R. Riba, K. Kahalerras, M. Moreno-Eguilaz, A. Kadechkar, and A. Gomez-Pau, "Black-box modelling of a dc-dc buck converter based on a recurrent neural network," in *2020 IEEE International Conference on Industrial Technology (ICIT)*, 2020: IEEE, pp. 456-461.

[154] M. Wu and L. Chen, "Image recognition based on deep learning," in *2015 Chinese automation congress (CAC)*, 2015: IEEE, pp. 542-546.

[155] M. T. Islam, B. N. K. Siddique, S. Rahman, and T. Jabid, "Image recognition with deep learning," in *2018 International conference on intelligent informatics and biomedical sciences (ICIIBMS)*, 2018, vol. 3: IEEE, pp. 106-110.

[156] V. Sessions and M. Valtorta, "The Effects of Data Quality on Machine Learning Algorithms," *ICIQ,* vol. 6, pp. 485-498, 2006.

[157] T. Y. Vega, V. F. Roig, and H. B. San Segundo, "Evolution of signal processing techniques in power quality," in *2007 9th International Conference on Electrical Power Quality and Utilisation*, 2007: IEEE, pp. 1-5.

[158] J. Pereira and F. Saraiva, "A comparative analysis of unbalanced data handling techniques for machine learning algorithms to electricity theft detection," in *2020 IEEE congress on evolutionary computation (CEC)*, 2020: IEEE, pp. 1-8.

[159] L. Fowl, M. Goldblum, P.-y. Chiang, J. Geiping, W. Czaja, and T. Goldstein, "Adversarial examples make strong poisons," *Advances in Neural Information Processing Systems,* vol. 34, pp. 30339-30351, 2021.

[160] I. J. Goodfellow, J. Shlens, and C. Szegedy, "Explaining and harnessing adversarial examples," *arXiv preprint arXiv:1412.6572,* 2014.

[161] G. Rockefeller, C. Wagner, J. Linders, K. Hicks, and D. Rizy, "Adaptive transmission relaying concepts for improved performance," *IEEE Transactions on Power Delivery,* vol. 3, no. 4, pp. 1446-1458, 1988.

[162] M. A. Kanawade and T. P. Hinge, "Designing and Development of virtual Power System Analysis Lab for Measurement of ABCD Parameters of a Medium Length Transmission Line," in *2022 International Conference for Advancement in Technology (ICONAT)*, 2022: IEEE, pp. 1-5.

[163] J. S. Colqui, S. Kurokawa, and J. Pissolato, "An alternative procedure to obtain the ABCD matrix of multiphase transmission lines: Validation and applications," *Electric Power Systems Research,* vol. 180, p. 106161, 2020.

[164] R. Gupta, S.-Y. Kim, and L. T. Pileggi, "Domain characterization of transmission line models and analyses," *IEEE transactions on computer-aided design of integrated circuits and systems,* vol. 15, no. 2, pp. 184-193, 1996.

[165] A. Shoukat, M. A. Mughal, and A. Hussain, "Short transmission line parameter estimation using firefly algorithm," in *2021 International Conference on Emerging Power Technologies (ICEPT)*, 2021: IEEE, pp. 1-5.

[166] R. Schulze and P. Schegner, "Parameter identification of unsymmetrical transmission lines," in *2009 IEEE Bucharest PowerTech*, 2009: IEEE, pp. 1-7.

[167] S. Elenius, K. Uhlen, and E. Lakervi, "Effects of controlled shunt and series compensation on damping in the Nordel system," *IEEE Transactions on Power Systems,* vol. 20, no. 4, pp. 1946-1957, 2005.

[168] M. R. Zaidan and S. I. Toos, "Optimal location of static var compensator to regulate voltage in power system," *IETE Journal of Research,* vol. 69, no. 4, pp. 2177-2185, 2023.

[169] A. Naderipour *et al.*, "Optimal designing of static var compensator to improve voltage profile of power system using fuzzy logic control," *Energy,* vol. 192, p. 116665, 2020.

[170] P. M. Anderson, C. F. Henville, R. Rifaat, B. Johnson, and S. Meliopoulos, *Power system protection*. John Wiley & Sons, 2021.

[171] A. Newbould and I. Taylor, "Series compensated line protection: system modelling and relay testing," in *1989 Fourth International Conference on Developments in Power Protection*, 1989: IET, pp. 182-186.

[172] B. Vyas, R. P. Maheshwari, and B. Das, "Protection of series compensated transmission line: issues and state of art," *Electric power systems research,* vol. 107, pp. 93-108, 2014.

[173] Z. Tang, Y. Yang, and F. Blaabjerg, "Power electronics: The enabling technology for renewable energy integration," *CSEE Journal of Power and Energy Systems,* vol. 8, no. 1, pp. 39-52, 2021.

[174] A. W. Manyonge, R. Ochieng, F. Onyango, and J. Shichikha, "Mathematical modelling of wind turbine in a wind energy conversion system: Power coefficient analysis," 2012.

[175] M. R. Patel and O. Beik, *Wind and solar power systems: design, analysis, and operation*. CRC press, 2021.

[176] S. M. Alizadeh, S. Sadeghipour, C. Ozansoy, and A. Kalam, "Developing a mathematical model for wind power plant siting and sizing in distribution networks," *Energies,* vol. 13, no. 13, p. 3485, 2020.

[177] S. K. LV and N. K. GV, "Power conversion in renewable energy systems: A review advances in wind and PV system," *International Journal of Energy Research,* vol. 41, no. 2, pp. 182-197, 2017.

[178] B. Vidales, M. Madrigal, and D. Torres, "High stepping DC/DC topology for voltage source converters in low power renewable energy applications," in *2016 IEEE PES Transmission & Distribution Conference and Exposition-Latin America (PES T&D-LA)*, 2016: IEEE, pp. 1-5.

[179] R. Sekar, D. Suresh, and H. Naganagouda, "A review on power electronic converters suitable for renewable energy sources," in *2017 International Conference on Electrical, Electronics, Communication, Computer, and Optimization Techniques (ICEECCOT)*, 2017: IEEE, pp. 501-506.

[180] V. R. Teja, S. Srinivas, and M. K. Mishra, "A three port high gain non-isolated DC-DC converter for photovoltaic applications," in *2016 IEEE International Conference on Industrial Technology (ICIT)*, 2016: IEEE, pp. 251-256.

[181] F. L. Luo and H. Ye, *Advanced DC/AC inverters: applications in renewable energy*. Crc Press, 2017.

[182] J. Hu, J. Zhu, and D. Dorrell, "A comparative study of direct power control of AC/DC converters for renewable energy generation," in *IECON 2011-37th Annual Conference of the IEEE Industrial Electronics Society*, 2011: IEEE, pp. 3578-3583.

[183] P. K. Shukla and K. Deepa, "Deep learning techniques for transmission line fault classification–A comparative study," *Ain Shams Engineering Journal,* vol. 15, no. 2, p. 102427, 2024.

[184] L. P. Suresh, "A brief review on multi level inverter topologies," in *2016 international conference on circuit, power and computing technologies (ICCPCT)*, 2016: IEEE, pp. 1-6.

[185] M. Chamana and S. B. Bayne, "Modeling, control and power management of inverter interfaced sources in a microgrid," in *2011 IEEE 33rd International Telecommunications Energy Conference (INTELEC)*, 2011: IEEE, pp. 1-7.

[186] A. Majumder and S. Chowdhuri, "Development of Hybrid SOGI-Resonant Controller in DQ reference frame for decoupled PQ control of a VSI under nonlinear loading," *Electrical Engineering,* pp. 1-15, 2024.

[187] Y. Chen and K. Smedley, "Three-phase boost-type grid-connected inverter," *IEEE Transactions on Power Electronics,* vol. 23, no. 5, pp. 2301-2309, 2008.

[188] M. Dietmannsberger and D. Schulz, "Ancillary services and dynamic behavior of inverters connected to the low voltage grid," in *2015 9th International Conference on Compatibility and Power Electronics (CPE)*, 2015: IEEE, pp. 49-56.

[189] B. Bahrani, A. Karimi, B. Rey, and A. Rufer, "Decoupled dq-current control of grid-tied voltage source converters using nonparametric models," *IEEE Transactions on Industrial Electronics,* vol. 60, no. 4, pp. 1356-1366, 2012.

[190] J. Nayak, S. Kumar, P. K. Sahu, S. Jena, R. Dash, and R. N. Dash, "Design and Analysis of DQ Current Control Techniques for Single-phase Inverter Application," in *2023 Second International Conference on Trends in Electrical, Electronics, and Computer Engineering (TEECCON)*, 2023: IEEE, pp. 395-400.

[191] W. Zahoor and S. H. Zaidi, "Synchronization and dq current control of grid-connected voltage source inverter," in *17th IEEE International Multi Topic Conference 2014*, 2014: IEEE, pp. 462-466.

[192] F. Janıcek, M. Mucha, and M. Ostrozlık, "A new protection relay based on fault transient analysis using wavelet transform," *Journal of Electrical Engineering,* vol. 58, no. 5, pp. 271-278, 2007.

[193] C. A. Cabrelli and U. M. Molter, "Wavelet transform of the dilation equation," *The ANZIAM Journal,* vol. 37, no. 4, pp. 474-489, 1996.

[194] A. S. Altaie, A. A. Majeed, M. Abderrahim, and A. Alkhazraji, "Fault detection on power transmission line based on wavelet transform and scalogram image analysis," *Energies,* vol. 16, no. 23, p. 7914, 2023.

[195] B. Masood, U. Saleem, M. N. Anjum, and U. Arshad, "Faults detection and diagnosis of transmission lines using wavelet transformed based technique," in *2017 IEEE Jordan Conference on Applied Electrical Engineering and Computing Technologies (AEECT)*, 2017: IEEE, pp. 1-6.

[196] C. Fan, K. Li, W. L. Chan, and W. Yu, "Study of protection scheme for transmission line based on wavelet transient energy," *International Journal of Electrical Power & Energy Systems,* vol. 28, no. 7, pp. 459-470, 2006.

[197] A. Osman and O. Malik, "Transmission line distance protection based on wavelet transform," *IEEE Transactions on Power Delivery,* vol. 19, no. 2, pp. 515-523, 2004.

[198] K. Chen, C. Huang, and J. He, "Fault detection, classification and location for transmission lines and distribution systems: a review on the methods," *High voltage,* vol. 1, no. 1, pp. 25-33, 2016.

[199] P. Tandan and A. Mandal, "Identification of faults and its location for the series compensated transmission line using discrete wavelet transform," *Int J Innov Sci Eng Technol,* vol. 2, no. 5, pp. 552-558, 2015.

[200] P. Ray, D. P. Mishra, and S. Mohaptra, "Fault classification of a transmission line using wavelet transform & fuzzy logic," in *2016 IEEE 1st International Conference on Power Electronics, Intelligent Control and Energy Systems (ICPEICES)*, 2016: IEEE, pp. 1-6.

[201] H. Malik and R. Sharma, "Transmission line fault classification using modified fuzzy Q learning," *IET Generation, Transmission & Distribution,* vol. 11, no. 16, pp. 4041-4050, 2017.

[202] P. Ray, D. P. Mishra, K. Dey, and P. Mishra, "Fault detection and classification of a transmission line using discrete wavelet transform & artificial neural network," in *2017 International Conference on Information Technology (ICIT)*, 2017: IEEE, pp. 178-183.

[203] N. Verma *et al.*, "Seismic inversion based on principal component analysis and probabilistic neural network for prediction of porosity from post-stack seismic data," *Earth Science Informatics,* vol. 18, no. 1, p. 98, 2025.

[204] R. Aguilar, F. Pérez, and E. Orduna, "High-speed transmission line protection using principal component analysis, a deterministic algorithm," *IET generation, transmission & distribution,* vol. 5, no. 7, pp. 712-719, 2011.

[205] T. Konishi, "Means and issues for adjusting principal component analysis results," *Algorithms,* vol. 18, no. 3, p. 129, 2025.

[206] M. Greenacre, P. J. Groenen, T. Hastie, A. I. d'Enza, A. Markos, and E. Tuzhilina, "Principal component analysis," *Nature Reviews Methods Primers,* vol. 2, no. 1, p. 100, 2022.

[207] B. M. S. Hasan and A. M. Abdulazeez, "A review of principal component analysis algorithm for dimensionality reduction," *Journal of Soft Computing and Data Mining,* vol. 2, no. 1, pp. 20-30, 2021.

[208] A. Mukherjee, P. K. Kundu, and A. Das, "Application of principal component analysis for fault classification in transmission line with ratio-based method and probabilistic

neural network: a comparative analysis," *Journal of The Institution of Engineers (India): Series B,* vol. 101, pp. 321-333, 2020.

[209] M. Jogin, M. Madhulika, G. Divya, R. Meghana, and S. Apoorva, "Feature extraction using convolution neural networks (CNN) and deep learning," in *2018 3rd IEEE international conference on recent trends in electronics, information & communication technology (RTEICT)*, 2018: IEEE, pp. 2319-2323.

[210] S. Zhang, J. Li, and Y. Li, "Reachable distance function for KNN classification," *IEEE Transactions on Knowledge and Data Engineering,* vol. 35, no. 7, pp. 7382-7396, 2022.

[211] Z. Wu, S. Zhou, Z. Yin, B. Ma, and Z. Yang, "Robust automatic modulation classification under varying noise conditions," *IEEE Access,* vol. 5, pp. 19733-19741, 2017.

[212] E. Y. C. Wong, D. C. K. Ho, S. So, C.-W. Tsang, and E. M. H. Chan, "Life cycle assessment of electric vehicles and hydrogen fuel cell vehicles using the greet model—A comparative study," *Sustainability,* vol. 13, no. 9, p. 4872, 2021.

[213] F. Suliman, F. Anayi, and M. Packianather, "Electrical faults analysis and detection in photovoltaic arrays based on machine learning classifiers," *Sustainability,* vol. 16, no. 3, p. 1102, 2024.

[214] E. Reyes-Archundia, E. Moreno-Goytia, and J. Guardado, "An algorithm based on traveling waves for transmission line protection in a TCSC environment," *International Journal of Electrical Power & Energy Systems,* vol. 60, pp. 367-377, 2014.

[215] S. Jiang, U. Annakkage, and A. Gole, "A platform for validation of FACTS models," *IEEE Transactions on Power Delivery,* vol. 21, no. 1, pp. 484-491, 2005.

[216] O. Kramer and O. Kramer, "K-nearest neighbors," *Dimensionality reduction with unsupervised nearest neighbors,* pp. 13-23, 2013.

[217] Z. Zhang, "Introduction to machine learning: k-nearest neighbors," *Annals of translational medicine,* vol. 4, no. 11, 2016.

[218] P. Srisuradetchai and K. Suksrikran, "Random kernel k-nearest neighbors regression," *Frontiers in big Data,* vol. 7, p. 1402384, 2024.

[219] X. Zhou and Q. He, "Modeling and simulation of buck-boost converter with voltage feedback control," in *MATEC web of conferences*, 2015, vol. 31: EDP Sciences, p. 10006.

[220] R. D. Shukla and R. K. Tripathi, "Low voltage ride through (LVRT) ability of DFIG based wind energy conversion system II," in *2012 Students Conference on Engineering and Systems*, 2012: IEEE, pp. 1-6.

[221] R. Pena, J. Clare, and G. Asher, "Doubly fed induction generator using back-to-back PWM converters and its application to variable-speed wind-energy generation," *IEE Proceedings-Electric power applications,* vol. 143, no. 3, pp. 231-241, 1996.

[222] T. Brekken, N. Mohan, and T. Undeland, "Control of a doubly-fed induction wind generator under unbalanced grid voltage conditions," in *2005 European conference on power electronics and applications*, 2005: IEEE, pp. 10 pp.-P. 10.

[223] L. Shang, H. Guo, and W. Zhu, "An improved MPPT control strategy based on incremental conductance algorithm," *Protection and Control of Modern Power Systems,* vol. 5, no. 2, pp. 1-8, 2020.